Numerical study of flame stability, stabilization and noise in a swirl-stabilized combustor under choked conditions

Corentin J Lapeyre

THÈSE

En vue de l'obtention du

DOCTORAT DE L'UNIVERSITÉ DE TOULOUSE

Délivré par :

Institut National Polytechnique de Toulouse (INP Toulouse)

Discipline ou spécialité :

Dynamique des fluides

Présentée et soutenue par :

M. CORENTIN LAPEYRE

le vendredi 18 septembre 2015

Titre :

ETUDE NUMERIQUE DE LA STABILITE, LA STABILISATION ET LE BRUIT DE FLAMME DANS UN BRULEUR TOURBILLONNAIRE EN CONDITIONS AMORCEES

Ecole doctorale :

Mécanique, Energétique, Génie civil, Procédés (MEGeP)

Unité de recherche :

Centre Européen de Recherche et Formation Avancées en Calcul Scientifique (CERFACS)

Directeur(s) de Thèse :

M. THIERRY POINSOT

M. FRANCK NICOUD

Rapporteurs :

M. FABIEN HALTER, UNIVERSITE D'ORLEANS

M. LUC VERVISCH, UNIVERSITE DE ROUEN

Membre(s) du jury :

M. SÉBASTIEN DUCRUIX, ECOLE CENTRALE PARIS, Président

M. CARLO SCALO, PURDUE UNIVERSITY EU, Membre

M. FRANCK NICOUD, UNIVERSITE MONTPELLIER 2, Membre

M. LAURENT GICQUEL, CERFACS, Membre

M. STÉPHANE MOREAU, UNIVERSITE DE SHERBROOKE QUEBEC, Membre

M. THIERRY POINSOT, INP TOULOUSE, Membre

Abstract

Air transportation is an essential part of modern business and leisure needs, and the number of passengers carried per year is rapidly increasing worldwide. The International Civil Aviation Organization estimates that this number went from 2.2 billion in 2009 to 3.0 billion in 2013, due in part to rapid growth in emerging countries such as China. Many challenges for aircraft designers arise from this increase in air traffic, such as meeting pollutant and noise emission regulations. The engines play a major part in these emissions, and combustor technology has evolved towards high-pressure Lean Prevaporized Premixed (LPP) combustion to increase efficiency and decrease pollutant emissions. Unfortunately, this technology tends to reduce engine robustness, with a decrease in flame stability and stabilization margins. Recent studies suggest that combustion noise could also be increased in these systems. New methods are needed to describe and understand the mechanisms at hand for future design and optimization in order to operate these engines safely while still achieving emission targets.

Large Eddy Simulation (LES) is a numerical approach to these problems which has shown excellent results in the past and is very promising for future design. The description of unsteady phenomena in these power-dense, confined and unsteady systems is essential to describe flame-turbulence interactions, acoustics and multi-physic couplings. As computing power grows, so does the amount of physics which can be modeled. Computational domains can be increased, and have gone from including only the reacting zone, to adding the fuel-air mixing areas, the heat liners and secondary flows, and the upstream and downstream elements.

In this Ph.D., a compressible LES solver named AVBP is used to describe an academic test rig operated at the EM2C laboratory named CESAM-HP, a pressurized combustion chamber containing a swirl-stabilized partially-premixed flame and ended by a choked nozzle with high-speed flow. This leads to an accurate description of the chamber outlet acoustic behavior, and offers the possibility to investigate the dynamic behavior of the full system, and the occurrence of flame-acoustic coupling leading to combustion instabilities. It also gives insight into the combustion noise mechanisms, which are known to occur both in the reacting zone and in the nozzle. As shown in this study, this behavior also has an impact on flame stabilization in this system.

This manuscript is organized as follows. In a first part, the context for chemistry, motion and acoustics of reacting multi-species flow is given. State of the art theories on reacting multi-species flow thermodynamics, thermo-acoustics, combustion noise and flame stabilization in swirled burners are presented. Basic toy models and test cases are derived to validate the understanding of direct and indirect combustion noise, and numerical validations are performed. In a second part, the practical details about numerical investigation of such systems are reported. Finally, the third part describes the application of these tools and methods to the CESAM-HP

test rig. The inclusion of the compressible nozzle in the LES computation yields results concerning three major issues for the burner: (1) flame stability, related to thermo-acoustic instabilities; (2) flame stabilization, and the occurrence of flame flashback into the system's injection duct; (3) combustion noise produced by the system, and identification of its separate contributions.

Short abstract

Civil air traffic increase requires to decrease future aircraft emissions. Aeronautic engine combustor technology has evolved towards Lean Prevaporized Premixed combustion to increase efficiency and reduce noxious emissions. Unfortunately, this technology tends to reduce engine robustness, with a decrease in flame stability and stabilization margins, and an increase in combustion noise. Compressible Large Eddy Simulation (LES), a promising numerical approach to describe full combustors, is used in this Ph.D on an academic test rig of a typical modern combustor flame in confined conditions. This investigation gives insight on the effects of full system dynamics on combustion instabilities, flame flashback and combustion noise. Is shows how these tools can yield understanding of the phenomena controlling flame stability and stabilization, which is essential in order to operate future engines safely.

Résumé

Le transport aérien est devenu un mode de déplacement primordial, et le nombre de passagers transportés chaque année est en rapide augmentation à travers le monde. La International Civil Aviation Organization estime que ce nombre est passé de 2.2 milliards en 2009 à 3.0 milliards en 2013, dû en partie à la croissance rapide de pays émergents comme la Chine. Les réglementations concernant les émissions polluantes et sonores s'adaptent et se durcissent, entraînant de nouveaux défis pour les constructeurs aéronautiques. Les chambres de combustion évoluent vers des technologies de combustion pauvre prémélangée prévaporisée pour améliorer l'efficacité et réduire la production de gaz néfastes. Malheureusement, cette technologie tend à réduire la robustesse des moteurs, en diminuant les marges de stabilité et de stabilisation de flamme. Des études récentes indiquent que cela pourrait aussi augmenter le bruit de combustion. Afin de poursuivre le design et l'optimisation des futurs moteurs, de nouvelles méthodes sont nécessaires pour décrire et comprendre les mécanismes en jeu, et d'opérer ces moteurs en toute sécurité tout en atteignant les objectifs de la réglementation.

La Simulation aux Grandes Échelles (SGE) est une approche numérique de ces problèmes, qui a montré d'excellents résultats par le passé et qui est très prometteuse pour les designs futurs. La comprehension de ces systèmes énergétiquement denses, confinés et instationnaires passe par la description des interactions flamme-turbulence, de l'acoustique et des couplages multi-physiques. À mesure que la puissance de calcul augmente, la quantité de physique qui peut être modélisée croît également, tout comme la taille des domaines de calcul. Autrefois limités à la zone de fluide réactif, la zone de mélange entre l'air et le carburant a pu être incluse, puis des parois de la chambre et des contournement de flux secondaire, jusqu'à finalement les éléments en amont et en aval de la chambre de combustion.

Dans cette thèse, un solveur SGE compressible nommé AVBP est utilisé pour décrire CESAM-HP, un banc d'essai académique situé au laboratoire EM2C: une chambre de combustion pressurisée, siège d'une flamme partiellement prémélangée stabilisée par un tourbillonneur, alimente une tuyère amorcée en fin de chambre. Ces calculs décrivent simultanément la chambre et la tuyère, tout en résolvant l'acoustique, ouvrant la voie à l'étude de la dynamique du système complet, et par là aux instabilités et au bruit de combustion. Cette étude montre enfin que la stabilisation de flamme est impactée par ce comportement dynamique, qui peut parfois entraîner des retours de flamme dans l'injecteur.

Ce manuscrit est organisé de la manière suivante : dans une première partie, le contexte pour la chimie, le mouvement et l'acoustique dans un écoulement réactif multi-espèces est donné. L'état de l'art en matière de thermodynamique, de thermo-acoustique, de bruit de combustion et de stabilisation de flamme dans les brûleurs tourbillonnaires est présenté. Des modèles simples et des cas test sont exposés pour valider la comprehension des phénomènes en jeu de manière isolée, et des

confirmations numériques sont apportées. Dans une seconde partie, les détails pratiques de la mise en œuvre de tels calculs sont donnés. Enfin, la troisième partie décrit l'application de ces outils et méthodes au banc CESAM-HP. L'inclusion de la tuyère compressible dans le domaine fournit des résultats concernant trois sujets majeurs pour le brûleur: (1) la stabilité de la flamme, en lien avec les instabilités de combustion; (2) la stabilisation de la flamme, et l'apparition de retour de flamme dans l'injecteur; (3) le bruit de combustion produit par le brûleur, ainsi que l'identification de ses diverses contributions.

Résumé court

Les chambres de combustion aéronautiques s'orientent vers la combustion pauvre prévaporisée prémélangée pour améliorer l'efficacité et réduire les émissions nuisibles des moteurs. Malheureusement, cette technologue tend à réduire les marges de stabilité et de stabilisation des flammes, tout en augmentant le bruit de combustion. La Simulation aux Grandes Échelles compressible, une approche numérique prometteuse pour décrire les chambres complètes, est utilisée dans cette thèse sur un cas académique de flamme typique des brûleurs modernes en conditions confinées. L'étude fournit des éléments clés sur l'effet de la dynamique du système complet sur les instabilités de combustion, le retour de flamme et le bruit de combustion. Elle montre comment ces outils peuvent aider à comprendre les phénomènes qui contrôlent la stabilité et la stabilisation de flamme, ce qui est essentiel pour opérer les moteurs futurs en toute sécurité.

Contents

1 Introduction **1**
- 1.1 Public health issues related to air traffic . . . 1
- 1.2 Combustion instabilities and combustion noise: two separate worlds? 4

I Theoretical framework **9**

2 Description of reacting flows **13**
- 2.1 Introduction . . . 13
- 2.2 Thermodynamic background . . . 13
- 2.3 Equations of motion for multicomponent gaseous flow . . . 22

3 Acoustics and Thermoacoustics **25**
- 3.1 Introduction . . . 25
- 3.2 Constitutive equations for acoustics . . . 25
- 3.3 Flame acoustic source terms and thermoacoustic instability mechanism 33

4 Realistic outlet conditions for combustion chambers **39**
- 4.1 Introduction . . . 39
- 4.2 Numerical modeling of a nozzle outlet . . . 39
- 4.3 Influence of outlet conditions on thermo-acoustic instabilities . . . 51

5 Combustion noise: sources and influence of outlet conditions **69**
- 5.1 Introduction . . . 69
- 5.2 Sources of sound associated with combustion . . . 70
- 5.3 Assessing combustion chamber noise . . . 86

6 Flame stabilization in swirled flows **101**
- 6.1 Flashback mechanisms in swirled combustors . . . 101
- 6.2 Flame stabilization in swirled combustors: flame propagation along a vortex axis . . . 103
- 6.3 A numerical illustration of flame flashback along a vortex axis . . . 109

II Tools and methodologies **119**

7 Numerical methods **123**
- 7.1 Introduction . . . 123
- 7.2 Numerical resolution strategies for the Navier-Stokes equations . . . 125
- 7.3 The AVBP LES solver . . . 127
- 7.4 The AVSP Helmholtz solver . . . 134

7.5 CHORUS methodology for wave extraction and combustion noise prediction . . . 135

8 Numerical approaches for nozzles and choked flows 137
8.1 Introduction . . . 137
8.2 LES of chambers with nozzles . . . 137
8.3 Nozzle impedances for chamber outlets . . . 150

III The CESAM-HP combustor 153

9 The CESAM-HP combustor 157
9.1 The CESAM-HP test rig . . . 157
9.2 Numerical setup to simulate CESAM . . . 160
9.3 Chemical model . . . 163
9.4 *A posteriori* validation of the chemical approach . . . 168

10 LES of unchoked regimes 171
10.1 Introduction . . . 171
10.2 Non reacting simulations . . . 173
10.3 OPEN reacting simulations . . . 178
10.4 Conclusion . . . 186

11 Choked flow study 187
11.1 Compressible LES strategy . . . 187
11.2 **CHOKED-PR**: Auto-excited AI-VCF in the fully premixed case . . . 189
11.3 **CHOKED-ST**: Control of AI-VCF using fuel staging . . . 195
11.4 Thermoacoustic Analysis . . . 199
11.5 Conclusions . . . 204

A NSCBC Inlet acoustic impedance 209

B LODI for spherically symmetric flows 211
B.1 The LODI formalism . . . 211
B.2 A non-reflecting boundary with the LODI formailsm . . . 212
B.3 LODI applied to a spherical problem . . . 213
B.4 A spherically symmetric problem is not LODI . . . 216

Bibliography 217

Chapter 1

Introduction

1.1 Public health issues related to air traffic

1.1.1 Pollutant emissions

The fuel consumption of aircraft engines has a direct impact on operational costs for airlines, and as a result continuous efforts to increase engine efficiency (or specific fuel consumption SFC) have been lead since the first civil aircraft jet engines were put in service. Grönstedt *et al.* (2014) showed the trends of SFC developments since the 1960's, reproduced here in Fig. 1.1. The current high bypass ratio technology used

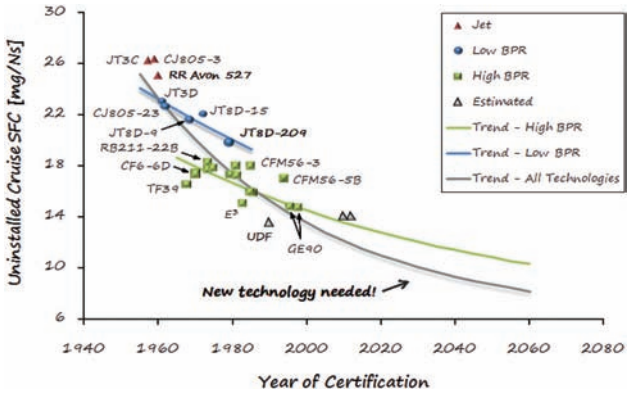

Figure 1.1: SFC trends since the 1960's for uninstalled cruise operation of common aircraft engines. From Grönstedt *et al.* (2014).

to decrease SFC has seen numerous improvements since the 1970's. Grönstedt *et al.* (2014) argue that the potential gain left with these technologies is reaching a plateau for simple thermodynamic reasons, and that only technological ruptures through advanced cycles, such as open rotor (Hendricks, 2011), intercooled recuperated engines (Xu & Grönstedt, 2010) or pulse detonation combustion (Wintenberger, 2004) can offer solutions to pursue the current improvement trend. The latter makes use of the Humphrey thermodynamic cycle, known to have a better theoretical efficiency than the classical constant pressure combustion cycle of Brayton used in most aircraft engines today. The recent concept of constant volume combustion (Aguilar, 2013) suggests to make use of this cycle using a rotating valves system, and for the 2050 SFC reduction objectives this is also a promising concept. Accurate numerical description of such systems is a difficult task, as many industry standard

tools have been optimized for decades on steady state engines (gas turbines). The physics of a pulsed combustor is of course unsteady, and new approaches are needed to describe it accurately, as in the work of Scalo *et al.* (2015).

While the reduction of fuel consumption has a direct and proportional impact on carbon dioxyde CO_2 emissions, it also has some negative side effects. Except for intercooler recuperated engines, these current and future engine concepts benefit from concentrated compact combustion zones, which tend to achieve high maximum chamber temperatures. This has a direct effect on nitrogen oxides NO_x production, which in turn are highly harmful to human health. As shown by Suder (2012), this is generally a direct effect of SFC increase (Fig. 1.2). This is due to the very

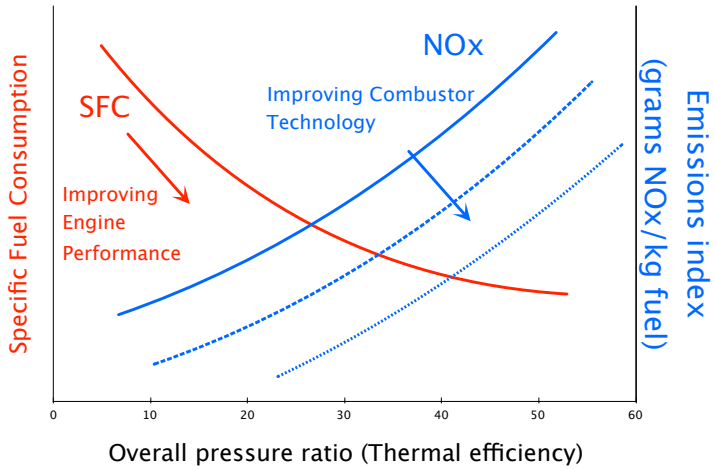

Figure 1.2: Specific fuel consumption and NOx emissions versus overall pressure ratio for present aircraft engine technologies. Reproduced from Suder (2012).

non-linear behavior of NO_x production with temperature (Zeldovich, 1946). As explained by Huang & Yang (2009), gas turbines have traditionally used diffusion flame combustors because of their robustness and reliability. This type of combustor however leads to intense localized combustion and high levels of NO_x. The most short-term feasible and widely used solution to reduce these emissions today is lean premixed combustion. However, this type of burner is very prone to difficulties in both flame stabilization (flame flashback can occur (Huang & Yang, 2009)) and flame stability (thermoacoustic instabilities can occur (Lieuwen & Yang, 2005)).

1.1.2 Noise emissions

The unharmed human ear can detect pressure variations ranging in air from 2×10^{-5} Pa (0 dB or 10^{-12} W m^{-2}) to 200 Pa (140 dB or 100 W m^{-2}) in amplitude, and 20 Hz - 20 kHz in frequency. When the combination of frequency, amplitude and exposure time reaches a certain threshold, a subject will start to feel pain and his hearing can be impaired permanently. However, exposure to lower levels of noise over longer periods of time, ranging from minutes to years, can also be the source of "annoyance". Studies in the past 40 years, such as partly summarized in the review of Knipschild

(1977) suggest that such annoyances lead to extra-auditory health effects such as sleep disturbances, mental disorders, psychosomatic symptoms, and even increase in cardiovascular diseases. Some of these studies should however be considered with caution, as suggested by Morrell *et al.* (1997), and more data should be collected and analyzed to clearly assess the effects of noise "annoyance" on human health. Nevertheless, it is clear that aircraft noise is an important issue in the domain of public health, and that major steps towards its reduction must be taken for next generation aircrafts.

Aircraft noise : perspectives and regulations Annoyance linked to aircraft noise is obviously in proportion with the amount of traffic. The International Civil Aviation Organization ICAO (2007) estimates that global traffic for 2025 should double compared to what it was in 2005. This strong increase is of course in part due to the rapid development of emerging countries such as China. The trend however also applies to areas already home to a dense traffic such as Europe and North America. Moreover, in these areas many populations already live close to aircraft traffic, and the possibilities to build new airports can be extremely limited. For these reasons, noise emissions must be reduced at their source. This assessment has lead the Advisory Council for Aeronautics Research in Europe (ACARE) to fix goals of overall reduction of aircraft generated noise by 10 EPNdB (Effectively Perceived Noise) by 2020 in comparison to 2002 (ACARE, 2002). The acoustic certification is obtained at three specific conditions, namely *sideline*, *approach* and *flyover cutback* (Fig. 1.3). Several strategies can be considered in order to reduce this perceived

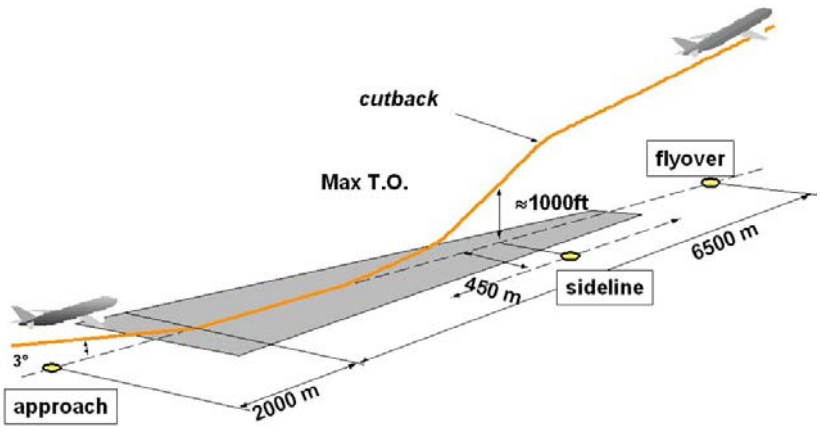

Figure 1.3: The three acoustic certification points for aircraft. From Huber & Illa (2007).

noise:

- adapt procedures concerning trajectories and engine regimes during take-off and landing;
- modify the directivity of noise sources and orientate them away for the ground;
- absorb sound produced using specific materials for outer coatings;

- reduce acoustic sources.

Reduction of aircraft noise Reduction of aircraft noise necessitates a global approach to all acoustic sources. Since noise is perceived by the human ear according to a logarithmic scale (measured in dB), reducing only one of two equivalent sources is very inefficient. For example, the noise produced by two non coherent acoustic sources is only reduced by 3 dB if one of these sources stops emitting completely. In order to decrease the noise emitted by a set of multiple non coherent sources, one must therefore reduce all sources by similar factors.

Noise generated by aircraft has various origins. Contributions can at first be classified in two obvious categories: airframe noise and engine noise. Modern approaches to airframe noise through numerical simulation, named computational aeroacoustics (CAA) have shown excellent results (Bailly *et al.*, 2005). The object of this PhD is to study engine noise, which is itself due to several origins, as displayed schematically in Fig. 1.4.

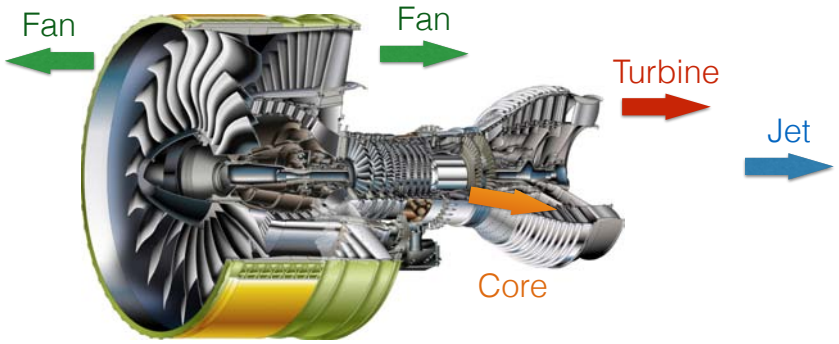

Figure 1.4: Various sources of noise in aircraft engines.

Huber & Illa (2007) produces the noise contributions for all three certification points of a typical Airbus four-engine plane. This data is reproduced in Fig. 1.5. While this seems to indicate that core noise has small contributions in all certification measuring configurations, recent studies indicate that the evolutions aimed at pollutant emissions such as lean premixed combustion could change this paradigm. Liu *et al.* (2014) suggest that because of increased unsteadiness in lean premixed combustors, the combustion noise rises drastically compared to current combustors. Because of this, a precise evaluation of combustion noise in future engines requires accurate description of the combustion chamber.

1.2 Combustion instabilities and combustion noise: two separate worlds?

In order to meet pollutant emissions regulations, engine manufacturers rely increasingly on lean premixed combustion for their industrial burners. These high power

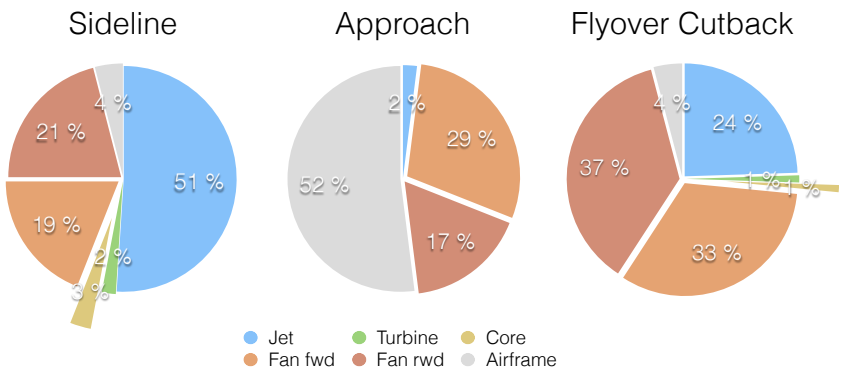

Figure 1.5: Noise contributions for all three certification points of a typical Airbus 4 engine plane.

- low bulk systems concentrate enormous amounts of energy, released in turbulent and unsteady flows. Such systems have been shown to be prone to combustion instabilities as well as increased *combustion noise* (CN). Combustion instabilities driven by acoustic phenomena are referred to as *thermoacoustic instabilities* (TI), and can rapidly lead to damage or even catastrophic failure of the system. Another known issue with lean premixed burners is *flame stabilization* (FS) problems, which can influence both CN and TI, or even lead to destruction of the burner.

1.2.1 Noise versus combustion studies

Traditionally, the community that studies CN has an aeroacoustic background. Additionally, CN evaluations generally come after the design process, once all operating points and safety margins for the engine at hand are well determined. TI and FS on the other hand are viewed as combustion-related issues, addressed by combustion specialists. These dangerous phenomena are detected during the engine design phase, and once eliminated from the engine operating zone the problem is considered solved. Because of these differences, these two fields of study are separated. Fig. 1.6 sketches the essential differences between CN and TI study approaches. The CN approach has focused for many years on the decomposition of noise production. Sources are identified both in the flame region (direct acoustic noise as well as entropic perturbations) and the system downstream of the combustion chamber. Note that this system, whether a turbine or a simple nozzle, will be referred to as the *expansion region* throughout this manuscript. Propagation of acoustics through the entire system and generation of sound in the expansion region by entropy waves are the two main subjects of CN. This analysis is therefore one-way only in the downstream direction. The chamber dynamics are generally considered as entry data, and no feedback of acoustics on the combustion process is considered.

TI studies on the other hand focuses on the combustion chamber dynamics. In order to model these correctly, the acoustic source terms are important, but the acoustic behavior of all combustor boundaries is also crucial, as the chamber acoustics

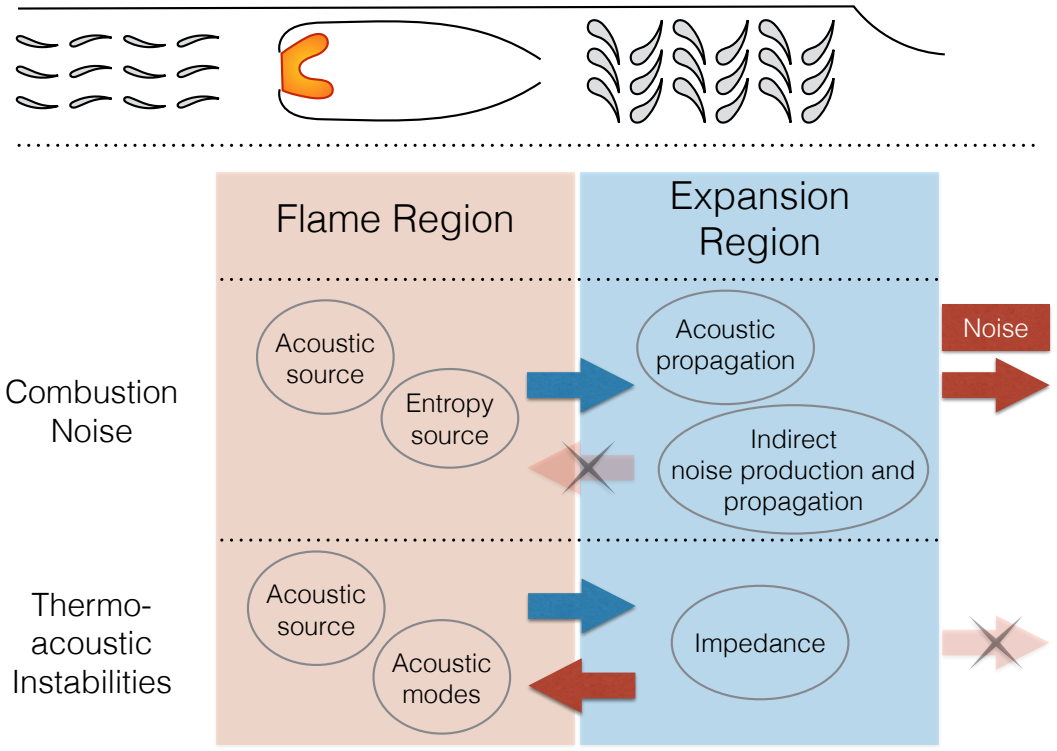

Figure 1.6: Comparison of the CN approach with the TI description. CN is a one-way downstream-only analysis. TI views the expansion region only as an acoustic impedance for the chamber.

influence the combustion process and drive the instability. The expansion region is therefore only considered for it's impedance as seen from the combustor, and the downstream propagation is of no concern. In practice, noise outside an engine often includes broadband noise (expected to correspond to CN) and discrete peaks (associated to TI). Even if these peaks are not detrimental for the engine structure, they do produce noise and their discrete tones are clearly head by passengers and people outside the aircraft. Therefore, there is not much doubt that a proper study of combustion noise must account for both CN *and* TI mechanisms.

TI and FS studies both rely on high-fidelity simulations of the combustion process. However, again these two approaches are often considered as separate. TI is closely linked to the acoustic behavior of the system, while FS is generally more dependant on flame speed *via* fuel mixing and turbulence levels, as well as thermal processes.

1.2.2 A unified approach

The present PhD work was initiated in the field of CN within the framework of the EC RECORD project coordinated by DLR (Dr. Bake). As will be shown later, TI rapidly entered the issues to be addressed because the target combustor at EM2C proved to exhibit multiple unstable modes, thereby making this study a mixed CN-TI work. In addition to these results, it was shown that this burner displayed multiple

FS positions, and that these were not independent of TI in the system. The purpose of this manuscript is to demonstrate the link that exists between CN, TI and FS. Several major reasons exist for this unified approach:

- the study of CN on academic or simplified test benches often implies that many damping systems available in full scale combustors are absent. The control of TI in this context can be difficult, hence the importance of understanding the link between instabilities and noise;
- TI are the result of amplified acoustic modes of cavities. In operating engines, these modes are damped to mechanically acceptable levels. However, the acoustic trace of these modes can remain and appear in CN, since the order of magnitude of power in acoustics is much lower than for mechanical forces on the structure. In such a case, the instability problem would be labeled "solved" by the TI community, yet assessing damped TI levels is essential to the correct prediction of CN;
- FS has also been shown to be more difficult in lean premixed combustion. In some cases it can be closely related to TI, and have a dramatic effect on CN. It requires an appropriate resolution of thermal phenomena in the combustor.

One of the difficulties in this unification is that these phenomena do not take place on the same scales. The mean power released by combustion can be of the order of $1\,\mathrm{GW\,m^{-3}}$, but acoustics are the study of very small perturbations of pressure around the mean state, with powers which are several orders of magnitude smaller (typically 10^{-7} times less than engine power). A unified approach must therefore be able to capture all these scales, as well as low and high Mach number flows with compressibility effects, and multi-species formulations inherent to combustion but usually dismissed in acoustics. While this seems like a tremendous task, the power of modern supercomputers combined with high-fidelity numerical simulation offers an excellent tool to bridge these gaps and provide new insight into CN, TI and FS phenomena.

This manuscript is organized as follows:

- **Part I : Theoretical framework**
  A tour of the physical and numerical models relevant to the study of CN, TI and FS in gas turbines will be given in this section. Since outlet nozzles are inherent to this approach, they will appear nearly throughout the entire part. Chap. 2 will present fundamental thermodynamic and mechanical background used to describe turbulent reacting compressible flows. Chap. 3 will give the framework for acoustic studies, in low Mach number flows and also in varying ones. With the basics of both mean flow and acoustics set, the subject of nozzle termination will be treated in Chap. 4, and the effect on acoustic behavior of the outlet will be investigated. In Chap. 5, the basics of combustion noise study will be reminded, and the according nozzle models described. A new toy model will be given for the ratio of indirect to direct noise created in a chamber feeding a nozzle. The concepts surrounding swirl-stabilization of flames will be introduced in Chap. 6, in the form of another toy model for the propagation of

a flame front in a swirled channel. These toy models allow the derivation of basic theoretical elements required to understand Part II and III.

- **Part II : Tools and methodologies**
  The high fidelity simulations needed to study acoustics are very sensible to numerical setups. The set of tools used to study both combustion and acoustics is described in Chap. 7, and the specificities of nozzle flow simulation and monitoring are grouped in Chap. 8.

- **Part III : The CESAM-HP Combustor**
  The previous developments will be applied in this part to the combustor of EM2C. While difficulties have been encountered in pursuit of the initial objective to study combustion noise, these have given excellent examples of the coupling between CN, TI and FS. After describing the experimental configuration and the associated numerical setup (Chap. 9), the set of simulations without nozzle will be presented (Chap. 10) before introducing the complete simulations with the actual nozzle included (Chap. 11). It will be shown that the stabilization of a premixed swirled flame can be a difficult task, and that its control is essential for the combustor dynamics. The argument will be made that to assess the noise produced by combustion, the complete combustor dynamics (including TI) must be captured. Through acoustic control or auto-excitation, combustion noise produced by a combustor exhibiting various behaviors will be compared.

Part I

Theoretical framework

Table of Contents

2 Description of reacting flows **13**

2.1 Introduction . . . 13

2.2 Thermodynamic background . . . 13

2.2.1 Laws of thermodynamics . . . 13

2.2.2 Link with measurable quantities . . . 14

2.2.3 Combined statement of the first and second law . . . 15

2.2.4 Intensive formulation . . . 16

2.2.5 Ideal gas . . . 18

2.2.6 Entropy and acoustics . . . 20

2.3 Equations of motion for multicomponent gaseous flow . . . 22

2.3.1 Governing equations for fluid flow . . . 22

2.3.2 Simplifications for gaseous reacting flows . . . 22

3 Acoustics and Thermoacoustics **25**

3.1 Introduction . . . 25

3.2 Constitutive equations for acoustics . . . 25

3.2.1 The Euler equations . . . 25

3.2.2 Simplified forms of the Euler equations . . . 27

3.2.3 Characteristic form . . . 28

3.2.4 The Linearized Euler Equations (LEE) . . . 30

3.3 Flame acoustic source terms and thermoacoustic instability mechanism 33

3.3.1 Euler equations with heat source . . . 33

3.3.2 LEE with heat source . . . 34

3.3.3 Thermoacoustic Instabilities . . . 35

4 Realistic outlet conditions for combustion chambers 39

4.1 Introduction . . . 39

4.2 Numerical modeling of a nozzle outlet . . . 39

4.2.1 Choosing a domain for combustion chamber LES . . . 39

4.2.2 Steady state flow through a nozzle . . . 44

4.3 Influence of outlet conditions on thermo-acoustic instabilities . . . 51

4.3.1 The Rijke tube as a toy model . . . 52

4.3.2 Bulk mode instability in choked combustors . . . 57

4.3.3 Conclusion . . . 67

5 Combustion noise: sources and influence of outlet conditions 69

5.1 Introduction . . . 69

5.2 Sources of sound associated with combustion . . . 70

5.2.1 The concept of “acoustic analogy” . . . 70

5.2.2 Noise associated with combustion in an aeronautic burner . . . 73

5.2.3 Flame or "direct" noise . . . 74

5.2.4 Sound production of a confined flame: "indirect" noise . . . 79

5.3 Assessing combustion chamber noise . . . 86

5.3.1 The toy model of Leyko (2010) . . . 86

5.3.2 Flame modelling: how to improve the toy model? . . . 90

5.3.3 Conclusion on the toy model . . . 99

6 Flame stabilization in swirled flows 101

6.1 Flashback mechanisms in swirled combustors . . . 101

6.2 Flame stabilization in swirled combustors: flame propagation along a vortex axis . . . 103

6.2.1 The question of flame speed along a vortex axis . . . 104

6.2.2 FPAVA in wall bounded flows . . . 108

6.3 A numerical illustration of flame flashback along a vortex axis . . . 109

6.3.1 A toy model for swirled flow: the Poiseuille SF . . . 110

6.3.2 Using the Poiseuille SF as a test case for FPAVA . . . 114

6.3.3 Conclusions for FPAVA simulation . . . 118

Chapter 2

Description of reacting flows

Numerical simulations have become an essential tool to study combustion noise as well as flame dynamics and combustion instabilities. These require modelling of turbulent unsteady chemically reacting gases. While some engines use liquid fuel, this PhD focuses only on prevaporized or gaseous fuel, and a single gaseous phase will be considered as used in the target experiment of Ecole Centrale. Usual acoustic studies deal with single component flows, and the adaptation to varying mixture composition flows is not necessarily straightforward. Because this PhD focuses both on combustion processes and acoustics, a rigorous thermodynamic background for combustion is derived, thus defining clearly the notion of acoustics for a multispecies gas mixture, and expliciting the concept of "excess density" in this context. The equations of motion for multicomponent gaseous flow will then be given, as well as the modelling of the chemical reactions that take place. This description is classical in the fluid mechanics and combustion studies, and is given here for completeness.

2.1 Introduction

The numerical study of modern combustion chambers implies at least the description of turbulent and chemically reacting gases, with varying density. In some cases, two-phase flows must also be considered. This "multispecies" approach is rare in the computational fluid dynamics (CFD) community, but is of course necessary in the field of combustion. Because this is uncommon, notably in the acoustic community where mixture fluctuations are generally ignored, the joint study of combustion and acoustics renders crucial a rigorous thermodynamic background to describe the combustion process.

2.2 Thermodynamic background

2.2.1 Laws of thermodynamics

To discuss specific issues like the noise generated by entropy spots in an accelerated flow, it is necessary to revisit a few concepts like entropy in a multispecies flow with varying composition. This is done here, and is largely inspired from the reference textbook of DeHoff (2006).

Let the system of interest be a mesoscopic fluid particle. The first law of thermodynamics states that the internal energy U of this system varies by a quantity $\mathrm{d}U$ according to:

$$\mathrm{d}U = \delta Q + \delta W + \delta W' \tag{2.1}$$

where :

- δQ is the quantity of heat that flows into the domain;
- δW is the mechanical work received by the system;
- $\delta W'$ is the sum of all other kinds of work received by the system.

The second law of thermodynamics applied to the same system introduces another extensive state function S known as *entropy*. When the system undergoes changes, it can exchange entropy with the outside and create entropy. This is noted $\Delta S = S_t + S_p$, where $_t$ denotes transferred entropy and $_p$ entropy production.

The second law states that for any variation in the system state:

$$S_p \geq 0 \tag{2.2}$$

In the specific case where $S_p = 0$, the transformation is said to be *reversible*.

An important property of entropy is that it is a *state function*. As such, let a system change from state A to state B. The entropy change has a unique definition $\Delta S = S_B - S_A$. This statement does not account for the path that has been followed in order for the change from A to B to occur. Therefore, while it can often be a difficult task to compute the entropy production of a transformation directly, if a reversible path from A to B can be characterized, the following equality holds:

$$\Delta S = S_t + S_p \tag{2.3}$$

$$= S_{t,rev} + 0 \tag{2.4}$$

where $S_{t,rev}$ represents the exchanged entropy in the reversible process case. If both transferred entropies can be computed, then the entropy production is simply $S_p = S_{t,rev} - S_t$.

2.2.2 Link with measurable quantities

When Sadi Carnot introduced the concepts surrounding the *Carnot Cycle*, he demonstrated that in the case of an ideal cycle $\mathcal{C}$ (that is, reversible, $S_p = 0$), the entropy transfer could be linked to heat transfer δQ_{rev} according to:

$$\Delta S = \oint_{\mathcal{C}} \frac{\delta Q_{rev}}{T} \tag{2.5}$$

Moreover, he demonstrated that any reversible transformation could be decomposed as an infinite series of Carnot cycles. In consequence, and according to the argument of Eq. (2.4), the entropy variation of any transformation can be computed by using the heat exchange δQ_{rev} of a reversible process that leads to the same total transformation.

A simpler argument applies to the mechanical work received by the system: it is the work done by the external pressure applied to the system. In case of a reversible (quasistatic) process, the external pressure balances at every instant the internal pressure. By definition, this work is:

$$\delta W_{rev} = -P\,\mathrm{d}V \tag{2.6}$$

In a multispecie monophase mixture, the change in the quantity of a specie (by echange with the outer medium, or conversion of some species to others through chemical reaction) can lead to energy change. The energy variation associated to a change in the quantity of the specie k, namely $\mathrm{d}n_k$, is quantified by the *chemical potential* of the specie k, defined as:

$$\mu_k = \left(\frac{\partial U}{\partial n_k}\right)_{S,V,n_{j\neq k}} \tag{2.7}$$

and all non-mechanical work received by the system writes:

$$\delta W'_{rev} = \sum_{k=1}^{N} \mu_k\,\mathrm{d}n_k \tag{2.8}$$

2.2.3 Combined statement of the first and second law

Like entropy, internal energy is a state variable that does not depend on the transformation path. In consequence, any transformation for which a reversible counterpart is exposed yields:

$$\begin{aligned}\mathrm{d}U &= \delta Q + \delta W + \delta W' \\ &= \delta Q_{rev} + \delta W_{rev} + \delta W'_{rev}\end{aligned}$$

Combining all the previous declarations, the *combined statement of the first and second law* can be exposed:

$$\mathrm{d}U = T\,\mathrm{d}S - P\,\mathrm{d}V + \sum_{k=1}^{N} \mu_k\,\mathrm{d}n_k \tag{2.9}$$

It is important to note that:

- the equivalence beween the δ terms and their measurable counterparts holds **only for reversible** processes, but
- the internal energy Eq. (2.9) holds for **any** transformation.

Internal energy is well suited to describe isochoric transformations ($\mathrm{d}V = 0$), since if species stay constant ($\mathrm{d}n_k = 0$) the internal energy variation is directly related to the entropy change:

$$\mathrm{d}U = T\,\mathrm{d}S$$

Extensive		Volume		Molar		Mass	
Not.	Unit	Not.	Unit	Not.	Unit	Not.	Unit
U	J	u_V	$\mathrm{J\,m^{-3}}$	u_m	$\mathrm{J\,mol^{-1}}$	u	$\mathrm{J\,kg^{-1}}$
H	J	h_V	$\mathrm{J\,m^{-3}}$	h_m	$\mathrm{J\,mol^{-1}}$	h	$\mathrm{J\,kg^{-1}}$
S	$\mathrm{J\,K^{-1}}$	s_V	$\mathrm{J\,K^{-1}\,m^{-3}}$	s_m	$\mathrm{J\,K^{-1}\,mol^{-1}}$	s	$\mathrm{J\,K^{-1}\,kg^{-1}}$
C_P	$\mathrm{J\,K^{-1}}$	$c_{P,V}$	$\mathrm{J\,K^{-1}\,m^{3}}$	$c_{P,m}$	$\mathrm{J\,K^{-1}\,mol^{-1}}$	c_P	$\mathrm{J\,K^{-1}\,kg^{-1}}$

Table 2.1: Notations for extensive and intensive quantities

Another measure of energy is the enthalpy H, defined as $H = U + PV$. It is sometimes more practical to use enthalpy than internal energy. The fluctuations of H write:

$$\mathrm{d}H = T\,\mathrm{d}S + V\,\mathrm{d}P + \sum_{k=1}^{N} \mu_k\,\mathrm{d}n_k \tag{2.10}$$

which shows that for a non-reacting isobaric transformation ($\mathrm{d}P = 0$), enthalpy and entropy variation are related by:

$$\mathrm{d}H = T\,\mathrm{d}S$$

2.2.4 Intensive formulation

Finite volume approaches are popular in computational fluid dynamics and require to solve the conservative equations, as will be described later on. The previous extensive formulations are not well suited for this description. For any extensive variable Φ, an intensive counterpart can be defined. In case of a volume value, this yields:

$$\phi = \lim_{V \to 0} \frac{\Phi}{V} \tag{2.11}$$

An example of this is the commonly used density ρ which can be defined as $\rho = \lim_{V\to 0} {}^{m}\!/_{V}$. Mass and molar values can be defined in an analogous manner. Energy and entropy can be defined according to these various approaches, and the subsequent notations and units are presented in Tab. 2.1. Let the system be defined as a small quantity of matter in gaseous phase, which can exchange work and heat but not mass with its surroundings. It contains k species, each quantity of which is noted n_k (in moles). All intensive properties across this domain are considered homogeneous : pressure P, temperature T and chemical potential μ_k. The species are therefore equally distributed in the entire volume V. The system can be described by its state functions U and S, or equivalently in volume formulations:

$$u_V = \frac{U}{V} \qquad\qquad s_V = \frac{S}{V}$$

since all quantities are homogeneous in the volume V. The differential of energy writes:

$$\mathrm{d}u_v = \mathrm{d}\left(\frac{U}{V}\right) = \frac{1}{V}\,\mathrm{d}U - \frac{U}{V^2}\,\mathrm{d}V \tag{2.12}$$

Because all intensive properties are homogeneous, Eq. (2.9) can be integrated at constant T, P and μ_k:

$$U = TS - PV + \sum_k \mu_k n_k$$

and Eq. (2.12) becomes:

$$\mathrm{d}u_V = T\left[\frac{1}{V}\,\mathrm{d}S - \frac{S}{V^2}\,\mathrm{d}V\right] - \underbrace{\left[\frac{1}{V}\,\mathrm{d}V - \frac{V}{V^2}\,\mathrm{d}V\right]}_{0} + \sum_k \mu_k\left[\frac{1}{V}\,\mathrm{d}n_k - \frac{n_k}{V^2}\,\mathrm{d}V\right]$$

$$\mathrm{d}u_V = T\,\mathrm{d}s_V + \sum_k \frac{\mu_k}{W_k}\,\mathrm{d}\rho_k \tag{2.13}$$

where W_k is the molar mass of specie k, as in the rest of this manuscript. This curious result can be unintuitive. If U and u_V were somehow equivalent, it could be expected that they depend on the same number of independent variables. Here however, $\mathrm{d}U$ relates to $N+2$ independant variables (T, P, μ_k for $k = 1$ to N, but $\mathrm{d}u_V$ only to $N+1$. This is because, as shown by Eq. (2.12), $\mathrm{d}U$ and $\mathrm{d}u_V$ are in fact very different in nature: while the energy in V can change both by changing the energy of each particle (temperature variation) or by changing the total volume, the energy per unit volume only varies in the former transformation, and not the latter.

This observation also applies to molar quantities, as $n = \sum_k n_k$ is not necessarily constant if chemical reactions take place in the domain. There is however an intensive property that is equivalent in nature to its extensive counterpart, namely energy per unit mas u. Since the total mass in the system is constant, it writes:

$$u = \frac{U}{m} = \frac{U}{\rho V} \qquad \text{hence} \qquad \mathrm{d}u = \frac{\mathrm{d}U}{\rho V} \tag{2.14}$$

and since mass conservation implies by definition:

$$\rho = \frac{m}{V} \qquad \text{hence} \qquad \frac{\mathrm{d}\rho}{\rho} = -\frac{\mathrm{d}V}{V} \tag{2.15}$$

and the relation between n_k and Y_k writes in differential form:

$$n_k = \frac{\rho V}{W_k} Y_k \qquad \text{hence} \qquad \mathrm{d}n_k = \frac{\rho V}{W_k}\,\mathrm{d}Y_k \tag{2.16}$$

the energy fluctuation per unit mass writes in fully intensive form:

$$\mathrm{d}u = T\,\mathrm{d}s + \frac{P}{\rho}\frac{\mathrm{d}\rho}{\rho} + \sum_k \frac{\mu_k}{W_k}\,\mathrm{d}Y_k \tag{2.17}$$

Variable	$\mathrm{d}S$	$\mathrm{d}s_m = \mathrm{d}\left(\frac{S}{n}\right)$	$\mathrm{d}s_V = \mathrm{d}\left(\frac{S}{V}\right)$	$\mathrm{d}s = \frac{\mathrm{d}S}{\rho V}$
Variation	0	$\neq 0$	$\neq 0$	0

Table 2.2: Description of entropy variations for a closed system undergoing an "isentropic" process: the intensive entropy variation is not necessarily 0, as it depends on the definition chosen.

It can be useful to rearrange this equation to yield the entropy per unit mass s:

$$\mathrm{d}s = \frac{\mathrm{d}u}{T} - \frac{P}{\rho T}\frac{\mathrm{d}\rho}{\rho} - \frac{1}{T}\sum_k \frac{\mu_k}{W_k}\,\mathrm{d}Y_k \tag{2.18}$$

For reacting flows, this expression directly shows the effect of composition fluctuation ($\mathrm{d}Y_k$) on the entropy. This is important because in the framework of combustion chambers, acoustics must take entropy perturbations into account, as explained in Chap. 5.

These observations show that the equivalence between various expressions of state variables is subject to the choice of the variable used for intensive description. Care must be taken when making this choice, as some transformations are often described according to their extensive properties, but description of a Eulerian field requires intensive properties. for example, an "isentropic" process is generally defined as a process where $\mathrm{d}S = 0$. Tab. 2.2 summarizes the implications for usual intensive descriptions of entropy.

2.2.5 Ideal gas

In order to close the equations of motion described in Sec. 2.3, it is necessary to introduce an equation of state for the fluid. This equation provides a relation between the characteristic variables describing the system, based on thermodynamic reasoning. When gas particles are close (high density) and hold strong amounts of energy (temperature), interactions between particles must be accounted for. However, in the context of this manuscript, pressures are low enough for these effects to be neglected. The gas is considered to be an *ideal gas at global thermodynamic equilibrium*, the equation of state of which writes:

$$PV = nRT \tag{2.19}$$

This fundamental equation is often written for a single specie fluid. A multispecies code requires several species, each with a different molar mass W_k. Fortunately, *Dalton's law* states that for an ideal gas, the total thermodynamic pressure is the sum of the partial pressures. Each partial pressure is defined as the pressure if only one specie were present in the volume, hence:

$$P = \sum_k P_k = \sum_k n_k \frac{RT}{V} \tag{2.20}$$

and since $n = \sum_k n_k$, Eq. (2.19) still holds for a multispecies gas.

For a single specie gas the internal energy can be written as a function of any pair of independent thermodynamic variables, *e.g.* T and P:

$$\mathrm{d}U = \left(\frac{\partial U}{\partial T}\right)_V \mathrm{d}T + \left(\frac{\partial U}{\partial V}\right)_T \mathrm{d}V$$

The term in front of $\mathrm{d}T$ is defined as the *heat capacity at constant volume* C_V. Starting from Eq. (2.19), generally in extensive form $PV = nRT$, DeHoff (2006) for example shows that the term in front of $\mathrm{d}V$ is 0, hence $\mathrm{d}U = C_V\,\mathrm{d}T$. This is a particular case for ideal gases where the internal energy depends only on one thermodynamic variable, namely the temperature. Similarly, the *heat capacity at constant pressure* C_P can be defined to relate enthalpy change $\mathrm{d}H$ to $\mathrm{d}T$. All these definitions amount to:

$$\mathrm{d}U = \left(\frac{\partial U}{\partial T}\right)_V \mathrm{d}T = C_V\,\mathrm{d}T \tag{2.21}$$

$$\mathrm{d}H = \left(\frac{\partial H}{\partial T}\right)_P \mathrm{d}T = C_P\,\mathrm{d}T \tag{2.22}$$

In an ideal gas mixture of several species, each behaves as an ideal gas and the two previous relations hold. The total gas energy and enthalpy write:

$$\mathrm{d}U = \sum_k C_{V,k}\,\mathrm{d}T = C_V\,\mathrm{d}T \tag{2.23}$$

$$\mathrm{d}H = \sum_k C_{P,k}\,\mathrm{d}T = C_P\,\mathrm{d}T \tag{2.24}$$

where the equivalent heat capacities are the sum of each species heat capacity.

The ratio of C_P to C_V is noted γ, and their difference equates to nR:

$$\gamma = \frac{C_P}{C_V} \tag{2.25}$$

$$nR = C_P - C_V = C_V(\gamma - 1) \tag{2.26}$$

Intensive formulations: State functions can be recast in intensive form, if great care is taken. The ideal gas law simply writes:

$$P = \rho RT \sum_k \frac{Y_k}{W_k} \tag{2.27}$$

but for internal energy, only the mass formulation behaves like the extensive expression of Eq. (2.23), for the reasons explained in the previous paragraph. Tab. 2.3 shows the relations of various forms of energy to temperature. All these simplifications for ideal gas mixtures enable a form of intensive mass entropy that relates only to measurable quantities, so that $\mathrm{d}s$ is easily computable in a Eulerian field. Eq. (2.18) writes:

$$\mathrm{d}s = c_V \frac{\mathrm{d}P}{P} - c_P \frac{\mathrm{d}\rho}{\rho} - \frac{1}{T}\sum_k \frac{\mu_k}{\mathrm{W}_k}\,\mathrm{d}Y_k$$

Extensive	Volume	Molar	Mass
$\mathrm{d}U = C_V\,\mathrm{d}T$	$\mathrm{d}u_V = c_{V,V}\left(\mathrm{d}T - T\frac{\mathrm{d}V}{V}\right)$	$\mathrm{d}u_m = c_{V,m}\left(\mathrm{d}T - T\frac{\mathrm{d}n}{n}\right)$	$\mathrm{d}u = c_V\,\mathrm{d}T$
$\mathrm{d}H = C_P\,\mathrm{d}T$	$\mathrm{d}h_V = c_{P,V}\left(\mathrm{d}T - T\frac{\mathrm{d}V}{V}\right)$	$\mathrm{d}h_m = c_{P,m}\left(\mathrm{d}T - T\frac{\mathrm{d}n}{n}\right)$	$\mathrm{d}h = c_P\,\mathrm{d}T$

Table 2.3: Energy variations according to various formulations.

but for many applications, a non dimensional form is preferred. An arbitrary but elegant choice for non-dimensionalizing s is c_P:

$$\frac{\mathrm{d}s}{c_P} = \frac{\mathrm{d}P}{\gamma P} - \frac{\mathrm{d}\rho}{\rho} - \frac{1}{c_P T}\sum_k \frac{\mu_k}{\mathrm{W}_k}\,\mathrm{d}Y_k \tag{2.28}$$

Recall the fixed-mass, energy exchanging homogeneous particle definition of Sec. 2.2.4. Because of mass conservation, the extensive non-dimensional entropy fluctuation of this particle is equal to the intensive quantity fluctuation:

$$\frac{\mathrm{d}s}{c_P} = \frac{\mathrm{d}S}{C_P}$$

This is very helpful to link processes in a Eulerian description with more intuitive general conservation laws. A practical example is a flow undergoing an isentropic transformation, as already shown in Tab. 2.2.

2.2.6 Entropy and acoustics

Acoustics focus on the propagation of sound waves in relatively simple mediums, such as a perfect constant gas mixture (usually air) at rest. Aeroacoustics concentrate on problems where the flow is not at rest, which makes the computation of propagation more complex. But combustion adds yet another level of complexity to this equation: the reacting flow generates both temperature and gas mixture inhomogeneities. We will see that, as shown by Marble & Candel (1977*a*), these non-homogeneities can later generate noise when they are convected in an accelerated flow such as a nozzle. Usual acoustic definitions must therefore be reexamined in this environment.

Acoustic waves can be defined as the isentropic pressure perturbations in a medium at rest. The sound speed c is accordingly defined as:

$$c^2 = \left(\frac{\partial P}{\partial \rho}\right)_{S,Y_k}$$

Since it is defined for isentropic fluctuations with constant species, the corresponding compressions follow the classical relations:

$$PV^\gamma = \mathrm{cst} \qquad\qquad T\rho^{1-\gamma} = \mathrm{cst} \tag{2.29}$$

as for a single specie fluid. Combining with the ideal gas mixture equation of state Eq. (2.20) yields the classical relations for c:

$$c^2 = \gamma \frac{R}{W} T = \frac{\gamma P}{\rho}$$

As explained in Chap. 5, some specific non-isentropic perturbations can become noise sources when accelerated, according to the phenomenon known as "indirect noise". The source term involved has been called *excess density* by Morfey (1973), and writes:

$$\rho_e = (\rho - \rho_\infty) - \frac{1}{c_\infty^2}(P - P_\infty) \tag{2.30}$$

In differential form this is:

$$\begin{aligned} \mathrm{d}\rho_e &= \mathrm{d}\rho - \frac{1}{c_\infty^2}\,\mathrm{d}P \\ \frac{\mathrm{d}\rho_e}{\rho} &= \frac{\mathrm{d}\rho}{\rho} - \frac{\mathrm{d}P}{\gamma P} \end{aligned} \tag{2.31}$$

This term appears directly in the definition of the entropy change $\mathrm{d}s$ in Eq. (2.28):

$$\frac{\mathrm{d}s}{c_P} = -\frac{\mathrm{d}\rho_e}{\rho} - \frac{1}{c_P T} \sum_k \frac{\mu_k}{\mathrm{W}_k}\,\mathrm{d}Y_k \tag{2.32}$$

From this equation, it is clear that when $\mathrm{d}Y_k = 0$, the excess density is directly proportional to the entropy perturbation. This explains the name of this variable, which in this context represents the density perturbations that are not isentropic, hence not related to acoustic fluctuations. Because of this relation, "entropy" and "excess density" are often considered equivalent in the acoustic literature.

This equation however also demonstrates the effect of mixture fluctuations on excess density. If $\mathrm{d}Y_k \neq 0$, the equivalence between excess density and entropy no longer holds. In fact, non acoustic density fluctuations can result from temperature changes, but also occur if a constant pressure and temperature mixture is submitted to changes in composition. The implication for noise evaluations is simply that "entropy" and "excess density" should be distinguished. In practice however, the evaluation of the "entropy wave" in the literature is rarely based on the actual entropy fluctuations, but on the definition of excess density Eq. (2.31) instead. In such cases, the present observation indicates that the source term evaluation will be correct.

2.3 Equations of motion for multicomponent gaseous flow

2.3.1 Governing equations for fluid flow

The equations of Navier-Stokes for a multicomponent single phase gaseous flow write:

$$\frac{\partial \rho Y_k}{\partial t} + \boldsymbol{\nabla} \cdot (\rho Y_k (\boldsymbol{u} + \boldsymbol{V_k})) = \dot{\omega}_k \tag{2.33a}$$

$$\frac{\partial}{\partial t}(\rho \boldsymbol{u}) + \boldsymbol{\nabla} \cdot (\rho \boldsymbol{u} \otimes \boldsymbol{u}) = -\boldsymbol{\nabla} p + \boldsymbol{\nabla} \overline{\overline{\boldsymbol{\tau}}} + \rho \sum_{k=1}^{N} Y_k \boldsymbol{f_k} \tag{2.33b}$$

$$\frac{\partial}{\partial t}(\rho E) + \boldsymbol{\nabla}(\rho \boldsymbol{u} E) = \dot{\omega}_T - \boldsymbol{\nabla} \dot{\boldsymbol{q}} + \boldsymbol{\nabla} \cdot (\overline{\overline{\boldsymbol{\sigma}}} \cdot \boldsymbol{u}) + \dot{Q} + \rho \sum_{k=1}^{N} Y_k \boldsymbol{f_k} (\boldsymbol{u} + \boldsymbol{V_k}) \tag{2.33c}$$

where:

- $\boldsymbol{V_k}$ is the diffusion velocity of specie k;
- $\overline{\overline{\boldsymbol{\tau}}}$ is the viscous stress tensor;
- $\boldsymbol{f_k}$ is the volume force applied to specie k;
- $\dot{\omega}_T$ is the heat released by combustion processes;
- $\dot{\boldsymbol{q}}$ is the energy flux due to temperature and species diffusion;
- $\overline{\overline{\boldsymbol{\sigma}}} = \overline{\overline{\boldsymbol{\tau}}} - p\overline{\overline{\boldsymbol{I}}}$;
- $\dot{Q}$ is the heat source term (induced by *e.g.* a spark or radiation but *not* by combustion).

2.3.2 Simplifications for gaseous reacting flows

2.3.2.1 Viscous stresses

The general relationship between the total stress tensor $\overline{\overline{\boldsymbol{\sigma}}}$ and the rate of strain tensor can be complex. However, many simple fluids such as water and air display a linear relation between these two tensors. Such a fluid is called a *Newtonian fluid*. The first part of the stress tensor is the stress distribution in a resting fluid, known as hydrostatic pressure. The second is a proportion of the rate of strain tensor. This proportion between two second order tensors reveals a fourth-rank tensor, hence 81 coefficients. However, it can be shown Gad-el Hak (1995) that in case of an isotropic fluid, these coefficients reduce to only two : the dynamic viscosity coefficient μ (related to shear), and the second viscosity coefficient λ (related to dilatation). These simplifications yield:

$$\sigma_{ik} = -p\delta_{ik} + \mu \left(\frac{\partial u_i}{\partial x_k} + \frac{\partial u_k}{\partial x_i} \right) + \lambda \left(\frac{\partial u_j}{\partial x_j} \right) \delta_{ik}$$

The hydrostatic pressure p defined here is the thermodynamic pressure. The hypothesises behind this include a medium at rest. The mechanical pressure P that is actually exerted on the fluid particle can be defined as the negative one third of the sum of normal stresses, hence:

$$\begin{aligned} P &= -\frac{1}{3}\left(\sigma_{11} + \sigma_{22} + \sigma_{33}\right) \\ &= p - \left(\lambda + \frac{2}{3}\mu\right)\boldsymbol{\nabla u} \end{aligned}$$

This formulation shows how the term $\left(\lambda + \frac{2}{3}\mu\right)$ contributes to dissipating pressure variations in proportion to the fluid dilatation. For this reason, it is called the *bulk viscosity*. For the study of flows in simple fluids such as water or air, the bulk viscosity is very small. Stokes (1845) proceeded to neglect this viscosity entirely in order to simplify the expression of the Navier-Stokes equations. The resulting *Stokes hypothesis* implies for $\overline{\overline{\boldsymbol{\sigma}}}$:

$$\sigma_{ik} = -p\delta_{ik} + \mu\left(\frac{\partial u_i}{\partial x_k} + \frac{\partial u_k}{\partial x_i}\right) - \frac{2}{3}\mu\left(\frac{\partial u_j}{\partial x_j}\right)\delta_{ik} \tag{2.34}$$

The Dynamic Viscosity Coefficient μ is assumed to be independent of the gas composition. The classical single-specie Sutherland law for dynamic viscosity of a single gas Sutherland (1893) writes:

$$\mu = c_1 \frac{T^{3/2}}{T + c_2} \frac{T_{ref} + c_2}{T_{ref}^{3/2}} \tag{2.35}$$

2.3.2.2 Diffusion

Molecular diffusion The Hirschfelder & Curtiss approximation (Hirschfelder *et al.*, 1964) states:

$$V_k X_k = -D_k \boldsymbol{\nabla} X_k \quad \text{where} \quad D_k = \frac{1 - Y_k}{\sum_{j \neq k} X_j / D_{jk}} \tag{2.36}$$

However, the computation of D_k, the coefficient of diffusion of the specie k in the local mixture, is expensive. A simplification arises by considering that all Schmidt numbers Sc_k are constant in space and time (but differ between species). This implies:

$$D_k = \frac{\nu}{Sc_k} \tag{2.37}$$

A byproduct of this approach is that the conservation of mass during species diffusion is no longer respected:

$$\sum_k Y_k V_{k,i} = 0 \tag{2.38}$$

To ensure mass conservation, a correction velocity V^c is added to fulfill Eq. (2.38). It writes:

$$V_i^c = \sum_k \frac{W_k}{W} D_k \frac{\partial X}{\partial x_i} \tag{2.39}$$

Heat diffusion The energy flux $\dot{q}$ must of course also be modeled. The Fourier law is well adapted to description of heat flux due to conduction:

$$\dot{q}_{conduction} = -\lambda \boldsymbol{\nabla} T \quad \text{where} \quad \lambda = \frac{\mu C_P}{Pr} \tag{2.40}$$

The diffusion of species also leads to heat diffusion. The sum of these fluxes writes:

$$\dot{q}_i = -\lambda \frac{\partial T}{\partial x_i} + \rho \sum_k h_k Y_k V_{k,i} \tag{2.41}$$

where $V_{k,i}$ has been corrected by V_i^c.

Chapter 3

Acoustics and Thermoacoustics

The complete set of Navier-Stokes equations contains all acoustic and non acoustic phenomena, but are strongly non-linear and very costly to solve. For many simple acoustic problems, the equations can be reduced to a linear form, and solved for a much lower cost. This chapter gives the basic formulations of linearized equations for acoustics. Some classical solutions are exhibited. Unsteady combustion appears in this simplification process as a source term for acoustic equations, which in turn provide a framework to describe the possible coupling between natural acoustic modes of the combustion chamber and acoustic production by the flame. Such equations and formulation for combustion source terms are given in the second part of this chapter.

3.1 Introduction

The Navier-Stokes equations Eq. (2.33) describe accurately all pressure perturbations in a gaseous flow. However, the cost of their resolution implies strong limitations for acoustic studies. Low frequency phenomena for example necessitate very long physical times to be accurately reproduced, and parametric studies are out of reach. A classical approach to study acoustic phenomena is based on the observation that the "non-acoustic" flow is zero (a concert hall for example) or negligible compared to the speed of sound (*e.g.* a siren on an ambulance driving at a constant speed). This leads to writing the speed u as the sum of its mean $\bar{u}$ an fluctuating u' part, and the previous observations that $\bar{u} \ll c$ where c is the sound speed leads to strong simplifications in the equations which become linear, yielding inexpensive resolution.

3.2 Constitutive equations for acoustics

3.2.1 The Euler equations

The field of acoustic studies takes interest in small isentropic perturbations of pressure and density that are detected by the human ear. This involves the description of sound sources, and of the propagation of these pressure perturbations. As pointed out by Lighthill (1952), dissipation of these waves into heat by viscosity and heat conduction while they propagate in a medium at rest such as the atmosphere is a slow process. He gives a luminous example as such:

> In the atmosphere only half the energy is lost in the first mile of propagation even at the frequency of the top note of the piano forte, while for other frequencies the required distance varies as their inverse square.

This observation has often lead to describe a continuum in which acoustic waves propagate using a simplified form of the Navier-Stokes equations called the Euler equations. All diffusions and heat sources are zero, as well as dynamic and bulk viscosity. Since the medium chemical composition does not vary it is described as a single-specie fluid. These approximations yield the following equations:

$$\frac{\partial \rho}{\partial t} + \boldsymbol{\nabla} \cdot (\rho \boldsymbol{u}) = 0 \tag{3.1a}$$

$$\frac{\partial}{\partial t}(\rho \boldsymbol{u}) + \boldsymbol{\nabla} \cdot (\rho \boldsymbol{u}\boldsymbol{u}) = -\boldsymbol{\nabla} p \tag{3.1b}$$

$$\frac{\partial}{\partial t}(\rho E) + \boldsymbol{\nabla} \cdot (\rho \boldsymbol{u} E) = -\boldsymbol{\nabla} \cdot (\boldsymbol{u} p) \tag{3.1c}$$

where $E = e + 1/2\|\boldsymbol{u}\|^2$.

The speed of sound is an important value for the description of acoustics. Consider the following differential form for pressure, which must be expressed in terms of a pair of independent thermodynamic variables ($P = P(\rho, s)$ in this case):

$$\mathrm{d}P = \left(\frac{\partial P}{\partial \rho}\right)_s \mathrm{d}\rho + \left(\frac{\partial P}{\partial s}\right)_\rho \mathrm{d}s \tag{3.2}$$

By definition, acoustic perturbations are the isentropic pressure perturbations. The *speed of sound* c therefore satisfies:

$$c^2 = \left(\frac{\partial P}{\partial \rho}\right)_s \tag{3.3}$$

According to Eq. (2.28), a single specie mixture undergoing an isentropic process complies with:

$$\frac{\mathrm{d}P}{\gamma P} = \frac{\mathrm{d}\rho}{\rho}$$

Additionally, the equation of state writes:

$$p = \rho e(\gamma - 1) = \rho \frac{R}{W} T \tag{3.4}$$

hence the speed of sound writes:

$$c_0^2 = \frac{\gamma P}{\rho} = \gamma \frac{R}{W} T \tag{3.5}$$

Entropy perturbations are of course the "rest" of the pressure perturbations. Again according to Eq. (2.28), for the mixture at hand:

$$\mathrm{d}s = c_V \frac{\mathrm{d}P}{P} - \gamma \frac{\mathrm{d}\rho}{\rho}$$

Rienstra & Hirschberg (2003) show that this yields an alternative form for the energy equation (Eq. (3.1c)) expressed with the variable s (specific entropy) instead of E, namely:

$$\frac{\partial s}{\partial t} + \boldsymbol{u} \cdot \boldsymbol{\nabla} s = 0 \tag{3.6}$$

3.2.2 Simplified forms of the Euler equations

The study of modern pressurized combustors necessitates the description of complex geometries. Three dimensional varying section ducts, such as nozzles or combustion chambers must be described. However, solving the complete 3 dimensional Euler equations of Eq. (3.1) is costly and generally offers no obvious analytical solution. A compromise is found in the set of quasi-1D Euler equations:

$$\frac{\partial \rho A}{\partial t} + \frac{\partial \rho u A}{\partial x} = 0 \tag{3.7a}$$

$$\left[\frac{\partial}{\partial t} + u \frac{\partial}{\partial x}\right] u + \frac{1}{\rho} \frac{\partial p}{\partial x} = 0 \tag{3.7b}$$

$$\left[\frac{\partial}{\partial t} + u \frac{\partial}{\partial x}\right] s = 0 \tag{3.7c}$$

where $A(x)$ designates the cross section area of the flow at the x abscissa. This simplified version of the Euler equations reduces the dimension d of the problem from 3 to 1, thus reducing the number of Euler equations n from 5 to 3. It leads to analytical formulations in some cases, as will be demonstrated later on.

The 1D Euler equations are the next logical step in simplification of the Euler equations. Many ducted acoustic problems can be partially described by the following equations:

$$\frac{\partial \rho}{\partial t} + \frac{\partial}{\partial x}(\rho u) = 0 \tag{3.8a}$$

$$\frac{\partial \rho u}{\partial t} + \frac{\partial}{\partial x}(\rho u u + p) = 0 \tag{3.8b}$$

$$\frac{\partial \rho E}{\partial t} + \frac{\partial}{\partial x}(\rho u E + u p) = 0 \tag{3.8c}$$

3.2.3 Characteristic form

Thompson (1987) suggests that this hyperbolic system can be written in a generic form for n equations and n unknowns:

$$\frac{\partial \tilde{\boldsymbol{U}}}{\partial t} + \frac{\partial \boldsymbol{F}(\tilde{\boldsymbol{U}})}{\partial x} + \boldsymbol{C}' = 0 \tag{3.9}$$

where $\tilde{\boldsymbol{U}}$ is the vector of conservative variables, $\boldsymbol{F}(\tilde{\boldsymbol{U}})$ is the flux vector, and $\boldsymbol{C}'$ regroups the source terms which contain no derivatives. In the case of the 1D Euler equations considered here, $\boldsymbol{C}' = 0$. Other terms in Eq. (3.9) write:

$$\tilde{\boldsymbol{U}} = \begin{pmatrix} \rho \\ \rho u \\ \rho E \end{pmatrix} \qquad \boldsymbol{F}(\tilde{\boldsymbol{U}}) = \begin{pmatrix} \rho u \\ \rho u u + p \\ \rho u E + u p \end{pmatrix} \tag{3.10}$$

While the conservative form is the most intuitive to write starting from the Euler equations, it is practical to rewrite the equations in primitive form:

$$\frac{\partial \boldsymbol{U}}{\partial t} + \boldsymbol{A}\frac{\partial \boldsymbol{U}}{\partial x} + \boldsymbol{C} = 0 \tag{3.11}$$

where $\boldsymbol{A}$ is an $n \times n$ matrix. Again, $\boldsymbol{C} = 0$. The new primitive vector $\boldsymbol{U}$ and matrix $\boldsymbol{A}$ write:

$$\boldsymbol{U} = \begin{pmatrix} \rho \\ u \\ p \end{pmatrix} \qquad \boldsymbol{A} = \begin{pmatrix} u & \rho & 0 \\ 0 & u & 1/\rho \\ 0 & \gamma p & u \end{pmatrix} \tag{3.12}$$

Eq. (3.11) are said to have a characteristic form when $n = 1$. The corresponding equation:

$$\frac{\partial U}{\partial t} + \lambda \frac{\partial U}{\partial x} = 0$$

can be easily solved, given some initial condition $U(x, t = 0) = U_0(x)$, yielding:

$$U(x, t) = U_0(x - \lambda t)$$

For $n > 1$, if $\boldsymbol{A}$ is diagonal, then Eq. (3.11) yields n characteristic equations that can easily be solved. For the one dimensional Euler equations, A is not diagonal (Eq. (3.12)), but it can be diagonalized. This yields 3 eigenvalues:

$$\lambda_1 = u - c, \qquad \lambda_2 = u, \qquad \lambda_3 = u + c \tag{3.13}$$

Left $\boldsymbol{l_i}$ and right $\boldsymbol{r_i}$ eigenvectors comply with:

$$\boldsymbol{l_i}\boldsymbol{A} = \lambda_i \boldsymbol{l_i} \qquad \boldsymbol{A}\boldsymbol{r_i} = \lambda_i \boldsymbol{r_i}$$

and the left eigenvectors $\boldsymbol{l_i}$ compose the rows of the diagonalization matrix $\boldsymbol{S}$. Eq. (3.11) can be multiplied by $\boldsymbol{S}$ to yield:

$$\boldsymbol{S}\frac{\partial \boldsymbol{U}}{\partial t} + [\lambda_i \boldsymbol{l_i}]\frac{\partial \boldsymbol{U}}{\partial x} = 0$$

and defining $\boldsymbol{V}$ by:

$$\mathrm{d}V_i = \boldsymbol{l_i}\,\mathrm{d}\boldsymbol{U} \tag{3.14}$$

yields:

$$\frac{\partial V_i}{\partial t} + \lambda_i \frac{\partial V_i}{\partial x} = 0 \tag{3.15}$$

This method leads to n scalar characteristic equations (one for each wave amplitude V_i), which can be solved independantly. The differential definition of $\boldsymbol{V}$ in Eq. (3.14) prevents an explicit form from being available. The quantities that are convected at the velocities λ_i, called the *characteristic waves* $\mathcal{L}_i$, defined as:

$$\frac{\partial V_i}{\partial t} + \mathcal{L}_i = 0 \tag{3.16}$$

can be explicitly computed:

$$\lambda_1 = u - c: \qquad \mathcal{L}_1 = \lambda_1\left(\frac{\partial p}{\partial x} - \rho c\frac{\partial u}{\partial x}\right) \tag{3.17a}$$

$$\lambda_2 = u: \qquad \mathcal{L}_2 = \lambda_2\left(c^2\frac{\partial \rho}{\partial x} - \frac{\partial p}{\partial x}\right) \tag{3.17b}$$

$$\lambda_3 = u + c: \qquad \mathcal{L}_3 = \lambda_3\left(\frac{\partial p}{\partial x} + \rho c\frac{\partial u}{\partial x}\right) \tag{3.17c}$$

Note that the $\boldsymbol{l_i}$ are the result of the diagonalization of $\boldsymbol{A}$. They can therefore be multiplied by any arbitrary constant, and still be valid. The $\boldsymbol{r_i}$ would simply be affected by the inverse constant, and the diagonalization matrix $\boldsymbol{S}$ would stay the same. This explains the variety of formulations for "convected quantities" (or characteristic waves) that can be found in the literature.

Another interesting point is that according to the definition of the $\mathcal{L}_i$ in Eq. (3.16), the spatial formulation of Eq. (3.17) is equivalent to a similar temporal formulation, *e.g.* for $\mathcal{L}_1$:

$$\mathcal{L}_1 = \left(\frac{\partial p}{\partial t} - \rho c\frac{\partial u}{\partial t}\right)$$

This equivalence offers some possibilities for the numerical implementation of waves calculation, either for boundary condition purposes or for acoustic evaluations in the flow. In some situations, the temporal fluctuation is easier to compute than the spatial gradients.

The characteristic form gives important insight into the physical quantities that are convected and propagated in the flow. Originally designed by Thompson (1987)

to create non reflecting boundary conditions for the Euler equations, it has been extended to the Navier-Stokes equation through the Navier-Stokes Characteristic Boundary Conditions (NSCBC) technique by Poinsot & Lele (1992). More recently, the formulation was generalized to 3D cases (Lodato *et al.*, 2008; Granet *et al.*, 2010).

3.2.4 The Linearized Euler Equations (LEE)

The threshold of pain for an acoustic wave is often considered to be 140 dB. This corresponds to a pressure fluctuation of 200 Pa, and a density fluctuation of 0.1 %. Most acoustic studies are therefore limited to very small perturbations. This is called the domain of linear acoustics. As a result, the Euler equations can be linearized around the mean state with no loss of generality for acoustic propagation. This linearization can be formerly described for any variable ϕ as:

$$\phi = \bar{\phi} + \phi' \tag{3.18}$$

where the subscript $_0$ represents the mean quantity and $'$ the time-dependant fluctuation. This linearization yields 2 simplifications:

- second and higher order terms can be neglected;
- the mean flow also satisfies the Euler equations and can be eliminated.

In case of a homentropic flow, $\mathrm{d}s = 0$ and Eq. (3.2) simplifies to:

$$p' = c_0^2 \rho' \tag{3.19}$$

In the context of linearized acoustics, this relation is referred to as the *constitutive equation*.

3.2.4.1 Quiescent flow

The most simple medium for acoustic studies is one that is both stagnant ($\bar{\boldsymbol{u}} = 0$) and uniform ($\bar{\rho}$, $\bar{p_0}$, $\bar{s_0}$, ...), called a *quiescent* medium. In this case, replacing all variables by their linearized equivalent from Eq. (3.18) and neglecting second order terms yields the Linearized Euler Equations (LEE) in the simplified following form:

$$\frac{\partial \rho'}{\partial t} + \rho_0 \boldsymbol{\nabla} \boldsymbol{u}' = 0 \tag{3.20a}$$

$$\rho_0 \frac{\partial \boldsymbol{u}'}{\partial t} + \boldsymbol{\nabla} p' = 0 \tag{3.20b}$$

$$\frac{\partial s'}{\partial t} = 0 \tag{3.20c}$$

Eliminating $\boldsymbol{u}'$ yields:

$$\frac{\partial^2 \rho'}{\partial t^2} - \boldsymbol{\nabla}^2 p' = 0$$

According to Eq. (3.19), this writes for pressure perturbations only:

$$\frac{\partial^2 p'}{\partial t^2} - c_0^2 \boldsymbol{\nabla}^2 p' = 0 \tag{3.21}$$

known as the *wave equation*. This wave equation can be solved in 1, 2 or 3 dimensions. An example of 2 dimensional case is the gravity waves propagating on the surface of water. In gaseous fluid dynamics, the 1 and 3 dimensional problems are more frequent. The 1D wave equation admits the general solution:

$$p'(x,t) = f(x - c_0 t) + g(x + c_0 t)$$
$$u'(x,t) = \frac{1}{\rho_0 c_o}(f(x - c_0 t) - g(x + c_0 t))$$

where f and g are right and right travelling quantities, respectively. Here the solution for u' is obtained using Eq. (3.20b). The system can be reversed to express f and g in terms of p' and u':

$$f(x - c_0 t) = \frac{1}{2}\left(p'(x,t) + \rho_0 c_0 u'(x,t)\right)$$
$$g(x + c_0 t) = \frac{1}{2}\left(p'(x,t) - \rho_0 c_0 u'(x,t)\right)$$

This important result is the basis for many acoustic reasonings. The presence of two acoustic waves travelling in opposite directions sheds light in many situations on the dynamics of pressure and velocity perturbations.

3.2.4.2 Presence of a homogeneous mean flow

The LEE cannot be simplified as much when the flow is no longer quiescent. An intermediate assumption is to consider the flow to have a homogeneous velocity field of value $\boldsymbol{u_0}$ everywhere. The resulting LEE can be found *e.g.* in Rienstra & Hirschberg (2003). They can still lead to a "convected" wave equation:

$$\left(\frac{\partial^2}{\partial t^2} + \boldsymbol{u_0} \cdot \boldsymbol{\nabla}\right) p' - c_0^2 \boldsymbol{\nabla}^2 p' = 0 \tag{3.22}$$

Solutions to this equation in 1D have been given in form of the characteristic waves in Eq. (3.17c) and (3.17a). The convection speeds of these quantities also suggests that they are upstream and downstream travelling acoustic waves, respectively. The third convected quantity however propagates at the mean flow field and does not have an acoustic equivalent.

Eq. (3.22) results from mass and momentum equations, as well as the constitutive equation for acoustics Eq. (3.19). The characteristic approach also made use of the energy equation, hence the third characteristic wave (3.17b). In order to identify this wave in terms of physical quantities, Morfey (1973) introduced the concept of *excess density* ρ_e, defined as:

$$\rho'_e = \rho' - \frac{p'}{c_0^2} \tag{3.23}$$

This quantity represents the difference between the density fluctuation and the one that would occur if the medium were homentropic and at rest. It is clear that ρ'_e is analogous to $\mathcal{L}_2$ in Eq. (3.17b).

If pressure fluctuations arise from acoustic perturbations alone, the density fluctuations are here split as the sum of acoustic perturbations (isentropic) and entropic perturbations. Let us now confirm the intuitive feeling that these excess density fluctuations are indeed linked to the entropy perturbations. According to Eq. (2.28) for a single specie fluid:

$$\frac{s'}{c_P} = \frac{p'}{\gamma p_0} - \frac{\rho'}{\rho_0} = \frac{\rho'_e}{\rho_0}$$

Because of this result, the term "excess density" is generally not used in the acoustic community. Instead, $\mathcal{L}_2$ is called the *entropy wave*. It should be noted that this equivalence is only true here because the flow was considered to be a single-specie flow, or more precisely because all $\mathrm{d}Y_k$ terms were neglected in Eq. (2.28). In the specific case of combustion noise, this assumption is not necessarily true, as species mass fractions change when chemical reactions occur. This is the subject of a short study in Sec. 5.2.4.3.

According to the preceding arguments, the characteristic waves solution to the 1D Euler equations Eq. (3.17) are recast in the linearized formulation. They are non-dimensionalized, yielding:

$$\omega^+ = \frac{p'}{\gamma p_0} + \frac{u'}{c_0}, \qquad \omega^- = \frac{p'}{\gamma p_0} - \frac{u'}{c_0}, \qquad \omega^S = \frac{p'}{\gamma p_0} - \frac{\rho'}{\rho_0} \tag{3.24}$$

where:

- ω^+ is the downstream travelling acoustic wave propagating at $u_0 + c_0$;
- ω^- is the upstream travelling acoustic wave propagating at $u_0 - c_0$;
- ω^S is the excess density — or *entropic* — wave propagating at u_0;

3.2.4.3 The linearized quasi-1D Euler equations

In ducted flow acoustics, 1D problems are rare. Ducts are generally 3D structures with contractions and widening portions, matching flow dilatation or compression. As mentioned in Sec. 3.2.2, the quasi-1D Euler equations (3.7) offer a compromise in which subsection change is described, but the full 3D equations are simplified. Linearization of these equations yields:

$$\left[\frac{\partial}{\partial t} + \bar{u}\,\frac{\partial}{\partial x}\right]\left(\frac{p'}{\gamma\bar{p}}\right) + u\,\frac{\partial}{\partial x}\left(\frac{u'}{\bar{u}}\right) = 0, \tag{3.25a}$$

$$\left[\frac{\partial}{\partial t} + \bar{u}\,\frac{\partial}{\partial x}\right]\left(\frac{u'}{\bar{u}}\right) + \frac{c^2}{u}\,\frac{\partial}{\partial x}\left(\frac{p'}{\gamma\bar{p}}\right) + \left[2\frac{u'}{\bar{u}} - (\gamma-1)\left(\frac{p'}{\bar{p}}\right)\right]\frac{\partial\bar{u}}{\partial x} = \frac{s'}{c_P}\,\frac{\partial\bar{u}}{\partial x}, \tag{3.25b}$$

$$\left[\frac{\partial}{\partial t} + \bar{u}\,\frac{\partial}{\partial x}\right]\left(\frac{s'}{c_P}\right) = 0. \tag{3.25c}$$

These equations are essential to describe the "indirect noise" phenomenon, *e.g.* the generation of sound by acceleration of entropy variations. This subject is treated in detail in Chap. 5.

3.3 Flame acoustic source terms and thermoacoustic instability mechanism

3.3.1 Euler equations with heat source

Let us consider a region of volume V containing a flame, surrounded by quiescent fluid. We will hereafter model the flame by its heat release rate $\dot{Q}$, distributed in the volume V such that:

$$Q_{total} = \int_V \dot{Q}\,\mathrm{d}\boldsymbol{y}$$

is known. Conservation equations for mass, momentum and energy for a non viscous gas with no mean flow (hence no convection, material derivatives and temporal derivatives are identical) are:

$$\frac{\partial \rho}{\partial t} + \rho \boldsymbol{\nabla}\cdot\boldsymbol{u} = 0 \tag{3.26}$$

$$\rho\frac{\partial \boldsymbol{u}}{\partial t} = -\boldsymbol{\nabla} p \tag{3.27}$$

$$\rho C_p \frac{\partial T}{\partial t} = \dot{Q} + \frac{\partial p}{\partial t} \tag{3.28}$$

Moreover, the fluid is considered ideal, hence $p = \rho r T$ and:

$$\begin{aligned}\mathrm{d}T &= \mathrm{d}p\left.\frac{\partial T}{\partial p}\right|_\rho + \mathrm{d}\rho\left.\frac{\partial T}{\partial \rho}\right|_p \\ &= \mathrm{d}p\frac{1}{\rho r} + \mathrm{d}\rho\frac{-p}{r\rho^2}\end{aligned}$$

Eq. 3.28 then becomes:

$$\rho C_p\left(\frac{1}{\rho r}\frac{\partial p}{\partial t} - \frac{p}{\rho^2 r}\frac{\partial \rho}{\partial t}\right) = \dot{Q} + \frac{\partial p}{\partial t}$$

which with the use of Eq. 6.5 leads to:

$$\frac{\partial p}{\partial t} + p\boldsymbol{\nabla}\cdot\boldsymbol{u} = \frac{r}{C_p}\left(\dot{Q} + \frac{\partial p}{\partial t}\right)$$

and since:

$$\begin{aligned}\frac{r}{C_p} &= \frac{\gamma-1}{\gamma} \\ 1 - \frac{r}{C_p} &= \frac{1}{\gamma}\end{aligned}$$

the energy equation can be expressed as:

$$\underbrace{\frac{1}{\gamma p}\frac{\partial p}{\partial t}}_{\frac{1}{\gamma}\frac{\partial}{\partial t}(ln(p))} + \boldsymbol{\nabla}\cdot\boldsymbol{u} = \frac{\gamma-1}{\gamma p}\dot{Q} \tag{3.29}$$

At this point, it can be noticed that Eq. 3.27 can be written as:

$$\begin{aligned}\frac{\partial \boldsymbol{u}}{\partial t} &= -\frac{\boldsymbol{\nabla} p}{\rho} \\ &= -rT\frac{\boldsymbol{\nabla} p}{p} \\ &= -rT\boldsymbol{\nabla}(ln(p))\end{aligned}$$

which suggests to derive Eq. 3.29 against time:

$$\frac{1}{\gamma}\frac{\partial^2}{\partial t^2}(ln(p)) + \boldsymbol{\nabla}\cdot \underbrace{\left(\frac{\partial \boldsymbol{u}}{\partial t}\right)}_{-rT\boldsymbol{\nabla}(ln(p))} = \frac{\gamma-1}{\gamma}\frac{\partial}{\partial t}\left(\frac{\dot{Q}}{p}\right)$$

$$\frac{\partial^2}{\partial t^2}(ln(p)) - \boldsymbol{\nabla}\cdot\left(\boldsymbol{\nabla}(ln(p))\underbrace{\gamma r T}_{c_0^2}\right) = (\gamma-1)\frac{\partial}{\partial t}\left(\frac{\dot{Q}}{p}\right) \tag{3.30}$$

3.3.2 LEE with heat source

Following the classical linearization of Eq. (3.18) p can be written as the sum of a constant part $\bar{p}$ and a varying part p': $p = \bar{p} + p'$, and linearized accordingly by considering that $p' \ll \bar{p}$. It follows that, to the first order of $\frac{p'}{\bar{p}}$:

$$ln(p) = ln(\bar{p} + p') = ln(\bar{p}) + ln(1 + \frac{p'}{\bar{p}}) \sim ln(\bar{p}) + \frac{p'}{\bar{p}}$$

which using Eq. 3.30 yields:

$$\frac{\partial^2 p'}{\partial t^2} - c_0^2\nabla^2 p' = \bar{p}(\gamma-1)\frac{\partial}{\partial t}\left(\frac{\dot{Q}}{p}\right)$$

and since $\dot{Q}$ is already a small perturbation, $\dot{Q}/p \sim \dot{Q}/\bar{p}$. This yields the wave equation with it's proper source term:

$$\frac{\partial^2 p'}{\partial t^2} - c_0^2\nabla^2 p' = (\gamma-1)\frac{\partial \dot{Q}}{\partial t} \tag{3.31}$$

Let us now consider the case where $\dot{Q}$ is a harmonic oscillation of pulsation ω. Let us assume that the resulting perturbation $p'(\boldsymbol{x}, t)$ is also harmonic of pulsation ω. Hence:

$$\begin{aligned}\dot{Q}(\boldsymbol{x}, t) &= \dot{Q}(\boldsymbol{x})e^{i\omega t} \\ p'(\boldsymbol{x}, t) &= p'(\boldsymbol{x})e^{i\omega t}\end{aligned}$$

Eq. 3.31 can be rewritten as:

$$\begin{aligned}-\omega^2 p' - c_0^2\nabla^2 p' &= (\gamma-1)i\omega\dot{Q} \\ \nabla^2 p' + k^2 p' &= -\frac{\gamma-1}{c_0^2}i\omega\dot{Q}\end{aligned} \tag{3.32}$$

where $k = \frac{\omega}{c_0}$. Eq. 3.32 is known as the Helmholtz equation with source term.

3.3.3 Thermoacoustic Instabilities

In terms of dynamic systems, Eq. (3.32) describes a simple resonator, with no damping and with a source term. Any introductory course on mechanics describes the behavior of such systems, called a *harmonic oscillator*. The homogeneous equation displays modes, *i.e.* frequencies at which mechanical energy can be stored in the system by making it oscillate. If the source term also oscillates at or close to this frequency, the mode amplitude can increase by several orders of magnitude.

In combustion systems, the energy release is of the order of $100\,\mathrm{MW\,m^{-3}}$ to $1\,\mathrm{GW\,m^{-3}}$, and if even a fraction of this energy accumulates on a mode, catastrophic combustor and engine failure can occur, as shown in Fig. 3.1.

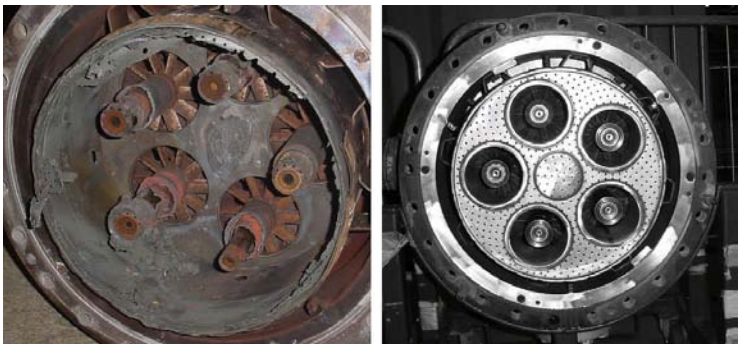

Figure 3.1: Combustor damaged by thermoacoustic instabilities (left) and rebuilt (right)(Goy *et al.* (2005)).

Crocco (1951) argued that if combustion reacts infinitely fast to inlet and outlet conditions, no instability can appear. But if the combustion fluctuations $\dot{Q}'$ react with a time-delay τ to mass flow rate $\dot{m}'$, pressure p' or velocity u' fluctuations, then self-sustained oscillations can appear. This approach is generally referred to as the Flame Transfer Function (FTF), and in practice the previous quantities are related by:

$$\frac{\gamma-1}{\bar{\rho}\bar{c}^2}\dot{Q}' = AN_1 e^{j\omega\tau} u'(\boldsymbol{x}_{ref}) \cdot \boldsymbol{n}_{ref} \tag{3.33}$$

where $\boldsymbol{x}_{ref}$ is a position of reference and $\boldsymbol{n}_{ref}$ a reference direction, A is the tube section area at the reference point, N_1 is Crocco (1951)'s interaction index and τ is the delay in s. The choice of these references can be important to describe the flame behavior, as shown by Truffin *et al.* (2003). With this formulation, the interaction index has no dimension. However, a simpler index, also without dimension, is often found in the literature:

$$\frac{\dot{Q}'}{\bar{\dot{Q}}} = N_2 e^{j\omega\tau} \frac{u'(\boldsymbol{x}_{ref})}{\bar{u}} \cdot \boldsymbol{n}_{ref} \tag{3.34}$$

A third formulation is sometimes used where the heat release and velocity fluctuations ($\dot{Q}'$ and u', respectively) are used in dimensional form, leading to yet another

interaction index N_3, which writes:

$$\dot{Q}' = N_3 e^{j\omega\tau} u'(\boldsymbol{x}_{ref}) \cdot \boldsymbol{n}_{ref} \tag{3.35}$$

In this formulation, N_3 has the dimension of $\dot{Q}/\bar{u}$, *i.e.* $\mathrm{J\,m^{-1}}$. All three formulations and notations for this manuscript are grouped in Tab. 3.1.

Name	Notation	Definition	Dimension
Crocco	N_1	$\frac{\dot{Q}'}{u'(\boldsymbol{x}_{ref})} \frac{\gamma-1}{A\bar{\rho}\bar{c}^2}$	$[-]$
Non-dimensional	N_2	$\frac{\dot{Q}'/\bar{\dot{Q}}}{u'(\boldsymbol{x}_{ref})/\bar{u}}$	$[-]$
Dimensional	N_3	$\frac{\dot{Q}'}{u'(\boldsymbol{x}_{ref})}$	$\mathrm{J\,m^{-1}}$

Table 3.1: Definitions of interaction index found in the literature, with according notations in this manuscript.

The coupling between the source term and the cavity depends on the modes of the cavity and the time delay τ. The study of system stability can be done analytically for some very simple cases, as described by Poinsot & Veynante (2011). In combustors with several burners, analytical and semi-analytical theories are also available, given reasonably simple geometries, such as the ATACAMAC approach of Bauerheim *et al.* (2013). When considering realistic combustor geometries, these simple approaches are not necessarily applicable, and full 3D acoustic solvers are used. One of such solvers, called AVSP and used in this Ph.D. is described in Chap. 7 of this manuscript.

3.3.3.1 Equivalence ratio fluctuations ϕ'

In situations where equivalence ratio fluctuations occur at the flame, heat release fluctuations will necessarily be visible. Lieuwen & Zinn (1998) have described the effect of ϕ' on $\dot{Q}'$ in the limit of lean regimes, and shown that for most equivalence ratios there is almost a one to one relation between their non-dimensional expressions:

$$\frac{\dot{Q}'}{\bar{\dot{Q}}} = M e^{j\omega\tau_\phi} \frac{\phi'}{\bar{\phi}} \tag{3.36}$$

where $M \approx 1$ for $\phi < 0.85$ and goes quickly to 0 for higher values of ϕ. These investigations however were performed for a one-dimensional setup. In a more general case, M can be measured for any given setup to account for the effect of equivalence ratio fluctuations on heat release, but its value for lean stratified regimes is expected to be close to 1.

In non-premixed configurations, the total heat release fluctuations therefore depend on two (potentially independent) parameters: u' and ϕ'. Choosing the interaction index non-dimensional form n yields a simple formulation including both

mechanisms:

$$\frac{\dot{Q}'}{\bar{\dot{Q}}} = N_2 e^{j\omega\tau} \frac{u'(\boldsymbol{x}_{ref})}{\bar{u}} \cdot \boldsymbol{n}_{ref} + M e^{j\omega\tau_\phi} \frac{\phi'}{\bar{\phi}} \tag{3.37}$$

Chapter 4

Realistic outlet conditions for combustion chambers

Combustion chambers are generally terminated by a nozzle or section restriction which allows to operate at higher pressure, but also creates a choked section at the chamber outlet. In this chapter, several methods to represent such an outlet condition numerically will be explicited. The influence of this condition on chamber acoustic modes and thermoacoustic instabilities will be investigated, in a general case and for the target setup of this Ph.D.

4.1 Introduction

The role of a combustion chamber in an aeronautical engine is to induce temperature rise in the highest pressure part of the cycle. In order to transform this thermal energy into mechanical energy, expansion systems such as nozzles and turbines are necessary downstream of the chamber. Numerical simulations of such an engine can take several forms: LES is now widely used and recognized as a mean to simulate turbulent reacting flows (Cocks *et al.*, 2013). Its main strength resides in the description of energy-containing scales of turbulence and their interaction with the flame. This however comes at a cost, which becomes prohibitive outside the reacting zone. One approach to simulate a complete engine resides in a hybrid approach using LES where it is necessary, and less expensive methods elsewhere (such as RANS). The question of where to limit the LES, and how to model the outlet boundary condition that results from this "cut" is essential for an LES code, as inlet turbulence levels, and acoustic behavior of all subsonic boundary conditions will have a direct influence on the domain.

4.2 Numerical modeling of a nozzle outlet

4.2.1 Choosing a domain for combustion chamber LES

Schlüter *et al.* (2005) have recently demonstrated the feasibility of a complete simulation of an aeronautical engine: RANS techniques were applied in the rotating parts (compressor and turbine), and an LES simulation was performed in the combustion

chamber. In this approach, the inlet/outlet environment of the combustion chamber is given by computing the physics upstream and downstream.

Unfortunately, such methods are not yet computationally accessible for industrial applications. In practice, LES for combustion chambers are performed on small sub-sections of the total fluid flow, and mean state conditions are imposed at the inlet and outlet of the domain to mimic the actual environment. At the inlet, the injection ducts are often included in the computation, as they are necessary to obtain the correct aerodynamics and mean flow in the chamber. For example, the swirl induced by modern injectors builds up in the cold injection ducts before reaching the flame. The amount and nature of swirl is known to influence directly the flame stabilization and its dynamic behavior (Syred & Beer, 1974). Therefore, the upstream conditions of the chamber are accurately represented by the detailed LES performed in the injection duct.

The downstream ducts have little influence on the mean flow and overall chamber aerodynamics. Once the combustion process is complete, LES is often considered unnecessary, and the numerical domain is severed. From a dynamic perspective, this means that the acoustic impedance of the outlet is left entirely to the outlet boundary condition, not relying on a portion of solved flow. This difference between upstream and downstream treatments is represented in Fig. 4.1.

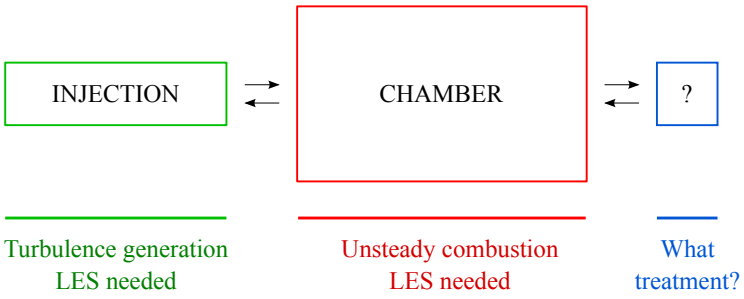

Figure 4.1: Functional graph of the chamber in its environment. Natural approaches tend to include the upstream region but not the downstream one.

4.2.1.1 The classical approach: OPEN outlet

Combustion systems for propulsion operate at pressures higher than the outer medium, in order to achieve high efficiency. The flow then exits the combustion chamber and expands into lower pressure areas, accelerating as it goes. In constant pressure chambers this occurs through section restrictions such as nozzles, called "high pressure distributors" (HPD) in aeronautical engines. For the sake of simplicity in this argument, the case of a simple converging-diverging nozzle will be considered. A direct analogy exists with turbomachines, in which the HPD is not axisymmetric but also has the function of expanding the hot gases.

The most common approach for LES is to focus on the combustion chamber only, stopping the computational domain upstream of the nozzle and imposing in this outlet section a fixed pressure region. This strategy will be called "OPEN". There

are several good reasons to do this, if it is not needed for the study at hand, some of which can be:

- incompressible codes are limited to low-Mach number flows. Since the flow in the expansion system is always at high Mach number, either high subsonic or supersonic, such codes do not offer the possibility to include any downstream domain, so that OPEN is the only possible strategy;
- compressible explicit codes have a global acoustic time step set by the most restrictive cell: ${}^{(u+c)}\Delta_t/\Delta_x \leq CFL$. If the Mach number approaches 1 in the domain, the size of the cells in this area must be carefully defined, otherwise the global time step could collapse because of this region.
- the simulation of the flow in a nozzle leaves little or no control on the downstream part of the domain. In unsteady numerical simulations, transient regimes are common and outlet conditions can be used to evacuate non physical perturbations due to initializations.

If the domain is truncated before the expansion system, the steady state outlet values are determined using a theoretical approach. Description of the steady state flow through the nozzle is therefore essential. Luckily, simple analytical theory is well known for this problem, and will be described in the next section. The numerical simulation of such a system can however present some additional challenges and pitfalls, as will be demonstrated in Chap. 8.

Unsteady behavior of the boundary conditions: In the context of High Fidelity LES (HFLES), the unsteady behavior of the boundary conditions is essential. Numerical dissipation in the domain is kept at a minimum, and spurious perturbations must be eliminated. The mean target values must however be imposed. The "NSCBC" approach of Poinsot *et al.* (1992) has been widely used by LES codes, as it is an excellent tool for this purpose (see Sec. 3.2.3 for details). However, this approach does not enable a total control over the inlet and outlet impedances of the system.

Let us consider the example of outlet conditions, once again in the case of an axisymmetric nozzle. If we want to avoid the computation of the nozzle we can replace it by an equivalent boundary condition. As shown by Selle *et al.* (2004*a*), an outlet condition acts as a filter, and only the cutoff frequency can be adjusted simply. The complex impedance of the environment (hence, its unsteady behavior) cannot be reproduced. In other terms, to first order the outlet behaves as a pressure node for the frequencies that it reflects, and is non-reflecting for the frequencies above the cutoff frequency. Typical high-subsonic or supersonic nozzles behave closer to a velocity node, as will be shown later in this thesis.

Including the nozzle for specific needs: An accurate description of the nozzle flow is not important for many studies that do not concentrate on chamber dynamics. However, several major domains of interest are concerned by unsteady nozzle behavior:

- on the chamber side, the chamber dynamics are dictated by both the flow and

the boundary conditions. The response of the nozzle to fluctuations (or more formally its impedance) can be determining for capturing the chamber behavior. This is particularly crucial to the thermoacoustic instability community, as nozzle impedances for example are known to be critical elements for the stability of rocket engines (Zinn, 1972; Culick & Kuentzmann, 2006);

- flame dynamics and chamber aerodynamics are also impacted by the downstream reflections, and as will be shown in this Ph.D. flame stabilization can be affected by its description;
- downstream of the nozzle, hot spots can have an effect on the design of heat-resistant parts, especially on turbine elements (Han *et al.*, 2000);
- nozzle flows transform entropy waves created by the chamber into noise, propagating downstream and creating a significant part of combustion noise (Marble & Candel, 1977*a*; Bake *et al.*, 2008; Duran & Moreau, 2013).

4.2.1.2 OPEN versus CLOSED approaches

In response to the issues cited above, two major approaches can be distinguished when choosing a numerical domain. These are represented in Fig. 4.2.

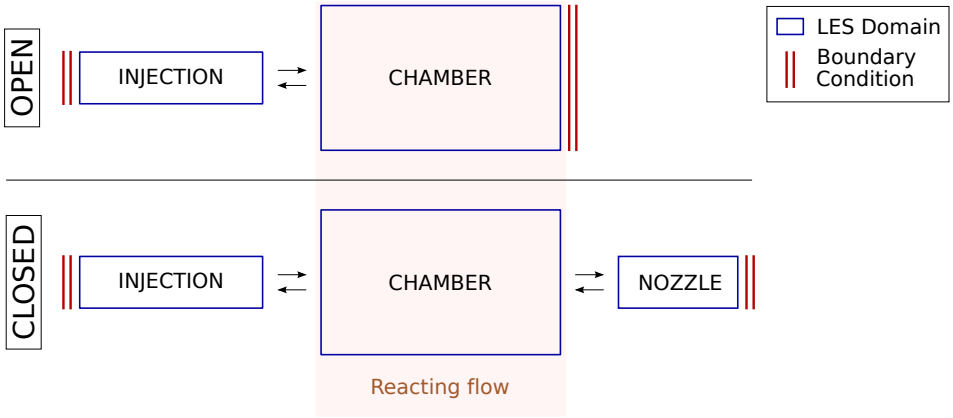

Figure 4.2: OPEN versus **CLOSED** domains for LES. Top: **OPEN** with no nozzle. The chamber sees LES input at its inlet but its outlet is a plane upstream of the nozzle. Bottom: **CLOSED** domain with (part of) the nozzle included. The inlet is unchanged, but the nozzle belongs to the LES domain, and the boundary condition is located further downstream.

The OPEN configuration matches the classical LES approach. The downstream expansion system is ignored, and the domain ends when the combustion process is complete. A boundary condition controls the entire behavior of the downstream duct, and whether this boundary condition can mimic the real world is an open question. However, using such a setup does not exclude the study of issues requiring accurate downstream description. In fact, it can serve as a point of comparison, to highlight the influence of downstream impedance on the chamber dynamics. It

also offers the possibility to explore downstream impedances numerically: as shown by Selle *et al.* (2004*b*), the complex reflection coefficient R_{out} of a wave exiting the domain by an NSCBC outlet condition is known for every frequency f and can be partially controlled using the relax coefficient K, according to:

$$R_{out} = -\frac{1}{1 - i\frac{4\pi f}{K}} \tag{4.1}$$

For passive conditions where energy only exits the domain, this reflection is expected to be in the unit circle, *i.e.* $|R| \leq 1$. Fig. 4.3 shows the location of R_{out} in the complex plane. The actual nozzle reflection is expected to be passive ($|R_{nozzle}| \leq 1$)

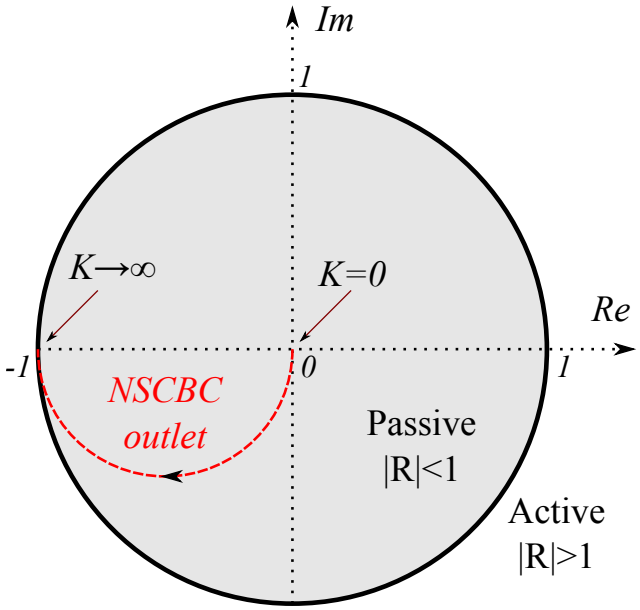

Figure 4.3: Reflection coefficient R_{out} of an NSCBC outlet in the complex plane, according to calculations of Selle *et al.* (2004*a*). R_{out} follows the red dotted arc circle as the relax coefficient K of the outlet changes. For $K = 0$, the condition is non reflective. If $K > 0$, the reflection coefficient is located in the complex plane, somewhere along the arc. The exact position depends on both the value of K and on the frequency f. In the limit of $K \to \infty$, the boundary condition becomes fully reflective for all frequencies and $R = 1$.

but it can be located anywhere inside the unit circle (the gray area in Fig. 4.3). There is therefore little chance that the NSCBC outlet condition can mimic the nozzle behavior. It can still be useful for practical reasons such as initialization of other configurations, as will be shown in Chap. 11.

The CLOSED setup includes part of the downstream duct and of the nozzle. The nozzle behavior is explicitly computed in the LES, as well as the waves emitted from the outlet and travelling upstream. If a sonic region separates the chamber from the outlet, no wave can travel through and the geometry itself determines the chamber outlet behavior, regardless of boundary condition treatment after the nozzle.

This setup is of course the most realistic, as the downstream impedance is "exact": it is computed by the compressible LES solver, and not inferred by any model. It does not offer the possibility to modify the downstream impedance for a given geometry. It is less an exploration tool than the previous approach: for example, its impedance cannot be changed. It is mainly defined by the nozzle geometry.

4.2.1.3 Nozzle behavior

The flow through a nozzle is a multifaceted problem. In a first approach, it is often treated as a "quasi 1D" flow, *i.e.* a 1D flow with varying section. At low Mach numbers, the steady flow in a nozzle follows the Bernouilli equations, often used in introductory fluid mechanic courses. At high subsonic regimes, compressible effects come into play, and this opens the way to the study of compressible flows. In the late nineteenth century, De Laval (1894) invented a converging-diverging nozzle geometry which opened the way to supersonic flows. The existence of supersonic flows was a subject of argument in the scientific community at the time, but Stodola (1905) later formalized the steady-state compressible flow theory describing these flows and confirmed the presence of supersonic conditions. Today, this type of flow is a classical compressible fluid mechanics introductory problem in its steady-state form, available in most textbooks on compressible flows (Saad, 1985; White, 1986; Candel, 1995).

The unsteady behavior of nozzles is an entirely different field of study, of critical importance for combustion noise as shown in Chap. 5. All analyses in the steady-state regimes make use of conservation of mass and momentum through the nozzle. This is of course not true if perturbations of the size of the nozzle or less are going through it, as the phase between inlet and outlet perturbations can differ. Solving for the nozzle behavior in this case is therefore a much more complicated task. It has been done however in several particular cases by the combustion noise community, as shown in Chap. 5.

4.2.2 Steady state flow through a nozzle

When a pressurized chamber is connected through a section restriction to an outer less pressurized medium, the flow accelerates due to the pressure gradient. While the exact flow can only be described by precise 3D simulations, much can be said about the general properties of such a depressurization, *e.g.* that the Mach number of the flow once it reaches the outer medium depends only on the pressure ratio (Candel, 1995). The appearance of a supersonic region and shock waves can be inferred based on section and pressure ratios alone.

When dealing with nozzle flow, an accurate description of the steady-state behavior is necessary before any dynamic behavior can be assessed. The present section presents the corresponding classical relations.

4.2.2.1 Nozzle relations for steady flow

Let us consider a converging-diverging isentropic nozzle (Fig. 4.4). Variables at the

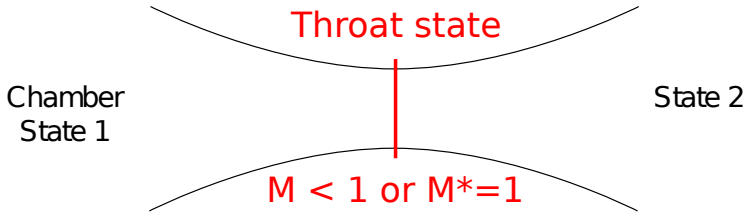

Figure 4.4: Schematic view of a basic converging-diverging nozzle

sonic line ($M = 1$) are represented by the superscript *. Total quantities will be represented with the subscript $_0$. Static quantities in the chamber will bear the subscript 1, whereas static quantities after the nozzle (at the outlet) will correspond to subscript 2. In the following, a steady-state configuration is considered.

For steady flow, the conservation of mass flux and enthalpy through the nozzle can be written as:

$$\rho\, UA = cst \tag{4.2}$$

$$h_0 = c_P T_0 = c_P T + \frac{1}{2}U^2 \tag{4.3}$$

where ρ is the fluid density, U the axial velocity, A the cross area of the nozzle, T the fluid static temperature, h its enthalpy and C_p its mass heat capacity. The subscript $_0$ corresponds to total values of otherwise static variables.

Hence by using the alternative definition of the speed of sound c and the classic relations:

$$c^2 = \gamma r T \tag{4.4}$$

$$r = c_P - c_V \quad \text{and} \quad \gamma = \frac{c_P}{c_V}$$

the evolution of the static temperature T versus the Mach number M can be simply expressed as:

$$\frac{T_0}{T} = 1 + \frac{U^2}{2C_P T} = 1 + \frac{(\gamma-1)U^2}{2c^2}$$

$$\frac{T_0}{T} = 1 + \frac{\gamma-1}{2}M^2 \tag{4.5}$$

Moreover, the isentropic relations:

$$\frac{T}{\rho^{\gamma-1}} = cst \quad \text{and} \quad \frac{P}{\rho^{\gamma}} = cst$$

lead to similar relations for density and pressure:

$$\frac{\rho_0}{\rho} = \left(1 + \frac{\gamma-1}{2}M^2\right)^{\frac{1}{\gamma-1}} \tag{4.6}$$

$$\frac{P_0}{P} = \left(1 + \frac{\gamma-1}{2}M^2\right)^{\frac{\gamma}{\gamma-1}} \tag{4.7}$$

Eqs. (4.5), (4.6) and (4.7) quantify the ratio of total to static values. This ratio is 1 for $M = 0$. As the Mach number increases, the dynamic part of all values increases. As long as the flow is not choked at the throat, the flow rate $\dot{m}$ depends on both upstream and downstream pressures and can be expressed according to Eq. (4.8). Eliminating references to T and ρ (using Eqs. (4.4) through (4.7)) yields:

$$\begin{aligned}\dot{m} &= A\frac{P_0}{\sqrt{rT_0}}\left(\frac{P}{P_0}\right)^{1/\gamma}\sqrt{\gamma r T_0 \frac{P_0}{\sqrt{rT_0}}^{\frac{\gamma-1}{\gamma}}}\sqrt{\frac{2}{\gamma-1}\left(\left(\frac{P_0}{P}\right)^{\gamma/\gamma-1}-1\right)} \\ &= A\frac{P_0}{\sqrt{rT_0}}\left(\frac{P}{P_0}\right)^{1/\gamma}\sqrt{\frac{2\gamma}{\gamma-1}\left(1-\left(\frac{P}{P_0}\right)^{\frac{\gamma-1}{\gamma}}\right)}\end{aligned} \tag{4.8}$$

This relation is valid for any isentropic flow starting from the chamber at rest and at pressure P_0. This is a good description of subsonic flows, as well as supersonic flows up to any shock. Shocks however are not isentropic, and must be treated specifically. Throughout a subsonic nozzle, no shock can appear, and this relation relates $\dot{m}$, P_0, P and A. However, to determine the flow through the nozzle $\dot{m}$, the only position where the static pressure is known is the outlet. Therefore, the mass flow rate $\dot{m}$ writes:

$$\dot{m} = A_{out}\frac{P_0}{\sqrt{rT_0}}\left(\frac{P_{out}}{P_0}\right)^{1/\gamma}\sqrt{\frac{2\gamma}{\gamma-1}\left(1-\left(\frac{P_{out}}{P_0}\right)^{\frac{\gamma-1}{\gamma}}\right)} \tag{4.9}$$

If the pressure ratio increases sufficiently, the Mach number M can reach 1. The matching value of P_0/P is called the *critical pressure ratio* r_C, and writes according to Eq. (4.7):

$$r_C = \left.\frac{P_0}{P}\right|_C = \left(\frac{\gamma+1}{2}\right)^{\frac{\gamma}{\gamma-1}} \tag{4.10}$$

This condition can be worded as follows: a volume containing a fluid of total pressure P_0 blowing through a section restriction into another volume of fluid at lower pressure will generate a choked flow as soon as there is a section at which the static pressure is P, such that $P_0/P > r_C$. The value of r_C depends only on γ, and varies between 1.89 for fresh gases and 1.81 for burnt gases in this Ph.D., as shown in Fig. 4.5. Note that it is possible for the static pressure to reach its the value before the outlet pressure does, meaning that in effect for such a nozzle the choking ratio r_{choke} differs from r_c. This subtlety is detailed in Sec. 4.2.2.2.

When the flow chokes at some point in the nozzle, the outlet pressure information can no longer travel upstream through the nozzle. However, some observations can be made on the Mach number M. It is therefore useful to rewrite Eq. 4.8 as a

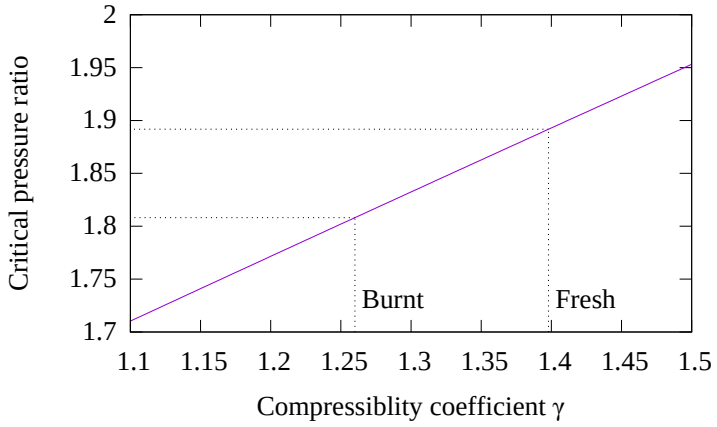

Figure 4.5: Critical pressure ratio r_C as a function of γ for a simple hole connecting two plenums of different pressure.

function of M instead of P. Rearranging Eqs. (4.5), (4.6) and (4.7) yields:

$$\dot{m} = A\rho M\sqrt{\gamma rT} = AM\rho_0\left(1+\frac{\gamma-1}{2}M^2\right)^{\frac{-1}{\gamma-1}}\sqrt{\gamma rT_0\left(1+\frac{\gamma-1}{2}M^2\right)^{-1}}$$

$$\text{or}\quad \dot{m} = AM\rho_0\sqrt{\gamma rT_0}\left(1+\frac{\gamma-1}{2}M^2\right)^{\frac{-1}{\gamma-1}-\frac{1}{2}} = A\rho_0\sqrt{\gamma rT_0}\frac{M}{\left(1+\frac{\gamma-1}{2}M^2\right)^{\frac{\gamma+1}{2(\gamma-1)}}} \tag{4.11}$$

Alternatively, Eq. (4.11) can be written with the total pressure p_0 instead of the total density ρ_0:

$$\dot{m} = AP_0\sqrt{\frac{\gamma}{rT_0}}\frac{M}{\left(1+\frac{\gamma-1}{2}M^2\right)^{\frac{\gamma+1}{2(\gamma-1)}}} \tag{4.12}$$

At the nozzle throat, $M = 1$ since the nozzle is choked. Hence, the mass flow rate through the throat, $\dot{m}^*$, which is also the mass flow rate anywhere in the nozzle, $\dot{m}$, can be written simply as:

$$\dot{m}^* = A^*P_0\sqrt{\frac{\gamma}{rT_0}}\left(\frac{2}{\gamma+1}\right)^{\frac{\gamma+1}{2(\gamma-1)}} \tag{4.13}$$

Eqs. (4.11) and (4.13) can be combined to express the ratio of area A to throat area A^* as a function of Mach number M:

$$\frac{A}{A^*} = \frac{1}{M}\left[\frac{2}{\gamma+1}\left(1+\frac{\gamma-1}{2}M^2\right)\right]^{\frac{\gamma+1}{2(\gamma-1)}} \tag{4.14}$$

A plot of this function is given in Fig. 4.6.

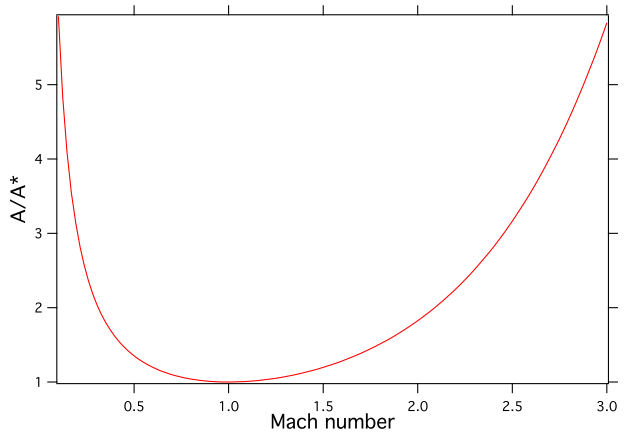

Figure 4.6: Plot of the $\frac{A}{A^*}$ area ratio versus Mach number

4.2.2.2 Theory of choked nozzles

Two types of nozzles are commonly used in LES:

- Simply converging nozzles, *i.e.* without diverging section (Fig. 4.7a)
- Converging-diverging nozzles (Fig. 4.7b)

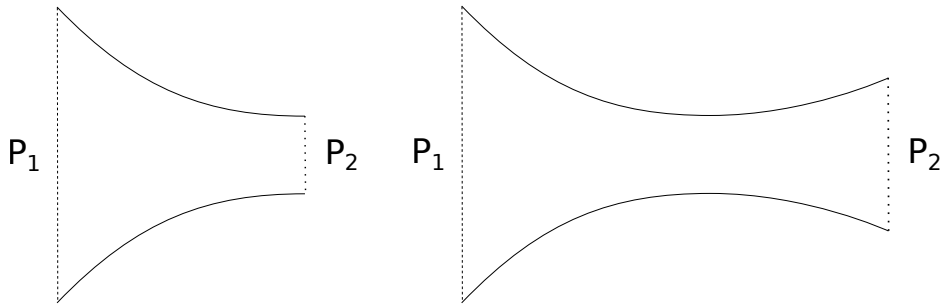

(a) Simply converging Nozzle **(b)** Converging-diverging Nozzle

Figure 4.7: Sketch of the two major types of nozzles studied here.

This distinction is important and each case must be treated specifically in order to understand the different regimes in which the nozzle can operate. In the following, the Mach number of the fluid in the chamber is considered negligible. Therefore, the static pressure P_1 and total pressure P_0 in the chamber are equal, and considered constant. The outlet pressure P_2 is then varied to demonstrate the various functioning regimes of the nozzle. For any other nozzle design, these arguments still apply. Of course, pressures P_0, P_1 and P_2 will be different, but the pressure *ratios* P_0/P_2 should be computed to estimate which regime the nozzle will function in.

Nozzle without diverging section Let us consider a simply converging nozzle connecting a chamber to an outlet region. In order to "choke" a flow, *i.e.* for the Mach number to reach a value of 1, a significant difference in pressure between the

chamber and the outlet must exist. At the point where the Mach number reaches 1, the static pressure is given by the total pressure in the chamber divided by the critical pressure ratio r_C, given in Eq. 4.10. Hence, if a straight duct connects a chamber to the atmosphere, or if a simple hole is made in a chamber wall, the flow will be choked as soon as the chamber total pressure P_0 is:

$$P_0 = r_C \cdot P_2$$

Nozzle with diverging section If a converging/diverging section connects two domains with different pressures, the previous condition changes. The critical pressure ratio of Eq. 4.10 yields the ratio of static pressure to outlet pressure, $r_{throat} = P_0/P_{throat}$ at the point where the Mach number is *exactly one*. According to the shape of A/A^* (Fig. 4.6), this point can only be *at the smallest section*, and is called the throat of the nozzle. The pressure can rise again in the divergent to meet P_2. The section variation between the outlet area and the throat, namely A_2/A^*, must be taken into account. The following explanation of this phenomenon is taken from the fluid mechanics textbook of White (1986).

Let $P_0 \sim P_1$ be constant. The following sequence describes the various operating conditions of the nozzle: the outlet pressure P_2 is initially supposed equal to the chamber pressure P_0. It is then progressively lowered, and the resulting flow in the nozzle is described.

$P_2 = P_0$:
The Mach number at the outlet is 0, there is no flow through the nozzle. The pressure ratio, $r = {}^{P_0}/_{P_2}$, is 1.

P_2 is lowered :
The pressure gradient drives the flow, which establishes through the nozzle. The highest Mach number is at the smallest section: the throat.

Mach number at throat reaches 1 :
For this critical value of P_2, called P_{choke}, the flow is still subsonic in the diverging section. The Mach number therefore increases up to 1 in the converging section, and decreases again according to A/A^* in the diverging section. The pressure ratio is $r_{choke} = P_0/P_{choke}$. At this regime, the critical pressure ratio r_C defined previously is the ratio of total pressure P_0 to static pressure at the point where the Mach number $M = 1$, *i.e.* the throat. Hence, $r_C = P_0/P_{throat}$ is called r_{throat} for a converging-diverging nozzle. For burnt gases flowing through a nozzle, $\gamma = 1.26$ and $r_{throat} = 1.81$ (Fig. 4.5). For cold flows, $\gamma = 1.398$ and $r_{throat} = 1.89$. The outlet pressure P_{choke} for this regime is higher than P_{throat}: Eq. (4.14) yields the outlet Mach number M_2, and P_{choke} is given by Eq. (4.7).

P_2 is further decreased :
Once the outlet pressure goes below P_{choke}, the flow in the divergent becomes supersonic immediately after the throat. Therefore, the flow continues to

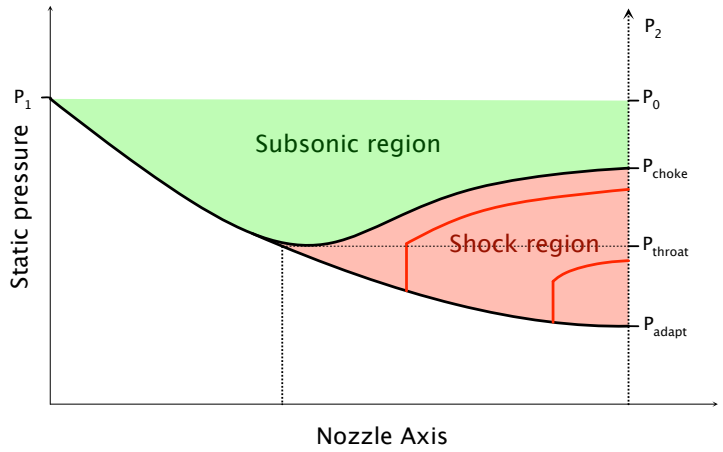

Figure 4.8: Plot of the static pressure throughout a nozzle for various operating conditions

accelerate after the throat, and the pressure continues to drop. Note that the static pressure at the throat P_{throat} stays constant, since the Mach number M can only be 1 at the throat. A shock appears in the diverging section and brings the flow back to subsonic conditions, and at the same time increases the pressure. This enables the static pressure at the end of the nozzle to meet P_2. This flow is said to be *under-expanded*.

For a new critical value of P_2, namely P_{adapt} :

If the outlet pressure P_2 is low enough, no shock is needed in the diverging section anymore to meet it. The flow is called an *adapted* flow, it is fully supersonic throughout the nozzle. The Mach distribution is entirely determined by A/A^*: knowing the outlet section A, Eq. (4.14) provides the outlet Mach (> 1) and Eq. (4.7) yields P_{adapt}. Like P_{choke}, P_{adapt} depends on the nozzle geometry. *Vice versa*, a nozzle can be designed to provide an adapted regime if the ratio P_0/P_2 is imposed.

When $P_2 < P_{adapt}$:

If the outlet pressure is lowered further, the flow no longer meets the outlet pressure P_2, but exits at a higher pressure than the outlet pressure. This flow is called *over-expanded*. Shocks still exist to meet the outlet pressure, but outside the nozzle. The present study is limited to the nozzle, hence the flow is exactly the same for all pressure ratios below r_{adapt}.

These various pressures are displayed in Fig. 4.8, originally plotted by Candel (1995). Let us now compute these ratios. At the outlet, Eq. 4.14 can be solved for Mach number, which leads to 2 values of Mach, one subsonic and one supersonic according to Fig. 4.6. The subsonic value, M_{sub}, corresponds to the maximum subsonic Mach number that can be achieved at the outlet, that is when the pressure

ratio is r_{choke}. It yields:

$$P_0 = P_{choke}\left(1+\frac{\gamma-1}{2}M_{sub}^2\right)^{\frac{\gamma}{\gamma-1}} \qquad \text{hence} \qquad r_{choke} = \frac{P_0}{P_{choke}} = \left(1+\frac{\gamma-1}{2}M_{sub}^2\right)^{\frac{\gamma}{\gamma-1}} \tag{4.15}$$

Similarly, the supersonic value M_{sup} is the Mach number at the outlet for the adapted flow. Hence, it yields:

$$P_0 = P_{adapt}\left(1+\frac{\gamma-1}{2}M_{sup}^2\right)^{\frac{\gamma}{\gamma-1}} \qquad \text{and} \qquad r_{adapt} = \frac{P_0}{P_{adapt}} = \left(1+\frac{\gamma-1}{2}M_{sup}^2\right)^{\frac{\gamma}{\gamma-1}} \tag{4.16}$$

For any pressure ratio less than r_{choked}, the pressure distribution in the nozzle is in the green area or "subsonic region". When the pressure in the chamber increases, as soon as the pressure ratio reaches r_{choked}, the flow is choked. A shock then appears in the diverging section in order to reach the target outlet pressure. The flow is then in the "shock region". If the pressure inside the chamber is further increased, it will eventually reach another critical value, namely r_{adapt}, for which the flow is exactly adapted, *e.g.* there is no more shock in the diverging section. The atmospheric pressure is met with a shock outside the nozzle.

4.2.2.3 Nozzle flow in aeronautic engine applications

The immediate section restriction after the flame in industrial applications is not necessarily choked at all regimes. However, it generally operates at high Mach number, and can present some choked regimes. The CESAM-HP setup is operated at unchoked regimes for non-reacting cases (but the flow is compressible) and at choked regimes for all reacting cases (see Chap.9). The description of compressible flow through the nozzle is therefore necessary, and the previous equations will be referred to throughout this manuscript. For combustion noise as well as instability studies however, this approach is insufficient. Indeed, the flow is supposed to have reached a steady-state here, but the dynamic behavior in unsteady conditions has not been described. Combustion noise is an entire field of study, and is thoroughly described in Chap. 5. The impact of the nozzle outlet on the combustor dynamics and stability is investigated in the rest of this chapter.

4.3 Influence of outlet conditions on thermo-acoustic instabilities

This section presents two simple analytical approaches which are useful to understand how using a nozzle modifies the combustion instabilities of a chamber. First, a 1D network model is applied to a chamber terminated either by an open outlet or by a nozzle (Sec. 4.3.1). This simple analysis shows that modes are very different when a nozzle is added to a chamber and that a bulk mode (where pressure fluctuations are

homogeneous in the chamber) can appear, and that it cannot if the chamber ends with a constant pressure volume. This bulk mode allows a much deeper analysis, known for a long time (Crocco, 1951; Zinn, 1972; Culick & Kuentzmann, 2006), described in Sec. 4.3.2.

4.3.1 The Rijke tube as a toy model

4.3.1.1 Position of the problem

Many academic combustors end with a direct connection to the atmosphere. This represents a big amount of fluid at rest, and its pressure cannot be easily modified. For this reason, from an acoustic point of view the outlet is often considered as a "constant pressure", or $P' = 0$ condition (Rienstra & Hirschberg, 2003). This is the opposite of a perfect wall behavior, which is impermeable and prevents slipping, thus imposing a zero velocity condition or $u' = 0$.

A high-subsonic or choked nozzle constitutes a strong section restriction at the combustion chamber outlet, and accordingly is often modeled as a wall for acoustic purposes. More elaborate theories exist, offering actual impedance for varying frequency (Duran & Moreau, 2013) and varying amplitude (Huet & Giauque, 2013), but they confirm that the $u' = 0$ hypothesis is a good first approach.

Unsteady fluctuations at the nozzle are bound to occur in a turbulent combustion chamber. When academic test benches swap a simple atmospheric outlet with a choked nozzle, the matching acoustic condition roughly changes from $P' \approx 0$ to $u' \approx 0$. The Rijke tube, which is an excellent toy model for understanding the concepts surrounding thermo-acoustic instabilities (Poinsot & Veynante, 2011), is based on the $P' = 0$ condition. This section will show how this toy model is influenced by the use of a $u' = 0$ outlet condition.

4.3.1.2 Resonant frequency of a Rijke tube: atmospheric versus nozzle outlet

Consider the model problem of Fig. 4.9. According to Poinsot & Veynante (2011),

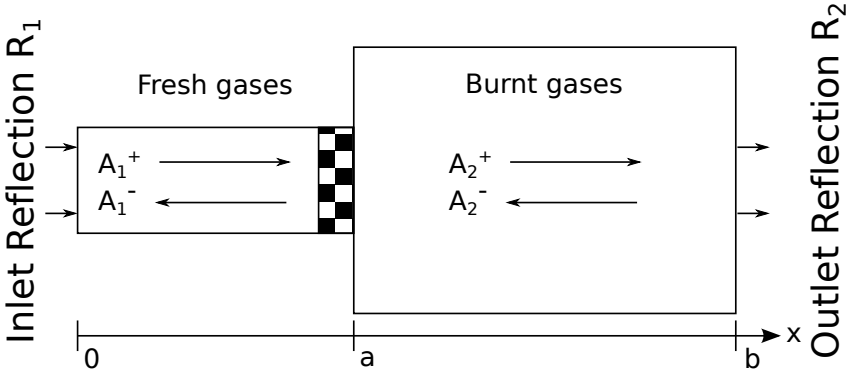

Figure 4.9: Model problem of the acoustics in a combustor.

if the flame is modeled using to the $n-\tau$ formalism, the following relation holds between left and right waves:

$$A_2^+ = \left[\cos(k_1 a) + \Gamma_1 i \sin(k_2 b)\left(1 + n e^{i\omega\tau}\right)\right] A_1^+$$
$$A_2^- = \left[\cos(k_1 a) - \Gamma_1 i \sin(k_2 b)\left(1 + n e^{i\omega\tau}\right)\right] A_1^+$$

The inlet condition for the tube is $R_1 = {}^{A_1^+}/_{A_1^-} = 1$, and the previous relations yield:

$$\left(R_2 e^{-2ik_2 b} - 1\right)\cos k_1 a - \left(R_2 e^{-2ik_2 b} + 1\right) i\Gamma_1 \sin k_1 a \left(1 + n e^{i\omega\tau}\right) = 0 \qquad (4.17)$$

The same author then proceeds to simplify these relations by using the reflection coefficient of the outlet $R_2 = {}^{A_2^+}/_{A_2^-}$. Suppose now that the outlet can have two different terminations:

- **OPEN**, the tube is open to the atmosphere. This implies $p' \approx 0$, and the reflection coefficient is $R_2 = -1$.
- **CHOKED**, the tube ends with a nozzle convergent. The nozzle blockage ratio is high, and its behavior resembles that of a wall. Consequently, $u' \approx 0$ and $R_2 = 1$.

Depending on which outlet is chosen, Eq. (4.17) will not write the same way. After some simplifications, **OPEN** and **CHOKED** write respectively:

$$\textbf{OPEN :} \quad \cos(k_1 a)\cos(k_2 b) - \Gamma_1 \sin(k_1 a)\sin(k_2 b)\left(1 + n e^{i\omega\tau}\right) = 0 \qquad (4.18a)$$
$$\textbf{CHOKED :} \quad \cos(k_1 a)\sin(k_2 b) + \Gamma_1 \sin(k_1 a)\cos(k_2 b)\left(1 + n e^{i\omega\tau}\right) = 0 \qquad (4.18b)$$

Exposing an analytical formulation for this general case is not easy. However, for the purpose of explanation, the problem can be extremely simplified. Suppose that $a = b$, $c_1 = c_2 = c$, $S_1 = S_2$ and $\rho_1 = \rho_2$. The resulting system is represented in Fig. 4.10. With these hypotheses, Eqs. (4.18) reduce to:

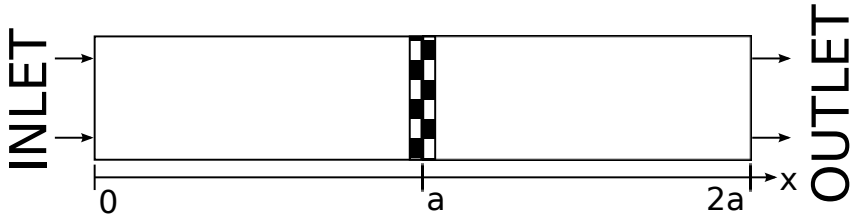

Figure 4.10: Extremely simplified model for ducted combustion, known as the Rijke tube.

$$\textbf{OPEN :} \quad \cos(2ka) = \frac{n e^{i\omega\tau}}{2 + n e^{i\omega\tau}} \qquad (4.19a)$$
$$\textbf{CHOKED :} \quad \sin(2ka)\left(2 + n e^{i\omega\tau}\right) = 0 \qquad (4.19b)$$

These already yield a very different shape. Without combustion ($n = 0$), the resonant frequencies of the cavity appear:

$$\textbf{OPEN :} \qquad \cos(2ka) = 0 \qquad \text{or} \quad k \equiv \pi/4a \ [\pi/2a] \tag{4.20a}$$

$$\textbf{CHOKED :} \qquad \sin(2ka) = 0 \qquad \text{or} \quad k \equiv 0 \ [\pi/2a] \tag{4.20b}$$

Fig. 4.11 represents the first modes' pressure and velocity distributions, according to each outlet. Note that for the CHOKED case, the $k \equiv 0$ mode exists: it is a mode of homogeneous pressure perturbations in the chamber. We will come back to this mode in the next section.

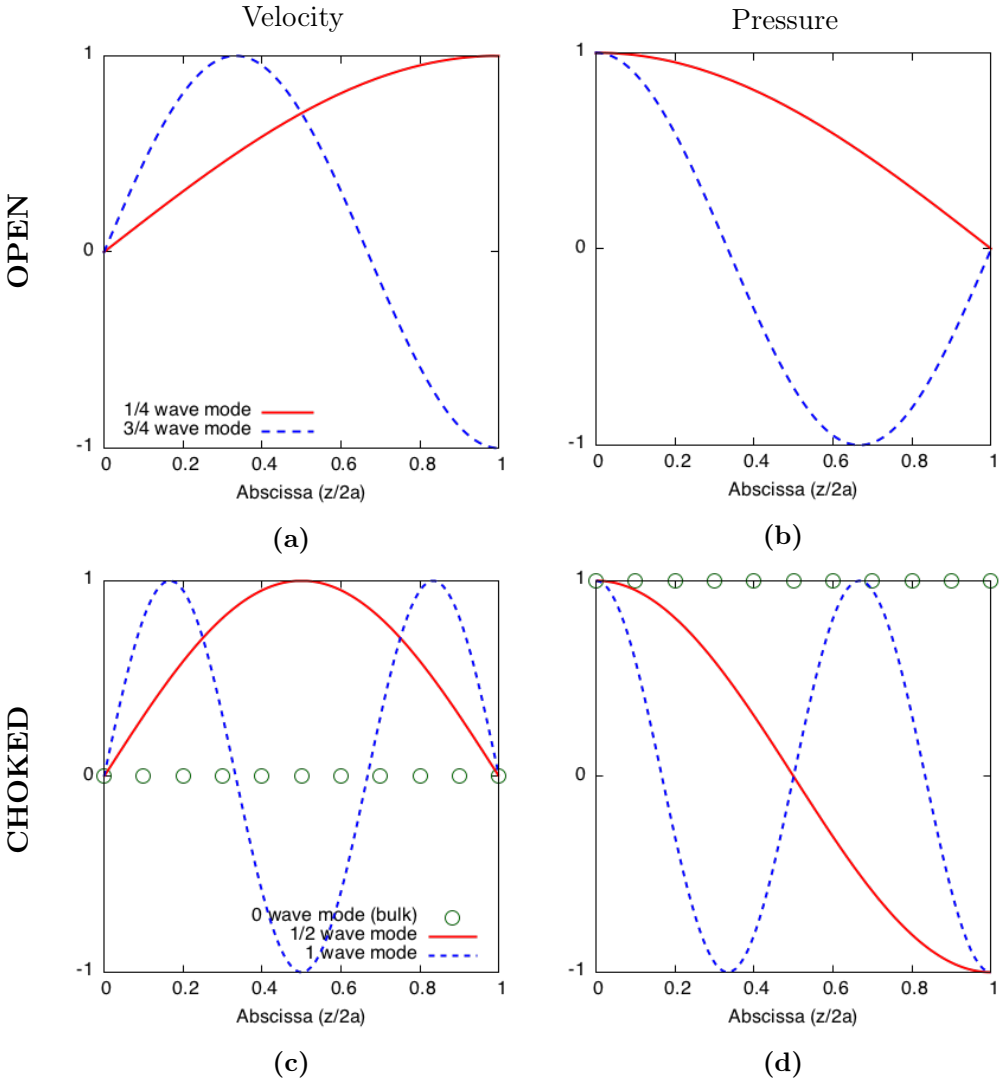

Figure 4.11: Velocity (left) and pressure (right) distributions of the first and second modes for the **OPEN** (top) and **CHOKED** (bottom) cases.

The first mode of the **OPEN** tube is the very classical 1/4 wave mode. The velocity perturbation at the inlet is imposed at zero by the inlet condition on all

acoustic modes (Fig. 4.11a). At the outlet, $p' = 0$ is also visible on the pressure traces (Fig. 4.11b).

The **CHOKED** tube however imposes $u' = 0$ at the outlet, which is visible in Fig. 4.11a. As a result, the velocity antinode is set in the middle of the domain, where the flame would be. This is also a pressure node. In fact, this suggests that in a mathematical sense, if the heat release occurs at $x = a$, it cannot fuel the acoustic mode. This explains Eq. (4.18b), which in fact does not necessitate the no combustion hypothesis $n = 0$ to yield Eq. (4.20b). This artifact is therefore due to the perfect symmetry of the system, which is only mathematical and must be broken to represent a realistic system more accurately. Two options are available to break this symmetry:

- the flame can be downstream from the pressure node and velocity antinode, referred to as case **CHOKED**$^+$;
- the flame can be upstream from the pressure node and velocity antinode, referred to as case **CHOKED**$^-$;

These two analogous situations are represented in Fig. 4.12. Eq. (4.18) now writes:

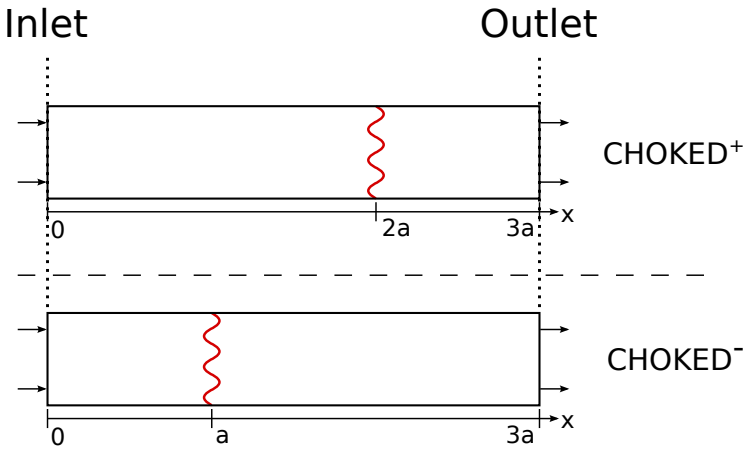

Figure 4.12: Non-symmetrical Rijke tubes to break symmetry artifacts.

$$\textbf{CHOKED}^+ : \quad \sin(3ka)\left(1+\frac{n}{2}e^{i\omega\tau}\right)+\sin(ka)\frac{n}{2}e^{i\omega\tau}=0$$

$$\textbf{CHOKED}^- : \quad \sin(3ka)\left(1+\frac{n}{2}e^{i\omega\tau}\right)-\sin(ka)\frac{n}{2}e^{i\omega\tau}=0$$

which again without combustion ($n = 0$) yields the simple tube resonant frequencies:

$$\sin(3ka)=0 \qquad \text{or} \quad k \equiv 0 \ [\pi/3a]$$

the symmetry rupture however has changed the nature of the dispersion relation with respect to n. In this case, if $n \neq 0$, the solutions will no longer be simply the cavity's resonant modes.

4.3.1.3 Linear stability theory

The Rijke tube is a good toy model for linear stability investigations. Following the example of Poinsot & Veynante (2011), consider the first non-trivial mode of the tube for no combustion ($n = 0$), at frequency ω_0. This writes for each outlet type:

$$k_0 = \frac{\omega_0}{c} = \begin{cases} \pi/2L & \text{for } \textbf{OPEN} \\ \pi/L & \text{for } \textbf{CHOKED}^{+/-} \end{cases}$$

where L, the total tube length is used because the symmetry breaking has led to different values of a for each case. Comparing total tube length is therefore more straightforward. Combustion can then be introduced using a value of $n \ll 1$, which induces a wave number $k = k_0 + k'$. For the **OPEN** case this yields:

$$\cos(2(k_0 + k')a) \approx \frac{n}{2} e^{i\omega_0 \tau}$$
$$k' = -\frac{n}{4a} e^{i\omega_0 \tau}$$

and linear stability theory states that the mode is unstable if the imagniary part of k' is strictly positive, *i.e.* the instability criterion is $\Im(k') > 0$ and writes $\sin(\omega_0 \tau) < 0$ hence:

$$\tau \in \left] \frac{\pi}{\omega_0}; \frac{2\pi}{\omega_0} \right[= \left] \frac{T}{2}; T \right[= \left] \frac{2L}{c}; \frac{4L}{c} \right[\tag{4.21}$$

where $T = 1/f_0$ is the natural mode period. It is often stated in the instability community that "for small time delay, no instability can occur": the time delay must be of at least half the natural mode period to observe an instability.

The same analysis can also be lead on the **CHOKED**$^+$ and **CHOKED**$^-$ configuration. Because $n \ll 1$, k' is expected to be small compared to k_0. Since $\sin(3k_0 a) = 0$, a reasonable assumption is that $\sin(k_0 a) \neq 0$. The dispersion relations become:

$$\frac{\sin(3ka)}{\sin(ka)} = \frac{n/2 e^{i\omega_0 \tau}}{1 + \frac{n}{2} e^{i\omega_0 \tau}} \begin{cases} \times(-1) & \text{for } \textbf{CHOKED}^+ \\ \times(1) & \text{for } \textbf{CHOKED}^- \end{cases}$$

and since:

$$\frac{\sin(3ka)}{\sin(ka)} = 2\cos 2ka + 1$$
$$-\frac{n e^{i\omega_0 \tau}}{2 + n e^{i\omega_0 \tau}} \approx -\frac{n}{2} e^{i\omega_0 \tau}$$

they write:

$$\cos(2ka) = \frac{2 + n e^{i\omega_0 \tau}}{4} = \begin{cases} \times(-1) & \text{for } \textbf{CHOKED}^+ \\ \times(1) & \text{for } \textbf{CHOKED}^- \end{cases}$$

Linearizing $k = k_0 + k'$ yields:

$$k' = \frac{2 + ne^{i\omega_0\tau}}{4\sqrt{3}a} \begin{cases} \times(1) & \text{for } \mathbf{CHOKED}^+ \\ \times(-1) & \text{for } \mathbf{CHOKED}^- \end{cases}$$

The instability criterion is still $\Im(k') > 0$, which yields:

$$\tau \in \left[0; \frac{\pi}{\omega_0}\right[= \left]0; \frac{T}{2}\right[= \left]0; \frac{L}{c}\right[\qquad \text{for } \mathbf{CHOKED}^+ \tag{4.22a}$$

$$\tau \in \left]\frac{\pi}{\omega_0}; \frac{2\pi}{\omega_0}\right[= \left]\frac{T}{2}; T\right[= \left]\frac{L}{c}; \frac{2L}{c}\right[\qquad \text{for } \mathbf{CHOKED}^- \tag{4.22b}$$

This result shows that the symmetry breaking strategy has a drastic influence on the stability analysis: depending on whether the flame is before or after the pressure node, the stability map is reversed. Note that a system with no delay $\tau = 0$ is still stable in this analysis. However, if the flame is downstream from the pressure antinode, very small time-delays lead to unstable behavior, and only time delays greater than the half-period lead to stable modes.

4.3.1.4 Key take-aways from the Rijke tube

The Rijke tube is an accessible toy model to study the influence of boundary conditions on thermo-acoustic instabilities. In this section, the changes induced by swapping an atmospheric outlet ($P' = 0$) by a nozzle ($u' = 0$) have been investigated. It appears that the stability map of a half-wave system can swap compared to the atmospheric case, depending on the relative positions of the flame and the pressure nodes of the mode. As will be shown in Chap. 11, this is in fact the case for the CESAM-HP setup, in which the Helmholtz solver predicts a stability map that matches the **CHOKED**$^+$. This is coherent with the mode shape, where the flame is downstream from the pressure node.

Another important observation made on all **CHOKED** cases is that they can exhibit a bulk mode where pressure oscillations are in phase in the whole chamber. The appearance of such a mode is the subject of Sec. 4.3.2.

4.3.2 Bulk mode instability in choked combustors

The previous section has shown that the **CHOKED** case can drive a bulk mode at low frequencies. This mode has been known for a long time, especially for rockets terminated by nozzles: these combustors have been studied extensively since World War II. While steady-state operation is sought, reports of unsteady phenomena have been made as early as the 50's, and sorted between low frequency (called "chugging") and high frequency (called "screaming") oscillations (Crocco, 1951). Chugging has been described as very low frequency (≈ 100 Hz) bulk fluctuations of the chamber pressure. Summerfield (1951) reports witnessing test fires of a 1000-lb pound thrust engine which proceeded smoothly upon ignition, but where combustion rapidly

became rough, with severe pressure fluctuations which often ruptured the chamber bolts before the test was stopped. These observations lead to the introduction of the concept of a time-delay τ between the pressure fluctuations and the pressure source, be it solid, liquid or gaseous combustion, or even the reaction time of a component of the complete system (*e.g.* injection valves). Culick & Kuentzmann (2006) offer a review of the many approaches to the description of this linear instability, and note that even though the formalism varies greatly, since the nature of the problem is often the same, the results all collapse to the same explanation.

As discussed in Chap. 11, numerical simulations of the CESAM-HP combustion chamber exhibit high acoustic levels. Numerical post-processing described in the same chapter indicates "bulk mode" type activity, as the pressure oscillations in the chamber are fairly homogeneous in space (see Figs. 11.10 and 11.11). Since the time-delay description of Crocco (1951) is used throughout this manuscript to describe the flame's dynamic behavior, the following section presents a rigorous application of Crocco (1951)'s method to the CESAM-HP combustor. The objective is to evaluate the frequency and growth rate of the first low-frequency mode of such combustion chamber. While more precise tools are available for this task (such as the AVSP Helholtz solver, described in Chap. 7), this simple description sheds light on the nature of the instability.

4.3.2.1 System definition

Domain In this zeroth dimensional approach, the domain of interest is limited to the combustion chamber. Its boundaries are:

- the flame, considered infinitely thin and located in the dump plane;
- the nozzle throat;
- the chamber walls.

This domain is represented in Fig. 4.13 as the filled color region. The hatched cold region is not part of the domain. Additionally, the inlet is supposed to be acoustically open so that no wave can reflect on the left of the domain. This corresponds for example to the situation of a long anechoic inlet duct. Compared to the network model of the previous section, the new ingredient introduced here is the nozzle response $m* = f(P)$. This new relation is enough to close the problem as shown below.

The total mass in the domain is ρV. The instantaneous mass flow entering the domain is denoted m_b, and the one exiting the domain through the nozzle throat is denoted m^*. The mode of interest is considered to have a constant phase in the chamber, according to the "bulk mode" hypothesis (as seen in Fig. 4.11). This implies that pressure is constant in the domain, and according to notations of Fig. 4.13, p_b is the pressure inside the entire combustion chamber. However, the total mass in the domain is not considered constant, and it is entirely possible at any moment that $m_b \neq m^*$. This is in fact what will drive the instability. The classical ideal gas

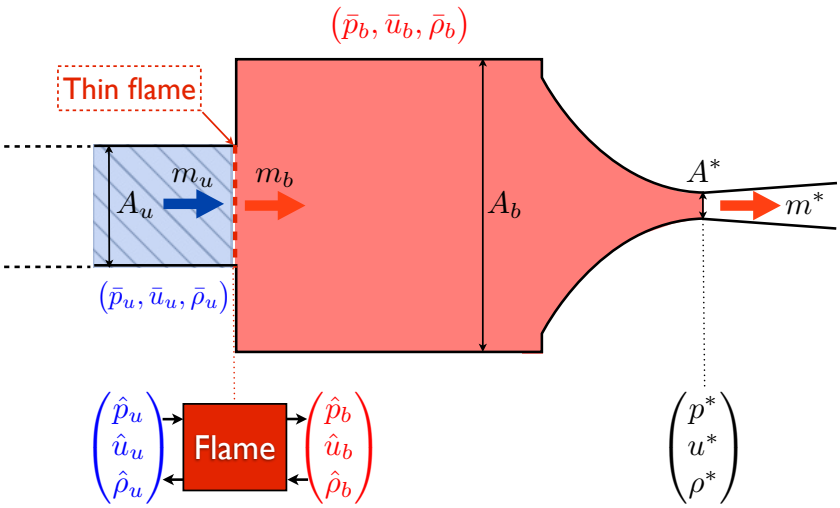

Figure 4.13: Schematic of the domain considered in this study. Filled color area is the domain of interest. Hatched area is not included.

relation is used to describe the fluid:

$$p = \rho r T \tag{4.23}$$

Compressions of the fluid in the chamber are considered adiabatic, as is customary in the acoustic community. Hence, compressions follow the Laplace laws for adiabatic compression of an ideal gas, yielding:

$$p\rho^{-\gamma} = cst \tag{4.24}$$

$$p^{1-\gamma}T^{\gamma} = cst \tag{4.25}$$

where γ is supposed constant in both burnt and unburnt sections.

Flame The flame is considered infinitely thin and located in the dump plane for this study. The mean unburnt flow characterisics are noted $(\bar{T}_u, \bar{\rho}_u, \bar{c}_u, \bar{u}_u)$, and the burnt flow mean characterisics $(\bar{T}_b, \bar{\rho}_b, \bar{c}_b, \bar{u}_b)$.

As shown later on, pressure is conserved through the flame, hence there is no need for different notations of pressure: this variable is simply denoted p.

The mean mass flow rate is of course conserved through the flame, as well as through the nozzle. It will have the unique notation $\bar{m}$, everywhere in the domain.

Strategy In order to describe the system behavior, an equation will be sought for the chamber pressure p. This approach is written in the time-domain. Quantites are linearized in time by decomposing each variable ϕ into constant and time varying parts:

$$\phi(t) = \bar{\phi} + \hat{\phi}(t)$$

4.3.2.2 Equation for system pressure

Mass conservation Writing mass conservation for the present system yields:

$$\frac{d}{dt}(\rho_b V) = m_b - m^* \tag{4.26}$$

The Laplace Eqs. 4.24 and 4.25 can be linearized. This yields respectively:

$$\frac{\hat{p}}{\gamma\bar{p}} = \frac{\hat{\rho}}{\bar{\rho}} \tag{4.27}$$

$$(\gamma - 1)\frac{\hat{p}}{\gamma\bar{p}} = \frac{\hat{T}}{\bar{T}} \tag{4.28}$$

This is true both in the cold and in the burnt gases. Introducing the sound speed $\bar{c}$:

$$\bar{c}^2 = \frac{\gamma p}{\rho} \tag{4.29}$$

The left-hand side of Eq. (4.26) becomes:

$$V\frac{d}{dt}\hat{\rho} = \bar{\rho}_b V \frac{d}{dt}\left(\frac{\hat{p}}{\gamma\bar{p}}\right)$$

Both in and out mass flow rates are written as:

$$m_b = \hat{m}_b + \bar{m}$$
$$m^* = \hat{m}^* + \bar{m}$$

Finally, Eq. (4.26) becomes:

$$\begin{aligned} \bar{\rho}_b V \frac{d}{dt}\left(\frac{\hat{p}}{\gamma\bar{p}}\right) &= \hat{m}_b - \hat{m}^* \\ \tau_c \frac{d}{dt}\left(\frac{\hat{p}}{\gamma\bar{p}}\right) &= \frac{\hat{m}_b}{\bar{m}} - \frac{\hat{m}^*}{\bar{m}} \end{aligned} \tag{4.30}$$

where $\tau_c = \frac{\bar{\rho}_b V}{\bar{m}}$ is the characterisic time needed for the mean mass flow rate to fill the combustion chamber.

The nozzle throat The outlet of the domain is controlled by the choked nozzle behavior. The mean mass flow rate through a choked nozzle can be expressed as:

$$\bar{m} = A^* P_0 \frac{1}{\sqrt{rT_0}} f(\gamma) \tag{4.31}$$

and in the current case, the Mach number in the chamber is very low. Hence, (P_0, T_0) can be assimilated to (p, T_b) in the chamber.

The perturbations of interest are of low frequency and of constant phase throughout the nozzle. For this reason, the compact nozzle assumption, as described by Zinn (1972) is justified here. This implies that Eq. (4.31) is actually true for the

time-dependant value m^* and not just $\bar{m}$. The last equation can be linearized, and simplified using Eq. (4.28), yielding:

$$\begin{aligned}\frac{\hat{m}^*}{\bar{m}} &= \frac{\hat{p}}{\bar{p}} - \frac{1}{2}\frac{\hat{T}_b}{\bar{T}_b} \\ &= \frac{\gamma+1}{2}\frac{\hat{p}}{\gamma\bar{p}}\end{aligned} \tag{4.32}$$

The dump plane and the flame The last term of interest in Eq. (4.26) is $\hat{m}_b$. This mass flux can be expressed and linearized as:

$$\begin{aligned}m_b &= \rho_b u_b A \\ \frac{\hat{m}_b}{\bar{m}} &= \frac{\hat{\rho}_b}{\bar{\rho}_b} + \frac{\hat{u}_b}{\bar{u}_b}\end{aligned} \tag{4.33}$$

A classical approach for dump combustors, described in Poinsot & Veynante (2011) is to write the acoustic jump conditions for thin flames. Starting from momentum and energy conservation equations, respectively, it is possible to show that:

$$\hat{p}_b = \hat{p}_u = \hat{p} \tag{4.34}$$

$$A\hat{u}_b - A_u\hat{u}_u = \frac{\gamma-1}{\gamma\bar{p}}\hat{q} \tag{4.35}$$

The modeling strategy for the flame here is the time-lag vision inspired by Crocco (1951, 1952), and the N_1 interaction index of Tab. 3.1:

$$\frac{\gamma-1}{\gamma\bar{p}}q(t) = A_u N_1 u_u(t-\tau) \tag{4.36}$$

Combined with Eq. (4.35) this yields:

$$A\hat{u}_b(t) = A_u\hat{u}_u(t) + N_1 A_u\hat{u}_u(t-\tau) \tag{4.37}$$

A link between this cold velocity $\hat{u}_u(t)$ and the pressure fluctuation $\hat{p}(t)$ is necessary to obtain an equation for pressure. The inlet is only subject to acoustic waves propagation, hence it is isentropic. Assuming low Mach number, the Euler equations produce the wave equation, known as the Helmholtz equation with no source terms, namely:

$$\frac{\partial^2\hat{p}}{\partial t^2} + c^2\nabla^2\hat{p} = 0 \tag{4.38}$$

the solutions to which are of the form:

$$\begin{aligned}\hat{p}(x,t) &= A^+(t - x/c) + A^-(t + x/c) \\ \hat{u}(x,t) &= \frac{1}{\bar{\rho}\bar{c}}(A^+(t - x/c) - A^-(t + x/c))\end{aligned}$$

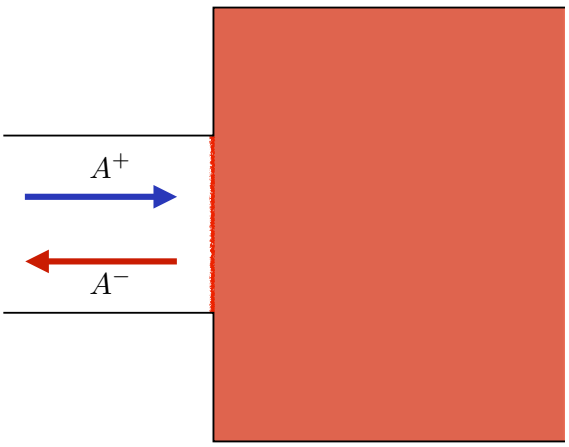

Figure 4.14: Left and right travelling waves in the inlet duct

where $A^+ = 1/2(\hat{p} + \bar{\rho}\bar{c}\hat{u})$ is a right travelling wave and $A^- = 1/2(\hat{p} - \bar{\rho}\bar{c}\hat{u})$ a left travelling one, as shown in Fig. (4.14). The non-reflecting inlet duct condition can therefore be expressed as $A^+ = 0$. The consequence for pressure and velocity is:

$$\hat{p}(t) + \bar{\rho}_u \bar{c}_u \hat{u}_u(t) = 0$$

$$\text{or:} \quad \hat{u}_u(t) = -\frac{\hat{p}(t)}{\bar{\rho}_u \bar{c}_u}$$

Eq. (4.37) therefore reads:

$$A\hat{u}_b(t) = -\frac{A_u}{\bar{\rho}_u \bar{c}_u}\left(\hat{p}(t) + N_1 \hat{p}(t-\tau)\right)$$

which in turn implies for Eq. (4.33):

$$\frac{\hat{m}_b(t)}{\bar{m}} = \frac{\hat{p}(t)}{\gamma\bar{p}} - \frac{\gamma\bar{p}}{\bar{u}_b\bar{\rho}_u\bar{c}_u}\frac{A_u}{A}\left[\frac{\hat{p}(t)}{\gamma\bar{p}} + N_1\frac{\hat{p}(t-\tau)}{\gamma\bar{p}}\right]$$

and since $\bar{m} = \bar{\rho}_u\bar{u}_u A_u = \bar{\rho}_b\bar{u}_b A_b$ and $\frac{\gamma\bar{p}}{\bar{c}_u} = \bar{c}_u\bar{\rho}_u$:

$$\frac{\hat{m}_b(t)}{\bar{m}} = \frac{\hat{p}(t)}{\gamma\bar{p}} - \frac{\bar{\rho}_b}{\bar{\rho}_u}\frac{1}{M_u}\left(\frac{\hat{p}(t)}{\gamma\bar{p}} + N_1\frac{\hat{p}(t-\tau)}{\gamma\bar{p}}\right) \tag{4.39}$$

The pressure RFDE At this point, Eqs. (4.30), (4.32) and (4.39) can be combined to produce an RFDE (Retarded Functional Differential Equation) for the pressure fluctuations in the domain:

$$\tau_c\frac{d}{dt}\left(\frac{\hat{p}}{\gamma\bar{p}}\right)(t) = \left(1 - \frac{\gamma+1}{2}\right)\frac{\hat{p}(t)}{\gamma\bar{p}} - \frac{\bar{\rho}_b}{\bar{\rho}_u}\frac{1}{M_u}\left(\frac{\hat{p}(t)}{\gamma\bar{p}} + N_1\frac{\hat{p}(t-\tau)}{\gamma\bar{p}}\right)$$

$$\text{or:} \quad \dot{\hat{p}}(t) = -\left[\frac{\gamma-1}{2\tau_c} + \frac{\bar{\rho}_b}{\bar{\rho}_u}\frac{1}{M_u\tau_c}\right]\hat{p}(t) - \frac{\bar{\rho}_b}{\bar{\rho}_u}\frac{N_1}{M_u\tau_c}\hat{p}(t-\tau) \tag{4.40}$$

Complex solutions to this equation yield frequency (real part) and growth rate (imaginary part) of the possible bulk oscillations of the chamber.

4.3.2.3 Solving the RFDE

The Gu *et al.* (2003) textbook on stability of RFDEs is used in this section to derive solutions to the pressure RFDE Eq. 4.40.

Theory of multiple time-delay systems stability Let the following RFDE with pointwise concentrated delays:

$$\begin{cases} \dot{x}(t) = \sum_{k=0}^{K} A_k x(t - r_k), & t \in]0, \infty[\\ x(t) = \phi(t), & \forall t \in [-\tau, 0] \end{cases} \tag{4.41}$$

where $\phi(t)$ is a known function of $[-\tau, 0]$ and represents the initial condition, A_k are given $n \times n$ real constant matrices, and r_k are given real constants, ordered such that:

$$0 = r_0 < r_1 < \cdots < r_K = r.$$

Defining the Laplace transform of x:

$$X(s) = \mathcal{L}[x(t)] = \int_0^\infty x(t) e^{-st} dt$$

where $s \in \mathbb{C}$, and applying to Eq. (4.41) yields:

$$sX(s) - \phi(0) = \sum_{k=0}^{K} A_k e^{-sr_k} X(s)$$

Solving for $X(s)$:

$$X(s) = \Delta^{-1}(s)\phi(0)$$

where:

$$\Delta(s) = sI - \sum_{k=0}^{K} A_k e^{-sr_k}$$

is called the *characteristic matrix*. The equation:

$$\det[\Delta(s)] = 0$$

is called the *characteristic equation*. Its solutions are called the *poles* of the system. A theorem of time-delay analysis states that:

Theorem 1. *For any scalar γ, the number of solutions (counting their mulitplicities) to the characteristic equation with real parts greater than γ is finite. Moreover, define the stability exponent α_0 as:*

$$\alpha_0 = \max_{s \in \mathbb{C}} \{ Re(s) |\ \Delta(s) = 0 \}$$

The following statements are true.

(i) The delay system (4.41) is stable if and only if $\alpha_0 < 0$

(ii) $\forall \alpha > \alpha_0,\ \exists L > 1$ *such that any solution* $x(t)$ *of (4.41) is bounded by:*

$$||x(t)|| \leq Le^{\alpha t} \left\|\phi(t)\right\|_\infty$$

(iii) α_0 *is continuous with respect to* τ*.*

According to this theorem, the study of the system stability reduces to the study of the characteristic poles of $\Delta(s)$. If all real parts are strictly negative, then the system is stable.

Solving for system pressure Here, the RFDE of interest can be cast to the simple form:

$$\dot{p}(t) = -Ap(t) - Bp(t-\tau)$$

where:

$$A = \frac{\gamma - 1}{2\tau_c} + \frac{\bar{\rho}_b}{\bar{\rho}_u}\frac{1}{\tau_c M_u}$$
$$B = \frac{\bar{\rho}_b}{\bar{\rho}_u}\frac{N_1}{\tau_c M_u}$$

The characteristic matrix of the system is a quasipolynomial here, since the dimension is 1, namely:

$$\Delta(s) = s + A + Be^{-s\tau}$$

It should be noted that $A + B > 0$. If this weren't the case, then $\Delta(0) < 0$ and since $\lim_{s\to+\infty} \Delta(s) = +\infty$, and $\Delta(s)$ is continuous, there would necessarily be a positive real pole, thus rendering the system unstable even for $\tau = 0$. Now, let $z = e^{-\tau s}$. The characteristic polynomial can be recast to:

$$a(s, z) = s + A + Bz$$

According to proposition *(i)* of Theorem 1, the system is stable if all its complex solutions have negative real parts. We have shown that the system was stable for $\tau = 0$, or equivalently that $a(s, 1) \neq 0,\ \forall s \in \bar{\mathbb{C}}_+$ where $\bar{\mathbb{C}}_+$ is the closed right half complex plane. Proposition *(iii)* states that the pole with highest real part (equal to the stability exponent) is continuous with respect to τ. Hence, the smallest deviation from $\tau = 0$ such that the system becomes unstable occurs when the stability exponent reaches 0, which means that the corresponding pole is a pure imaginary. The critical τ at which this happens is the *delay margin* $\bar{\tau}$, defined as:

$$\bar{\tau} = \min\left\{\tau \geq 0 \mid a(j\omega, e^{-j\tau\omega}) = 0 \text{ for some } \omega \in \mathbb{R}\right\} \tag{4.42}$$

Let:

$$a(j\omega_i, e^{-j\theta_i}) = 0, \qquad \omega_i > 0, \qquad \theta_i \in [0, 2\pi[, \qquad i = 1, 2, \cdots, N$$

which implies in the present case:

$$\bar{\tau} = \min_{1 \leq i \leq N} \left\{ \frac{\theta_i}{\omega_i} \right\}$$

One of the properties of real quasipolynomials is that all its complex roots appear in conjugate pairs. Therefore, if $a(j\omega, z^{-j\theta}) = 0$, then $a(-j\omega, z^{j\theta}) = 0$. This yields the following system:

$$\begin{aligned} j\omega + A + Be^{-j\theta} &= 0 \\ -j\omega + A + Be^{j\theta} &= 0 \end{aligned}$$

Eliminating $e^{j\theta}$:

$$\omega^2 + A^2 - B^2 = 0 \tag{4.43}$$

which has a non-trivial solution only if $A < B$. This implies that if in fact $A \geq B$, the system is stable independant of delay. If not, the frequency is $\omega_1 = \sqrt{B^2 - A^2}$ and:

$$\theta_1 = \angle \frac{B}{j\omega_1 + A} - \pi = \pi - \arctan(\frac{\omega_1}{A})$$

and finally:

$$\bar{\tau} = \frac{\theta_1}{\omega_1} = \frac{\pi - \arccos \frac{A}{B}}{\sqrt{B^2 - A^2}} \tag{4.44}$$

4.3.2.4 Discussion of the results

Critical N_1 The previous resolution has shown that a critical position for domain stability is when $A = B$, implying:

$$\frac{\gamma - 1}{2\tau_c} + \frac{\bar{\rho}_b}{\bar{\rho}_u} \frac{1}{\tau_c M_u} = \frac{\bar{\rho}_b}{\bar{\rho}_u} \frac{n}{\tau_c M_u}$$

In terms of flame interaction index $N_{1,crit}$, this equates to:

$$N_{1,crit} = 1 + M_u \frac{\gamma - 1}{2} \frac{\bar{\rho}_u}{\bar{\rho}_b}$$

which means that for the system to be capable of exhibiting an instability, it is necessary that $N_1 > N_{1,crit}$.

Delay margin $\bar{\tau}$ If $N_1 > N_{1,crit}$, the system is still stable for $\tau = 0$. It is however unstable for any flame delay higher than the delay margin $\bar{\tau}$. If such an instability occurs, its frequency will be:

$$\omega = \frac{\bar{\rho}_b}{\bar{\rho}_u} \frac{1}{\tau_c M_u} \sqrt{N_1^2 - N_{1,crit}^2}.$$

The time delay of the flame should then exceed:

$$\bar{\tau} = \frac{1}{\omega} \left(\pi - \arccos \left(\frac{N_{1,crit}}{N_1} \right) \right)$$

For values of N_1 close to $N_{1,crit}$, $\omega\bar{\tau} \approx \pi$. For higher values of N_1, $\omega\bar{\tau} \to \pi/2$. The evolutions of ω, $\omega\bar{\tau}$ and $\bar{\tau}$ with $N_1/N_{1,crit}$ are displayed in Fig.(4.15).

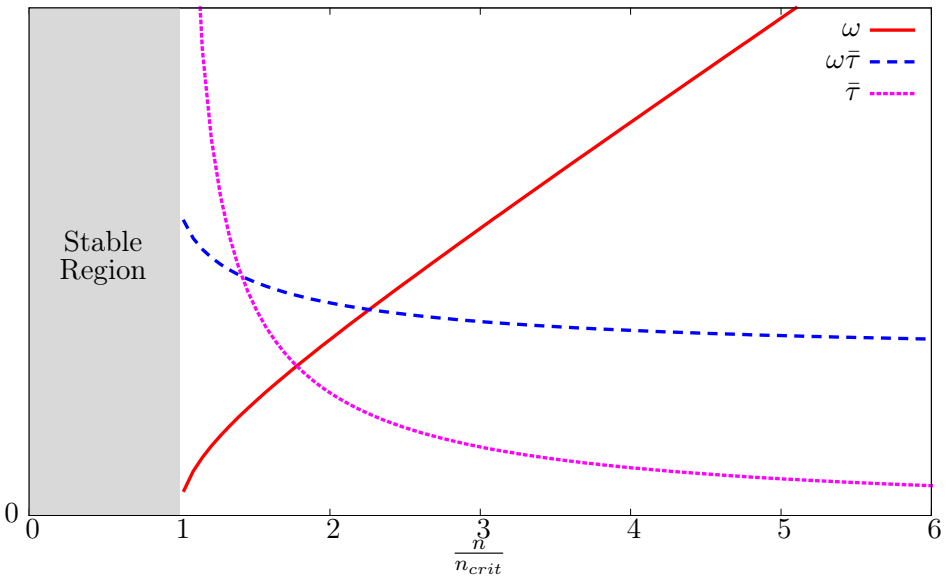

Figure 4.15: Evolution of ω, $\omega\bar{\tau}$ and $\bar{\tau}$ vs $N_1/N_{1,crit}$.

Interpretation The stability criterion can be stated as follows:

$N_1 < N_{1,crit}$ The system is stable, independant of delay.

$N_1 = N_{1,crit}$ The system is unstable, but the delay margin is $+\infty$. In practice, τ is finite, and the system cannot be unstable

$N_1 > N_{1,crit}$ The system can be unstable if $\tau > \bar{\tau}$. However, N_1 must be significantly larger than $N_{1,crit}$ in order for $\bar{\tau}$ to regain reasonable values.

Note that because Theo. 1 states that "(iii) α_0 is continuous with respect to τ", it is clear that an unstable zone exists when τ exceeds $\bar{\tau}$. However, for higher values of τ, it is possible that a new stability region can be found. Therefore, $N_1 > N_{1,crit}$ and $\tau > \bar{\tau}$ are necessary but not sufficient conditions for instability.

4.3.2.5 Application to the CESAM-HP setup

Operating point This model can give insight in the CESAM-HP burner stability. The values needed to run the model are summarized in Tab. (4.1).

$\bar{m}$	Fuel	Φ	T_u	T_b	M_u	A_u	gamma
18 g/s	C3H8	0.9	300 K	2200 K	0.02	0.0007 m^2	1.26

Table 4.1: Operating point of the CESAM-HP setup

Linking LES to this analytical model In the CESAM-HP setup, $N_{1,crit} = 1.019$. As expected, this value is slightly larger than 1, indicating that the flame must "react" more than it receives in order for the gain of the system to exceed 1.

The **CHOKED-ST** LES described in Chap. 11 will be used in that chapter to study the acoustic behavior of the system. Flame transfer functions are therefore computed, yielding the values of N_3 and τ as defined in Tab. 3.1. The value of interest for the current model, namely N_1, is related to N_3 by:

$$N_1 = \frac{\gamma - 1}{\gamma \bar{p} A_u} N_3 \tag{4.45}$$

The LES yields $N_1 = 900$ and $\tau = 1.8$ ms. The model parameters are then computed for this operating point, and summarized in Tab. (4.2). It is therefore clear that both instability criterion are met, namely $N_1 > N_{1,crit}$ and $\tau > \bar{\tau}$.

4.3.3 Conclusion

This chapter has shown that the stability of a choked combustor is not directly analogous to the classical atmospheric outlet setup. In terms of acoustics, a nozzle with a strong section restriction is indeed very reflective, and the acoustic energy is trapped inside the domain. Additionally, the $u' = 0$ condition can lead to different stability maps than the $p' = 0$ condition.

Moreover, this type of setup is known to lead to low-frequency "bulk" instabilities under some specific conditions. An example of theoretical derivation has been given, showing that the CESAM-HP setup studied in this Ph.D can potentially present low frequency instabilities.

N_1	ω	$f = \omega/2\pi$	$\bar{\tau}$
1.05	1173 rad/s	187 Hz	1.49 ms

Table 4.2: Stability variables for the CESAM test-rig

Chapter 5

Combustion noise: sources and influence of outlet conditions

Unsteady combustion can be a strong source of sound in high energy combustion systems. Sec. 5.2 attempts to clarify the mechanisms by which chemical processes of combustion can lead to sound generation, known mostly as direct and indirect combustion noise. While the acoustic community often simplifies the problem to a single specie one, an attempt is made here to explain the effect of accounting for multi-species fluids in noise evaluation. In a second part, namely Sec. 5.3, this approach is applied to a general flame model, in order to estimate the relative level of each noise type (direct and indirect) that can be expected in an actual burner. A simple toy model for the flame from the literature (Leyko, 2010) is improved to include more physical effects, and the corresponding change in expected noise contributions is exposed.

5.1 Introduction

The noise produced by unsteady combustion is an intuitive phenomenon. When one opens the feeding line of a blowtorch for example, moderate sound levels are perceived. However, as soon as the torch is ignited, a loud rumbling sound can be heard (Truffaut, 1998). This result has reasonable consequences on a household blowtorch with a power output of the order of 2 kW. When a Boeing 777 takes off however, each of its GE90 engines burns approximately 200 MW worth of fuel (based on data from the ICAO Aircraft Engine Emissions Databank). Sound is of course perceived by the human ear in a logarithmic manner, but these 5 orders of magnitude nevertheless highlight the fact that even if noise production processes are inefficient, very intense noise can be produced and radiated by such powerful systems.

Combustion itself is not necessarily a noisy phenomenon. Laminar flames for example are steady-state processes, hence no time fluctuations are associated and no acoustic radiation is observed. This is the case for example in a candle or lighter flame. The key element in high power combustion is the unsteadiness that is introduced, resulting in possible acoustic radiation. Unsteady combustion is very frequent in industrial applications, as laminar systems permit only very low power outputs: any need for higher mass flow rates leads to higher Reynolds numbers and the flow

becomes turbulent. Intuitively, this unsteady dilatation acts as a fluctuating volume (monopolar) source, quite similarly to a loudspeaker (Crighton *et al.*, 1992). The precise description of the processes involved is difficult, as the unsteadiness results from turbulence-flame interactions (Strahle, 1971, 1972).

In confined environments such as combustion chambers, acoustics are intertwined with hydrodynamics, and the flame dynamics become more complex. Evaluation of sound sources in such a case is a subtle issue, and various approaches have been proposed, as discussed in this chapter. Another effect of confinement is that the mean flow is no longer at rest, and the flow perturbations (*e.g.* entropy waves) are accelerated through the expansion system downstream of the combustion chamber. This can result in so called *indirect noise* production, where the accelerated perturbations radiate noise (Marble & Candel, 1977*b*). This striking result obtained in the last 40 years implies that the farfield noise of a gas turbine may be due not only to the unsteady monopole sound sources in the combustion chamber but also to the convection of entropy spots created *e.g.* by combustion through the turbine stages. The total noise prediction therefore depends on correct evaluations of direct noise production and transmission through the nozzle on the one hand, and entropy fluctuation and convection, with the associated noise production through the turbine on the other. The outlet boundary condition of the combustion chamber therefore controls the farfield combustion noise, and atmospheric combustion studies (which are very common in practice) will miss many aspects found in real chambers terminated by nozzles and operating at high pressures.

5.2 Sources of sound associated with combustion

5.2.1 The concept of "acoustic analogy"

5.2.1.1 Non reacting aeroacoustics

There are two essential aspects to the study of acoustics: noise production and propagation. Classical approaches such as described in Chap. 3 take interest in sound propagation, but sources modelling is overlooked at best, if not ignored. However, the field of aeroacoustics and combustion acoustics cannot afford such simplifications, as the most difficult aspect of the noise evaluation is often the determination of the sources (Clanet & Searby, 1975; Goldstein, 1976). The production of sound can be the result of many phenomena, such as the vibration of a solid object. In turbulent gaseous flows, the sound is generally produced by a small volume of the flow itself, *e.g.* the wake behind an object, or a jet. One of the issues with this problem is the orders of magnitude of difference in size between the sound production zone and the propagation zone. In the case of aircraft noise, sound sources are localized near small variations of fuselage shape, and in the engines region. The size of each sound production zone is in the order of a few centimeters, or even barely a couple of millimeters. At the other end of the spectrum, this sound propagates to the populations living near airports, several hundred meters away at the very least.

In order to address this problem, Lighthill (1951) suggested a so called "acoustic analogy". It is an alternative formulation of the Navier-Stokes equations in the form of a wave equation and a source term. By rearranging flow equations, the density fluctuations in the flow are expressed as an external stress applied to a uniform acoustic medium at rest. This stress tensor is called the “Lighthill tensor”:

$$T_{ij} = \rho u_i u_j + p_{ij} - c_0^2 \rho \delta_{ij}$$

which represents the source of all aeroacoustic noise and leads to the wave equation with source term :

$$\frac{\partial^2 \rho}{\partial t^2} - c_0^2 \nabla^2 \rho = T_{ij} \tag{5.1}$$

This approach does not require any hypotheses and is exact. However, it is difficult to work with, since of course all non linear terms are contained in Lighthill's tensor. For this reason, many authors have used this analogy as a starting point for the development of simplified analogies adapted to more specific problems.

Powell (1964) suggested the use of a simplified source term in which the fluid is considered ideal and incompressible. In this case, Powell argues that vorticity is the most important contribution to the total aerodynamic noise, mostly because his primary field of interest is sound generation in ducts. This approach seemed valid for the cases that he considered, but its field of application was very limited. Noticeably, the radiation of noise by solid surfaces was not taken into account. One decade earlier, Curle (1955) had derived a source term enabling the modeling of interactions between rigid motionless surfaces and the flow. However, for many applications such as turbomachinery or helicopter rotor noise, these assumptions were obviously too restrictive. In 1969, Williams & Hawkings (1969) suggested an alternative analogy also based on Lighthills study but with a considerably extended field of use, as it was capable of considering any mobile and non rigid surface as a source of sound.

In parallel to these developments, other studies attempted to describe the propagation of sound through a non uniform medium. By using a convective derivative instead of assuming a medium at rest, Phillips (1960) derived an acoustic analogy enabling both velocity and speed of sound spatial variations to be taken into account for the propagation of sound waves. His version of the source terms also enabled entropy sources to be accounted for. Lilley (1974) extended this analogy by including additional convective terms in the wave equation, hence including refraction effects to the propagation. Unfortunately, these modifications basically tend to bring the analogy back to a complete description of the physics. As can be expected, the simplification introduced by the analogy approach tends to disappear, and the solutions to such equations become very complex. Nevertheless, both these analogies have lead to many developments concerning aero jet engines.

Finally, it should be noted that two analogies were derived based on the *stagnation enthalpy* $B = H + {}^1\!/_2 \boldsymbol{U} \cdot \boldsymbol{U}$ by Howe (1975) and Doak (1973). The author does not know of any major application of this approach. A summary of the different wave equations for reacting flows can be found in the paper of Bailly *et al.* (2010).

5.2.1.2 Acoustic analogy for reacting flows

Reacting flows present several major differences with the usual medium considered for acoustics:

- the flame produces heat, hence dilatation and acoustic source terms;
- several species are involved in the gas mixture, and the distribution between these species varies in time and in space;
- usual orders of magnitude of all effects must be reviewed and usual simplifications cannot necessarily be made;
- the sound speed itself changes with temperature and composition.

Crighton *et al.* (1992) and Bailly *et al.* (2010) give the complete exact form of Lighthill's acoustic analogy of Eq. (5.1) for a reacting flow:

$$\begin{aligned}\frac{1}{c_0^2}\frac{\partial^2 p}{\partial t^2} - \nabla^2 p = & \underbrace{\boldsymbol{\nabla}\cdot\boldsymbol{\nabla}\cdot(\rho\boldsymbol{u}\boldsymbol{u}-\boldsymbol{\tau})}_{\text{aerodynamic sound}} \\ & + \frac{\partial}{\partial t}\left[\frac{\rho_0}{\rho}\frac{\gamma-1}{c^2}\left(\boldsymbol{\nabla}\left(\lambda\boldsymbol{\nabla}T\right) + \underbrace{\dot{\omega}_T}_{\text{direct combustion noise}} + \boldsymbol{u}:\boldsymbol{\nabla}\boldsymbol{\tau} - \rho\sum_k Y_k c_{P,k}\boldsymbol{u}_k\cdot\boldsymbol{\nabla}T\right) + \rho_0\frac{\partial}{\partial t}\left(\ln r\right)\right] \\ & + \frac{1}{c_0^2}\frac{\partial}{\partial t}\left[\left(1-\frac{\rho_0 c_0^2}{\rho c^2}\right)\frac{\partial p}{\partial t} - \frac{p-p_0}{\rho}\frac{\partial \rho}{\partial t}\right] \\ & + \underbrace{\boldsymbol{\nabla}\cdot\frac{\partial}{\partial t}\left(\rho_e\boldsymbol{u}\right)}_{\text{indirect combustion noise}}\end{aligned} \tag{5.2}$$

Three important sources can be identified in the lowest order terms of this analogy:

aerodynamic sound includes two sources: the first is the interaction of velocity perturbations with solid boundaries, an efficient dipolar source of sound; the second is the generation of sound due to turbulence, which is much less efficient and radiates like a quadrupole;

indirect combustion noise arises at locations where excess density perturbations are accelerated by the mean flow;

direct combustion noise a volume source related to the unsteady flame dilatation which acts as a volume source, hence radiates efficiently as a monopole.

Lighthill (1952) showed that aerodynamic sound production scales with the fifth power of the Mach number. This implies that for the low Mach numbers encountered in combustion chambers, aeroacoustic sound production is a highly inefficient phenomenon. The specific case of quadrupolar sources were in fact shown in the same study to scale with the *eighth* power of the Mach number. In the context of combustors, monopolar sources linked to combustion are therefore expected to be the primary sources of sound, at least for direct combustion noise.

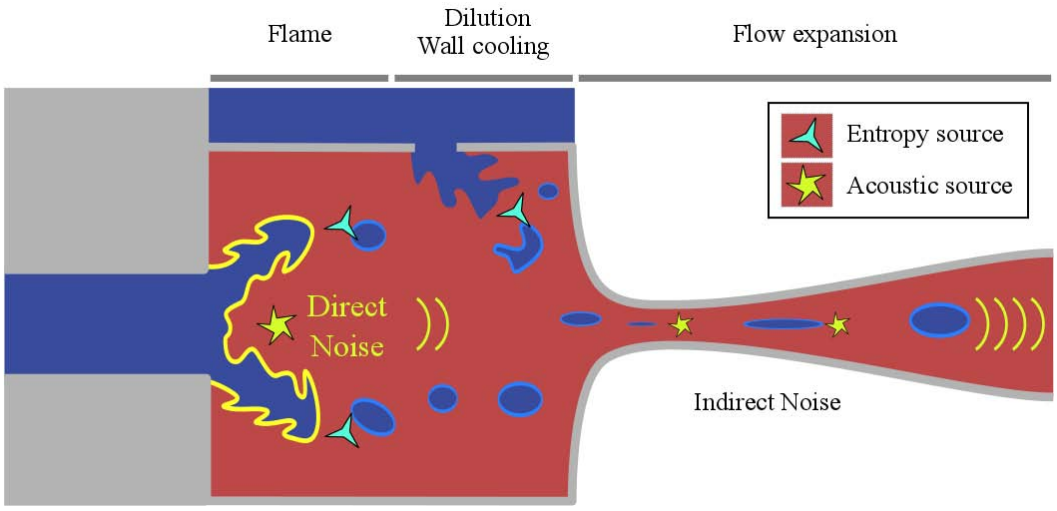

Figure 5.1: Direct and indirect sources of combustion noise. Both propagate through the nozzle before radiating downstream.

5.2.2 Noise associated with combustion in an aeronautic burner

A combustion chamber is home to a wide range of unsteady phenomena. Fig. 5.1 shows a schematic combustion chamber with its nozzle. The fresh gases on the left are mixed, and the turbulent burning process leads to both acoustic waves propagating in all directions, and entropic density perturbations convected with the mean flow. A non premixed flame can burn over a spectrum of equivalence ratios, leading to different burnt gases temperature and composition. Inside the chamber, wall cooling and dilution processes also contribute to the overall density perturbation, as dilution systems inject cold (dense) air in the flow, with a composition that can vary strongly from the burnt gases. As mentioned in the previous section, the aerodynamic sound produced by all chamber processes is not zero, but it is expected to be small compared to heat-related processes because the Mach number in the chamber is small. Turbulent mixing takes place in the chamber, smoothing somewhat high frequency perturbations, but is very inefficient to damp high wavelength perturbations.

Acoustics in this closed medium behave according to its resonant properties. Resonators are excellent candidates for noise production: musical instruments, where noise efficiency is sought, usually comprise an acoustic source (a vibrating object such as a string, a reed or even the lips of the musician) and a resonator. The resonator offers the possibility to excite acoustic modes, which in turn increases the radiation efficiency of the excited frequency. In the case of wind instruments, the source and resonator can couple, increasing the power of the source, and in turn the amplitude of the resonator mode (Fabre *et al.*, 2012).

A combustion chamber holds a curious resemblance to these musical devices. The chamber is an excellent resonator, often with some highly reflecting boundaries: the outlet nozzle for example also almost acts like a wall ($u' = 0$) for acoustic waves. The flame on the other hand acts as a wide-band acoustic source, which can couple with

the chamber modes, and in extreme cases can lead to combustion instability (see Chap. 3). In general, knowledge of the noise emitted by the free flame is insufficient to predict the noise emission by such systems. Much like the musical instrument, the combustion chamber plays the role of a resonator. Some frequencies are cut, and energy accumulates on others. The acoustic waves exiting the chamber are the result of this complex dynamic. This makes modeling "chamber noise" a difficult task, even if good tools are available for flame direct noise.

Once the nozzle is reached, both acoustic and entropic waves propagate downstream. Density gradients produce sound (indirect noise), according to term 3 in Eq. (5.2). The sum of this transmitted sound and sound produced in the nozzle then propagates further downstream, eventually adding up to other exterior noise sources. Once downstream from the nozzle, Mach numbers can be high and aerodynamic sources increase considerably. Jet noise for example becomes important in this zone. This chain of events leads to the following context for combustion noise studies:

1. heat related noise, *i.e.* direct and indirect noise, is expected to be the major noise source in the combustion chamber. This is why combustion noise and core noise are two expressions found in the literature designating the same sources;
2. high frequency perturbations are trapped inside the engine and strongly dissipated by both the hot viscous flow and turbulence. The noise that subsides at the engine outlet without being significantly damped is expected to be in the low-frequency range. Engine manufacturers estimate that combustion noise is expected in the 0 - 5000 Hz range.

5.2.3 Flame or "direct" noise

Combustion occurs in a variety of propulsive (engines) and non propulsive systems. Many parallels exist between the two fields, and a review of combustion noise in non-propulsive systems is available (Putnam & Faulkner, 1983), but in the scope of this manuscript, the specific case of propulsive systems will be addressed.

5.2.3.1 Literature on flame noise

The first manifestations of combustion noise in engines were associated to combustion instabilities confirming again the similarities between these two research fields. Rocket engines designed in the 50's and 60's unveiled a number of failures due to "screaming" or "chugging" (Bragg, 1962). Both were in fact thermoacoustic phenomena, with intense associated noise but also severe to catastrophic consequences. But in the 60's, consciousness that "normal" combustion (*i.e.* with no clear instability) was also a very noisy process started to appear. Smith & Kilham (1963) characterized experimentally the noise produced by open turbulent flames, and Bragg (1963) derived a first analytical theory where the flame was assimilated to numerous incoherent volume sources, thus predicting a correlation between the heat release fluctuations and the radiated noise. Thomas & Williams (1966) later derived a neat experimental

test case to quantify precisely the monopole source term associated with combustion: premixed gases were trapped in soap bubbles before being ignited in their center (Fig. 5.2). In this case, the combustion process is not turbulent, but it is unsteady by nature since the flame surface is a sphere of increasing radius, hence increasing area. This was the first experimental demonstration of the proportionality between time variations of heat release and noise. Because of the simplicity of the setup, the data was even successfully compared to the theoretical values. Hurle *et al.* (1968) conducted a series of experiments on a set of burners which represented a realistic burner more accurately. Here the flow was turbulent, but using low-pass filters to select only frequencies for which the flame was compact, he showed that optical measurements of heat release based on OH* emission were directly correlated to the associated noise. These inspired theoretical efforts to try to express clearly the link between noise and combustion. Strahle (1971, 1972) started from Lighthill's analogy, and considering frequencies for which the flame was compact gave a general formulation of direct noise scaling in turbulent combustion, regardless of the flame structure. Chiu & Summerfield (1974) on the other hand proposed to use Phillips' analogy (Phillips, 1960). Both analogies however imply only little simplifications, and in the context of complex turbulent flow, they could lead to results only under very restrictive conditions. Hassan (1974) suggested a modified version of Doak's analogy which gave good agreement with experimental results for both power and frequency, but only for low Mach number flows. By the end of the 70's, no specific combustion noise theory had been identified in the community (Strahle, 1978). This is due to the fact that the complete multi-species Lighthill analogy does not yield analytical solutions for complex turbulent flows, and that approximations are necessary. It has become clear at that time however that combustion noise was expected to be a low-frequency problem. Clavin & Siggia (1991) raised the specific issue of the power spectrum of combustion noise, from a purely theoretical point of view.

Another motivation for the study of these systems is the accurate description of the acoustic behavior of non-homogenous flows. Marble & Candel (1974) investigated experimentally the effect of vaporized water into the flow, aiming for noise reduction. Liu (1977) then studied more generally the acoustics of "relaxing" mediums, hence including the case of temperature inhomogeneities which simply have a long relaxation time. This definition also applies to species inhomogeneities, which can produce sound as shown by Sinai (1980). Non-homogenous conditions can become critical in cases such as non-premixed flames, as studied by Klein & Kok (1999). They showed that Strahle's model was inaccurate for non-premixed flames, and derived an expression of the sound source from the multispecies Lighthill analogy. Using this expression in a RANS simulation, they successfully compared predicted noise to experiments over the frequency spectrum.

Finally, the study of Schuller *et al.* (2002) should be mentioned, as it showed how flame-wall interactions could amplify very efficiently the noise production mechanism: flame annihilation can occur very rapidly when the wall quenches a large portion of the flame, leading to very rapid flame surface variation and noise production.

This first numerical approach has since been extended to more accurate solvers.

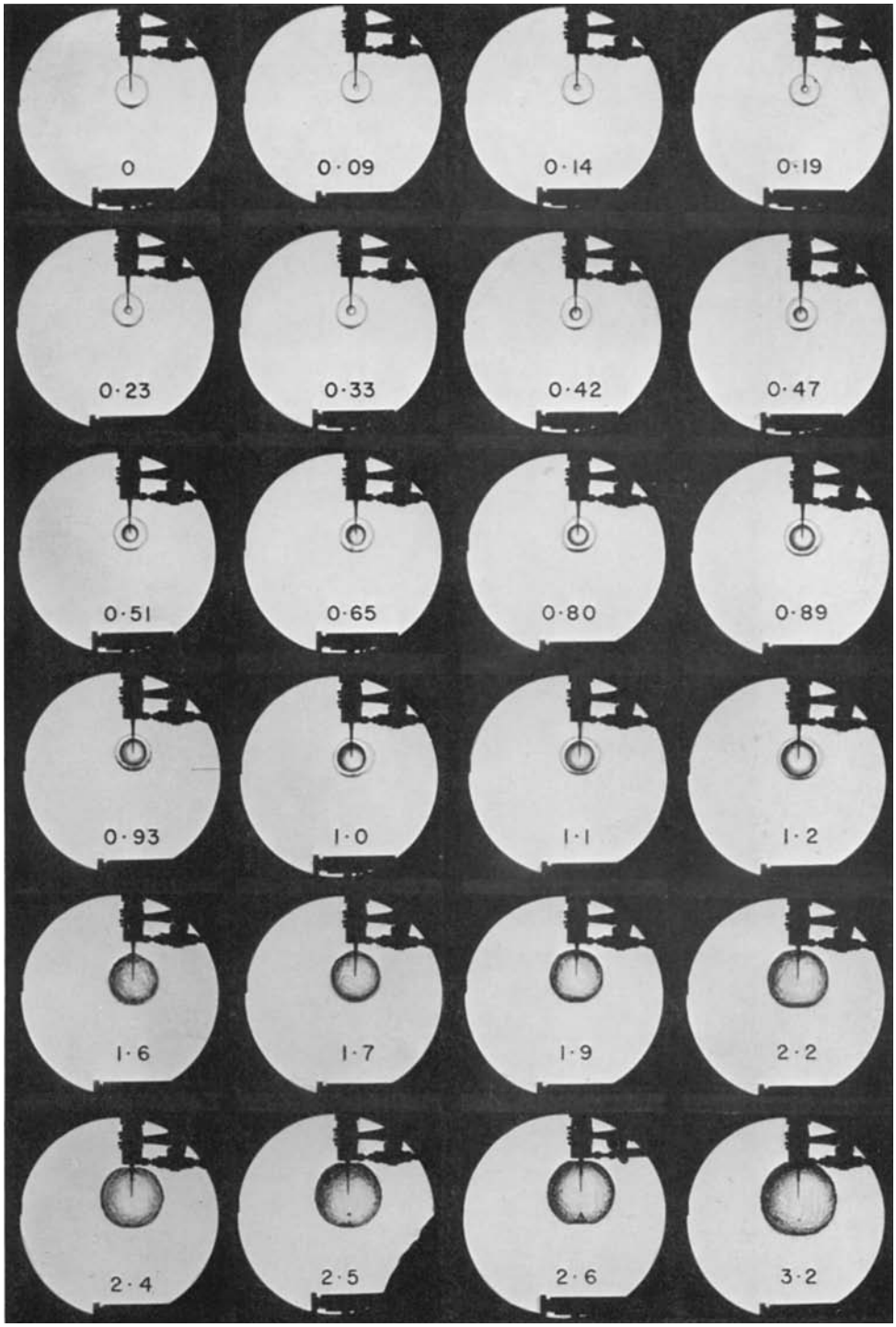

Figure 5.2: Instantaneous spark schlieren of spherically expanding flame in premixed gas trapped in soap bubbles. Sound is measured in an anechoic enclosure by a microphone at 37 cm from the bubble centrer, *i.e.* well in the acoustic far-field. Reproduced from Thomas & Williams (1966). Numbers in each image indicate approximate time since spark in ms.

Ihme *et al.* (2005, 2009) suggested an identification of sound sources in an LES computation of the flame, hence enabling the characterization of three major contributions: a quadrupole source due to unsteady Reynolds stresses, a dipole source due to fluctuating mass flux, and a monopole source due to heat release. The sum of these sources lead to a successful prediction of the total sound spectrum and levels emitted by the flame. Talei *et al.* (2009) validated a high precision numerical solver called NTMIX on a test case of an oscillating premixed flame. It was shown that the regions of spherical burning droplets were responsible for important noise sources, but that "pinching" zones lead to much quicker time variations of heat release, hence to more important levels of direct noise. This of course is in agreement with Strahle's original analysis, but gives an insight on the dynamics of this simple flame and thus on the origin of heat release fluctuations. Liu *et al.* (2012) used DNS to show that two-point correlation between the sound emitted and the heat release depended on the separation distance and the direction but not on the positions inside the flame brush. Talei *et al.* (2011) explored the noise efficiency of different flame configurations (spherical, cylinder...). The effect of Lewis number on this "flame annihilation" process is suspected to be strong, and Talei *et al.* (2010) explored this effect numerically but with simple chemistry, and Jiménez *et al.* (2014) employed the NTMIX-CHEMKIN solver which is both high order in space and time and includes detailed chemistry. The fuel chosen in this case was H_2, and the detailed chemistry was shown to be unnecessary for lean conditions (in this case, Lewis number below or equal to one), but in very rich premixed flows however (Lewis number above one) the simple chemistry did not predict the emitted noise correctly. This suggests that when dealing with rich flames or non-premixed flames containing rich combustion, correct noise prediction might not be possible with usual solvers with low resolution chemistry.

5.2.3.2 Sound production of a free unconfined flame

When a flame burns in a free domain (no walls, such as flares), the sound which it creates is not reflected and the whole problem of combustion noise can be formulated as a classical farfield aeroacoustic problem where a propagator is used in the farfield and sources are due to the flame. Turbulent isobaric combustion can be described by the multi-species Lighthill analogy of Eq. 5.2. In such a case, Bailly *et al.* (2010) shows that the only non-negligible source term is due to heat release. The analogy therefore writes:

$$\frac{1}{c_\infty^2}\frac{\partial^2 p}{\partial t^2} - \nabla^2 p = \frac{\partial}{\partial t}\left[(\gamma-1)\frac{\rho_0}{\rho}\frac{c_\infty^2}{c^2}\dot{\omega}_T\right] \tag{5.3}$$

γ can vary by approximately 10 % in a reacting flow, but it is often supposed constant in the field of acoustics, as this does not change the fundamental mechanisms described, but it leads to an interesting simplification. Indeed, since the relation $c^2 = \gamma r T = \gamma p/\rho$ holds, this approximation implies for isobaric combustion that γp is constant over the entire domain, so is ρc^2 and $\rho c^2 = \rho_\infty c_\infty^2$. For purely

harmonic regimes we write $p(\boldsymbol{x},t) = \Re\big(\tilde{p}(\boldsymbol{x})e^{-j\omega t}\big)$ and $\dot{\omega}_T(\boldsymbol{x},t) = \Re\big(\tilde{\omega}_T(\boldsymbol{x})e^{-j\omega t}\big)$, and Eq. (5.3) becomes:

$$\left(\nabla^2 + k^2\right)\tilde{p}(\boldsymbol{x}) = j\omega\frac{\gamma-1}{c_\infty^2}\tilde{\omega}_T(\boldsymbol{x}) \tag{5.4}$$

where $k = \omega/c_\infty$. This is simply the zero Mach number Helmholtz equation Eq. 3.32. The source term $\dot{\omega}_T$ is supposed to have the following properties:

- it is time-harmonic;
- it is distributed inside a volume source region V, and is zero outside this region.

The analytic study of solutions to Eq. (5.4) in simplified geometric cases can be done using the so called Green functions.

Green functions. Finding solutions to non-homogeneous linear differential equations can be difficult analytically, depending on the source term. So called *Green functions* can be used to express an integral formulation of such a solution in all cases. Let L a linear differential operator, and Q a source term. The function ϕ that must be found can be described as:

$$L\phi = Q \tag{5.5}$$

Let G be a function such that:

$$LG = \delta \tag{5.6}$$

It can be shown, with $\star$ the convolution symbol, that:

$$\phi = \phi\star\delta = \phi\star(LG) = (L\phi)\star G = Q\star G \tag{5.7}$$

Hence, if Eq. 5.6 can be solved, an integral formulation of ϕ can be given using Eq. 5.7, simply by convolving the source term Q with the Green solution G. The Green function solution to Eq. (5.4) submitted to a perturbation produced at position $\boldsymbol{x}$ and time t by a δ perturbation at position $\boldsymbol{y}$ and time τ, namely:

$$-\frac{1}{c_\infty^2}\frac{\partial^2}{\partial t^2}G(\boldsymbol{x},t;\boldsymbol{y},\tau) + \nabla^2 G(\boldsymbol{x},t;\boldsymbol{y},\tau) = \delta(\tau-t)\delta(\boldsymbol{x}-\boldsymbol{y})$$

For harmonic regimes, the Fourier transform of G, noted $\tilde{G}$ and defined as:

$$G = \int_{-\infty}^{\infty}\tilde{G}e^{j\omega t}\,\mathrm{d}\omega \tag{5.8}$$

is solution to:

$$\left(\nabla^2 + k^2\right)\tilde{G} = \delta(\boldsymbol{x}-\boldsymbol{y})e^{-j\omega\tau}$$

and writes in one and three space dimensions:

$$\tilde{G}_{1D} = -\frac{j}{2k}e^{-j\omega(\tau+r/c_\infty)} \tag{5.9a}$$

$$\tilde{G}_{3D} = \frac{1}{4\pi}\frac{e^{-j\omega(\tau+r/c_\infty)}}{r} \tag{5.9b}$$

where $r = |\boldsymbol{x} - \boldsymbol{y}|$. According to Eq. (5.7), the solution to Eq. (5.4) can be obtained by simply convolving its source term (*i.e.* its right hand side term) with the appropriate green function for each dimension, *i.e.*:

$$\tilde{p}(\boldsymbol{x}) = \int_V j\omega \frac{\gamma - 1}{c_\infty^2} \tilde{\omega}_T(\boldsymbol{y}) \tilde{G}(\boldsymbol{x}; \boldsymbol{y}) \, \mathrm{d}\boldsymbol{y} \tag{5.10}$$

yielding:

$$\tilde{p}_{1D}(x) = \frac{\gamma - 1}{c_\infty^2} \frac{\omega}{2k} \int_V \tilde{\omega}_T(\boldsymbol{y}) A^{-1} e^{-j\omega(\tau + r/c_\infty)} \, \mathrm{d}\boldsymbol{y}$$

$$\tilde{p}_{3D}(x) = j \frac{\gamma - 1}{c_\infty^2} \frac{\omega}{4\pi} \int_V \tilde{\omega}_T(\boldsymbol{y}) \frac{e^{-j\omega(\tau + r/c_\infty)}}{r} \, \mathrm{d}\boldsymbol{y}$$

where A is the area resulting from the 2 dimension integration performed to go from the volume source to the 1 dimensional formulation.

The final integration in the general case is not easy. However, for practical purposes, two simplifications can be made:

- the nearfield region, where $\boldsymbol{x} \approx \boldsymbol{y}$, is of little interest for noise assessment. The farfield sound, corresponding to regions where $\boldsymbol{x} \gg \boldsymbol{y}$, implies that r is independent of $\boldsymbol{y}$, and terms depending on r can come out of the integral;
- the total unsteady heat release rate can be written as:

$$\int_S \omega_T(\boldsymbol{y}) \, \mathrm{d}\boldsymbol{y} = \dot{Q}$$

yielding the final forms for pressure perturbation:

$$\tilde{p}_{1D}(x) = \frac{\gamma - 1}{c_\infty} \frac{1}{2A} \dot{Q} e^{-j\omega(\tau + r/c_\infty)} \tag{5.11a}$$

$$\tilde{p}_{3D}(x) = j \frac{\gamma - 1}{c_\infty^2} \frac{\omega}{4\pi} \dot{Q} \frac{e^{-j\omega(\tau + r/c_\infty)}}{r} \tag{5.11b}$$

5.2.4 Sound production of a confined flame: "indirect" noise

The previous section has described the noise created by a free flame and is very similar to the usual aeroacoustic studies as described in numerous essays on acoustics (Crighton *et al.*, 1992; Rienstra & Hirschberg, 2003; Bailly *et al.*, 2010), which give insight on the mechanism of sound production by an isobaric flame. However, this resolution is based on the assumption that none of the sound produced by the flame is reflected towards it, enforced by a Sommerfeld condition. In other words, it applies only to a "free" flame burning in an infinite medium. In the case of present interest however, as in most flames, this source is positioned inside a potentially resonating combustion chamber, and simple approaches using Green functions are inadequate to compute the associated noise. The first difficulty here is that most chambers are terminated by a nozzle, generating a whole class of acoustic problems. For these chambers, the noise produced by the flame is not the only source and the nozzle itself produces additional noise. Moreover, all these acoustic waves have to travel through the nozzle, leading to additional complexity.

5.2.4.1 Transmission and production in a nozzle

The first questions about nozzle acoustic behavior arose in the 50's with the study of combustion instabilities. At first, according to Eq. (4.7), the mass flow rate through the nozzle was always considered to be directly proportional to the chamber pressure. Tsien (1952) derived the quasi-1D Euler mass and momentum equations for a linear velocity nozzle, and showed that for high-frequency oscillations this relation no longer holds, replaced instead by a complex impedance. Zinn (1972) specifically evaluated the acoustic losses through any "short" nozzle, *i.e.* for modes with a large wavelength compared to the nozzle length. This is referred to as a *compact nozzle* in the community, as represented in Fig. 5.3. This work which initially aimed

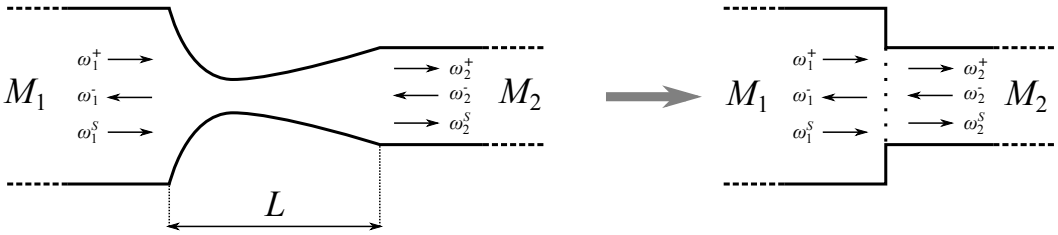

Figure 5.3: Compact nozzle representation: a nozzle converts a flow at Mach number M_1 to M_2 using section change (whether simply converging/diverging or combined converging-diverging as shown here). For acoustic wavelengths λ much larger than the nozzle length L (*i.e.* $\lambda \gg L$), the nozzle can be represented as a Mach number discontinuity.

at describing thermoacoustic instabilities was reused for noise purposes, in part because in the 70's the Concorde project was the starting point to much research concerning aircraft noise, and specifically jet engine noise. Candel (1972) added the energy equation to Tsien's analysis, thus including non-acoustic energy fluctuations due to temperature inhomogeneities. The 3 wave decomposition of Chap. 3 which describes axial fluctuations of upstream acoustics ω^+, downstream acoustics ω^- and convected entropy ω^S was later used to express the nozzle transmission and reflection coefficients in the now famous analysis by Marble & Candel (1977*b*) of the complete set of reflection and transmission coefficients of a compact nozzle to acoustic and temperature (or entropic) perturbations, reproduced in Tab. 5.1 and referred to as the Marble & Candel relations. After this initial streak, research on combustion noise slowed down, and little work was published in the next two decades.

Recently however, interest in core noise spiked because of ever more restrictive regulations on noise emissions. Stow *et al.* (2002) extended the Marble & Candel analysis using an asymptotic expansion to the first order in frequency, and included a second momentum equations, including therefore the reflection and transmission of circumferential modes. Reflection coefficients were corrected due to first-order terms, introducing a phase correction. Goh & Morgans (2011) developed this approach to account for transmission coefficients. Moase *et al.* (2007) and later Huet & Giauque (2013) looked into non-linear models and their effect on choked nozzle unchoking / overchoking, as well as on the noise production and transmission.

	Reflection	
	Subsonic $M_2 < 1$	Supersonic $M_2 \geq 1$
ω_1^-/ω_1^+	$\frac{M_2 - M_1}{1 - M_1} \frac{1 + M_1}{M_1 + M_2} \frac{1 - 1/2(\gamma - 1)M_1 M_2}{1 + 1/2(\gamma - 1)M_1 M_2}$	$\frac{1 - 1/2(\gamma - 1)M_1}{1 + 1/2(\gamma - 1)M_1}$
ω_1^-/ω_1^S	$-\frac{M_2 - M_1}{1 - M_1} \frac{M_1}{1 + 1/2(\gamma - 1)M_1 M_2}$	$-\frac{M_1}{1 + 1/2(\gamma - 1)M_1}$
ω_1^-/ω_2^-	$\frac{2M_1}{1 - M_1} \frac{1 - M_2}{M_1 + M_2} \frac{1 + 1/2(\gamma - 1)M_1^2}{1 + 1/2(\gamma - 1)M_1 M_2}$	–
	Transmission	
	Subsonic $M_2 < 1$	Supersonic $M_2 \geq 1$
ω_2^+/ω_1^+	$\frac{2M_2}{1 + M_2} \frac{1 + M_1}{M_1 + M_2} \frac{1 + 1/2(\gamma - 1)M_2^2}{1 + 1/2(\gamma - 1)M_1 M_2}$	$\frac{1 + 1/2(\gamma - 1)M_2}{1 + 1/2(\gamma - 1)M_1}$
ω_2^+/ω_1^S	$\frac{M_2 - M_1}{1 + M_2} \frac{M_2}{1 + 1/2(\gamma - 1)M_1 M_2}$	$\frac{M_2 - M_1}{2} \frac{1}{1 + 1/2(\gamma - 1)M_1}$
ω_2^+/ω_2^-	$-\frac{M_2 - M_1}{1 + M_2} \frac{1 - M_1}{M_1 + M_2} \frac{1 - 1/2(\gamma - 1)M_1 M_2}{1 + 1/2(\gamma - 1)M_1 M_2}$	–

Table 5.1: Nozzle reflection and transmission coefficients according to Marble & Candel (1977*a*).

The role of indirect combustion noise has long been controversial at best. Groups like Sattelmayer's team at TU Munich argued that entropy waves created in the combustion chamber would be dissipated before they reach the outlet nozzles, thereby killing totally indirect noise processes. Muthukrishnan *et al.* (1978) exposed experimental results suggesting that at very low Mach numbers, direct noise was predominant over indirect noise, but that for more realistic Mach numbers the indirect noise mechanism became predominant. Tam *et al.* (2005) however showed a complete set of experimental measurements on an aircraft auxiliary power unit in which no evidence of indirect combustion noise was found. At the German Aerospace Center (DLR), Bake *et al.* (2009) built an Entropy Wave Generator meant to measure the noise generated by electrically produced temperature perturbations when accelerated through a nozzle at both subsonic and supersonic velocities. While at first this experiment did seem to give reliable proof of the indirect combustion noise mechanisms, further analysis showed unexplained phenomena, *e.g.* a noise drop when the flow Mach number reached approximately 0.6. Howe (2010) used his analogy and a Green function solution to calculate the noise produced by this configuration and inferred that this was due to a jet forming in the divergent part of the nozzle. In fact, he believed that the resulting vorticity field was responsible for the noise drop. Leyko *et al.* (2008) on the other hand lead a numerical investigation suggesting that the noise drop could be explained by the reflecting properties of the ends of the chamber. His study also suggested that the noise observed in the DLR experiment was affected

by reflections on the inlets and outlets of the rig, and since the entropy generator noise production was not evaluated, it cast doubt once again on the mechanisms involved. Leyko *et al.* (2009) however used a "cold flame" model to evaluate the wave production by the flame, thereby suggesting that in the operating range of aircraft engines, the indirect to direct noise ratio was of the order of 10 to 100.

Very recently, a semi-analytical approach was suggested by Duran & Moreau (2013) based on the linearized Euler equations rearranged in a wave describing form and again into invariants across the nozzle. This method seems coherent with the formulation of Marble & Candel for low frequencies, and agrees with numerical simulations for higher frequencies. It is the most efficient method to compute nozzle impedance for a Helmholtz solver available today. A parallel approach proposed by Huet & Giauque (2013) stays in the compact-nozzle validity range but explores the effect of perturbation levels, with higher order non-linear terms included. This is also a good approach in the context of combustion noise, since the nozzle is in practice very short compared to the wavelengths of interest, and perturbation levels at the end of the combustion chamber can be high as shown in Chap. 3.

5.2.4.2 Turbine noise

Of course, in a realistic engine the flow does not travel through a simple nozzle, but through a series of turbine stages (Fig. 5.4). In order to connect the previous

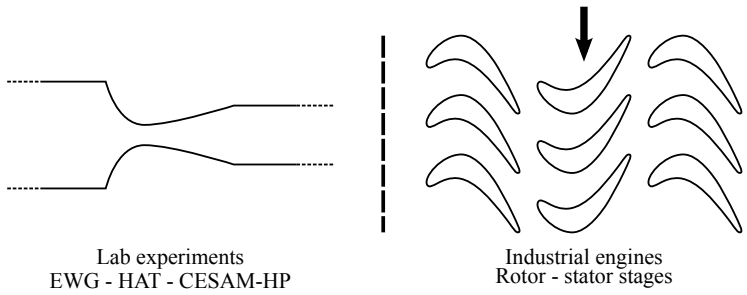

Figure 5.4: Simplified lab experiment dilatation systems (generally a simple nozzle) differ from realistic rotor stator stages of industrial turbines.

work with the noise perceived outside an engine, the propagation and generation of noise in rotor/stator arrangements must be taken into account. Such a system includes at least two major differences with a chain of nozzles: deviation and rotation. The most basic representation is to see any rotor or stator stage as an infinitely thin (hence compact) actuator disk and use the Marble & Candel jump conditions modified to include deviation and rotation, as well as the total length for propagation. This approach was employed by Cumpsty & Marble (1977*a*) to derive a strategy to compute the noise produced by a complete engine, and compared with some success to three datasets of engine noise measurements (Cumpsty & Marble, 1977*b*). Turbines however lead to strong mixing, which in turn contributes to dissipate entropy waves very rapidly: this was the reason why Sattelmayer (2003) derived an analytic formulation of entropy dissipation, showing that it is strong even in the

low-frequency range. Leyko *et al.* (2010) measured this dissipation numerically by sending entropy waves through a blade row in an unsteady LES, and showed that indeed for high frequencies this dissipation could yield strong discrepancies with the compact theory of Cumpsty & Marble (1977*a*). Nevertheless, these authors conclude that in actual systems, low frequencies are expected to be heard most. As engines and therefore combustors become more compact, less travel distance exists for the heat waves to dissipate. In this Ph.D., the CESAM-HP setup studied in Chap. 9 has been conceived with this in mind, and the nozzle is very close the end of the reacting zone, so little entropy dissipation is expected between the two. It should be noted that Bodony & Lele (2008) lead an interesting study on the sound produced by an entropy perturbation impinging on an airfoil-type object. Turbine noise and indirect noise are often seen as one and only thing, but entropy spots interacting with a solid object is also known to generate sound. The CHORUS tool developed at CERFACS (Leyko *et al.*, 2013; Duran *et al.*, 2013*a*) allows to couple LES in the combustion chamber with propagation in a full turbine using the theory of Cumpsty & Marble (1977*b*).

Turbine noise however exceeds the scope of the current study. Of course, the study of combustion noise mostly has applications for civil aircraft engines and therefore turbines. The developments of this chapter are however centered on the sources associated with the chamber, which implies that they apply equally to academic benches and to industrial combustion chambers. For this reason, only axisymmetric nozzles are considered throughout this manuscript, without loss of generality.

5.2.4.3 Specificities of multispecie flows

Most theories for indirect noise use the term "entropy" spots to designate the hot zones entering the nozzle. In a reacting flow this question must be revisited and the present study section shows that the right quantity to consider is not entropy but excess density, which differ in a reacting flow. Indeed acoustic analysis is usually based on a single-specie description of the flow. The fluid is most often air, and otherwise it is considered a perfect mixture of ideal gases, resulting in a new ideal gas with proportional characteristics. Euler equations for a single species fluid (Eq. (3.1)) are used according to these assumptions. In the case of combustion however, the gas composition varies between the fresh and burnt gases, and it can vary spatially in the combustor. Cooling with fresh air also contributes to creating species inhomogeneities in the flow entering the turbine. At the entrance of the turbine, waves pertaining to the combustion noise analysis from Eq. (3.24) are:

$$\omega^+ = \frac{p'}{\gamma p_0} + \frac{u'}{c_0}, \qquad \omega^- = \frac{p'}{\gamma p_0} - \frac{u'}{c_0}, \qquad \omega^S = \frac{p'}{\gamma p_0} - \frac{\rho'}{\rho_0}$$

where ω^S is the excess density wave. Eq (2.31) has demonstrated that $\omega^S = -\frac{\rho'_e}{\rho}$. In case of a multispecie ideal gas mixture according to the definition of entropy

fluctuations from Eq. (2.32):

$$\omega^S = -\frac{\rho'_e}{\rho} = \frac{s'}{c_P} + \frac{1}{c_P T}\sum_k \frac{\mu_k}{W_k} Y'_k \tag{5.12}$$

Therefore if $Y'_k \neq 0$, there is no direct equivalence between the excess density wave ω^S, *i.e.* the source term of the multispecies Lighthill equations, and the fluid entropy wave s'. In some multispecies codes, ω^S is evaluated using the actual entropy fluctuation s' only. If species perturbations arise where the waves are evaluated, Eq. (5.12) shows that this leads to an inaccurate evaluation of ω^S. In most codes this is not a problem however since the general definition for ω^S based on pressure p' and density ρ' perturbation is used, and it is still valid when $Y'_k \neq 0$. It is important to notice however that the true entropy wave s' in this case is not directly related to indirect combustion noise and should not be used to predict it: excess density ω^S is the right input quantity creating indirect noise.

In order to illustrate this point, a test case is derived here. A 2D domain with two different constant height subsections connected by a convergent nozzle is computed with the Euler equations. The section decreases by a factor 5. The inlet Mach number is 0.01, and the outlet one is 0.05. Various entropy and density waves are imposed in the upwind subsection, and the sound produced is measured at the outlet of the domain. An illustration of the domain with a density wave injection (harmonic) is shown in Fig. 5.5.

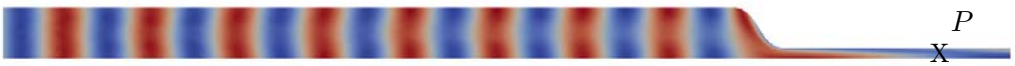

Figure 5.5: Domain for entropy waves indirect noise test case.

Three test cases are derived and presented in Fig. 5.6. Various fluctuations are sent in the domain inlet and through the section change, and the resulting noise produced is observed at a position downstream of the section restriction, noted P in Fig. 5.5. The three fluctuations considered are the following:

Case 1 only based on a fluctuating inlet temperature in a single specie flow (namely N_2);

Case 2 where the flow is air (N_2 and O_2), temperature is constant and the fluctuation of excess density $\rho'_e = \delta\rho_e$ results only from species fluctuations (*i.e.* the mass fractions of N_2 and O_2 are varied, with of course $Y_{N_2} + Y_{O_2} = 1$ at all times);

Case 3 is also a constant temperature - fluctuating species approach, but making use of two species with the same molar mass (namely C_3H_8 and CO_2) this fluctuation induces no density fluctuation: $\rho'_e = 0$. However, it does constitute an entropy fluctuation s', since the mixture between two different gases is varied.

The objective is to demonstrate that it is the excess density fluctuation $\rho'_e/\rho_0 = -\omega_1^S$ that controls the quasi-one dimensional indirect noise production mechanism. Cases 1 and 2 are expected to produce the same amount of noise, and Case 3 is expected to be almost completely silent.

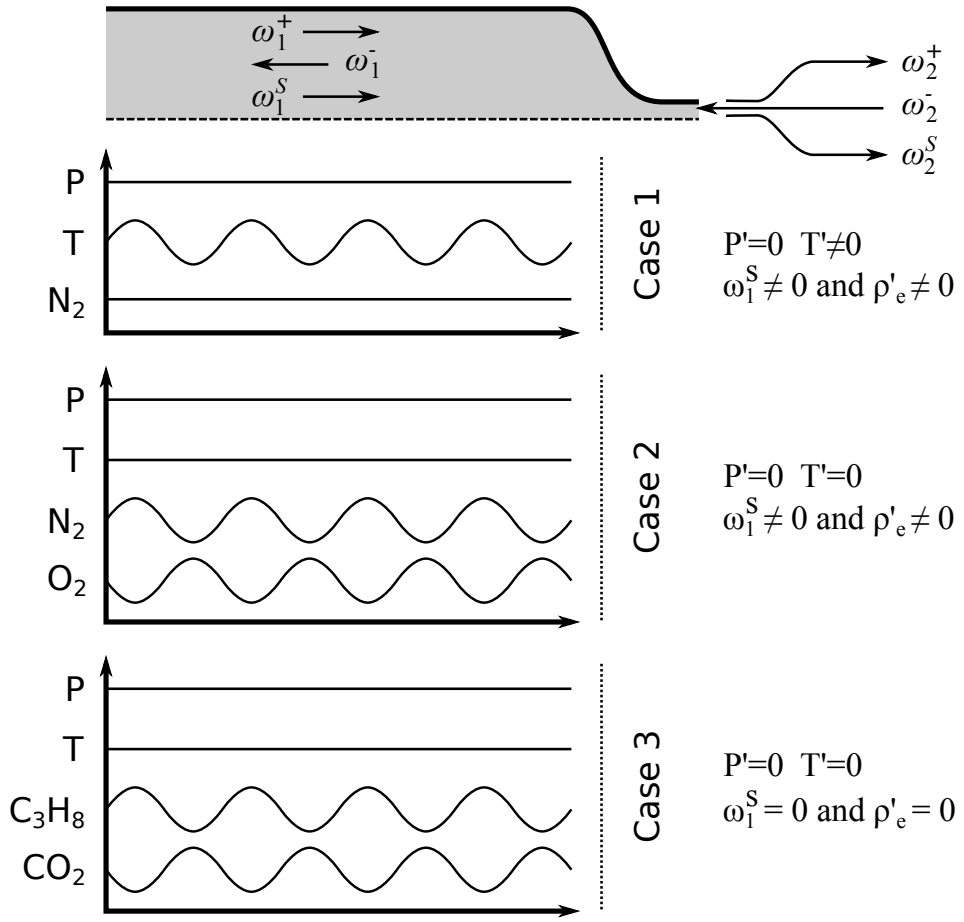

Figure 5.6: Representation of the 3 test cases derived for multispecies entropy noise assessment. Perturbations are imposed at the inlet of the domain of Fig. 5.5.

Tab. 5.2 presents the results of the tests, obtained by running an AVBP simulation for each one. The direct conclusions from this table are the following:

Case 1 a density fluctuation ω_1^S due to temperature fluctuations T' produces indirect noise;

Case 2 the same density fluctuation ω_1^S caused by a species wave with constant temperature produces the same amount of noise;

Case 3 a species fluctuation causing a true entropy wave $s' \neq 0$ without density change ($\omega_1^S = 0$) does not produce indirect noise.

These results confirm that even though the word "entropy" is used to designate ω^S, the quantity of interest for combustion noise is in fact excess density ρ'_e, and that ρ'_e can differ from the true entropy wave s' in the specific case of multi-species flows. "Excess density" should be used to assess indirect combustion noise, especially for multi-species flows.

In this manuscript, although this remark is kept in mind for wave assessment, ω^S is still referred to as the entropy wave, to keep definitions in agreement with usual acoustic vocabulary and with the literature.

	Cases definitions					AVBP Results	
	P'	T'	Y'	$\rho'_e \propto \omega_1^S$	s'	ω_1^S	ω_2^+
Case 1	0	$\neq 0$	0	$\delta\rho_e$	$\neq 0$	1.25	0.022
Case 2	0	0	$\neq 0$	$\delta\rho_e$	$\neq 0$	1.25	0.021
Case 3	0	0	$\neq 0$	0	$\neq 0$	10^{-3}	10^{-4}

Table 5.2: Test cases for multispecies entropy noise

Entropy jump through a flame The entropy jump through a lean flame is given by Eq. 2.28:

$$\frac{\Delta s}{c_P} = \int_f^b \left(\frac{\mathrm{d}P}{\gamma P} - \frac{\mathrm{d}\rho}{\rho} - \frac{1}{c_P T} \sum_k \frac{\mu_k}{\mathrm{W}_k} \mathrm{d}Y_k \right)$$

where f and b represent the fresh and burnt states, respectively. For an isobaric flame, $\mathrm{d}P = 0$ and this reduces to:

$$\frac{\Delta s}{c_P} = \int_f^b \left(\frac{\mathrm{d}T}{T} - \frac{1}{c_P T} \sum_k \frac{\mu_k}{\mathrm{W}_k} \mathrm{d}Y_k \right)$$

These two terms have been evaluated separately in a side-study not presented in detail here. A stoichiometric ($\phi = 1$) reaction of propane in air was considered, and both contributions to entropy variation were evaluated. As a result:

$$\int_f^b \frac{\mathrm{d}T}{T} = 2236\,39\mathrm{JKmol}$$
$$\int_f^b \frac{1}{c_P T} \sum_k \frac{\mu_k}{\mathrm{W}_k} \mathrm{d}Y_k = 100\,96\mathrm{JKmol}$$

This shows that the species contribution to the entropy variation is low but not negligible compared to the density (or temperature) variation. However, for combustion noise evaluations, the evaluation of ω^S is sufficient, and this observation does not apply.

5.3 Assessing combustion chamber noise

5.3.1 The toy model of Leyko (2010)

Original description. A recurrent issue for combustion noise is to determine which mechanism (direct or indirect) dominates combustion noise, and when. Simple theoretical models are used for this: Leyko (2010) derived a "toy model" to describe the acoustic and entropic waves produced by a flame. The following hypotheses were made for the flame:

1. it is one-dimensional. 3D effects are neglected;
2. it is compact, *i.e.* its thickness is very small compared to the wavelengths of interest;
3. it is *cold*. This apparently strange assumption means that the mean heat release $\bar{\dot{Q}}$ is set to 0, and only a time fluctuation of heat release $\dot{Q}' \neq 0$ is included. The source of this fluctuation is not considered;
4. the origin of heat release fluctuations does not have to be determined. No acoustic or entropic waves reach the flame, and its variations are of some other nature.

This restrictive context offers a simple evaluation of acoustic and entropy waves created by the flame. Fig. 5.7 shows the notations adopted for this model. Index for

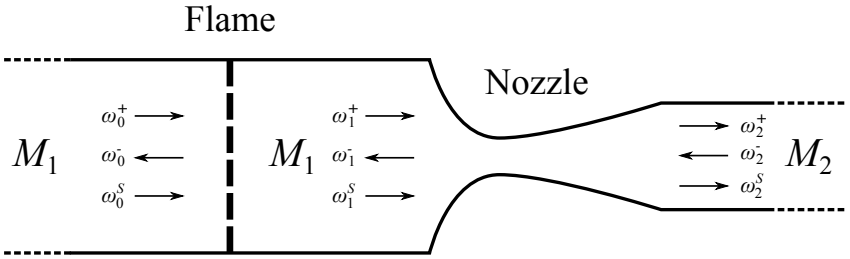

Figure 5.7: Notations for the toy model of Leyko (2010).

the waves before the flame is $_0$. The jump conditions for mass flow, total enthalpy and entropy through the flame front yield:

$$(\dot{m})_0 = (\dot{m})_1 \tag{5.13a}$$

$$(\dot{m}h_t)_0 + \dot{Q} = (\dot{m}h_t)_1 \tag{5.13b}$$

$$(\dot{m}s)_0 + \frac{\dot{Q}}{T} = (\dot{m}s)_1 \tag{5.13c}$$

and can be linearized. The flame is isolated and no upstream perturbations exist, which implies $\omega_0^S = \omega_0^+ = \omega_1^- = 0$. Since $\bar{\dot{Q}} = 0$, $T = \bar{T}$ is constant in space, and for entropy Eq. (5.13c) writes once linearized:

$$\left(\frac{s'}{c_P}\right)_0 + \frac{\dot{Q}'}{\bar{\dot{m}} c_P \bar{T}} = \left(\frac{s'}{c_P}\right)_1$$

This yields the excess density wave s'. The inlet entropy s'_0 is supposed to be zero. A similar development yields the downstream acoustic wave (Leyko, 2010).

$$\omega_1^S = \frac{\dot{Q}'}{\bar{\dot{m}} c_P \bar{T}} \tag{5.14a}$$

$$\omega_1^+ = \frac{M_1}{1 + M_1} \frac{\dot{Q}'}{\bar{\dot{m}} c_P \bar{T}} \tag{5.14b}$$

The conclusions of this approach are as follows:

- the noise and entropy waves produced by a flame are proportional to the time fluctuating heat release $\dot{Q}'$;
- the ratio of these waves is constant for a given flame, whatever the amplitudes of heat release fluctuations;
- the ratio ω_1^S/ω_1^+ diverges when $M \to 0$.

Ratio of indirect to direct noise One of the important questions concerning combustion noise is the evaluation of relative importance of direct and indirect noise. In the compact approach, the relations of Marble & Candel (1977*a*) explicit the direct noise $\eta_{dir} = \omega_2^+/\omega_1^+$ and indirect noise $\eta_{ind} = \omega_2^+/\omega_1^S$ produced by a nozzle. In order to compare these relations, two thought experiments are designed:

- one where acoustic waves ω_1^+ only are sent in the nozzle. The resulting acoustic waves reflected (R_{AA}) and transmitted (T_{AA}) define the "acoustic-acoustic" behavior of the nozzle;
- one where entropic waves ω_1^S are sent, leading to acoustic waves propagating back up in the chamber (R_{SA}) and others produced in the nozzle and propagating downstream (T_{SA}).

Fig. 5.8 shows these 4 coefficients in a context of a "black-box" nozzle or other generic system leading to flow acceleration. Indirect to direct noise is therefore the

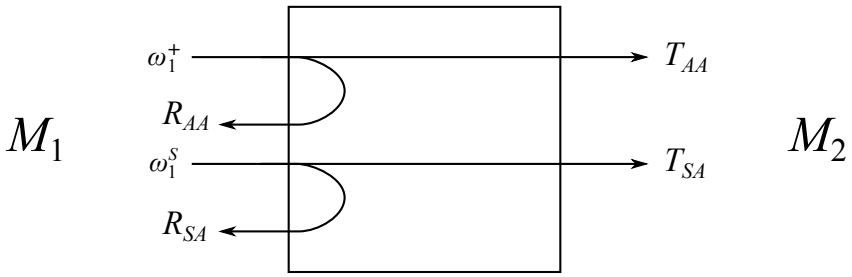

Figure 5.8: Notations for transmission and reflection coefficients through a nozzle.

comparison of T_{SA} and T_{AA}. However, these "transmissions" are related to waves of different nature, namely acoustic ω_1^+ and entropic ω_1^S, respectively. In order to compare these quantities, a scaling between ω_1^+ and ω_1^S must be chosen. Leyko *et al.* (2009) developed the toy model for this purpose, with $\eta_{tm} = \frac{\omega_1^S}{\omega_1^+}$ and consequently built the *indirect to direct noise ratio*:

$$\eta = \underbrace{\frac{\omega_1^S}{\omega_1^+}}_{\eta_{tm}} \times \frac{T_{SA}}{T_{AA}} \tag{5.15}$$

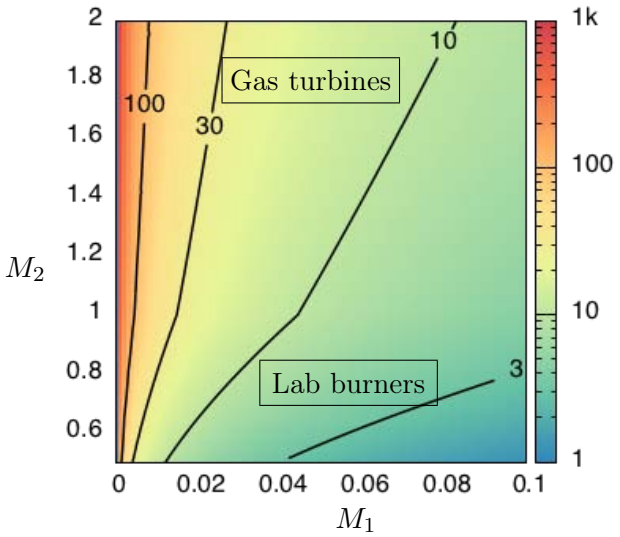

Figure 5.9: Indirect to direct combustion noise ratio η using the toy model of Leyko (2010) as a function of the inlet (M_1) and outlet (M_2) Mach numbers of the nozzle.

The indirect T_{SA} and direct T_{AA} transmissions through the nozzle are given in Tab. 5.1, and the scaling given by the toy model yields η_{tm}:

$$T_{AA} = \begin{cases} \dfrac{M_2 - M_1}{1 + M_2} \dfrac{1 + M_1}{M_1 + M_2} \dfrac{1 + {}^1\!/_2(\gamma - 1)M_2}{1 + {}^1\!/_2(\gamma - 1)M_1 M_2} & \text{if } M_2 < 1 \\ \dfrac{1 + {}^1\!/_2(\gamma - 1)M_2}{1 + {}^1\!/_2(\gamma - 1)M_1} & \text{if } M_2 \geq 1 \end{cases} \tag{5.16a}$$

$$T_{SA} = \begin{cases} \dfrac{M_2 - M_1}{1 + M_2} \dfrac{M_2}{1 + {}^1\!/_2(\gamma - 1)M_1 M_2} & \text{if } M_2 < 1 \\ \dfrac{M_2 - M_1}{1 + M_2} & \text{if } M_2 \geq 1 \end{cases} \tag{5.16b}$$

$$\eta_{tm} = \frac{\omega_1^S}{\omega_1^+} = \frac{1 + M_1}{M_1} \tag{5.16c}$$

The resulting value of η is a function only of chamber Mach number M_1 and outlet Mach number M_2, which is an attractive simplification of the full problem. A map of this ratio is plotted in Fig. 5.9. Several conclusions can be drawn from this figure:

- indirect noise is at least of the order of direct noise;
- indirect noise tends to overcome direct noise when the outlet Mach number M_2 increases;
- the ratio diverges when the inlet Mach number $M_1 \to 0$.

Leyko *et al.* interpret this result by noticing that industrial burners operate at high pressures, and usually display low M_1 values in the chamber and high subsonic or

choked high-pressure distributors, hence high values of M_2. According to Fig. 5.9, very high levels of indirect noise are expected compared to direct noise.

In the attempt to study combustion noise, academic test benches can and have been constructed. These generally operate at low pressures for technical reasons. As a result, high outlet Mach numbers M_2 are difficult to achieve. The indirect noise expected in such a configuration is considerably lower than in an industrial burner. The current approach therefore suggests that the study of combustion noise would require a pressurized setup ended by a nozzle with high outlet Mach — possibly choked.

5.3.2 Flame modelling: how to improve the toy model?

One conclusion of the toy model approach of Leyko (2010) is surprising: when the chamber Mach number $M_1 \to 0$, the ratio $\eta \to \infty$. This singularity does not seem to have a physical interpretation and we try to correct it here by improving the initial model. First, the separate contributions to η in the Leyko model are plotted in Fig. 5.10. A straightforward interpretation of Fig. 5.10 is that the extreme values of the η ratio depend essentially on the flame model η_{tm}, and not on the nozzle model. Looking at Eq. (5.14b), it is clear that the acoustic wave produced by the flame $\omega_1^+ \to 0$ when $M_1 \to 0$. This does not fit the immediate intuition, as a very low Mach number flame would still cause direct noise. On the other hand, a very slow convection of entropy would probably lead to high dissipation, which is of course not accounted for in this model.

This remark is important: the *cold flame* assumption of the toy model of Leyko (2010) is very strong. The fact that it has such an influence on the ratio η proves that great care must be taken in the flame modelling part to correctly assess indirect to direct combustion noise ratio at the nozzle outlet. In the next section, a new model is proposed for ω_1^S and ω_1^+ where the mean heat release is not 0, and the unsteady heat release is written as a function of the upstream velocity instead of being arbitrarily imposed, leading to a more physical result. The new model is based on a more precise description of the jump conditions through flame. When this formulation is injected into Leyko's model to correct it, results are much better in the limit cases, but also quite different.

5.3.2.1 Flame jump conditions

To improve Leyko's model, we try yo express now $\dot{Q}'$ as a function of u' instead of imposing it without further cause. The link $\dot{Q}'(u')$ is an old topic, not only for combustion noise but also for thermoacoustics. Crocco (1969) proposed the so called $n-\tau$ model to describe the relation between heat release fluctuations $\dot{Q}'$ and acoustic waves, or u' near the flame. Even if the relation $\dot{Q}'(u')$ is known, jump conditions through the flame front also require attention. For zero Mach number, the jump condition used usually states that $u'_0 A_0 = u'_1 A_1$, *i.e.* the volume perturbation is conserved through the flame. For low but non-zero Mach numbers,

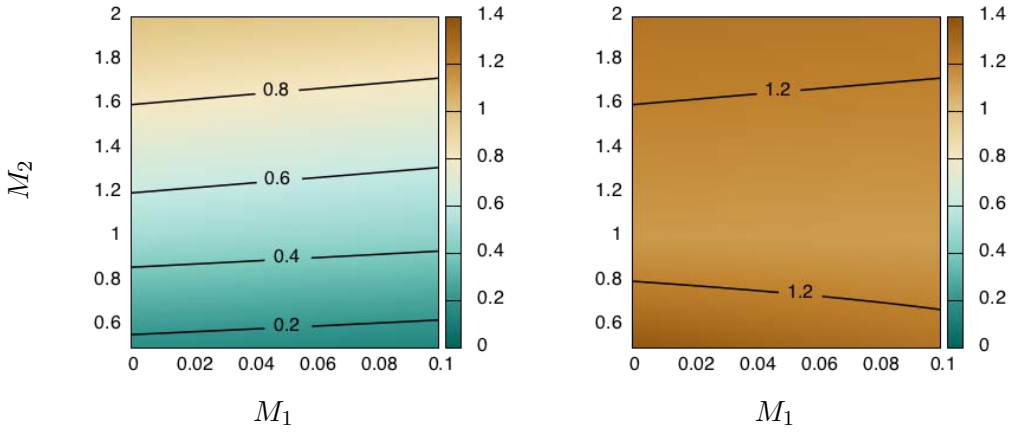

(a) Indirect nozzle transmission T_{SA} **(b)** Direct nozzle transmission T_{AA}

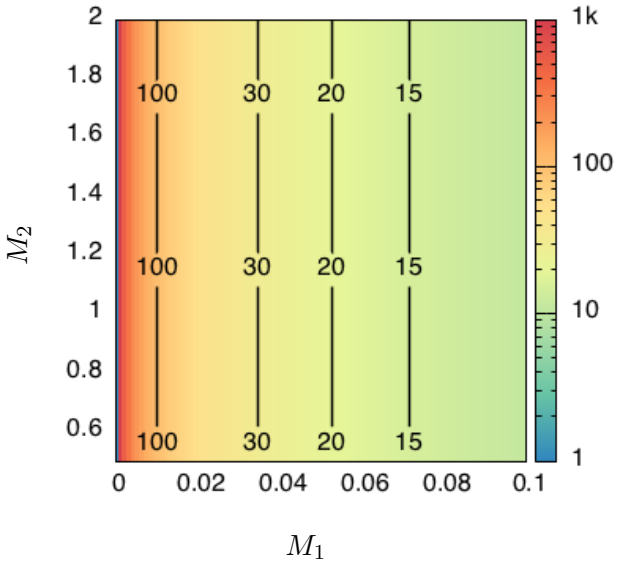

(c) Toy model entropic to acoustic wave ratio η_{tm}

Figure 5.10: Contributions of the various subterms to η in the model of Leyko (2010).

the natural jump condition ensues from the mass flow rate perturbation conservation, *i.e.* $\bar{\rho}_0 u'_0 A_0 = \bar{\rho}_1 u'_1 A_1$. Bauerheim *et al.* (2014) recently looked into this paradox, concluding that mass flow rate should be conserved for non-zero Mach number but that such a flame submitted to an incoming acoustic perturbation produced both acoustic and entropic downstream waves.

Infinitely thin flame models generally overlook flame dynamics, arguing that the flame is simply a fixed discontinuity, possibly of constant heat release (Bauerheim *et al.*, 2014) or varying heat release but uncorrelated with the flow (Leyko, 2010). However, as shown by Dowling (1995), this assumption is strong, and the $\dot{Q}'(u')$ relation can radically change both the acoustic and entropic waves expected to be produced by the flame. Chen *et al.* (2014) introduced yet another degree of modeling by considering that the flame front can also move: using the Rankine-Hugoniot relations to describe the flame, the interface speed u_s appears in the model. Allowing the flame to move changes conclusions drastically: Tab. 5.3 presents a summary of these approaches.

	$\bar{Q}$ Mean heat release	Q' Heat release fluctuations	u'_s Flame front absolute speed	s'_1 Entropy wave
Leyko (2010) (CT model)	0	$\neq 0$	0	$\neq 0$
Bauerheim *et al.* (2014)	$\neq 0$	0	0	$\neq 0$
Dowling (1995)	$\neq 0$	$\neq 0$	0	≈ 0
Chen *et al.* (2014) (HT model)	$\neq 0$	0	$\neq 0$	≈ 0
Present model	$\neq 0$	$\neq 0$	0	$\neq 0$

Table 5.3: Various jump conditions for flames with mean flow ($M > 0$).

5.3.2.2 Simplified hot toy (HT) flame model for acoustic and entropic generation

In order to improve the model of Leyko, we propose here to consider the flame as "hot" and release the $\bar{\dot{Q}} = 0$ assumption of Leyko , since this is a very strong assumption for a flame and it leads to a peculiar behavior when $M_1 \to 0$. In order to better represent the generation of both acoustics and entropy by the flame, the generation mechanisms will now be detailed for hot flames in premixed regimes but where the equivalence ratio can vary in time, according to the notations of Fig. 5.11. In the CT model of Leyko, instead of assuming that the flame is creating a $\dot{Q}'$ without asserting where it comes from as done by Leyko (2010) for the CT model, we will try to elucidate where $\dot{Q}'$ comes from. This will require introducing the perturbations of equivalence ratio ϕ' into the model because they are the real major source of entropy fluctuations. Indeed, a fully premixed flame can only produce

entropy fluctuations *via* inlet temperature variations, but in a non perfectly premixed flame the equivalence ratio effects add up and strongly overcome these temperature effects.

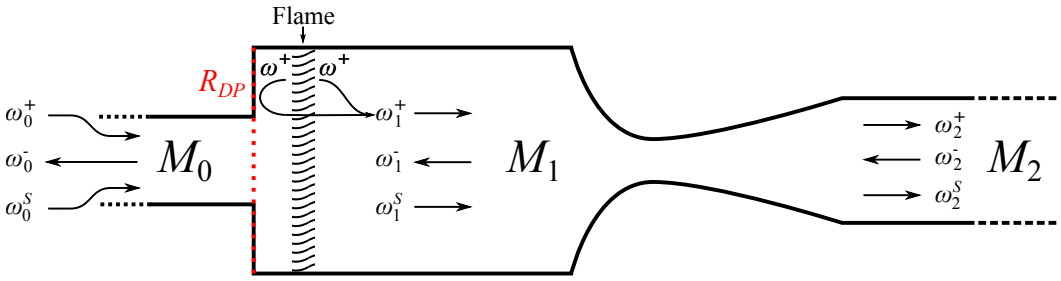

Figure 5.11: The new HT (hot toy) model, replacing the cold toy (CT) model of Leyko (2010).

Linearization of entropy jump The entropy jump through the flame is taken according to the single-specie formulation (*c.f.* Sec. 5.2.4.3):

$$\frac{s'}{c_P} = \frac{T'}{\bar{T}}$$

which yields for the complete transformation from fresh to burnt gases:

$$\frac{\Delta s'}{c_P} = \frac{T_1'}{\bar{T}_1} - \frac{T_0'}{\bar{T}_0}$$

where $T_0' \equiv T_{cold}'$ and $T_1' \equiv T_{adiab}'$. Inlet temperature fluctuations T_0' have an effect on the entropy produced by the flame. These fluctuations can be caused by an acoustic (isentropic) wave or by an incoming entropic wave. Adiabatic flame temperature fluctuations T_1' can have multiple origins. Let us consider a lean system, where $\bar{\phi} < 1$ but also $\phi < 1$ at all times, whatever the equivalence ratio fluctuations ϕ'. Writing the adiabatic temperature in its simplest form (Poinsot & Veynante, 2011):

$$T_{adia} = T_{cold} + \phi \frac{\Delta Q}{C_P}$$

yields after linearization:

$$\begin{aligned} T_1' &= T_0' + \phi' \frac{\Delta_f H_F^0 - \Delta_f H_P^0}{C_P} \\ &= T_0' + \frac{\phi'}{\bar{\phi}} \left(\bar{T}_1 - \bar{T}_0\right) \end{aligned}$$

hence the entropy fluctuation writes:

$$\frac{\Delta s'}{c_P} = \omega_1^S = \left(1 - \frac{\bar{T}_0}{\bar{T}_1}\right) \left[\frac{\phi'}{\bar{\phi}} - \frac{T_0'}{\bar{T}_0}\right] \tag{5.17}$$

A simple interpretation can be given for this result: if the equivalence ratio of the mixture increases, the adiabatic temperature T_1 increases, and one expects the entropy jump through the flame to increase. However, if the temperature of the fresh gases T_0 increases, the entropy goes the other way. This is in fact a perfectly normal behavior, although not necessarily intuitive at first. Recall Eq. (2.5), which states that the entropy change is the integral of the heat received by the temperature. In an isothermal exchange at T_{ref} for example this writes:

$$\Delta S = \frac{\Delta Q}{T_{ref}}$$

The implication is that if the reference temperature T_{ref} changes, a given heat exchange will not produce the same entropy change. This is expressed in Eq. (5.17) through the dependency of $\Delta S'$ to T_0'.

Both inlet temperature and mixture fluctuations can occur in an engine. The mixture is never fully premixed, and $\phi'/\bar{\phi}$ can easily change by 10% or more. Temperature fluctuations can be due to acoustic waves or inlet variations. Acoustic waves have a very small impact on temperature, and inlet feeding lines generate a very constant temperature.[1] Therefore, the ϕ' term is expected to be the dominant part of Eq. (5.17).

An important conclusion from this short study is that for an entropy wave to be created, inlet perturbations of temperature T_0' or of equivalence ratio ϕ' must be present. If none of these occur, $T_0' = \phi' = 0$ and $\omega_1^S = 0$. However, for a turbulent flame it is quite possible to observe heat release fluctuations $\dot{Q}' \neq 0$ even if $T_0' = \phi' = 0$: this occurs *e.g.* when the flame surface changes due to unsteady motion. Therefore, the direct link established by Leyko (2010) between ω_1^S and $\dot{Q}'$ does not withstand physical analysis of the origin of entropy fluctuations: for an entropy wave to appear, either the inlet equivalence ratio must differ, or the inlet temperature must change.

Acoustic generation As shown in this chapter (Sec. 5.2.3), a turbulent flame is also a direct noise source, mostly in the low frequency range. In the following, a crude approximation will be made to estimate the acoustic wave radiated downstream by the flame: the acoustic source is supposed to be entirely in the chamber, but very close to the dump plane (Fig. 5.11). The acoustic left and right travelling wave amplitudes both write, according to the 1D Green solutions of Eq. (5.11a):

$$\begin{aligned}\omega^+ &= \frac{\gamma-1}{\gamma P}\frac{\dot{Q}'}{2A_1\bar{c_1}} = \frac{\gamma-1}{\gamma P}\frac{\bar{\dot{Q}}}{2A_1\bar{c_1}}\frac{\dot{Q}'}{\bar{\dot{Q}}} \\ &= \left(1-\frac{\bar{T_0}}{\bar{T_1}}\right)\frac{M_1}{2}\frac{\dot{Q}'}{\bar{\dot{Q}}}\end{aligned}$$

[1] This also implies that in a perfectly premixed flame with constant inlet temperature, entropy fluctuations will be very small.

where A_1 is the chamber cross-section area and $\dot{Q}$ is the total heat release (in $\mathrm{J\,s^{-1}}$) in the domain, and has been expressed as:

$$\dot{Q} = \dot{m} c_P (T_1 - T_0) \tag{5.18}$$

Fig. 5.11 shows that in the current model, the waves generated by the flame travel both upstream and downstream from it. To account for the total acoustic wave radiated downstream ω_1^+, the reflection of the upstream propagating wave on the dump plane R_{DP} should be given. The resulting wave would then be:

$$\begin{aligned} \omega_1^+ &= \omega^+ + R_{DP}\, \omega^+ \\ &= (1 + R_{DP}) \left(1 - \frac{\bar{T_0}}{\bar{T_1}}\right) \frac{M_1}{2} \frac{\dot{Q}'}{\bar{\dot{Q}}} \end{aligned} \tag{5.19}$$

Rienstra & Hirschberg (2003) give the reflection of the left travelling wave on the section and sound speed discontinuity at the dump plane R_{DP}:

$$R_{DP} = \frac{A_2 c_1 - A_1 c_2}{A_2 c_1 + A_1 c_2} \tag{5.20}$$

which is a constant in this context, and will not affect the trends that are sought. A typical value of R_{DP} is 0.5.

Small Mach number limit: $M_1 \ll 0$. The CT model has a peculiar behavior in the limit of zero Mach number. While the discussions about flame jump conditions for exactly zero Mach number are subject to controversy in the acoustic community (see Sec. 5.3.2.1), a physical model should exhibit bounded behavior for "small" Mach numbers $M_1 \ll 1$.

In the CT model, Eqs. 5.14 show that when $M_1 \to 0$, since $\bar{m} \propto M_1$ the two source terms behave as:

$$\lim_{M_1 \to 0} \omega_1^S = +\infty \tag{5.21a}$$

$$\lim_{M_1 \to 0} \omega_1^+ = \frac{\dot{Q}'}{c_P \bar{T}} \tag{5.21b}$$

$$\tag{5.21c}$$

Note that there is a fundamental difference between this HT model and the original CT model of Leyko (2010): even though the chamber Mach number M_1 appears, this is only because the heat release fluctuations $\dot{Q}'$ are non-dimensionalized by the mean heat release fluctuations $\bar{\dot{Q}}$. In the limit case of zero Mach number $M_1 \to 0$, $\dot{m} \to 0$ hence also $\bar{\dot{Q}} \to 0$, and the acoustic production ω_1^+ stays bounded.

As detailed in Chap. 3, the heat release fluctuations $\dot{Q}'$ are often modeled according to the $n - \tau$ model in combustion chambers, thus relating it to inlet

velocity and equivalence ratio fluctuations. Indeed recall Eq. (3.37):

$$\frac{\dot{Q}'}{\bar{\dot{Q}}}(t) = N_2 \frac{u'}{\bar{u}}(t-\tau) + M\frac{\phi'}{\bar{\phi}}(t-\tau_\phi)$$

This implies for the acoustic wave amplitude:

$$\omega_1^+ = (1+R_{DP})\left(1-\frac{\bar{T}_0}{\bar{T}_1}\right)\frac{M_1}{2}\left[N_2\frac{u_0'}{\bar{u}_0} + M\frac{\phi'}{\bar{\phi}}\right] \tag{5.22}$$

5.3.2.3 Reformulation of the toy model: the hot toy (HT) model

The toy model of Leyko (2010) was an attempt to quantify the generation of entropy and acoustic wave amplitudes by a flame before they hit the nozzle. As shown in the previous section, this first approach could lead to unphysical values in some cases. The developments of this section can be used to propose a more physical approach to describe creation terms of the flame. Only the terms created by the flame are modified in the HT model.

According to previous developments, there is no direct link between the Mach number in the chamber and the entropic wave. Therefore, the ratio η_{tm} from Leyko (2010) becomes with the HT model η_{ht}:

$$\eta_{ht} = \frac{\omega_1^S}{\omega_1^+} \tag{5.23}$$

and can no longer be drawn against M_1. In fact, the parameters directly related to noise are the fluctuations of equivalence ratio $\phi'/\bar{\phi}$, of inlet temperature $T_0'/\bar{T}_0$ and of inlet velocity $u_0'/\bar{u}_0$. In order to evaluate η_{ht}, the following assumption is made: inlet perturbations (upstream of the flame) are of acoustic nature. This implies that the velocity fluctuations $u_0'/\bar{u}_0$ are only due to acoustics, so that temperature fluctuations can be related to velocity fluctuations by the isentropic relation:

$$\frac{T_0'}{\bar{T}_0} = (\gamma-1)M_0\frac{u_0'}{\bar{u}_0}$$

Usually this will lead to very small temperature changes. The flame ratio η_{ht} is only a function of two variables with this assumption: $\eta_{ht} = \eta_{ht}(\phi'/\bar{\phi}, u_0'/\bar{u}_0)$. The total indirect to direct noise ratio writes:

$$\begin{aligned}\eta &= T_{SA}(M_1,M_2)\times\eta_{ht}(\phi'/\bar{\phi}, u_1'/\bar{u}_1)\times\frac{1}{T_{AA}(M_1,M_2)}\\ &= \underbrace{\frac{T_{SA}}{T_{SA}}}_{\eta_{Noz}}(M_1,M_2)\times\eta_{ht}(\phi'/\bar{\phi}, u_1'/\bar{u}_1)\end{aligned}$$

where η_{Noz} is the ratio of acoustic to entropic noise transmitted by the nozzle submitted to equal ω_1^+ and ω_1^S waves. η_{Noz} therefore writes:

$$\eta_{Noz} = \begin{cases} \dfrac{M_2}{1+1/2(\gamma-1)M_2}\dfrac{M_1+M_2}{1+M_1} & \text{if } M_2 < 1 \\ \dfrac{M_2-M_1}{1+M_2}\dfrac{1+1/2(\gamma-1)M_1}{1+1/2(\gamma-1)M_2} & \text{if } M_2 \geq 1 \end{cases} \tag{5.24}$$

and is plotted in Fig. 5.12. This shows the compared efficiencies of the nozzle for

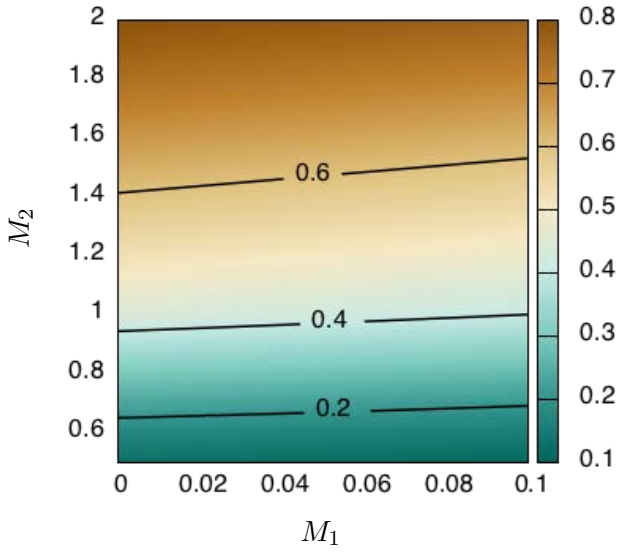

Figure 5.12: Nozzle contributions to the overall combustion noise ratio $\eta_{Noz}(M_1, M_2)$

direct and indirect noise production. The order of magnitude of this ratio is 1 for high outlet Mach numbers M_2, and 0.1 for low values of M_2. Since $\eta = \eta_{Noz} \times \eta_{ht}$, and η ranges from 1 to 1000 (Fig. 5.9), it is clear that in all cases the nozzle effect contributions cannot explain the drastic efficiency variations between the indirect noise production and direct noise transmission. Fig. 5.13b however demonstrates how under strong equivalence ratio fluctuations, the indirect noise become largely predominant. This further confirms that the indirect to direct noise ratio η is dominated by the chamber effects, and not by the dynamics in the nozzle.

The flame ratio for the HT model η_{ht} writes, using Eq. 5.17 for ω_1^S and Eq. 5.22 for ω_1^+:

$$\eta_{ht} = \frac{\omega_1^S}{\omega_1^+} = \frac{2}{M_1(1+R_{DP})}\frac{\phi'/\bar{\phi} - (\gamma-1)M_0 u_0'/\bar{u_0}}{M\phi'/\bar{\phi} + N_2 u_0'/\bar{u_0}} \tag{5.25}$$

In order to plot η_{ht}, values which are representative of the CESAM-HP setup (Chap. 9) are chosen for the constants involved. They are summarized in Tab. 5.4. η_{ht} can then be computed. The new flame model η_{ht} is plotted next to the old toy model of Leyko (2010) in Fig. 5.13. The functions are also compared in Tab. 5.5.

M_0	M_1	T_0/T_1	n	m	γ
0.05	0.05	7	1	1	1.4

Table 5.4: Constant values chosen to compute η_{ht}

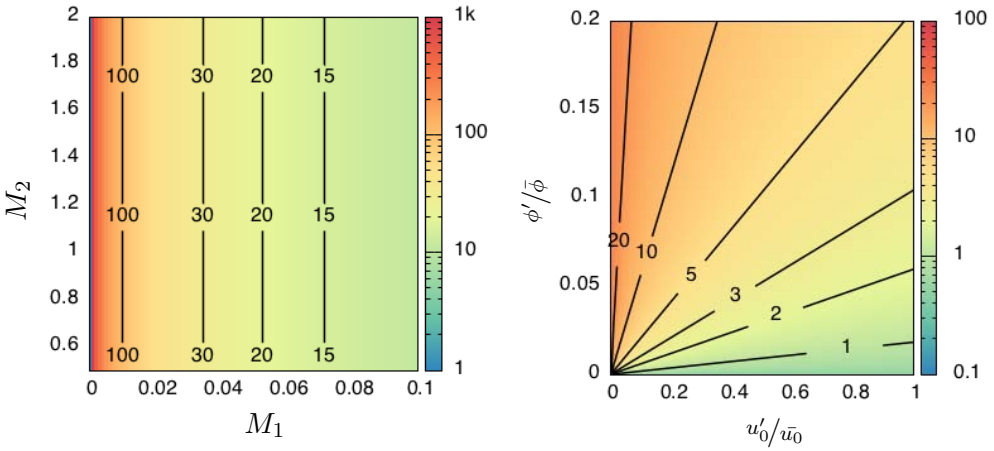

(a) $\eta_{tm}(M_1, M_2)$ **(b)** $\eta_{ht}(\phi'/\bar{\phi}, u'_0/\bar{u_0})$

Figure 5.13: Model for the combustion chamber: (a) η_{ht} toy model of Leyko (2010) and (b) η_{ht} of the current approach.

Several interesting limit cases can be mentioned:

- For a perfectly premixed flow, as often occurs in lab burners, the equivalence ratio fluctuations are 0, and the flame ratio η_{ht} reduces to:

$$\eta_{ht} = 2\frac{M_0}{M_1(1+R_{DP})}\frac{\gamma-1}{n} \tag{5.26}$$

  This is a function only of N_2. When N_2 is small, η_{ht} can become large: an inlet variation of u'_0 will lead to a finite entropy wave ω_1^S, and to a vanishingly small acoustic wave ω_1^+.

- When N_2 is large, we know that η_{ht} remains bounded by its low frequency value $T_1/T_0 - 1$ (Poinsot & Veynante, 2011). The flame ratio becomes in this case $\eta_{ht}^{min} = 2\frac{M_0}{M_1}\frac{\gamma-1}{T_1/T_0-1}$, which is small ($\approx 0.1$ with the values of Tab. 5.4).

- If the equivalence ratio fluctuations $\phi'/\bar{\phi}$ dominate the flame response, and as long as $u'_0/\bar{u_0}$ stays bounded, $N_2 u'_0/\bar{u_0} \ll M\phi'/\bar{\phi}$ and η_{ht} becomes:

$$\eta_{ht} = \frac{2}{M_1(1+R_{DP})}\frac{1}{M} \tag{5.27}$$

  which depends only on M_1 and can become large when $M_1 \to 0$. However, because the hypothesis has been made that $u'_0/\bar{u_0}$ stayed bounded, this implies that when $M_1 \to 0$, so does u'_0. Therefore, any form of acoustics are destroyed

Model	$\dot{Q}'$	ω_1^S	ω_1^+
Leyko (2010) Cold Toy (CT) model	Arbitrary	$\frac{\dot{Q}'}{\bar{\dot{m}} c_P \bar{T}_1}$	$\frac{M_1}{1+M_1} \frac{\dot{Q}'}{\bar{\dot{m}} c_P \bar{T}_1}$
Current Hot Toy (HT) model	Imposed by a u' or ϕ' upstream of the flame front (Eq. 3.37)	$\left(1 - \frac{\bar{T}_0}{\bar{T}_1}\right) \times \left[\frac{\phi'}{\bar{\phi}} - (\gamma - 1) M_0 \frac{u_0'}{\bar{u}_0}\right]$	$(1 + R_{DP}) \times \left(1 - \bar{T}_0/\bar{T}_1\right) \times \frac{M_1}{2}\left[M \frac{\phi'}{\bar{\phi}} + N_2 \frac{u_0'}{\bar{u}_0}\right]$

Table 5.5: Toy model of Leyko (2010) compared to the current model

by the hypothesis, and it is obvious that the zero Mach number limit case will make η_{ht} diverge. In practice, this divergence can therefore not occur in a real system.

5.3.3 Conclusion on the toy model

The present study has demonstrated that the isolated "cold flame" assumption used in Leyko *et al.* (2009) can lead to unphysical evaluation of the indirect to direct noise ratio η. This comes from the fact that acoustic and entropic generation for this flame are not correlated to physical perturbations upstream of the flame, thus yielding an incorrect scaling between the two. A more physical approach called the "hot toy" (HT) flame model has been derived, where the waves produced are related to perturbations (of velocity u_0 and equivalence ratio ϕ) reaching the flame. The scaling between acoustic and entropy waves created by the flame is therefore based on a more physical flame behavior description, and stays bounded when $M_1 \to 0$. The new HT model changes the usual approach advocated by Leyko *et al.* (2009) where the ratio of indirect to direct noise (η from Eqs. 5.15 and 5.16c) was controlled by the chamber Mach M_1 and the nozzle outlet Mach M_2. In the new model, η is a function of M_1 and M_2 but also of the level of fluctuations of equivalence ratio ϕ' and upstream velocity u'. This is only due to the changes of the flame model η_{ht}. This new model, as plotted in Fig. 5.13b, demonstrates that it is the level of equivalence ratio fluctuations $\phi'/\bar{\phi}$ that pilots the indirect noise generation. Direct noise is directly related to acoustic perturbations impinging on the flame, represented here *via* $u_0'/\bar{u}_0$. In order to characterize the indirect to direct noise production of a complete setup, not only the chamber M_1 and nozzle outlet M_2 Mach numbers must be considered,

but also the levels of $\phi'/\bar{\phi}$ and $u'_0/\bar{u_0}$. These however result from the complete chamber and flame dynamics, and are difficult to estimate *a priori* for a given setup without performing unsteady simulations or experimental measurements: the HT model provides values of η_{ht} which range from $2\frac{M_0}{M_1}\frac{\gamma-1}{T_1/T_0-1}$ to $+\infty$. As explained at the end of the previous section however, the case where $\eta_{ht} \to \infty$ cannot be met in practice, and this quantity is in fact always bounded. These values of η_{ht} will however lead to values of indirect to direct noise ratio η which can vary on a large range, and require more precise evaluation methods than the simple toy model analysis presented in this chapter.

Chapter 6

Flame stabilization in swirled flows

Flashback is one of the risks associated to lean premixed combustion, and it is very dangerous for burners as the injection duct is not designed to sustain flame temperatures. As shown in the first section of this chapter, many different mechanisms can lead to flashback. The EM2C burner contains a swirl-stabilized flame, i.e. facing a swirled duct and where stabilization relies on aerodynamics alone. In this case, swirl also interacts with combustion instabilities and with flashback. The most obvious risk of flashback in this case is for the flame to enter the vortex core that it is facing and propagate upstream. This chapter offers an overview of the state of the art in flame propagation along a vortex axis (FPAVA). A numerical toy model of FPAVA is proposed, in order to grasp the physics of this problem and validate the numerical approach to it against known experimental data. Both sections prepare the analysis of the LES performed in Part III.

6.1 Flashback mechanisms in swirled combustors

As discussed in Chap. 1, lean premixed combustors are ever more popular in the aeronautic industry. A popular method to achieve lean premixed combustion is to use aerodynamic swirl stabilization, as this creates recirculation zones of hot gases which constantly reignite the flame (Syred & Beer, 1974). An undesired byproduct of swirl in lean premixed combustion is the occasional flashback of the flame which stabilizes at a new unwanted position upstream of the chamber. Five major mechanisms have been described as leading to flame flashback (Fritz *et al.*, 2004; Sommerer *et al.*, 2004):

1. **wall boundary layer flashback** (WBLF) along walls in case of weak velocity gradients;
2. **vortex core flashback** (VCF), when the turbulent flame speed exceeds the flow velocity in the vortex core;
3. **thermoacoustic instabilities** generating strong velocity oscillations;
4. **combustion induced vortex breakdown** (CIVB);
5. **autoignition**.

Mechanism 1: Wall boundary layer flashback (WBLF) WBLF involves the interaction of low velocity flow near walls and flame propagation in this zone if the flame speed is larger than the local flow velocity and the zone over which this is true is larger than a typical quenching distance. Early observations yielded a simple criterion based on comparisons between boundary layer and flame thickness (Lewis & von Elbe, 1943) which leads to an expression where flashback is controlled by the velocity gradient at the wall. However, finer investigations of this mechanism using direct numerical simulation (Gruber *et al.*, 2012) and experiments (Eichler & Sattelmayer, 2011) recently showed that this mechanism is more complex, as the flame modifies the boundary layer ahead of itself.

This phenomenon is unlikely in swirled systems, as the swirled flow achieves maximum velocity very close to the walls. In practice, it has not been observed in the context of this study, and will not be further discussed.

Mechanism 2: Vortex core flashback (VCF) Flashback in a swirled flow can take place along the vortex core axis (Sommerer *et al.*, 2004). The mechanism involved in this upstream flame propagation has been the subject of numerous models (Lovachev, 1976; Chomiak, 1977; Ashurst, 1996; Umemura & Tomita, 2001). The combination of a radial pressure gradient and an axial density gradient induces a negative velocity leading to upstream propagation. In swirled systems without bluff body, a strong axial vortex can develop, and VCF can occur.

Mechanism 3: Thermoacoustic instabilities The reference study of Keller *et al.* (1982) showed a backward facing step in which the flame stabilization position was strongly influenced by self-excited acoustic waves: for a given set of boundary acoustic impedances, a self-sustained thermoacoustic instability could trigger temporary flame flashback. This behavior was also reproduced with active acoustic excitation. Thibaut & Candel (1998) later showed that this could be accurately reproduced using LES, and a thickened flame strategy for combustion modelling. The flashback mechanism in this case is simple : the acoustic oscillation leads to velocity perturbations larger than the mean flow, thus inducing flow reversal at the flame location. This flashback may oscillate at the thermoacoustic frequency or lead the flame to stabilize permanently at another location. The fact that flashback is due to thermoacoustics may not be clear in the latter case because in a few thermoacoustic cycles, the flame might move from one position to another, leaving only a small acoustic signature.

Mechanism 4: Combustion induced vortex breakdown (CIVB) Vortex breakdown can occur both at a brutal section change or a density discontinuity. Swirl-stabilized burners use vortex breakdown to stabilize the flame (Syred & Beer, 1974). The breakdown creates a recirculation zone which keeps hot gases close to the dump plane, continuously reigniting the cold flow. Vortex breakdown is controlled by the amount of swirl: an increase in swirl can reinforce the recirculation zone and

lead to low or negative values of axial velocity, opening the way for flame flashback (Kröner *et al.*, 2002). The CIVB mechanism includes another effect of the flame itself on swirl. When the flame approaches the swirled region, it affects the local vorticity, thus changing swirl and the breakdown. This process can be self amplified, and ultimately lead to flashback. RANS simulations (Kiesewetter *et al.*, 2003) were used to reproduce this type of flashback. Kiesewetter *et al.* (2007) later showed that CIVB is driven by baroclinic torque, and its triggering is controlled by flame quenching in the vortex core.

This mechanism is a possible precursor to Mechanism 2: once the CIVB mechanism leads to flashback, the flame finds itself inside the upstream swirled duct, and the flame can propagate along the vortex axis. However, in a dump combustor, other mechanisms than CIVB can lead the flame from the chamber into the upstream duct, such as Mechanism 3. In any case however, once the flame is inside the upstream duct, Mechanism 2 alone determines whether the flame continues further upstream.

Mechanism 5: Autoignition As the temperature of the fresh charge increases and premixing is used in many recent gas turbine injection systems, autoignition times within the passages may decrease enough to induce flame ignition in the swirlers. Such mechanisms may be interpreted as flashback. They only occur when inlet temperatures are high enough, and are not relevant to this study.

In a real gas turbine chamber, all these mechanisms may appear, combine and lead to unexpected flashback. Compressible reacting LES permits the exploration of the complete system, and reveals the occurrence of each mechanism individually as well as their combination.

As stated above, mechanisms 1 and 5 are unlikely in swirled combustors with low inlet temperature and cooled walls. However, mechanisms 2 to 3 can quite possibly be observed. Thermoacoustic instabilities are treated in Chap. 3: even if this field has received much interest in the past decades much less work has addressed the question of flashback to instabilities. Mechanisms 2 and 4 are not yet very well described, as they include complex interactions between flame, large scale aerodynamics and turbulence. The purpose of this chapter is to give the framework of the past studies of these mechanisms, and show that these phenomena are well predicted by LES.

6.2 Flame stabilization in swirled combustors: flame propagation along a vortex axis

Swirl is the most common stabilization method in combustion chambers (Syred & Beer, 1974). Its main advantage is to create a recirculation zone of burnt gases which fix the anchoring point of the flame. However, one known risk associated to swirled combustors is flashback. It can mostly appear according to two modes: VCF (Mechanism 2) and CIVB (Mechanism 4). Both phenomena imply the interaction between the flame and a vortex.

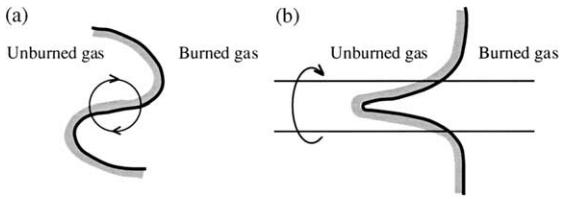

Figure 6.1: Two major modes of flame vortex interaction, as described by Kadowaki & Hasegawa (2005): (a) vortex convected towards the flame front; (b) FPAVA.

Flame-vortex interaction is an important subject when modeling turbulent combustion: burning mechanisms at the smallest scales of motion are essential to the overall combustion regime (Peters, 2001; Williams, 1985; Pitsch, 2006). This issue controls the construction of multiple "turbulent combustion diagrams", as described thoroughly by Poinsot & Veynante (2011). The various interactions of a flame with a vortex are generally divided into two approaches (Hasegawa *et al.*, 1995):

- the vortex axis is parallel to the flame: the vortex goes through the flame front;
- the vortex axis is normal to the flame, which propagates along the vortex axis.

An illustration of these two modes is given in Fig. 6.1. The first has received much attention both numerically (Karagozian & Marble, 1986; Poinsot *et al.*, 1991) and experimentally (Jarosinski *et al.*, 1988; Roberts & Driscoll, 1991), as it offers a well defined test case for flame-vortex interaction. The second, flame propagation along a vortex axis (FPAVA) is quite different in nature, and has received less attention. Of course, three-dimensional studies of flame-turbulence interactions such as Trouvé & Poinsot (1994) include all kinds of flame-vortex interaction, but the peculiar matter of FPAVA is rarely detailed while it certainly plays a role and should be included in the derivation of efficiency functions for example (Meneveau & Poinsot, 1991; Charlette *et al.*, 2002).

Characterization of FPAVA implies a correct definition of the nature of the vortex that interacts with the flame. A simple dichotomy can be made in the studies available: free vortices and duct flow vortices. Three dimensional turbulence contains free vortices, but industrial combustion systems relying on swirl often present large scale flow rotations perpendicular to the flame front.

6.2.1 The question of flame speed along a vortex axis

Even if all experts understand what a flame speed is, defining it for a FPAVA scenario is a difficult task because it is controlled more by the flow than it is by chemistry: even a non reacting front will have a FPAVA speed. A usual definition for flame speed v_f in a laminar duct is:

$$v_f = s_L \frac{A_f}{A_{tube}}$$

where s_L is the laminar flame speed, A_{tube} the cross-sectional area of the tube and A_f the flame area. A spherically expanding flame yields a different absolute flame

speed, namely :

$$v_f = s_L \frac{\rho_u}{\rho_b}$$

The existence of different flame speeds is well known (Poinsot & Veynante, 2011) and defining a flame speed requires first to identify whether absolute, displacement or consumption speeds are considered. For a spherical laminar flame, s_L is the consumption speed while $s_L \frac{\rho_u}{\rho_b}$ is the displacement speed. This can be explained by a ratio of the order of the fresh to burnt gas densities by the fact that the dilatation of burnt gases accelerates the flame front. In many complex situations, flame propagation and dilatation effects can combine to increase the overall effective flame front speed. This is expected to occur to some extent in the case of FPAVA, thus making flame speed in FPAVA a non-trivial subject. It has been known for several decades that the flame speed along a vortex axis (Fig. 6.1(b)) can differ very significantly from its value in a flow at rest. McCormack *et al.* (1972) performed the first flame speed measurements in FPAVA on free vortex rings, showing that the flame speed largely exceeded that of a laminar flame. In fact, evidence was given that the flame speed increases approximately linearly with vortex strength. Lovachev (1976) attempted to explain this velocity increase by analogy with a flame propagating on a ceiling: buoyancy effects increase the flame speed by a factor two, as dilatation of hot gases pushes the flame front. Similarly, the density change beween fresh and hot gases in the rotating flow induces stretching of the hot gases along the vortex axis. This explanation stayed fully qualitative. Note also that these authors considered implicitely absolute flame speeds, meaning only the flame movement is a fixed reference frame. Therefore, they have no access to displacement or consumption speeds.

Chomiak (1977) later pointed out that the method of vortex generation of McCormack *et al.* (1972) did not permit to distinguish if the vortex strength or the maximum tangential velocity was the determining factor increasing the absolute flame speed. He then went on to suggesting the first quantitative model. Considering that combustion produces a nearly discontinuous breakdown of the vortex, the pressure difference between two Rankine vortices of cold and hot gases is responsible for the "pull" on the flame front. This simple model, known as *vortex bursting*, leads to a flame velocity of $v_f = v_{\theta_{max}} \sqrt{\frac{\rho_u}{\rho_b}}$. It should be noted that the laminar flame speed doesn't even appear in this formulation, as it is considered to be of second order compared to the density ratio mechanism. This is the case with most FPAVA models which view the flame as an inactive discontinuity between two fluids of different densities. By considering the conservation on angular momentum through the flame, Daneshyar & Hill (1987) derived an associated propagation velocity of $v_f \approx v_{\theta_{max}} \sqrt{\frac{2}{3} \frac{\rho_u}{\rho_b}}$. These approaches brought first estimations of the flame speed in a vortex core. Experimental measurements of both pressure jump through the flame and flame propagation velocity by Ishizuka & Hirano (1994) showed however that even though the pressure jump was correctly estimated, flame speeds were overpredicted by this model. Asato *et al.* (1997) later confirmed these experimental

results, and offered a correction to the original theory by accounting for flame diameter. Unfortunately, this flame speed formula is complex and still strongly overestimates the measured values.

Sakai & Ishizuka (1996) suggested that one problem with the vortex bursting theory is that during propagation, the flame tip is small, hence the pressure jump does not simply result from the jump from a high density to low density vortex. Correcting the pressure jump with empirical data lead to a good estimation of v_f. Ishizuka *et al.* (1998) lead a more detailed theoretical analysis of this correction, and successfully compared it to measured flame propagation velocities. He named this mechanism the *back-pressure drive* mechanism which yielded for v_f:

$$v_f = s_L + v_\theta^{max} \sqrt{1 + \frac{\rho_u}{\rho_b}} \tag{6.1}$$

The flame speed is included, but as is obvious from the formulation it is simply added to the density ratio mechanism. In practice, the second term is generally orders of magnitude higher than the laminar flame speed s_L, confirming that the flame movement in FPAVA scenarios is mostly due to the convection of the flame front by density gradients combined with swirl, and not to flame propagation.

These approaches are based on the idea that a pressure gradient is created at the flame interface, "pulling" the flame into the fresh gases. Other efforts however have chosen the perspective of vorticity: starting from the vorticity transport equation and keeping only the significant source term yields:

$$\frac{\partial \omega}{\partial t} \approx -\boldsymbol{\nabla}\left(\frac{1}{\rho}\right) \times \boldsymbol{\nabla} P = \frac{\boldsymbol{\nabla}\rho \times \boldsymbol{\nabla} P}{\rho^2} \tag{6.2}$$

where $\omega = \boldsymbol{\nabla} \times \boldsymbol{v}$. The flame generates a strong density gradient $\boldsymbol{\nabla}\rho$ along the vortex axis, and the vortex induces a radial pressure gradient $\boldsymbol{\nabla} P$. The resulting induced vorticity is along the azimuthal direction, and tends to pull the cold gases into the hot ones near the wall, and the hot gases into the cold ones on the axis. This force is known as the *baroclinic torque*, and is widely used in the geophysics community to explain atmosphere dynamics when pressure and density gradients are not aligned. Fig. 6.2 presents this effect for FPAVA, as first described by Ashurst (1996). This

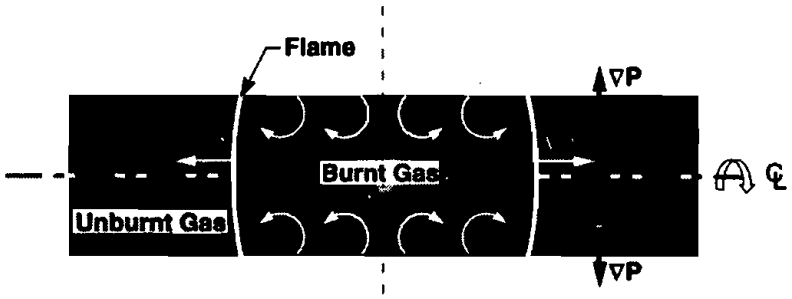

Figure 6.2: The baroclinic torque mechanism, from Ashurst (1996).

effect can be precisely estimated when the flame front is planar, but once the flame

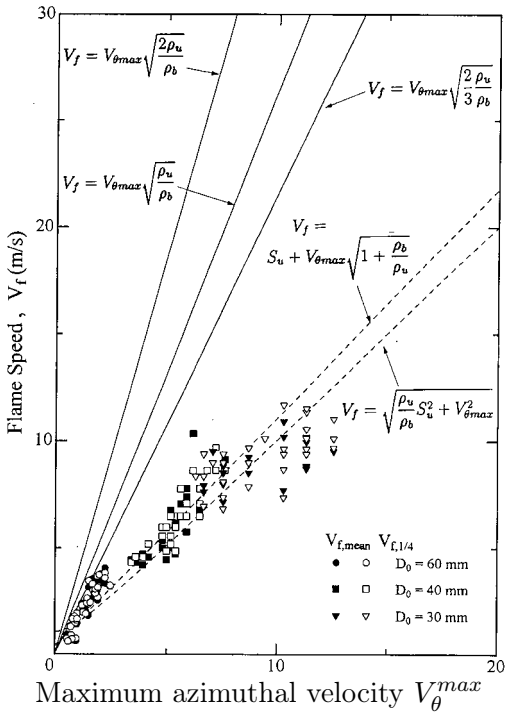

Figure 6.3: Experimental measurements (symbols) compared to several theories (lines). From Ishizuka *et al.* (1998)

tip penetrates the cold gases, its definition and effect are much less clear. Hasegawa *et al.* (2000) used a numerical simulation to show that while baroclinic torque did explain the initial flow acceleration, it overpredicted the stationary flame propagation velocity once achieved. Finer observations of the dynamics of vorticity along a vortex filament through the flame discontinuity were proposed *e.g.* by Umemura & Tomita (2001) and a thorough review of studies surrounding this subject was done (Ishizuka, 2002). These models, as well as some experimental measurements are displayed in Fig. 6.3.

The development of numerical capacities allows to investigate the mechanisms involved in FPAVA. Kadowaki & Hasegawa (2005) demonstrated the capability of LES to reproduce and explain the parameters controlling flame speed in an unconfined vortex core, and assessed the effect of density ratio. Domingo & Vervisch (2007) described a DNS of a free vortex impinging on a plane flame front. A non reacting simulation demonstrates the baroclinic torque effect during the initial stage of the density discontinuity propagation, but again this agreement only exists during the initial stages of propagation. Combustion must then come into play to sustain FPAVA. In a different context, Gruber *et al.* (2012) recently described a wall-bounded flame with no mean flow swirl, in which the main phenomena driving flashback is the influence of the flame on the hydrodynamics of the flow near the walls. In these regions, the flame modifies the flow and creates pockets of backflow, which increase considerably the flashback speed. In a non-swirled context, this nevertheless

supports the theory that the dilatation produced by the flame can drive its own flashback. This is however more difficult to demonstrate for a rotating flow, where the wall cannot isolate these phenomena. Moreover, there is no strict equivalent of the periodic channel for a swirled flow.

6.2.2 FPAVA in wall bounded flows

Flame-vortex interaction is an important subject for turbulent combustion, as turbulence is bound to send vortices in every possible direction onto the flame front. For this reason, numerous studies have been performed on free vortices interacting with flame fronts (McCormack *et al.*, 1972; Ishizuka *et al.*, 1998; Hasegawa *et al.*, 2002).

In modern combustors however, swirled injectors induce large scale coherent vortices, often normal to the flame front. These vortices are confined by the chamber walls, and have a different nature than free vortices. In order to investigate this particular FPAVA, several experimental campaigns have also been lead for flames in confined swirled flows.

Two possibilities appear in this case to induce flow rotation, as sketched in Fig. 6.4:

- gas is trapped in a tube, which undergoes rotation. As shown in Fig. 6.4(a), the azimuthal velocity is simply linear, with its maximum at the rotating wall. Once solid body rotation is achieved, the flow is ignited and the expanding gases exit the open end(s). This case is called the Solid Body Rotation (SBR) case;
- a swirled flow is injected in a tube at rest at one end, and exits through the other end, as shown in Fig. 6.4(b). The azimuthal velocity is both 0 at the axis and the outer wall, and the profile depends on the type of and the distance to the injectors. This case is called the Swirled Flow (SF) case.

The rotating tube (SBR) is a clearly defined problem. Once solid body rotation is achieved, the velocity is known at every point in the domain. Ignition at the center of such a tube provides precise measurements of flame speeds, as shown by Sakai & Ishizuka (1996). However, it is not representative of the type of flow encountered in most combustion chambers.

On the contrary, for the fixed tube (SF), the radial and axial velocity distributions depend on the injection method, and the position in the tube. Even without swirl, this is a complex problem as flames propagating in tubes can exhibit highly unsteady phenomena known as “tulip flames” (Clanet & Searby, 1996). In laminar cases, initially planar flames shape into a forward pointing finger, and then suddenly switch to a backward facing cusp, with a strong effect on flame speed. Ishizuka & Hirano (1993) reported such behavior in long tubes with swirling flow, but Ishizuka (1990) demonstrated that this phenomenon did not appear in the first 15 tube diameters. Combustion chambers for aeronautic applications generally have very strict size limitations, and the injection tubes are as short as possible. 15 tube diameters is much longer than any industrial configuration so that FPAVA can be assumed to

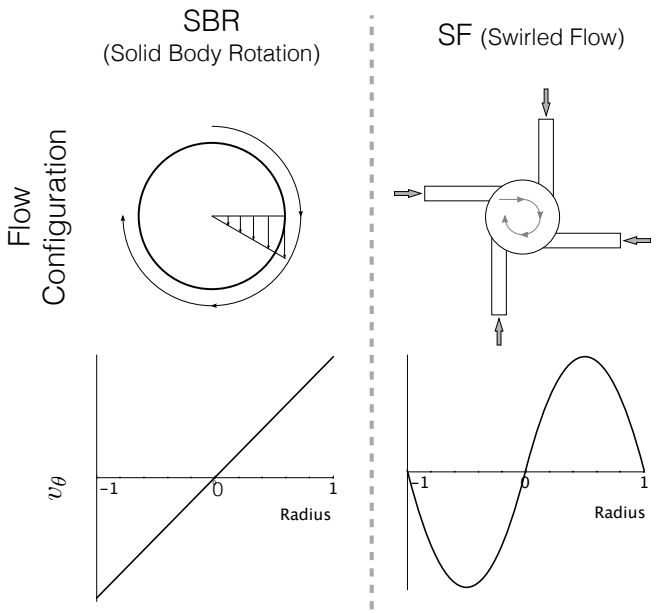

Figure 6.4: Experimental setup (top) and azimuthal velocity profile (bottom) for solid body (left) and swirler-induced (right) rotations.

occur long before tulip flames appear.

6.3 A numerical illustration of flame flashback along a vortex axis

A first numerical study performed in this PhD focused on FPAVA in the simplest possible configuration. Defining this configuration is already a problem as shown in Fig. 6.4. This section presents this preliminary study, starting from the unswirled, non reacting Poiseuille flow as a target illustration of this exercise.

The Poiseuille flow is a toy model in fluid mechanics which can be used for code validation: in such a laminar unswirled flow, a source term on axial momentum (equivalent to an imposed pressure gradient) is sufficient to completely define the flow. The resulting flow is known as the Poiseuille flow. The Reynolds number Re of the flow in the pipe is directly related to the imposed pressure drop. The steady-state flow is therefore uniquely determined by the Reynolds number, *i.e.* by the source term.

From a numerical perspective, this case yields a simple test for numerical fluid flow solvers: for a given source term, the velocity profile is unique, and can be analytically derived. A possibility to test the code validity is to set up a pipe simulation in which a source term matching negative pressure drop is introduced. If the code performs correctly, the fluid must accelerate and ultimately reach everywhere in the tube a velocity profile that matches the analytical derivation.

The propagation of a flame along a vortex axis is however a much more complex

phenomenon with incomplete modeling to this date and no simple reference configuration such as the Poiseuille flow. The ability of an LES solver to reproduce the flame speed in FPAVA conditions is nevertheless critical to prove the reliability of flame stabilization prediction. To check the behavior of the solver used in this study, we have built a simple toy model (Sec. 6.3.1) which tries to be as generic for FPAVA as the Poiseuille flow is for laminar non-reacting flows. This toy problem relies on a laminar front propagating in a cylindrical duct with imposed pressure gradient (to impose the mass flow rate) and imposed azimuthal force (to impose the swirl). A hot front is added to this flow and its speed is then monitored and compared to experimental data in Fig. 6.3.2.

6.3.1 A toy model for swirled flow: the Poiseuille SF

The experimental data available for flame speed along a vortex axis can be segregated in two major configurations, as described in the previous section:

- solid body rotation (SBR) experiments;
- swirled flow (SF) experiments.

The major drawback of the SF approach is that the flow is not clearly defined. In fact, a classical definition of the swirl number Sw:

$$Sw = \frac{\iint_{(CS)} \rho U (rW)\, dS}{R \iint_{(CS)} \rho U U\, dS} \tag{6.3}$$

where (CS) is the cross section of interest, shows that for a given swirl number Sw, an infinite number of axisymmetric flows can exist. This is a bad property when designing a test case, as it is thus impossible to obtain the exact same flow as in the experiment. Choosing profiles for U and W is an equally arbitrary solution.

The approach followed here is to build a Poiseuille SF depending only on two source terms: instead of imposing a mean swirl or a velocity profile, mean source terms are imposed on axial and swirling directions so that a physically meaningful flow is obtained (like for the Poiseuille flow). Consider a circular periodic pipe of radius R. Its Reynolds number based on the bulk velocity v_z^{bulk} is defined as:

$$Re = \frac{v_z^{bulk} 2R}{\nu} \tag{6.4}$$

It is described with the cylindrical coordinate systems, namely by the variables (r, θ, z). The velocity in this coordinate system is written (v_r, v_θ, v_z). The following hypotheses are used:

- no volume forces other than the imposed source term;
- steady-state regime;
- axisymmetric flow ($\frac{\partial}{\partial \theta} = 0$);
- periodic flow ($\frac{\partial}{\partial z} = 0$);
- parallel flow ($v_r = 0$).

The mass and movement quantity equations are simplified according to these hypotheses, and write in cylindrical coordinates :

$$\frac{\partial v_z}{\partial z} = 0 \tag{6.5}$$

$$\frac{\rho v_\theta^2}{r} - \frac{\partial P}{\partial r} + S_r = 0 \tag{6.6}$$

$$\mu \left[\frac{1}{r} \frac{\partial}{\partial r} \left(r \frac{\partial v_\theta}{\partial r} \right) - \frac{v_\theta}{r^2} \right] + S_\theta = 0 \tag{6.7}$$

$$\mu \frac{1}{r} \frac{\partial}{\partial r} \left(r \frac{\partial v_z}{\partial r} \right) - \frac{\partial P}{\partial z} + S_z = 0 \tag{6.8}$$

where S_r, S_θ, S_z are the radial, azimuthal and axial source terms, respectively.

In a periodic pipe flow, the flow is often imposed simply by setting a constant source term in one direction of the momentum equation matching the pipe axis, *e.g.* S_z. The simplest analogy to obtain a rotating flow is therefore to impose a constant source term in the azimuthal direction, namely S_θ. Tab. 6.1 gives an overview of these two approaches. This approach is not meant to represent accurately a given

	S_r	S_θ	S_z
Poiseuille	0	0	Constant
Poiseuille SF	0	Constant	Constant

Table 6.1: Source terms for non-swirled and swirled periodic pipe test cases.

experiment, as swirl is not known with precision in these. Instead, it offers a swirled flow that is uniquely defined by S_z and S_θ, that is to say by the Reynolds Re and swirl Sw numbers and which satisfies the Navier-Stokes equations. These constant value source terms are used in the momentum equations and bring the flow to a steady state. This flow is proposed as a good prototype to investigate FPAVA because it is generic, depends only on Re and Sw and fully satisfies the NS equations.

In order to characterize the Poiseuille SF, the relation between the imposed values S_z, S_θ and the non dimensional numbers Re, Sw must be found. Solving Eq. (6.8) with $\dfrac{\partial P}{\partial z} = 0$ (because the flow is periodic) is straightforward, and yields a Poiseuille flow :

$$v_z(r) = \frac{S_z R^2}{4\mu} \left(1 - \left(\frac{r}{R} \right)^2 \right) \tag{6.9}$$

which is independant of S_θ. Note that because of the axisymmetric and axiperiodic assumptions, the axial v_z and azimuthal v_θ velocities are decoupled: v_z behaves as if there were no swirled motion, and does not exhibit a minimum value on the axis. Real swirled flows however show axial decay, and coupling between the azimuthal,

radial and axial velocities, which can lead to the v_z profile being different from the Poiseuille solution. To obtain v_θ, Eq. (6.7) can be cast in the form:

$$x^2y'' + xy' - y = -ax^2$$

The homogeneous equation has two simple non-proportional solutions, namely x and $1/x$. A particular solution can be found in the form bx^n, yielding ${}^{ax^2}/_3$. Summing these yields the solution of the form :

$$y(x) = C_1x + \frac{C_2}{x} - \frac{a}{3}x^2$$

Applying boundary conditions, namely zero azimuthal velocity at the axis and the wall, yields values for C_1, C_2 :

$$C_1 = \frac{S_\theta R}{3\mu} \qquad\qquad C_2 = 0$$

Finally, the azimuthal velocity can be exhibited :

$$v_\theta(r) = \frac{S_\theta R^2}{3\mu}\frac{r}{R}\left(1 - \frac{r}{R}\right) \tag{6.10}$$

Combining the definitions of Re from Eq. (6.4) and Sw from Eq.(6.3) with Eqs. (6.9) and (6.10) yields :

$$Re = \frac{\rho S_z R^3}{4\mu^2} \tag{6.11}$$

$$Sw = \frac{22}{105}\frac{S_\theta}{S_z} \tag{6.12}$$

Or equivalently, v_z and v_θ can be recast without source terms :

$$v_z(r) = \frac{\nu Re}{R}\left(1 - \left(\frac{r}{R}\right)^2\right) \tag{6.13}$$

$$v_\theta(r) = \frac{70}{11}\frac{\nu Re}{R}Sw\frac{r}{R}\left(1 - \frac{r}{R}\right) \tag{6.14}$$

yielding the maximum values expected for v_z and v_θ :

$$v_z^{max} = \frac{\nu Re}{R} \qquad\qquad v_\theta^{max} = \frac{35}{22}Sw v_z^{max}$$

Eq. (6.13) and (6.14) are a generalization of the Poiseuille unswirled result. They give the reduced axial $\frac{Rv_z}{\nu}$ and azimuthal $\frac{Rv_\theta}{\nu}$ velocities of a periodic swirled flow, only as a function of its axial Reynolds number Re and its swirl number Sw[1]. Tab. 6.2 summarizes the characteristics of the Poiseuille SF.

In order to validate this development, a numerical experiment is performed to compare a DNS with AVBP to the results of Tab. 6.2. A "pancake" periodic domain

[1]To the authors knowledge, this result has not been published before

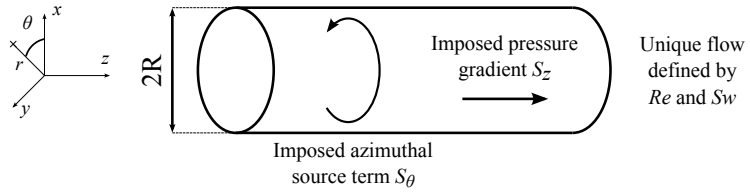

Velocity profile	Link between variables	Max speeds
$v_z(r) = \frac{\nu Re}{R}\left(1 - \left(\frac{r}{R}\right)^2\right)$	$Re = \frac{\rho S_z R^3}{4\mu^2}$	$v_z^{max} = \frac{\nu Re}{R}$
$v_\theta(r) = \frac{70}{11}\frac{\nu Re}{R} Sw \frac{r}{R}\left(1 - \frac{r}{R}\right)$	$Sw = \frac{22}{105}\frac{S_\theta}{S_z}$	$v_\theta^{max} = \frac{35}{22} Sw v_z^{max}$

Table 6.2: Summary of the characteristics of the Poiseuille SF.

is used, with fluid at rest initially. At $t = 0$, constant S_z and S_θ source terms are imposed, computed according to Eqs. (6.11) and (6.12). Once the kinetic energy in the domain is stabilized, the axial and radial velocity profiles are extracted. Fig. 6.5 shows the domain once the flow is established. Fig. 6.6 shows both profiles versus the analytical values of Eqs. (6.9) and (6.10). Tab. 6.3 resumes the target and

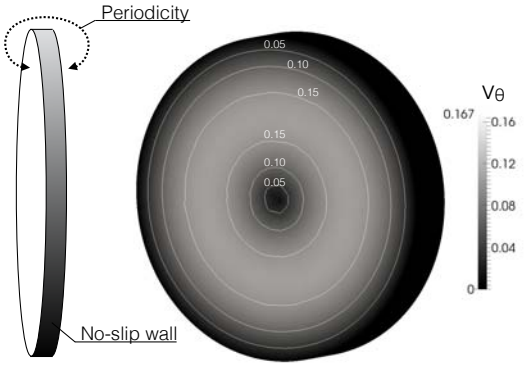

Figure 6.5: View of the pancake domain for Poiseuille SF tests, coloured by azimuthal velocity, after 20 seconds of physical time.

achieved integral values for this test case. It shows that the short theory presented

	Re	*Sw*	S_θ	S_z
Target	100.0	1.0	0.0338	0.161
LES	99.1	0.990	0.0338	0.161

Table 6.3: Target values and actual measurements in the LES converged solution for the pancake flow.

in this section is correct. Note that simulation times to obtain convergence are long compared to what is customary in the field of LES: several seconds here versus milliseconds more often. This is because imposing source terms and waiting for the flow to establish is slow, as the source term acts as a spring with small rate. In

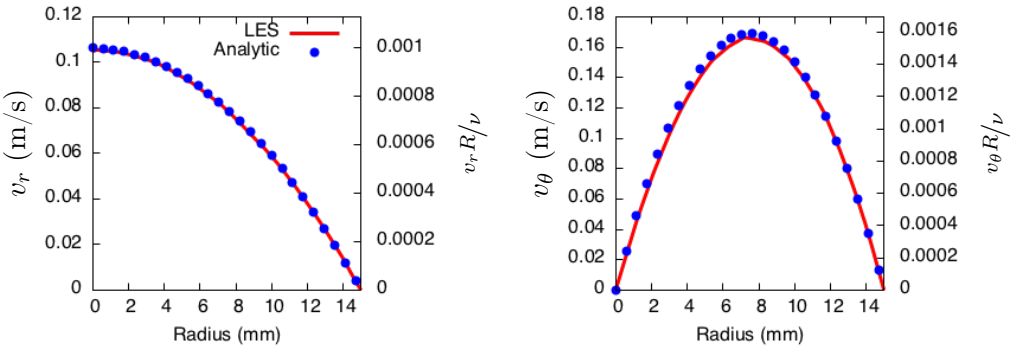

(a) **(b)**

Figure 6.6: (a) Axial and (b) radial velocity profiles for $Re = 100$ and $Sw = 1.0$ in the pancake test case. Solid lines: LES profiles once the flow is converged. Markers: analytical profiles from Eqs. (6.9) and (6.10).

non-swirled ducts where the relation between source term and Reynolds number has been validated, this can be accelerated by relaxing the source term around the target Reynolds number, as explained by Cabrit (2009). Here, the objective is to validate the theory, hence no Swirl number is imposed *via* a relaxation in order not to alter the results. The very long time span of these simulations is instead addressed with a "cryo" technique available in AVBP, where the flow pressure and temperature are simultaneously decreased. This lowers the sound speed, hence increases the time step. The Mach number is monitored in order not to exceed 0.1, thus guaranteeing that compressibility effects stay negligible and do not affect significantly the final results.

6.3.2 Using the Poiseuille SF as a test case for FPAVA

According to the previous development, a periodic non-reacting swirled pipe uniquely defined by its Reynolds (Re) and Swirl (Sw) is now available. This can be used to derive a precisely defined test case for FPAVA validation. The literature on FPAVA suggests that this phenomenon depends mostly on the density difference between cold and hot gases, and to much lesser extent on the flame speed. Domingo *et al.* (2007) showed that this is especially true during the first stages of FPAVA. As a result, the test case defined here is done in a non reactive context. The presence of cold (dense) and hot (light) gases will be used to simulate fresh and burnt gases. This hypothesis might of course lead to a slight under-estimation of the flame speed. However it will also offer a simplified access to density ratio investigations, and eliminate many interrogations such as the effect of turbulence on flame speed or the impact of the Lewis number.

The test case used here is a cylindrical tube of radius $R = 15\,\text{mm}$ and of length $L = 60\,\text{mm}$. The methodology is presented in Fig. 6.7. First, the domain is filled with cold gases (T=300 K) and constant source terms are applied as done for the SP flow, using Eq. (6.13) and (6.14) to impose the initial velocity field. A slab of

burnt gases (T=2200 K) surrounded by the cold gases is then deposited by simply replacing the density in the middle section. The configuration is axisymmetrical.

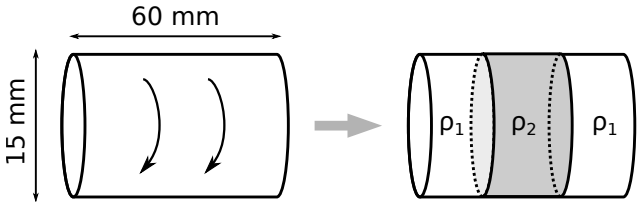

Figure 6.7: Initialization strategy for the FPAVA test case. A cold field at $T = 300\,\mathrm{K}$ of density ρ_1 is put in rotation with a constant azimuthal source term (SP flow). Then, the middle third of the domain is modified: pressure is kept constant, but temperature is set to $T = 2200\,\mathrm{K}$, inducing a decrease of density according to the equation of state to ρ_2. The right-hand side field is the initial field for the FPAVA test case.

The objective is to demonstrate how the hot gases will intrude into the fresh ones, measure their invasion speed and compare it to the models of Fig. 6.3. At the initial instant, the pressure gradient everywhere is radially distributed. The density change induced by the heating of the central portion induces an axial density gradient at the flame, hence these two gradients are not aligned and the baroclinic torque vorticity source term of Eq. (6.2) is expected to induce spreading of the hot gases along the rotation axis.

A reference Reynolds number of $Re = 1000$ is used, and several azimuthal source terms S_θ are computed to achieve various Swirl numbers Sw. Tab. 6.4 shows one value of source term and matching swirl obtained. As shown in this table, a simple

	Re	Sw	S_θ	S_z
Target setup	1000	1.0	1.074	0.338
Actual setup	0	NA	1.074	0

Table 6.4: Target and actual source terms used in the test case for FPAVA in a SP flow.

version of the general result (6.13) and (6.14) can be used: the axial Reynolds number is set to 0 which means that there is no axial velocity. In this case, Sw becomes infinite. This ensures that the front speed can be precisely estimated in the reference frame of the tube. Otherwise, the front speed would be the speed measured in the fixed reference, minus some characteristic speed of the incoming fluid that would be difficult to estimate.

The reader should note that this is still very close to the SF experiment, and different in nature from the SBR case. The tube here does not rotate, and the flow speed at the wall is zero. The azimuthal velocity profile matches that of a swirled case with constant azimuthal source term, and the axial velocity is 0.

Fig. 6.8 presents the threshold of temperature above 1000 K obtained numerically after 5 ms. The natural axial propagation of the hot zone along the vortex axis is

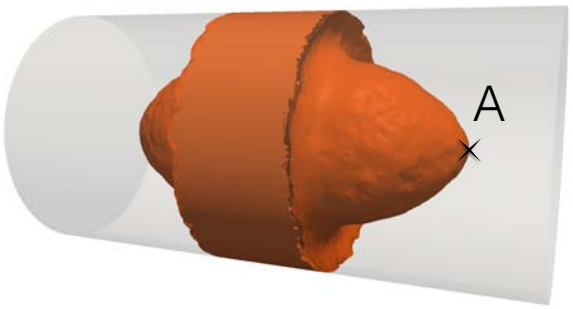

Figure 6.8: Periodic cylindrical domain for $Sw = 0.5$. Threshold of $T > 1000\,\mathrm{K}$ after 5 ms of run time. Point A represents the tip of the isosurface on the axis.

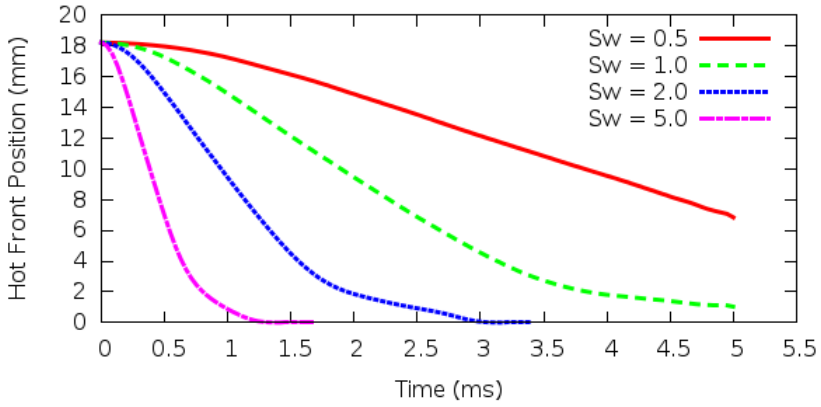

Figure 6.9: Position of 1000 K isosurface on the axis versus time, for four values of swirl number Sw. The behavior is autosimilar: after a short acceleration phase, the velocity stabilizes until the end of the domain is reached.

clearly visible and the fastest point is found on the tube axis (point A). Even though the flame speed is zero (no combustion) and the initial axial velocity is are also zero, the flames are swallowed at high speed along the vortex axis, leading to an apparent "flame speed" while there is actually no true propagation here (no combustion). The tip of this threshold, noted A, can be tracked in time to obtain the maximum flame velocity $v_A = v_f$. Fig. 6.9 shows the position of point A (flame tip) versus time. Results of flame speeds compared to several models are given in Fig. 6.10.

The sensitivity to density ratio has also been investigated numerically (Hasegawa *et al.*, 1996) and experimentally (Hasegawa *et al.*, 2002), but for a free vortex configuration. It showed a linear increase of the velocity ratio v_f/v_θ^{max} versus the density ratio $\rho_u/\rho_b - 1$. This correlation is investigated here, as shown in Fig. 6.11 but with a limited agreement.

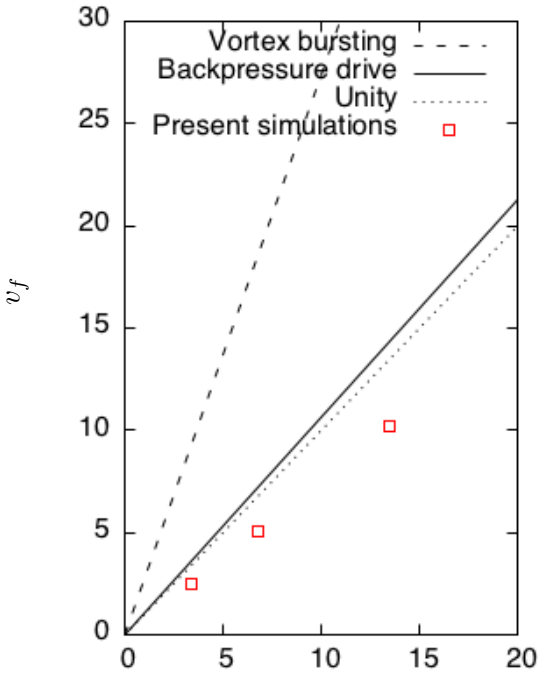

Figure 6.10: Flame speed versus maximum tangential velocity

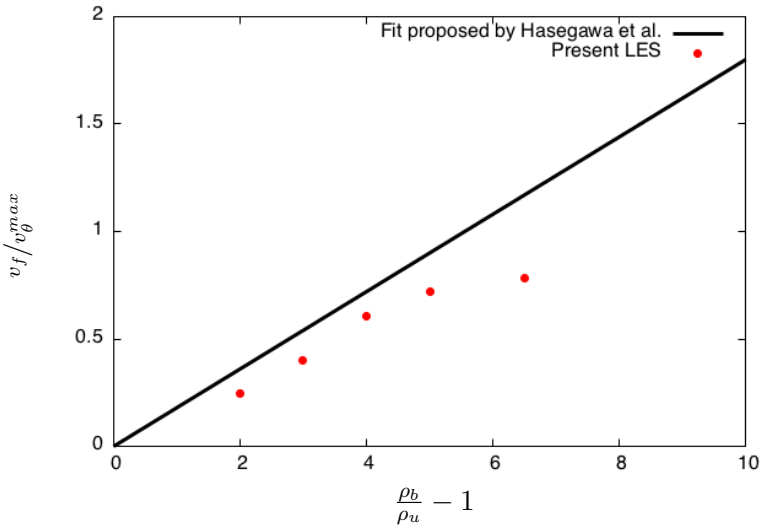

Figure 6.11: Dependency of velocity ratio versus density ratio in the LES of confined swirl, compared to the fit proposed by Hasegawa *et al.* (2002) for a free vortex.

6.3.3 Conclusions for FPAVA simulation

In this section, a toy model has been built to study flame propagation in a vortex: the Poiseuille SF is a generalization of the Poiseuille flow to cases which are swirled. A fully analytical solution for the velocity field has been obtained and validated in the LES. This analytical solution has then been used to initialize a simulation of a density front in a swirled flow. The latter is performed without combustion and used to measure the velocity of the front between fresh and burnt gases. This velocity is called a flame speed but it is obviously an absolute flame speed using the classification of Poinsot & Veynante (2011) where the front is convected by the flow but not propagating (since the reaction rate is zero). The first outcome of this section is to confirm that this speed which will allow flashback in swirled burners is not related at all to combustion and cannot be explained by arguments linked to chemistry. It is the combination of the density gradient and the swirl which creates a baroclinic torque and displaces the flame front. This explains why this speed scales like the azimuthal velocity v_θ^{max} and not like the flame speed.

The linear behavior of flames speed versus v_θ^{max} described in the literature is reproduced. Slight underestimations of flame speed are compared to experimental measurements are consistent with the absence of reaction, which should enhance the flame speed slightly. In the light of this test case, for the rest of this manuscript, the LES is expected to provide reliable FPAVA speeds of this mechanism if it appears in the EM2C combustor (and it will, as shown in Part. III).

Part II

Tools and methodologies

Table of Contents

7 Numerical methods **123**

7.1 Introduction . . . 123

7.2 Numerical resolution strategies for the Navier-Stokes equations . . . 125

7.3 The AVBP LES solver . . . 127

7.3.1 Boundary conditions for compressible LES . . . 128

7.3.2 Sub-grid scale turbulence modeling . . . 129

7.4 The AVSP Helmholtz solver . . . 134

7.5 CHORUS methodology for wave extraction and combustion noise prediction . . . 135

8 Numerical approaches for nozzles and choked flows **137**

8.1 Introduction . . . 137

8.2 LES of chambers with nozzles . . . 137

8.2.1 Numerical setup for choked nozzle LES . . . 138

8.2.2 Practical LES of a choked nozzle test case . . . 142

8.3 Nozzle impedances for chamber outlets . . . 150

8.3.1 The “wall” limit . . . 150

8.3.2 The “compact” limit . . . 150

8.3.3 Non-compact analytical formulation . . . 151

Chapter 7

Numerical methods

The numerical study lead in this Ph.D. rests on two different numerical approaches to solving fluid flow. The first, called large eddy simulation and commonly referred to as LES is an attempt to solve the complete set of either Euler or Navier-Stokes equations for fluid mass, momentum and energy conservation. This is the most costly method, but also the most complete one which attempts to integrate as many physical phenomena as possible. The matching numerical methods used in this study are detailed in Sec. 7.3. The subject at hand here however requires sometimes broad ranges of acoustic investigations on the setup. While this information is included in the complete Navier-Stokes equations solved by the LES solver, the high cost of such simulations renders it impractical at best. A simplified and much less costly approach is to consider only zero mean flow acoustic propagation in the domain, and solve for acoustic modes using a Helmholtz equation solver. This is done with the AVSP code here, as described in Sec. 7.4. Finally, the study of combustion noise produced and propagated through a nozzle is described by numerous analytical theories (see Chap. 5). The methodology of wave evaluation and combustion noise assessment is described in Sec. 7.5.

7.1 Introduction

The Navier-Stokes equations Eq. (2.33) are notoriously hard to solve. While many specific cases leading to simplifications of the set of equations yield exact descriptions, the analytical solution to the general equations is a mathematical enigma. Among the 7 famous "millennium problems" of the Clay Mathematics Institute, no claim has been made to this date of the $ 1 million prize for the Navier-Stokes problem [1]. This challenge is to bring proof to any one of the following assertions:

1. Existence and smoothness of Navier-Stokes solutions on $\mathbb{R}$.
2. Existence and smoothness of Navier–Stokes solutions on $\mathbb{R}/\mathbb{Z}^3$.
3. Breakdown of Navier-Stokes solutions on $\mathbb{R}$.
4. Breakdown of Navier-Stokes solutions on $\mathbb{R}/\mathbb{Z}^3$.

The mere existence and properties of this general solution are questioned. However, the physicist is not interested in the existence of the solution, but rather in the field quantities themselves. The velocity field $\boldsymbol{U}(\boldsymbol{x}, t)$ for example is three-dimensional

[1] To get your $ 1 million, follow this link: http://www.claymath.org/millenium-problems/navier-stokes-equation

and varies with time. Luckily, the range of scales of fluid motion is not infinite. In turbulent problems, the velocity field is random, and the largest scales of motion l_0 are of the order of the system size $\mathcal{L}$. They are generally anisotropic and specific to the system geometry. Richardson (1922) suggested that kinetic energy entered turbulent motion at these scales, and that inviscid processes then transfer this energy to smaller scales, and motion becomes isotropic. The smaller the scales of motion become, the more they are subject to viscosity, and dissipation of the energy occurs. At one point, the viscosity becomes so strong compared to the flow inertia that smaller motion is no longer possible. This sequence is referred to as the *energy cascade* (Fig. 7.1). Kolmogorov (1941) quantified this description, introducing the

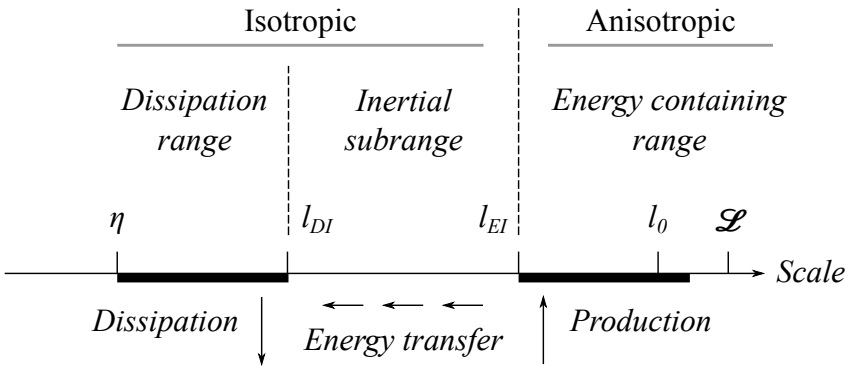

Figure 7.1: Schematic representation of the turbulent energy cascade, versus motion scales. From (Pope, 2000, chap. 6), who notes l_{DI} the demarcation line between Dissipation (D) and Inertial (I) ranges, and l_EI the one between Energy (E) and Inertial (I) ranges.

smallest dissipation scale η, and showed that l_0 and η were related by the Reynolds number Re:

$$\frac{l_0}{\eta} = Re^{3/4} \tag{7.1}$$

According to Pope (2000, chap. 6), the Navier-Stokes equations for isotropic turbulence yield good physical understanding when examined in wavenumber (or Fourier) space. First, the velocity field can be split using the *Reynolds decomposition* into mean and fluctuating part:

$$\boldsymbol{U}(\boldsymbol{x},t) = \left\langle \boldsymbol{U}(\boldsymbol{x},t) \right\rangle + \boldsymbol{u}(\boldsymbol{x},t) \tag{7.2}$$

where $< \cdot >$ represents the *ensemble average* of the velocity field, *i.e.* the average over an infinite (or sufficiently high) number of independent realizations of the flow. $\boldsymbol{u}(\boldsymbol{x},t)$ can then be replaced by its counterpart $\hat{\boldsymbol{u}}(\boldsymbol{\kappa},t)$ called the Fourier transform of $\boldsymbol{u}(\boldsymbol{x},t)$, and defined as:

$$\boldsymbol{u}(\boldsymbol{x},t) = \sum_{\boldsymbol{\kappa}} e^{i\boldsymbol{\kappa}\cdot\boldsymbol{x}} \hat{\boldsymbol{u}}(\boldsymbol{\kappa},t) \tag{7.3}$$

where $\boldsymbol{\kappa}$ is the *wavenumber vector*, of magnitude κ.

Pope (2000, chap. 9) explains that so-called "pseudo-spectral" methods, which solve the equations of motion in wavenumber space, are popular to represent the velocity field of isotropic turbulence. These are referred to as "Direct Numerical Simulations" (DNS) because the objective is to obtain all the scales of fluid motion by directly solving the Navier-Stokes equations. In order to represent all scales of motion, *i.e.* ranging between η and l_0, the domain must be big enough to capture the wide scales, and $\boldsymbol{\kappa}_{\max}$ must be high enough to capture the highest order modes (smallest size) of $\hat{\boldsymbol{u}}(\boldsymbol{\kappa}, t)$. Using these two critera, the number of modes needed in each direction to represent all fluid motions can be determined. It is noted N, and the total number of modes is therefore N^3. Because the distance between these two scales increases with Re (Eq. (7.1)), N scales with Re. The same author shows that for high enough Reynolds number, N and N^3 scale as:

$$N \sim 1.6Re^{3/4} \qquad \text{hence} \qquad N^3 \sim 4.4Re^{9/4} \tag{7.4}$$

and that the number of time-steps M needed to obtain satisfactory statistical convergence scales as:

$$M \sim \frac{120}{\pi} Re^{3/4} \tag{7.5}$$

The total cost of such a simulation scales with the number of mode-steps, *i.e.* the number of time steps M times the total number of grid points N^3:

$$N^3 M \sim 160Re^3 \tag{7.6}$$

The extreme steepness of this scaling explains why DNS, even though it is very accurate and straightforward, will not catch up with realistic problem sizes in the near or intermediate future. To illustrate this, a $Re = 1000$ DNS requires approximately 160 billion mode-steps. Suppose that each mode-step necessitates 10 000 floating-point operations. On a 12-core Intel Xeon E5, one of the fastest processors available at this date, this DNS requires approximately 1 hour of computing time (supposing perfect scaling of the parallelization). A $Re = 10000$ DNS would then require 41 days of non-stop computation on this same computer, and a small-sized combustion chamber with $Re \approx 100000$ would require 114 years. In bigger systems such as land gas turbines however, Re frequently exceeds 1 000 000, making DNS out of reach even in long term projections for computing power increase.

7.2 Numerical resolution strategies for the Navier-Stokes equations

As explained in the previous section, complete numerical resolution of the Navier-Stokes equations is possible, but mostly out of reach for realistic problems today. For many problems however, the quantities of interest are limited to the mean, minimum, maximum and root-mean-square of the fields. Many numerical approaches have

been derived to take advantage of this by offering good approximations of mean and fluctuating parameters, but without solving the complete flow motion field.

Two major alternatives to DNS are presented here. The first, known as Reynolds Averaged Navier Stokes or RANS, offers to solve only for time-independent statistics. The second, called Large Eddy Simulation or LES, is a hybrid approach where part of the motion scales are modeled, and part are solved and time-resolved.

Reynolds Averaged Navier Stokes approaches are based on the ensemble averaging used for the Reynolds decomposition of Eq. (7.2). The complete Navier-Stokes equations can be averaged in the same way. The substantial derivative and its mean write (Pope, 2000, chap. 4):

$$\frac{DU_j}{Dt} = \frac{\partial U_j}{\partial t} + \frac{\partial U_i U_j}{\partial x_i} \tag{7.7}$$

$$\left\langle \frac{DU_j}{Dt} \right\rangle = \frac{\partial \langle U_j \rangle}{\partial t} + \langle U_i \rangle \frac{\partial \langle U_j \rangle}{\partial x_i} + \frac{\partial \langle u_i u_j \rangle}{\partial x_i} \tag{7.8}$$

where the mean velocity field $\langle U_j \rangle$ appears, as well as the velocity covariances $\langle u_i u_j \rangle$, known as the *Reynolds stresses*. These include all velocity fluctuations, from large scale anisotropic eddies to the smallest dissipative eddies at the Kolmogorov scale η. In order to obtain closure for the RANS equations, this term must be modeled. Boussinesq (1877) suggested that for Newtonian fluids, this term behaved analogously to an added viscosity term for the mean flow, yielding the *turbulent-viscosity hypothesis*. Because all scales of fluctuating velocity are described by this term, including small scale isotropic and large scale anisotropic eddies, constructing a general model which performs well in all flows is a very difficult task. Among the numerous models which have been proposed over the past half century, some of the most popular have been:

- the mixing-length model proposed by Smagorinsky (1963), an algebraic model computed at each point of the flow simply using the mean velocity quantities;
- the one-equation model proposed by Kolmogorov (1942), where a transport equation for the turbulent kinetic energy k is used, or the popular Spalart & Watmuff (1993) model which offers a good performance to cost ratio.
- the two-equations models, such as the $k - \varepsilon$ model of Jones & Launder (1972) and its popular variants like realizable $k - \varepsilon$, or the $k - \omega$ model of Wilcox *et al.* (1998).

Large Eddy Simulation is a different approach. Pope (2000, chap. 9) shows that, in terms of energy, the representation of Fig. 7.1 is slightly misleading: for a well resolved DNS of homogeneous isotropic turbulence at sufficiently high Re, 99.98 % of the computed modes are in the dissipative range, and only 0.016 % are in the energy containing and inertial ranges. Based on this observation, the LES approach suggests to resolve only the energy containing and part of the inertial range. To do this, small scale fluctuations must be filtered out, and modeled. Because only

isotropic ranges are modeled, it is much easier to derive good models for these small scales.

In order to filter the fluctuation by sizes, the scalar quantities of interest f are convolved with a filter F_Δ linked to the cutoff size Δ, yielding the filtered quantity $\bar{f}$:

$$\bar{f}(\boldsymbol{x}) = \int f(\boldsymbol{x}')F(\boldsymbol{x}-\boldsymbol{x}')\,\mathrm{d}\boldsymbol{x}' \tag{7.9}$$

For LES, the filter F can be a cutoff filter in spectral space, a Gaussian filter, or a more elaborate formulation. For variable density approaches, the Favre filtering is preferred (Poinsot & Veynante, 2011):

$$\bar{\rho}\tilde{f}(\boldsymbol{x}) = \int \rho f(\boldsymbol{x}')F(\boldsymbol{x}-\boldsymbol{x}')\,\mathrm{d}\boldsymbol{x}' \tag{7.10}$$

which is related to the basic filtering operation $\bar{\cdot}$ by $\tilde{f} = \overline{\rho f}/\bar{\rho}$. Favre filtering of the multi-species Navier-Stokes equations (Eq. (2.33)) yields:

$$\frac{\partial \overline{\rho}\widetilde{u}_j}{\partial t} + \frac{\partial \overline{\rho}\widetilde{u}_i\widetilde{u}_j}{\partial x_i} + \frac{\partial \overline{P\delta_{ij}}}{\partial x_i} = \frac{\partial}{\partial x_i}\left[\overline{\tau}_{ij} - \overline{\rho}(\widetilde{u_i u_j} - \widetilde{u}_i\widetilde{u}_j)\right] \quad \text{for } j = 1,3 \tag{7.11a}$$

$$\frac{\partial \overline{\rho}\widetilde{Y}_k}{\partial t} + \frac{\partial \overline{\rho}\widetilde{u}_i\widetilde{Y}_k}{\partial x_i} = \frac{\partial}{\partial x_i}\left[\overline{J}_{i,k} - \overline{\rho}(\widetilde{u_i Y_k} - \widetilde{u}_i\widetilde{Y}_k)\right] + \overline{\dot{\omega}}_k \quad \text{for } k = 1,N \tag{7.11b}$$

$$\frac{\partial \overline{\rho}\widetilde{E}}{\partial t} + \frac{\partial \overline{\rho}\widetilde{u}_i\widetilde{E}}{\partial x_i} + \overline{\frac{\partial u_i P\delta_{ij}}{\partial x_i}} = \frac{\partial}{\partial x_i}\left[\overline{q_i} - \overline{\rho}(\widetilde{u_i E} - \widetilde{u}_i\widetilde{E})\right] + \overline{\tau_{ij}\frac{\partial u_i}{\partial x_j}} + \overline{\dot{\omega}}_T + \dot{\mathcal{Q}}_{sp} \tag{7.11c}$$

where the velocity covariance term $\overline{\rho}(\widetilde{u_i u_j}$ is the "turbulent viscosity" due to the spatially filtered scales. These are isotropic, hence algebraic models are generally used. They are referred to most often as *sub-grid scale* fluctuations, because in numerical approaches the filter size Δ is generally of the order of the local grid size. More details about these models are available in Sec. 7.3.2.

These three main approaches for solving the Navier-Stokes equations are represented schematically in Fig. 7.2. In the DNS approach, all scales are resolved. In the LES approach, only the large-scale fluctuations are resolved, and the rest are modeled. In RANS, all fluctuations are modeled.

7.3 The AVBP LES solver

In the context of this study, the following elements must be taken into account before choosing a numerical solver:

- combustion necessitates a multi-species and variable density formulation;
- high subsonic and supersonic flows inside choked nozzles make a compressible formulation compulsory, as does the resolution of acoustics;
- acoustics, be it for noise or instabilities, are intrinsically unsteady phenomena, and an unsteady formulation must be used here;

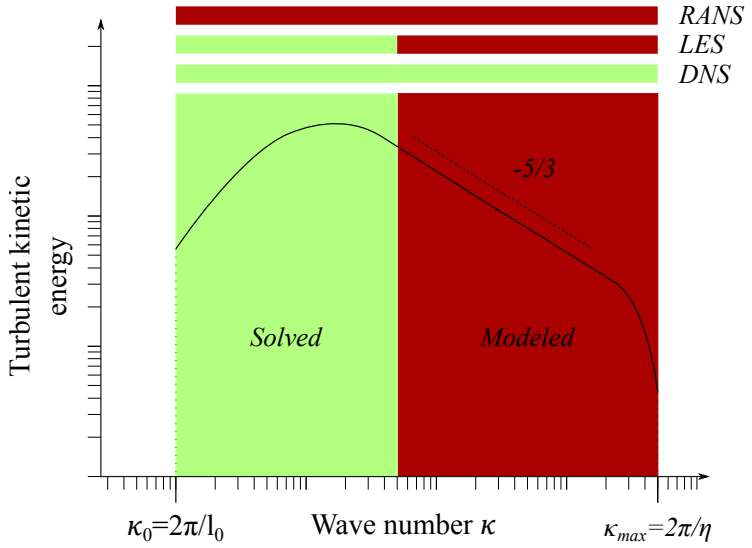

Figure 7.2: Turbulent kinetic energy spectra versus wave number κ. RANS approach: model all scales. LES approach: solve energy containing anisotropic scales, model isotropic inertial and dissipative scales. DNS approach: solve all motion scales.

- acoustics are of interest, hence time-stepping will be done according to acoustic constraints. The speed advantage of an implicit solver over an explicit one might be small in such a situation;
- while not on the same complexity level as an industrial burner, the CESAM-HP test-bench has a rather complex geometry, noticeably in the injection section. An unstructured formulation would be a good argument to simplify the meshing process.

For these reasons, a RANS solver was not appropriate for this study. The choice was set on the AVBP solver, an unstructured, explicit, compressible LES solver developed at CERFACS and IFP Énergies nouvelles.

7.3.1 Boundary conditions for compressible LES

The convected vortex test case (De Oliviera, 2015) is a typical example of what LES codes must represent accurately: in a periodic box with mean laminar flow, an isentropic vortex is imposed at the center. It returns to the initial position every convection time, and can be compared to the initial value to estimate dissipation and dispersion precisely. This test case has been run on several CFD codes, and the results are available online [2].

To achieve good results in these tests, compressible high-fidelity LES uses highly accurate numerical schemes with very low dissipation and dispersion. A consequence of this trend is that when perturbations arise inside an unsteady fluid domain computed with LES, the matching energy is inefficiently dissipated. In many turbulent cases, the unsteady source is strong, and this can lead to a buildup of fluctuation levels

[2] see http://elearning.cerfacs.fr/numerical/benchmarks/vortex2d/index.php

and eventually cause the code to crash. The most physical solution to this problem is to mimic what occurs in the real configurations: let the unsteady fluctuations exit through the boundaries of the computational domain. To this end, non-reflecting boundary conditions must be designed.

Thompson (1987) formalized exact non-reflecting boundary conditions for 1 and 2D simulations of the Euler equations. The strategy was based on the characteristic decomposition of the flow at the boundary, as described in Chap. 3. Poinsot *et al.* (1992) extended this to the Navier-Stokes equations, resulting in the Navier-Stokes Characteristic Boundary Conditions approach, or NSCBC. This extension was made possible by formalism called LODI, for Locally One Dimensional Inviscid. These are implemented in AVBP and used in this Ph.D for all inlet and outlet boundaries. This enables to impose target values and simultaneously sending the smallest possible perturbations back inside the domain, using a relaxed ingoing wave computed to still ensure the mean targets. For outlets, the corresponding condition is called `OUTLET_RELAX_P` in AVBP. This strategy also offers the possibility to impose the ingoing wave, in order to force the computation. This is done for example in the **OPEN-FO** simulations described in Chap. 10, using a condition called `OUTLET_RELAX_P_PULSE`.

The LODI formalism can be restrictive in a turbulent computation, where the flow is not necessarily locally one dimensional, either because the boundary is not normal to the mean flow, or because the turbulent fluctuations significantly deviate the flow from its mean direction. Yoo *et al.* (2005) pointed this problem out and offered a solution based on corrections using the transverse fluctuations. Yoo & Im (2007) generalized this framework further by including viscous and reaction effects. The latter has not yet been included in AVBP, but transverse corrections have been implemented and tested in AVBP (Granet *et al.*, 2010). The matching condition is called `OUTLET_RELAX_P_3D` in AVBP.

7.3.2 Sub-grid scale turbulence modeling

Recall the velocity covariance term from Eq. (7.11a), which needs closure. The Boussinesq approximation for Newtonian fluids writes:

$$\widetilde{\bar{\rho} u_i'' u_j''} = -\mu_t \left(\frac{\partial \tilde{u}_i}{\partial x_j} + \frac{\partial \tilde{u}_j}{\partial x_i} - \frac{2}{3}\delta_{ij} \frac{\partial \tilde{u}_k}{\partial x_k} \right) + \frac{2}{3}\bar{\rho}_k \tag{7.12}$$

where $\mu_t = \rho \nu_t$ is the *turbulent viscosity*. This turbulent viscosity represents the sub-grid scale (SGS) dissipation of kinetic energy by unresolved eddies. Many models have been proposed and used for this closure. Deciding what the best model is depends on the case at hand, and can sometimes only be done after running small computations with each model and assessing the SGS model behavior.

7.3.2.1 Behavior of models proposed in the literature

Smagorinsky (1963) proposed a simplified model for ν_t:

$$\nu_t = (C_S \Delta)^2 |\bar{S}| = (C_S \Delta)^2 \sqrt{2 \bar{S_{ij}} \bar{S_{ij}}} \tag{7.13}$$

where Δ is a characteristic local mesh size and C_S is the model constant. This model has been extensively used and tested in LES in the last half-century. It relates the turbulent viscosity to the local strain rate, *i.e.* the smallest resolved scales of motion. DNS results of Wray & Hunt (1989) have suggested that improvements were needed to accurately describe dissipation in isotropic turbulence, and Métais & Lesieur (1992) proposed a more elaborate model based on the second order velocity structure function F_2.

Moreover, the in rate is evaluated in all directions, which means that at a wall it is not zero. This leads to overestimation of the dissipation at the wall, since the actual sub-grid scale motions are zero at the wall with the correct y^+ degeneration. Several methodologies have been proposed to handle this wall behavior. Various functions have been applied to the Smagorinsky constant C_S to account for this wall degeneration (Van Driest (1956), Germano *et al.* (1991)). Other approaches aimed at modifying F_2 instead of the model constant (Ducros *et al.* (1996)).

A more recent approach called the Wall-Adapting Local Eddy-viscosity (WALE) has been proposed by Nicoud & Ducros (1999). It is easy to compute, includes both strain and rotation rates, and is generic because it naturally goes to zero at the wall. Because of these advantages, it is often considered state of the art in modern LES simulations to this date. It writes:

$$s_{ij}^d = \frac{1}{2}(\tilde{g_{ij}^2} + \tilde{g_{ji}^2}) - \frac{1}{3}\tilde{g_{kk}^2}\delta_{ij} \tag{7.14a}$$

$$\nu_t = (C_w \Delta)^2 \frac{(s_{ij}^d s_{ij}^d)^{3/2}}{(\tilde{S_{ij}}\tilde{S_{ij}})^{5/2} + (s_{ij}^d s_{ij}^d)^{5/4}} \tag{7.14b}$$

where $\tilde{g_{ij}}$ is the resolved velocity gradient tensor.

There is however yet another known issue with this model, as recently reported by Nicoud *et al.* (2011): its evaluation for ν_t does not vanish in the presence of solid rotation. In fact, the issue with the original Smagorinsky model can be formulated as the exact opposite, as it does not vanish in the presence of pure shear. The same authors propose a sum up list of properties that a "smarter" SGS model should demonstrate:

1. be defined only locally (*i.e.* based on local gradients of the resolved field) for simplicity reasons. It should also always be positive, for stability reasons;
2. decay to the wall as the third power of distance;
3. vanish in case of solid body rotation, or generally any 2 dimensional or 2 component flow;
4. vanish also for isotropic expansion or contraction (*e.g.* an acoustic monopole).

These considerations have lead to propose the so called "SIGMA" model — named after the three singular values $\sigma_1, \sigma_2, \sigma_3$ of the velocity gradient tensor g_{ij}. It meets

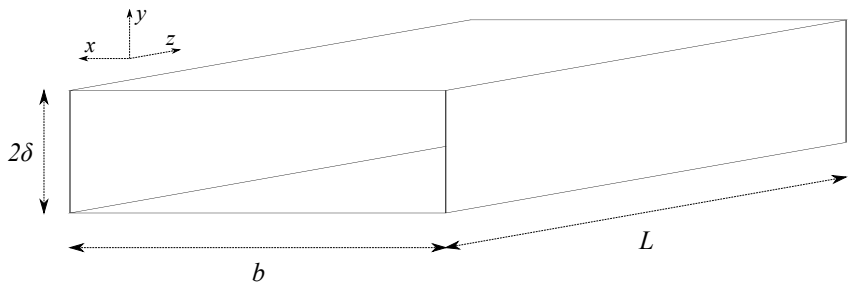

Figure 7.3: Channel for turbulent flow specificities assessment.

all 4 requirements listed above. This very recent development is not yet widespread in the CFD community, but it is readily available in AVBP.

7.3.2.2 Strategies for wall modeling

Turbulent flows in channels are an important subject in the turbulence community (Pope, 2000). A set of tools has is available to model such a flow. Consider a channel of length L in direction x, height 2δ in the y direction and of width b in direction z. Both length and width are considered large compared to the channel height: $L \gg \delta$ and $b \gg \delta$. The flow velocity is referenced on each reference direction by U, V, W matching the x, y, z directions, respectively (see Fig. 7.3). The time average of velocity is noted $\langle U \rangle$, and the bulk velocity $\bar{U}$ is defined as:

$$\bar{U} = \frac{1}{\delta} \int_0^\delta \langle U \rangle \, \mathrm{d}y \tag{7.15}$$

The Reynolds number Re based on bulk velocity is:

$$Re = \frac{2\delta \bar{U}}{\nu}$$

The *shear stress* τ is the sum of viscous and Reynolds stresses, and writes:

$$\tau(y) = \rho\nu \frac{\mathrm{d}\langle U \rangle}{\mathrm{d}y} - \rho \langle uv \rangle \tag{7.16}$$

where u, v are the fluctuating parts of U, V, respectively. The *wall shear stress* therefore writes:

$$\tau_w = \rho\nu \left(\frac{\mathrm{d}\langle U \rangle}{\mathrm{d}y} \right)_{y=0} = -\delta \frac{\mathrm{d}P}{\mathrm{d}x} \tag{7.17}$$

which is in fact only the viscous contribution to shear stress. Because of this peculiar behavior near the wall, it is useful to define *viscous scales* analogous to the channel quantities $\bar{U}, \delta, y$ but appropriate to describe the flow near the wall: *friction velocity*

u_τ, *viscous lengthscale* δ_ν and *wall units* y^+. They write:

$$u_\tau = \sqrt{\frac{\tau_w}{\rho}} \tag{7.18}$$

$$\delta_\nu = \nu\sqrt{\frac{\rho}{\tau_w}} = \frac{\nu}{u_\tau} \tag{7.19}$$

$$y^+ = \frac{y}{\delta_\nu} = \frac{u_\tau y}{\nu} \tag{7.20}$$

y^+ is an excellent indicator of the importance of viscous stresses. As shown by Kim *et al.* (1987) for two different DNS at $Re = 5600$ and 13750, viscous effects account for 100 % of shear stress at $y^+ = 0$. They then decrease and reach 50 % at $y^+ \approx 12$, and by $y^+ = 50$ they produce less than 10 % of the total stress τ.

Because of the very different behavior between the free shear flow in the channel and the viscous flow near the wall, models appropriate for do not necessarily behave well for the other. Two major approaches are found in the LES approach: wall-resolved and wall-modeled simulations.

Wall-resolved simulations where the viscous layer is sufficiently resolved by the mesh for the solver to capture all viscous effects. The nodes at the wall are treated with "no slip" conditions, *i.e.* the velocity at the node is set to 0 at each iteration. This implies that the numerical scheme is responsible for the computation of the full friction and shear at the wall. Turbulent channel theory such as Pope (2000) indicates that this can predict the correct pressure loss and velocity profile only if certain mesh refinement conditions are met ($y^+ \sim 1$).

This is the best solution from a physical standpoint, as the exact physics near walls is computed. However, in practice the refinement criterion of $y^+ \sim 1$ is extremely costly in a realistic simulation. For this reason, the mesh is often coarser than this in practice, which implies that the true physics are under-resolved at the wall.

Wall-modeled approaches, where the viscous layer near the wall is not included in the mesh, hence not determined by the numerical scheme. To do this, the first mesh node (or cell in an cell-centered code) is placed outside the viscous layer, at wall units of typically $y^+ > 50$. A dedicated model reproduces the state of the flow at the edge of the viscous layer, *i.e.* at the first off-wall node.

Of course, this approach yields much smaller meshes and generally lower computation costs than the previous. $y^+ \approx 50$ is not a very restrictive criterion for modern codes in realistic gas turbines. However, industrial geometries are complex, and have little in common with the academic channel of Fig. 7.3.

Which strategy to choose? Wall-resolved and wall-modeled approaches both have drawbacks. Solving the flow all the way to the wall is an attractive method, as it eliminates the need for a complex model, which is a potential additional

source of errors. While this can be adapted to low Reynolds number configurations, unfortunately in many industrial applications this implies a number of mesh nodes that is out of reach with current computational power.

Wall-modeling is therefore a good candidate for such systems and the subsequent under-resolved meshes. This is in fact a requirement of the method ($y^+ \geq 30$). But industrial burners not only present high Reynolds numbers: they also have complex geometries, whereas wall-models are tuned for turbulent channels, and their behavior far from these conditions is unknown. In a cell-vertex code such as AVBP, the wall-law approach uses a slipping condition at the wall to obtain the correct friction at the first off-wall node. This is an artifact that has no effect on the straight duct for which the wall-model is tuned, but that again does not sit well with complex industrial geometries and numerous sharp edges. For more details on this specific issue, see *e.g.* Cabrit (2009).

No-slip wall with under-resolved mesh: assessing the impact Because of the current limits of wall models, a no-slip wall approach is sometimes used even though the mesh is under-resolved for the Reynolds numbers at hand. From the CFD code user perspective, this comes down to using no-slip wall conditions, and not compensating for the lack of mesh resolution. While this is theoretically incorrect, it is a pragmatic choice due to the lack of solutions available. In order to accept this compromise, its impact on the simulation must be assessed. To do so, a simple analytic derivation of the effect of under-resolution in the straight duct of Fig. 7.3 is done in the following.

A mesh resolution of 10 nodes in the duct height is chosen: this is typical of the resolution that can be achieved in small passages in realistic configurations. The first off-wall node is therefore at $y_1 = \delta/5$, and again from Pope (2000) for $Re > 10^4$ this is in the log-law region and outside the viscous sublayer where the first node should be in an appropriate wall-resolved approach. In other words, the wall distance associated to this first node $y_1^+ > 50$, and the wall shear stress τ_w is not correctly estimated. The pressure drop through the duct writes:

$$-\frac{\partial p}{\partial x} = 2\frac{\rho \nu U_0}{\delta^2}$$

For an incompressible flow (a reasonable assumption in the combustion chamber area of a gas turbine), the mass flow rate conservation ensures the relationship between the mean velocity U_0 and the duct half-height δ when passing through various duct sections in the combustor:

$$\dot{m} = \rho U_0 \delta^2 = \text{constant}$$

which yields for the pressure drop:

$$-\frac{\partial p}{\partial x} = 2\frac{\nu \dot{m}}{\delta^4}$$

This implies that in wide passages (such as the combustion chamber), the pressure drop is very small and few errors are introduced. However, in small passages, the pressure drop is much more important. In an typical combustion chamber, half duct heights can vary by an order of magnitude, yielding 4 orders of magnitude in the pressure drop per unit length in the smallest ducts compared to the largest passages. Because the wall friction is poorly estimated in these small sections, errors in pressure drop estimation are expected.

In the context of the CESAM-HP simulations, the pressure drop in the system however is of no specific interest. Estimations using the previous relations yield an expected maximum pressure drop of $0.135\,\mathrm{Pa\,m^{-1}}$ in the smallest passages. However, because the pressure in the system is fixed by the nozzle dynamics, the mean pressure cannot be set with a precision of more than $1\,\%$ at best, which represents $2500\,\mathrm{Pa}$. As a result, any pressure drop estimation error due to an under-resolved mesh is of no importance in this setup. Based on this observation, the no-slip wall strategy will be used in this Ph.D, even if mesh resolution goes down to only 10 nodes in the smallest ducts of the domain.

7.4 The AVSP Helmholtz solver

A zero-Mach number 3D acoustic solver called AVSP (Nicoud *et al.*, 2007) is used to compute the eigenmodes of the cavity. Recall the variable sound speed Helmholtz equation:

$$\boldsymbol{\nabla}\left(c(\boldsymbol{x})^2\boldsymbol{\nabla}\hat{p}(\boldsymbol{x})\right)+\omega^2\hat{p}(\boldsymbol{x})=i\omega\hat{q}(\boldsymbol{x}) \tag{7.21}$$

This equation has been obtained by considering that the mean flow velocity $\bar{u}=0$, which is known as the *zero Mach number assumption*. However, no assumption has been made on the sound speed c, the density ρ, the ideal gas constant r or the compressibility factor γ. The AVSP solver therefore reads on input a field of these four variables, which can come *e.g.* from the average of an LES run. The strong difference in sound speed between the cold and burnt gases is therefore included, and this procedure is known as the "passive flame" approach.

In order to obtain the solutions to the wave equation Eq. 7.21, boundary conditions must be defined. Several conditions are available in AVSP:

1. a constant pressure condition ($\hat{p}=0$), corresponding to an atmospheric or plenum connexion if no end-correction is introduced. This constitutes a Dirichlet condition for the pressure field;
2. a constant velocity condition ($\hat{\boldsymbol{u}}\cdot\boldsymbol{n}=0$), representing a perfectly rigid wall. In practice, only the pressure field is solved for in AVSP, and such a condition is converted using the moment equation to a Neumann condition: $\boldsymbol{\nabla}\hat{p}\cdot\boldsymbol{n}=0$;
3. an impedance condition, where a table of complex impedance versus frequency is read, then imposed according to:

$$Z=\frac{\hat{p}}{\hat{\boldsymbol{u}}\cdot\boldsymbol{n}} \tag{7.22}$$

Once the problem is defined, it is discretized on an unstructured mesh, and converted into an eigenvalue problem. It is then solved numerically for eigenvalues in increasing real part order. This provides the lowest frequency modes first (the "fundamental modes"), followed by the harmonics. Typically, only the first 5 to 20 modes are solved for before interrupting the computation, as the high order modes are of high frequency in small configurations such as CESAM-HP. High frequency modes have short wavelengths, and thus induce strong gradients, which are in turn damped by viscous effects. In the case of CESAM-HP, very little activity was observed experimentally above 2000 Hz, confirming this hypothesis.

7.5 CHORUS methodology for wave extraction and combustion noise prediction

Combustion noise prediction in real gas turbines is a tedious task. The perturbations at the combustion chamber end must be correctly evaluated, then propagated through the turbine stages, with additional production and dissipation correctly captured. Finally, the noise directivity results from its propagation through the temperature and velocity gradient of the engine jet, before freely propagating in the atmosphere.

The CHORUS methodology (Duran *et al.*, 2013*b*) has been developed in order to define:

- a strategy to compute primitive quantity fluctuations, using some spatial filtering to eliminate turbulent fluctuations in unwanted directions;
- a Fourier-space strategy to estimate the acoustic, entropic and vorticity waves at the turbine entrance, accounting for convection and acoustic propagation speeds for increased fidelity;
- a propagation method through the turbine stages based on the work of Cumpsty & Marble (1977*a*);
- a dissipation function for entropy waves through the turbine stages.

In the context of this Ph.D., turbines are not considered. However, the wave extraction methodology in CHORUS can be used to assess the acoustic and entropic waves at the end of the setup. Strategies to compute nozzle transmission and reflection coefficients such as that of Marble & Candel (1977*b*), or the more recent Magnus expansion of Duran & Moreau (2013) can then be fed by this data, both for instability prediction and combustion noise evaluation purposes.

Chapter 8

Numerical approaches for nozzles and choked flows

Compressible large eddy simulation offers the possibility to explore high-subsonic or even supersonic flows. 1D theory for isentropic nozzles is a classic introduction on high Mach number fluid dynamic course, and has been reminded in Chap. 2. The numerical simulation of a realistic 2D or 3D configuration using LES can however lead to numerous issues. Setting boundary conditions in a flow where the outlet can choke is a first question. A second one is the determination of nozzle impedances for acoustic simulation. In this chapter, Sec. 8.2 describes a methodology for LES of a choked nozzle, as well as the tools developed to monitor it. For acoustic approaches based on Helmholtz solvers, a model for the nozzle impedance is discussed In Sec. 8.3.

8.1 Introduction

Very few studies address the problem of combustion LES in a chamber terminated by a nozzle. This is due to (1) the fact that it requires a compressible solver, small time steps and complex boundary conditions, and (2) the observation that most lab burners operate at low pressure, without outlet nozzle. Therefore, the difficulties associated to LES of combustion in choked chambers are rarely discussed. This is done here in Sec. 8.2, beginning with a methodology for choked nozzle LES (Sec. 8.2.1) and followed by an application on a test case (Sec. 8.2.2). The question of equivalent impedance of nozzles when it is not possible to include it in a flow solver simulation is discussed in Sec. 8.3.

8.2 LES of chambers with nozzles

While choked nozzle theory has been discussed in Chap. 4, the practical realization of a compressible LES with a choked outlet yields several challenges. This section proposes a methodology for such a computation, followed by a practical example on a test case. This offers the opportunity to demonstrate how nozzle behavior can be monitored, as well as an important caveat of the method that must be avoided.

8.2.1 Numerical setup for choked nozzle LES

Before starting a nozzle computation, several theoretical points must be discussed to explain the differences with a more classical "pressure outlet" simulation.

8.2.1.1 Replacing a pressure outlet by a choked nozzle: the problem of well-posedness

For a non-reacting Navier-Stokes solver, 5 variables must be specified at the boundary conditions for well-posedness of the problem (see Poinsot & Veynante (2011), chapter 9). A classical approach is to impose 4 variables at the inlet, namely u, v, w, T and one at the subsonic outlet, p. This approach is meaningful as long as the flow stays subsonic at the outlet, *i.e.* that the pressure information imposed at the outlet can travel upwind in the flow.

However, for a flow through a geometry restriction, *e.g.* a nozzle, if the pressure ratio is higher than the critical ratio r_C defined in Eq. 4.10, the flow becomes supersonic and may be entirely supersonic on the outlet boundary surface. In such a case, the flow travels faster than the speed of sound at the outlet, and the pressure information at the outlet is no longer transmitted to the domain. The pressure condition, however, is replaced by another condition on the Mach number : $M = 1$ at the throat (see for example Candel (1995)). As a result, Eq. 4.14 shows that the geometry of the domain imposes a unique Mach number distribution in the entire domain. This information however is redundant with the conditions at the inlet : imposing the temperature leads to a unique value of the sound speed c (Eq. 4.4), and imposing the velocities in addition leads to a unique value of the Mach number. The problem is no longer well posed, the pressure is not imposed and can drift freely. In other words, imposing inlet velocities and temperature in a choked domain for a compressible solver is ill-posed.

A solution to this problem is to modify the set of values imposed at the inlet so as not to impose the Mach number directly. For example, the following variables can be imposed at the inlet: $(\rho u, \rho v, \rho w, T)$. This leads to a well-posed problem, as it does not impose the Mach number which can then adjust to the choked outlet. The pressure in the chamber will rise until the throat flow rate corresponds to the imposed inlet flow rate. The problem therefore stays well-posed if the nozzle becomes choked and the outlet no longer imposes the pressure.

Table 8.1 assesses the different cases (sub- and supersonic) for the two inlet types. Another advantage of this alternative inlet boundary condition is the ability to impose a specific mass flow rate $\dot{m}$. In a pressure-outlet configuration, the simple control of the inlet velocity u and temperature T are enough to precisely determine the mass flow rate. In a choked setup however, the pressure in the domain is controlled by the nozzle, and therefore imposing u and T at the inlet would not guarantee the value of $\dot{m}$. Imposing ρu however adapts to any pressure fluctuations by adjusting the density and the velocity, while still achieving the target mass flow rate.

	Inlet	Outlet	Nozzle	Posedness
Classical Inlet				
Subsonic	u, v, w, T	p	$\varnothing$	Well-posed
Supersonic	u, v, w, T	$\varnothing$	M	Ill-posed
Alternative Inlet				
Subsonic	$\rho u, \rho v, \rho w, T$	p	$\varnothing$	Well-posed
Supersonic	$\rho u, \rho v, \rho w, T$	$\varnothing$	M	Well-posed

Table 8.1: Well-posedness of numerical problem depending on boundary conditions: list of variables imposed at each condition depending on the numerical setup and the state (choked or unchoked) of the flow.

8.2.1.2 Achieving convergence

The convergence of a choked nozzle simulation depends on two important choices:

- the initial solution for the domain;
- the relaxation coefficients of the partially reflecting boundary conditions when a method such as NSCBC is used.

At convergence, the flow will be supersonic at the outlet, hence no pressure wave can be injected by this condition in the domain. In AVBP, the boundary condition in this case is called `OUTLET_SUPER`, and corrects none of the characteristic waves since they are all exiting the domain. The initial state however is not necessarily choked[1]. This implies that the code has to transition from a subsonic outlet (where pressure *must* be imposed) to a supersonic one (where pressure *cannot* be imposed). Note that, in AVBP, such a behavior is normally automatically achieved when using a classical `OUTLET_RELAX_P` condition: this condition measures the velocities at each outlet point and when the flow is supersonic it imposes nothing, thereby reverting to the simple `OUTLET_SUPER` condition.

However, choosing the relaxation coefficient to avoid instabilities during the initial subsonic phase is delicate because the speeds are large. Typically a simple solution for users is to start with a chamber where the pressure is large and uniform and the flow is at rest. Then AVBP has to manage to start the flow moving, first at subsonic speeds and then reach choking when needed. This is the procedure used here. This approach however is very violent for the outlet condition. It results in the presence of the maximum static pressure for the domain on the same nodes (the outlet nodes) on which the outlet static pressure is imposed. The pressure gradient at the outlet boundary is therefore extreme for the first iterations. Hence, the choice of the relaxation coefficient of the boundary condition for the outlet is crucial:

[1] While in simple tests cases it is possible to generate an initial guess of the field analytically which is already choked, this in not the case for general problems. We are interested here in the strategy for the general case, where no choked initial field is available.

- if this coefficient is too high, for example with a fully reflecting NSCBC boundary condition (called "WAVE" in AVBP), it can cause unwanted acoustic reflections during the establishment of the flow. More importantly, since it is fully reflecting, the initial pressure gradient is interpreted as a very strong wave hitting the boundary condition. It is then reflected into the domain, and usually causes the computation to crash because of the extreme gradient imposed;

- if it is too low however, the strong gradient will cause a high pressure drift at the boundary. This can be a big problem for computations in which the nozzle is *not* supposed to be choked, since it might choke during the establishment of the flow and stay choked, even though this behavior is unexpected in a given configuration. A study lead during this Ph.D on a high subsonic nozzle ($M = 0.8$) that is not reproduced here has demonstrated these difficulties. In the present case, a pressure drift leading to nozzle choking is however not a problem.

For the case at hand, a low relaxation coefficient at the outlet is acceptable, as long as the outlet pressure does not drift upwards and prevents choking.

The role of low relaxation coefficients is to evacuate the unwanted spurious perturbations due to the system initialization. However, as has been shown in Chap. 5, a choked nozzle has a high reflection coefficient from the chamber's point of view. As a result, spurious perturbations in the nozzle are not likely to be evacuated through the outlet condition, even if the associated relaxation is low. The role of the inlet in the elimination of these perturbations is therefore critical, and the inlet relaxation must also be set to low values, so long as the mass flow rate is well imposed.

8.2.1.3 Final choice for boundary condition setup

The boundary condition setup chosen given the previous observations is summarized in Tab. 8.2. Note that the walls are chosen as slip conditions, in order to ensure that

Boundary	Condition type	Condition name in AVBP	Relaxation coefficient
Inlet	$\rho u, T$ inlet	`INLET_RELAX_RHOUN_T_Y`	50
Outlet	Pressure or supersonic outlet (automatic switch)	`OUTLET_RELAX_P`	50
Walls	Slip walls	`WALL_SLIP`	N/A

Table 8.2: Boundary conditions for choked nozzle LES, starting with a subsonic initial solution.

the effective section at the throat is as close as possible to reality. In the real setup, the walls impose no-slip conditions, but the boundary layers associated are very thin,

and the mesh used here cannot reproduce them. It is therefore a better estimation to allow velocity up to the wall than to limit the velocity in the first cell.

8.2.1.4 Monitoring the LES: the XNozzle tool

In Sec. 4.2.2, a theoretical description of the flow through a nozzle was given, and a relationship between the mass flow rate $\dot{m}$, the total pressure P_0 and temperature T_0, as well as the compressibility factor γ was given for subsonic (Eq. (4.9)) and supersonic (Eq. (4.13)) conditions:

$$\dot{m} = A_{out}\frac{P_0}{\sqrt{rT_0}}\left(\frac{P_{out}}{P_0}\right)^{1/\gamma}\sqrt{\frac{2\gamma}{\gamma-1}\left(1-\left(\frac{P_{out}}{P_0}\right)^{\frac{\gamma-1}{\gamma}}\right)} \qquad \text{if } M<1$$

$$\dot{m} = A^* P_0\sqrt{\frac{\gamma}{rT_0}}\left(\frac{2}{\gamma+1}\right)^{\frac{\gamma+1}{2(\gamma-1)}} \qquad \text{if } M\geq 1$$

where P_{out} is the outlet pressure, which determines the flow for subsonic conditions but has no influence for supersonic conditions. In a nozzle at a combustion chamber outlet, the total temperature T_0 can undergo important variations. For non-premixed or partially premixed systems, combustion is not necessarily homogeneous, and the gases can enter the nozzle at any temperature between the fresh gases inlet temperature T_f and the adiabatic temperature T_{adia}. As a result, the expected relationship between $\dot{m}$ and P_0 is in fact expected to be in between two curves computed as described above, one with T_f and the other with T_{adia}. Note that in the supersonic case, these reduce to a linear relation between $\dot{m}$ and P_0:

$$\dot{m} = P_0 * C \qquad \text{where} \qquad C \in \sqrt{\frac{\gamma}{r}}\left(\frac{2}{\gamma+1}\right)^{\frac{\gamma+1}{2(\gamma-1)}}\left[\frac{1}{\sqrt{T_{adia}}},\frac{1}{\sqrt{T_f}}\right] \tag{8.1}$$

In order to monitor this behavior, the XNozzle tool has been developed. The mass flow rate through the outlet patch is recorded versus time, along with the total pressure in the chamber using a probe located in a "quiet" region (generally near the wall). XNozzle then plots the locus of P_0 versus $\dot{m}$ during the computation, along with the two extreme theoretical curves of Eq. (8.1). Fig. 8.1 shows a typical XNozzle output. The filled square symbols indicate the point where the nozzle chokes. The curves below and above this point are therefore computed with the subsonic and supersonic flow relations, respectively. Note that XNozzle requires two sections:

- A^*, the throat area, to compute the supersonic $P_0(\dot{m})$ curve;
- A_{out}, the outlet area, to compute the subsonic curve.

moreover, as explained in detail in Sec. 4.2.2.2, the choking point is computed by solving Eq. (4.14) at the outlet for Mach number and injecting the resulting subsonic value in Eq. (4.15). This implies the need of both A^* and A_{out}.

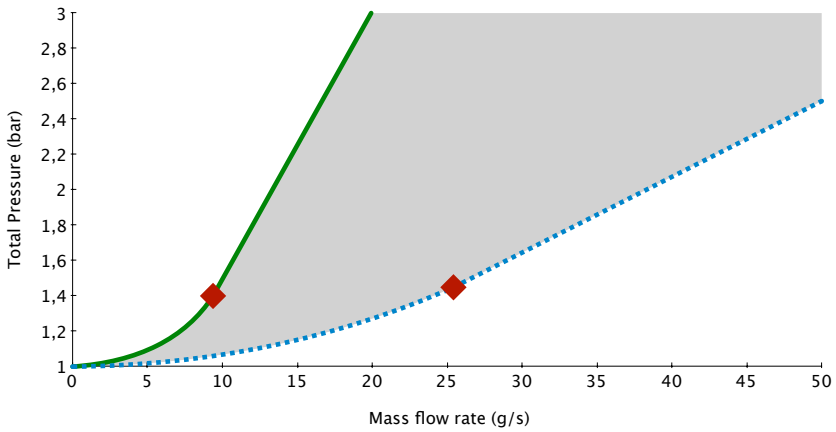

Figure 8.1: Graph plotted by the XNozzle tool to monitor the state of a choked chamber. Full line: lower limit of $P_0(\dot{m})$ computed with T_f. Dotted line: upper limit computed with T_{adia}. Squares: choking points of the nozzle. Gray area: possible states of the flow in a reacting setup.

8.2.2 Practical LES of a choked nozzle test case

In order to validate the methodology exposed in Sec. 8.2.1, a numerical test case of a nozzle matching the general characteristics of the CESAM-HP setup is derived. Historically, this test case was performed before the final geometry of the CESAM-HP nozzle was determined, hence this geometry does not match the final geometries of Part. III.

8.2.2.1 Test case definition

As explained above, this study was performed on the preliminary bench geometry of CESAM-HP, which is shown in Fig. 8.2. This preliminary design was never

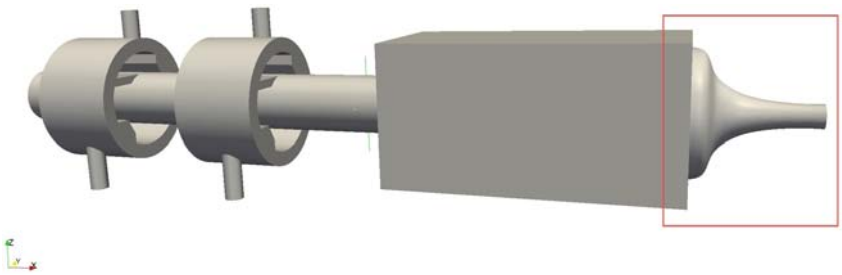

Figure 8.2: View of the preliminary CESAM-HP test bench. The red diamond shows the region that is used for the present test case.

computed as a whole reacting case. However, it is representative of the target geometry and operating points of the experiment, hence its use for validation of the nozzle simulation methodology. The nozzle chosen is mostly converging. A small diverging subsection has been kept, in order for the $M = 1$ surface to be

Mass flow rate	Inlet area	$P_0(\approx P_1)$	T_0	γ	W
$18.0\,\mathrm{g\,s^{-1}}$	$49\,\mathrm{cm^2}$	2.5 bar	2225.28 K	1.25	$28.36\,\mathrm{g\,mol^{-1}}$

Table 8.3: Operating conditions for the test case

included in the computational domain at all times. This simplifies the boundary condition treatment, which can be designed for exclusive use on supersonic boundary conditions.

In order to accelerate the computations and focus on the nozzle issue, only the end of the chamber and the nozzle will be computed for this test case. Therefore, the fluid entering the domain, which is normally the result of the combustion in the chamber, will be set to hot homogeneous burnt gases. The target parameters are given in Tab. 8.3. The resulting domain is shown in Fig. 8.3.

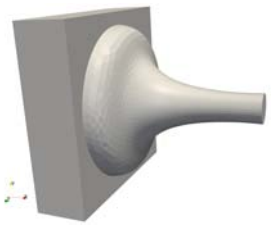

(a) View of the domain used in the present test case.

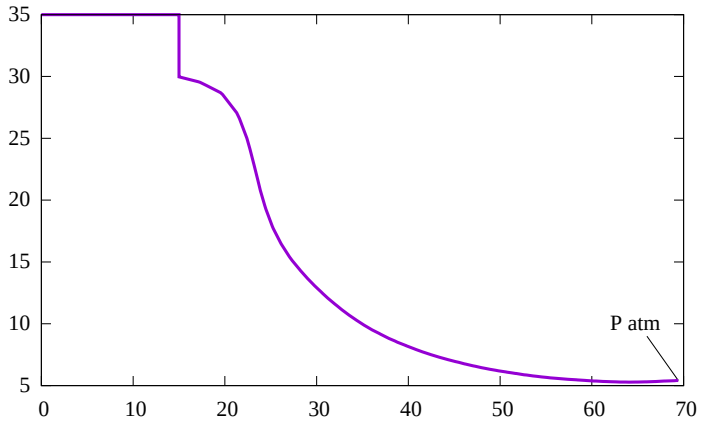

(b) Nozzle profile (in mm).

Figure 8.3: Geometry for the choked nozzle test case.

According to Eq. 4.15, the pressure ratio needed to choke the nozzle is $r_{choke} = 1.43$. The pressure values for the test case are $P_0 \sim P_1 = 2.5$ bars and $P_1 = P_{atm} = 1.013$ bars. Hence, $P_0/P_{atm} = 2.47 > r_{choke}$. This shows that the nozzle should be choked under normal operating conditions. In fact, the nozzle is purposefully designed to obtain an adapted flow. Eq. 4.15 yields $r_{adapt} = 1.43$, which is exactly the pressure ratio computed above. All critical pressures and pressure ratios are summarized in Tab. 8.4.

In order to check the quality of the nozzle response to chamber fluctuations, P_0 must be compared to its analytical value. If the nozzle behaves correctly, the relation between total pressure P_0 and mass flow rate $\dot{m}$ should be described by Eq. 4.13. This relation is linear, since the composition (hence γ, r) and the total temperature T_0 of the hot gases are considered constant and homogeneous. Several values of $\dot{m}$ must be used in order to evaluate the response of the nozzle for a range of mass flow rates. These values are summarized in Tab. 8.5, as well as the matching pressure

State	Atm.	Choke	Throat	Adapt
Pressure P_0 (bar)	1.013	1.45	1.82	2.5
Ratio r	1	1.43	1.80	2.46

Table 8.4: Critical chamber pressures and pressure ratios for the test case, for $P_{out} = 1$ atm = 1.013 bars. The chamber pressure is 2.5 bar in the CESAM-HP chamber.

ratios.

Computation number	0	1	2	3	4
$\dot{m}$ (g/s)	No inlet	8	12	18	24
r	Initially 2.46	1.25	1.64	2.46	3.29

Table 8.5: Mass flow rate $\dot{m}$ and pressure ratio r for each numerical test case. All cases correspond to burnt gases flowing through a nozzle.

Comparison of Tab. 8.4 and 8.5 shows that the smaller mass flow rate (8 g/s) is in the subsonic area. The next target (12 g/s) is in the "shock region". The third is approximately the adapted regime, and the last mass flow rate target is in the under-expanded region. Note that an additional run (0) is present with no inlet: it represents the emptying of an initially pressurized tank through the nozzle. This is meant to show what happens when the pressure in the chamber is gradually lowered, until the point of unchoking is reached. It is treated in Sec. 8.2.2.3.

The initialization of the test cases is done as follows. All variables are set to their total values, *i.e.* total pressure, total temperature, total density. The velocity field is set to zero. The pressure at the outlet is the static atmospheric pressure, and the pressure difference in between the domain and the outlet will drive the flow.

8.2.2.2 Results

Transient state Fig. 8.4 shows the result of the *xl* tool on a probe at the center of the inlet, for the $18\,\mathrm{g\,s^{-1}}$ case, during the entire computation. This tool plots generic values versus time at a probe location in the fluid. It shows how the flow establishes in less than 1 ms. XNozzle results combined for all four computations are shown in Fig. 8.5. This figure displays the traces of total pressure in the chamber versus mass flow rate through the nozzle. Total pressure is computed using a probe at the inlet and using Eq. 4.7. All four computations start with their target ideal 1D total pressure, and zero velocity. Hence, the initial mass flow rate is 0 and all traces start from the left axis. Then, as the computation starts, the gas accelerates and the mass flow rate increases. At the same time, the total pressure decreases slightly due to pressure losses. All four traces meet the predicted "full combustion case" line and stay on it until the end of the computation. This test case uses a mixture of fully burnt hot gases at the inlet, hence this is the expected behavior.

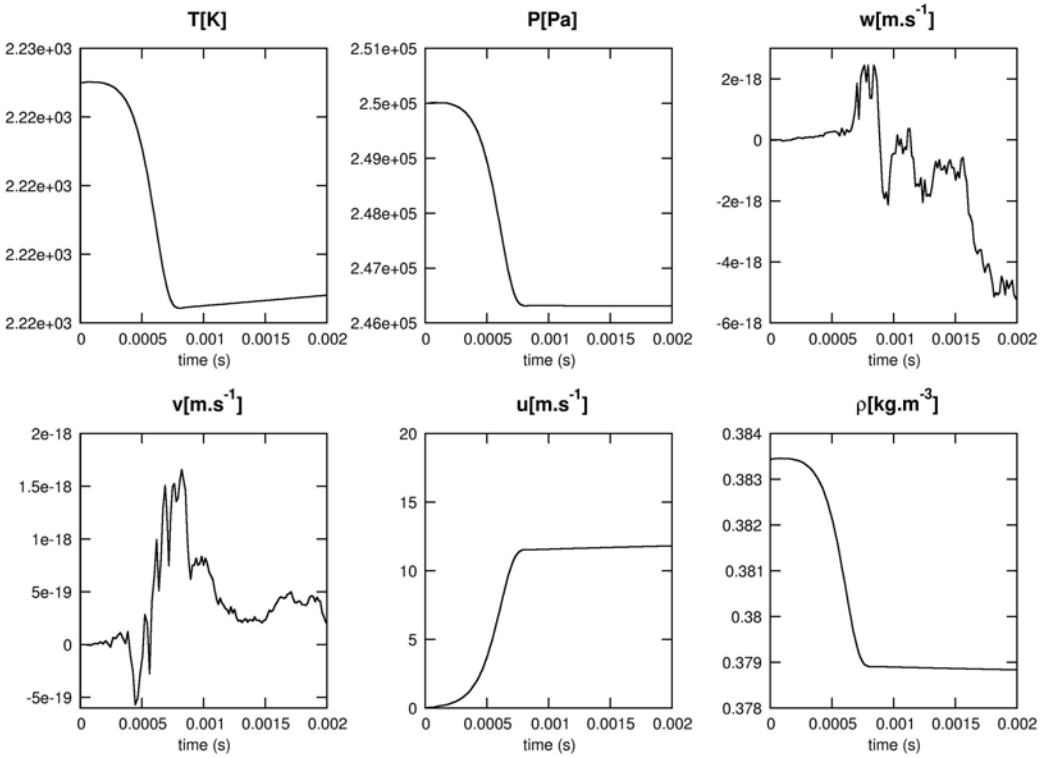

Figure 8.4: *xl* tool on a node at the center of the inlet patch.

As expected, the lowest flow rate ($8\,\mathrm{g\,s^{-1}}$) leads to an unchoked case (below the diamond symbol on the XNozzle curve) while the three others are choked. Note that while this result seems simple to obtain, other initialization techniques may lead to much more complex evolutions in the XNozzle plots.

Steady flow (converged state) A plot of a cross-subsectional cut of the converged Mach field is given in Fig. 8.6. Mach and axial velocity profiles at the throat are displayed in Fig. 8.7. These plots show that the 1D approximation is true within a 5 % margin, since it predicts the Macn number to be equalt to 1 at the throat. However, the small variation can be characterized using a discharge coefficient c_d defined as follows: let f be the function described in Eq. 4.12, such that $P_0 = f(\dot{m})$. In the numerical configuration, a linear fit of the points can be described as:

$$P_0 = c_d f(\dot{m}) \tag{8.2}$$

The measure of c_d in the present case leads to a value (averaged over the four runs) of 0.985, only 1.5% away from the analytical solution.

Mean profiles for the $18\,\mathrm{g\,s^{-1}}$ reference case are shown in Fig. 8.8.

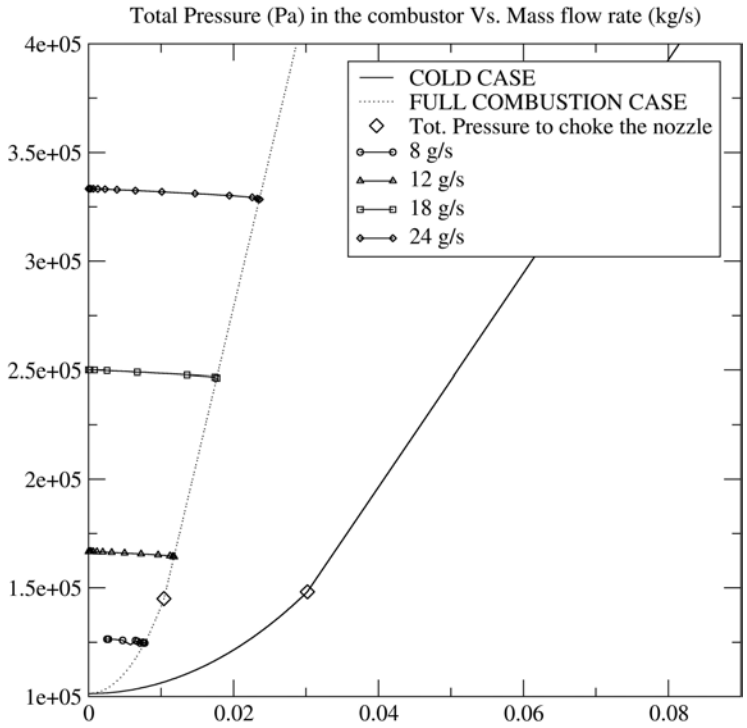

Figure 8.5: Result of the XNozzle tool applied to the 4 test cases of Tab. 8.5 : total pressure P_0 in the flow is plotted versus mass flow rate $\dot{m}$. All points converge to the XNozzle upper limit for a hot flow (full combustion case).

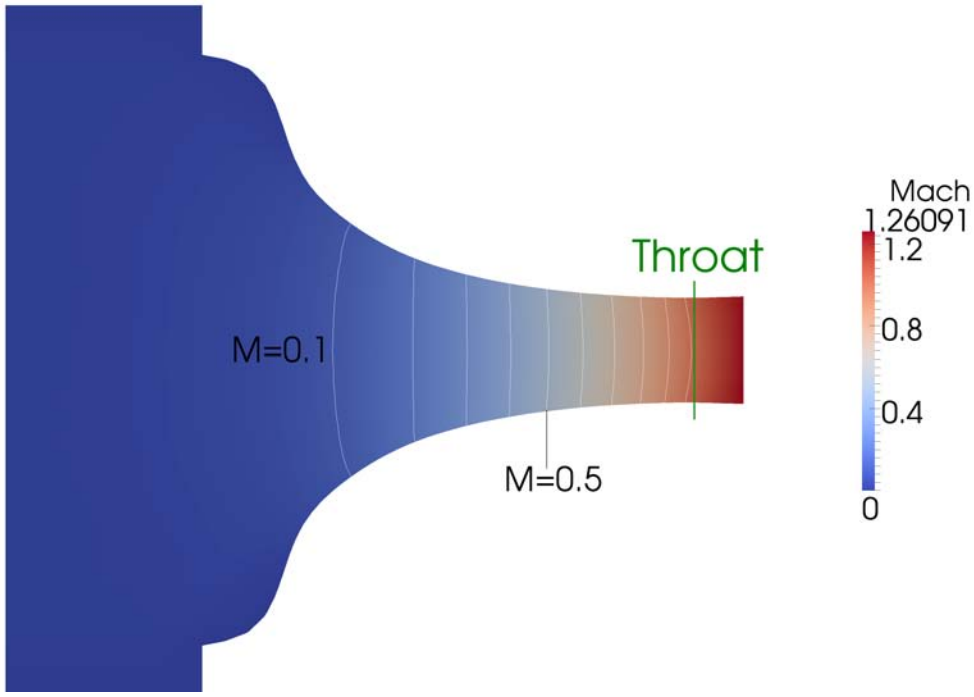

Figure 8.6: Mach number field in a cross subsectional cut along the axis of the nozzle, for $\dot{m} = 18$ g/s. White lines are Mach number isolines from 0.1 to 1.0 with a step of 0.1.

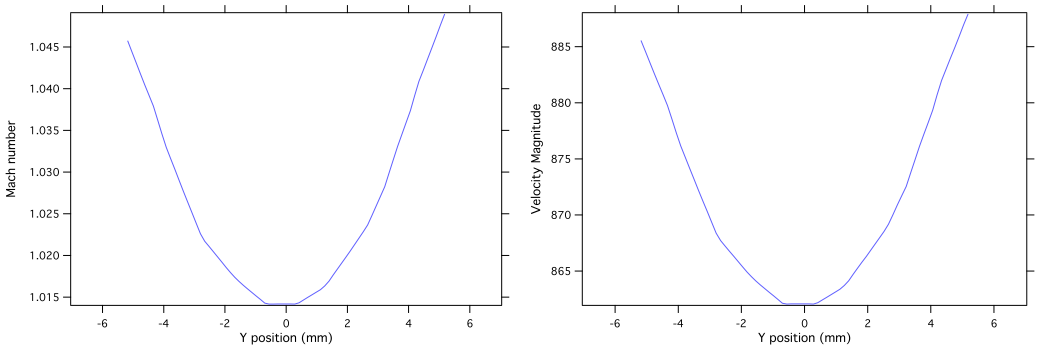

(a) Mach number **(b)** Velocity magnitude

Figure 8.7: Mach number (a) and velocity magnitude (b) profiles at the geometric throat.

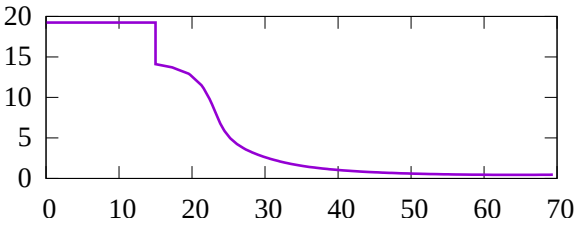

(a) A/A^* ratio

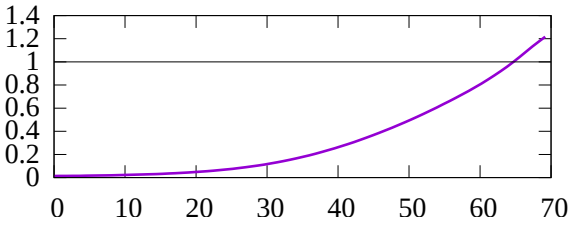

(b) Mach number

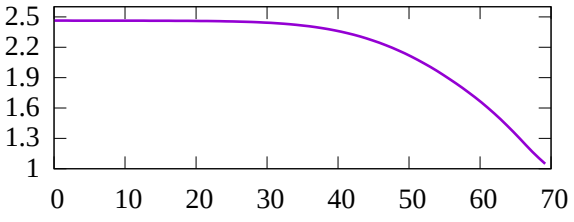

(c) Pressure

Figure 8.8: A/A^* ratio (a), Mach number (b) and pressure (c) profiles along the nozzle axis for the $18\,\mathrm{g\,s^{-1}}$ reference case.

8.2.2.3 A specific caveat of the numerical approach: unchoking the nozzle

In the current setup, the walls are impermeable but have a "slip" condition, *i.e.* the velocity at the wall is close to that of the flow. Additionally, the domain ends immediately after the flow becomes supersonic. This implies that the downstream pressure information is not imposed, and could not travel upstream (*e.g.* through boundary layers) even if it were imposed. Consequently, during a computation, if the physical parameters indicate that the nozzle should no longer be choked, the code cannot see this fact. Once the Mach distribution switches to the supersonic case, the computation cannot come back to a subsonic configuration. This can be dangerous if one does not realize that the computation should unchoke itself, therefore one must take care when using the XNozzle tool to check that the temporal trace of total pressure never goes below the critical total pressure to choke the nozzle.

To illustrate what happens if a computation goes into this area, *i.e.* when it is successively choked and then the pressure ratio goes below r_{choked}, the present test case is run again and initialized as the $18\,\mathrm{g\,s^{-1}}$ case. However, the inlet patch is replaced by a wall. This case is referred to as run 0. Physically, the flow should quickly become choked, but then the chamber should empty itself until the flow becomes subsonic once again since there is no inflow. Fig. 8.9 shows the result of the *xl* tool on a probe on the former inlet patch, yielding general variables at this probe versus time. In the simulation, the pressure drops below the atmospheric

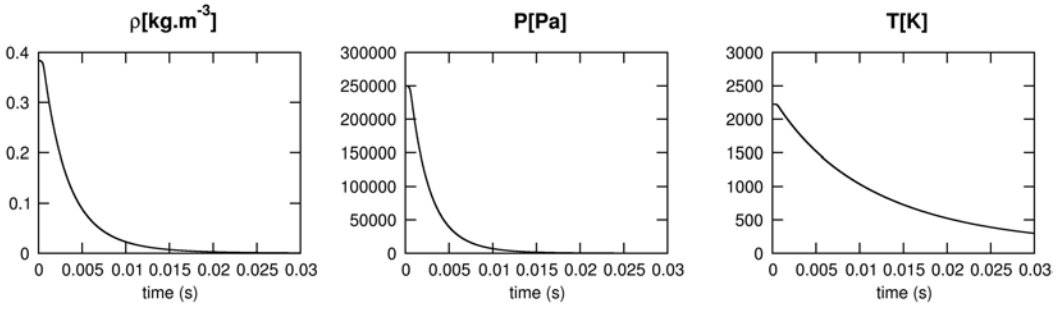

Figure 8.9: Result of the *xl* tool applied to the former inlet patch, now a wall, in run 0 where the outlet condition remains choked beyond the point where the physical system would naturally unchoke itself. Here, unphysical behavior is observed.

pressure and down to zero, as does the density. Since the fluid remaining in the domain significantly expands as the chamber empties itself, the temperature drops. The Mach number, however, stays constant, as can be seen in Fig. 8.10.

The XNozzle tool (Fig. 8.11) applied to this test case shows how the flow stays supersonic (*i.e.* follows the supersonic line) and is non physical as soon as the total pressure drops below the critical total pressure.

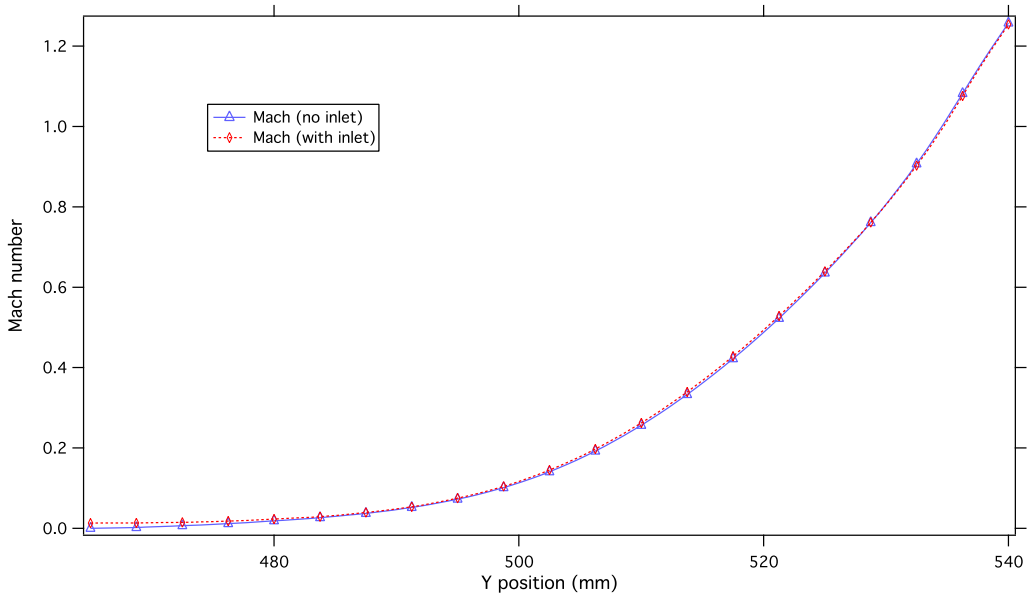

Figure 8.10: Comparison of axial Mach numbers of the flows with and without inlet. With inlet : converged state. With wall instead of inlet : after 30 ms of run. The outlet remains choked and the flow keeps going out at a supersonic speed.

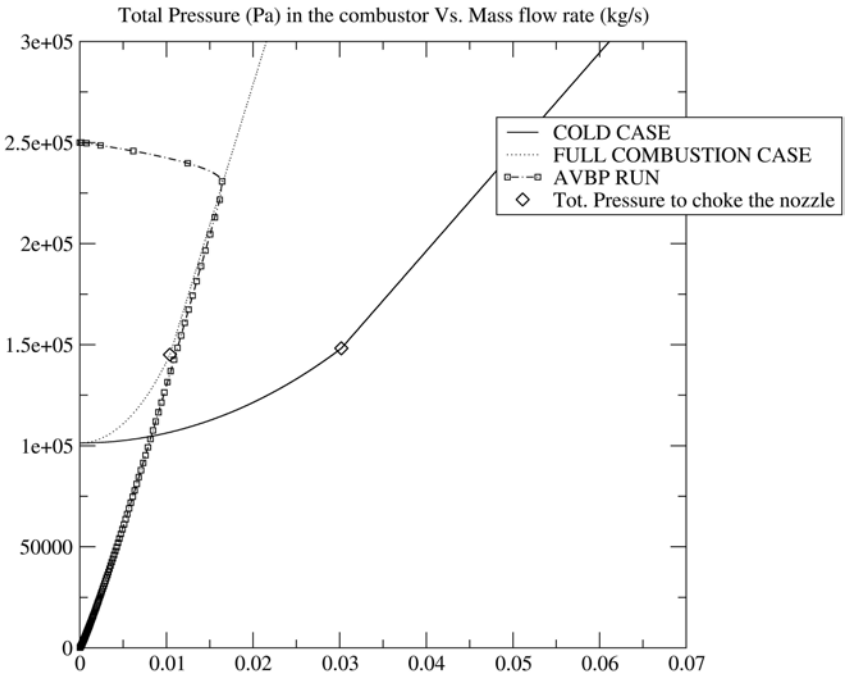

Figure 8.11: XNozzle tool applied to run 0 (no inlet).

8.3 Nozzle impedances for chamber outlets

Sec. 8.2 has presented tools to perform LES of chambers terminated by nozzles. In some cases however, it is not possible to include the nozzle inside the resolution domain. This is true *e.g.* for LES codes that cannot take compressibility effects into account. In the context of this Ph.D, and for noise and instability studies in general, Helmholtz solvers where the Mach number is supposed to be zero are used, implying that the high Mach number flow must be replaced by an equivalent impedance.

When the nozzle cannot be included in the computational domain (*e.g* for incompressible LES or zero-Mach number Helmholtz simulations), several simplified assumptions can be made to evaluate the nozzle outlet impedance. Three successive methods of increasing accuracy are discussed in this section. To compare these approaches, the resulting *impedance* $Z = {}^{p'}/_{\bar{\rho}\bar{c}u'}$ and *reflection coefficient* $R = {}^{Z-1}/_{Z+1}$ of each will be discussed.

8.3.1 The "wall" limit

To first order, a nozzle is often replaced by a wall because the area restriction is strong and $u' = 0$ is a close approximation for subsonic as well as for choked nozzles (Marble & Candel, 1977*a*). This will be confirmed for all the frequencies of interest by the most accurate method available in Sec. 8.3.3. The impedance in this case is $Z = +\infty$, and the reflection coefficient is $R = 1$.

8.3.2 The "compact" limit

Zinn (1972) proposed a representation of so-called "short" nozzles, *i.e.* nozzles which are shorter than the characteristic wavelength of the acoustic waves propagating through it. In this more precise framework, he showed that it is in fact not $u' = 0$ that is imposed by the nozzle, but $M' = 0$. In the presence of entropy waves, *i.e.* temperature perturbations, this condition differs from the wall limit, and imposes instead:

$$M = \frac{u}{\sqrt{\gamma r T}} = \frac{u}{\sqrt{\gamma p/\rho}} = Cst \tag{8.3}$$

$$\frac{u'}{\bar{u}} - \frac{1}{2}\frac{T'}{\bar{T}} = 0 \text{ and } \frac{u'}{\bar{u}} + \frac{1}{2}\left[\frac{\rho'}{\bar{\rho}} - \frac{P'}{\bar{P}}\right] = 0 \tag{8.4}$$

Marble & Candel (1977*b*) built on this assumption in the context of combustion noise, leading to the full set of reflection/transmission coefficients of the nozzle. This has been detailed in Chap. 5 (see Tab. 5.1 for the complete set of coefficients). According to Eq. (8.4), the impedance and reflection coefficient write:

$$Z = \frac{2}{(\gamma-1)M} \qquad\qquad R = \frac{2-(\gamma-1)M}{2+(\gamma-1)M}$$

respectively. For low inlet Mach numbers, Z goes to $+\infty$ and R goes to 1, as predicted by the "wall limit" of Sec. 8.3.1.

8.3.3 Non-compact analytical formulation

Little achievements occurred in the decades following the compact theory of Marble & Candel (1977*a*). The same study had in fact given a non-compact description for the specific case of a linear velocity nozzle, but no solution was found for the general case. Moase *et al.* (2007) had the idea to discretize a generic geometry into a piecewise linear-velocity nozzle, and apply the solution of Marble & Candel (1977*a*) in each section. Stow *et al.* (2002) investigated an entirely different solution based on an asymptotic expansion of the compact case to one more order, leading to an "effective nozzle length" which corrected the reflection coefficient phase. But the only suitable solution for all frequencies stayed the direct resolution of the Euler or Navier-Stokes equations inside the nozzle (Duran & Moreau, 2011).

Recently, a significant improvement was proposed by Duran & Moreau (2013) which shares similarities with the approach of Stow *et al.* (2002). In the compact nozzle assumption, this study notes that three quantities are invariant through the nozzle, namely:

$$I_A = \left(\frac{\dot{m}'}{\bar{\dot{m}}}\right) \tag{8.5a}$$

$$I_B = \left(\frac{T_t'}{\bar{T}_t}\right) \tag{8.5b}$$

$$I_C = \left(\frac{s'}{c_P}\right) \tag{8.5c}$$

and that the Euler equations can be rewritten in terms of these invariants:

$$\frac{D}{D\tau} I_A = \frac{\bar{u}}{(\gamma-1)M^2}\left[\frac{\partial}{\partial\xi} I_C - \left(1 + {}^1\!/_2(\gamma-1)M^2\right)\frac{\partial}{\partial\xi} I_B\right] \tag{8.6a}$$

$$\frac{D}{D\tau} I_B = -\frac{(\gamma-1)\bar{u}}{1 + {}^1\!/_2(\gamma-1)M^2}\left[\frac{\partial}{\partial\xi} I_A + \frac{\partial}{\partial\xi} I_C\right] \tag{8.6b}$$

$$\frac{D}{D\tau} I_C = 0 \tag{8.6c}$$

where $\xi = {}^x\!/_L$ and $\tau = tf$ are the dimensionless space and time variables, respectively, L is a characteristic length of the nozzle and f is a characteristic frequency of the perturbation. This is then rewritten in matrix form:

$$E(\xi)\frac{\mathrm{d}}{\mathrm{d}\xi}\boldsymbol{I} = 2\pi i\Omega\boldsymbol{I} \tag{8.7}$$

and for $M \neq 1$ the determinant of E is non zero, hence the system can be inverted:

$$\frac{\mathrm{d}}{\mathrm{d}\xi}\boldsymbol{I} = A(\xi)\boldsymbol{I} \tag{8.8}$$

Duran & Moreau (2013) show that this form is a correction to the compact framework to account for non-compact effects, and that these results degenerate to the compact results in the zero frequency limit. An asymptotic expansion to the n-th order was

then performed on the invariants $\boldsymbol{I}(\xi) = \boldsymbol{I}^{(0)} + \Omega\boldsymbol{I}^{(1)} + \cdots + \Omega^n\boldsymbol{I}^{(n)}$, reading for the n-th order:

$$\frac{\mathrm{d}}{\mathrm{d}\xi}\boldsymbol{I}^{(n)} = \frac{A(\xi)}{\Omega}\boldsymbol{I}^{(n-1)} \tag{8.9}$$

A clever use of the Magnus expansion then yielded the solution in form of an infinite series of terms which could be computed recursively, but the author showed that this series converged very rapidly and only a few terms were needed to obtain a value with satisfactory precision.

This methodology has been implemented during a previous Ph.D (Duran, 2013) and is known as the ANozzle tool. It has been shown to perform with excellent precision compared to fully resolved Euler methods, but with several orders of magnitude less computational cost.

The reflection coefficient of the nozzle of the CESAM-HP setup has been computed using the ANozzle tool. It is displayed for frequencies ranging from 0 to 2000 Hz in Fig. 8.12. On this frequency range, the tool confirms that the behavior of this nozzle

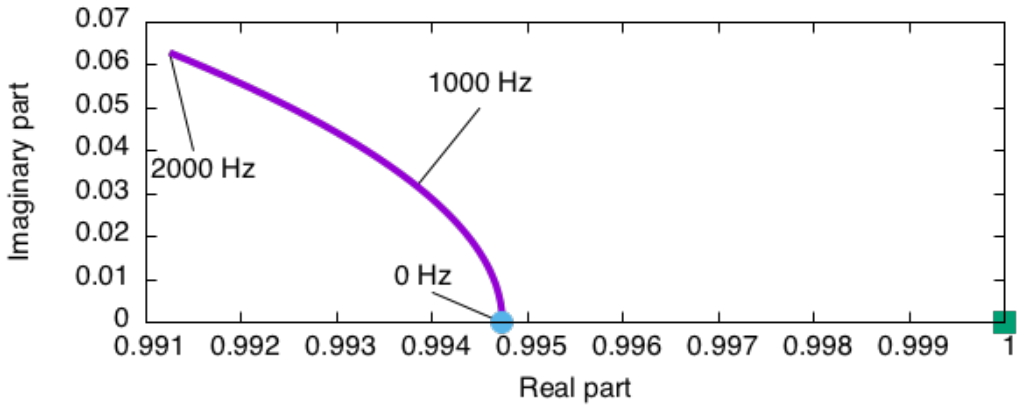

Figure 8.12: Reflection coefficient of the CESAM-HP nozzle under choked conditions, plotted in the complex plane. Square symbol: wall limit $u' = 0$. Round symbol: compact formulation. Full line: Magnus expansion result with the ANozzle tool.

is indeed very close to that of a wall. The reflection coefficient is strong (> 99 %) and the phase is close to 0, as for a $u' = 0$ condition.

These results are used for all Helmholtz simulations of Chap. 11, as it is the best combination of cost and accuracy available to estimate the nozzle impedance.

Part III

The CESAM-HP combustor

Table of Contents

9 The CESAM-HP combustor **157**

9.1 The CESAM-HP test rig . . . 157

9.1.1 Experimental investigations . . . 159

9.2 Numerical setup to simulate CESAM . . . 160

9.2.1 Boundary conditions . . . 160

9.2.2 Numerical domain . . . 160

9.2.3 Sub-grid scale model for CESAM-HP . . . 163

9.3 Chemical model . . . 163

9.3.1 Reference for the model . . . 165

9.3.2 Model and results . . . 166

9.4 *A posteriori* validation of the chemical approach . . . 168

10 LES of unchoked regimes **171**

10.1 Introduction . . . 171

10.1.1 Effect of uncertainties on geometry . . . 172

10.2 Non reacting simulations . . . 173

10.2.1 Operating point . . . 173

10.2.2 Numerical results . . . 174

10.2.3 Comparison with experiments . . . 175

10.2.4 Impact of the geometry discrepancy correction . . . 178

10.3 OPEN reacting simulations . . . 178

10.3.1 Numerical simulation . . . 178

10.3.2 Swirl sensitivity study . . . 182

10.3.3 Forced outlet numerical investigation . . . 185

10.4 Conclusion . . . 186

11 Choked flow study **187**
11.1 Compressible LES strategy 187
11.1.1 Operating points 187
11.1.2 Initialization strategy 188
11.2 **CHOKED-PR**: Auto-excited AI-VCF in the fully premixed case . . 189
11.3 **CHOKED-ST**: Control of AI-VCF using fuel staging 195
11.4 Thermoacoustic Analysis 199
11.4.1 Passive flame 199
11.4.2 Active flame 201
11.4.3 On the role of convective phenomena 203
11.5 Conclusions 204

A NSCBC Inlet acoustic impedance **209**

B LODI for spherically symmetric flows **211**
B.1 The LODI formalism 211
B.2 A non-reflecting boundary with the LODI formailsm 212
B.3 LODI applied to a spherical problem 213
B.4 A spherically symmetric problem is not LODI 216

Bibliography **217**

Chapter 9

The CESAM-HP combustor

The EM2C laboratory has developed several test benches to study turbulent premixed combustion in small scale, well instrumented conditions. The CESAM bench (Lamraoui, 2011) provide an excellent case for atmospheric investigations, and the DISCERN ANR project was dedicated to the creation of a pressurized version in 2012: CESAM-HP. This bench is used for pressurized chamber investigations in the EC RECORD project, and multiple numerical investigations have been lead throughout these projects in parallel to the experimental measurements. The matching numerical setups retained for flow (AVBP) and acoustic (AVSP) solvers are exposed in this chapter. All tools and concepts described in Chap. 7 and 8 will be applied and compared to experimental data in Chap. 10 and 11.

9.1 The CESAM-HP test rig

The theoretical and numerical tools presented in the previous chapters to study noise, instabilities and flashback are applied now to a real swirled burner: the CESAM-HP setup. A significant part of this study has been performed in collaboration with the EM2C team, *i.e.* Marek Mazur, Franck Richecœur, Philippe Scouflaire and Sébastien Ducruix.

The CESAM-HP test bench located in EM2C is a small burner (up to 35 kW) designed for lean premixed combustion of gaseous propane at pressures up to 2.5 bars. A schematic of the experimental setup is shown in Fig. 9.1. It is composed of:

- two plenums where air and propane are mixed, which feed the injection tube and create the mean flow swirl;
- an "Impedance Control System" or ICS, described hereafter;
- a swirl tube, ended upstream by the ICS and downstream by the dump plane;
- a square section combustion chamber with optical diagnostics;
- a converging nozzle.

The flow is injected at three different locations: the ICS and two swirl plenums. Propane is only injected through the swirl plenums. The flow split between the two flow injectors controls the aerodynamics at the chamber entrance and has an important effect on flashback. The fuel staging between the two plenums is also an important parameter. As demonstrated recently by Sattelmayer *et al.* (2014), fuel deficit in the center of the swirling flow can increase VCF limits.

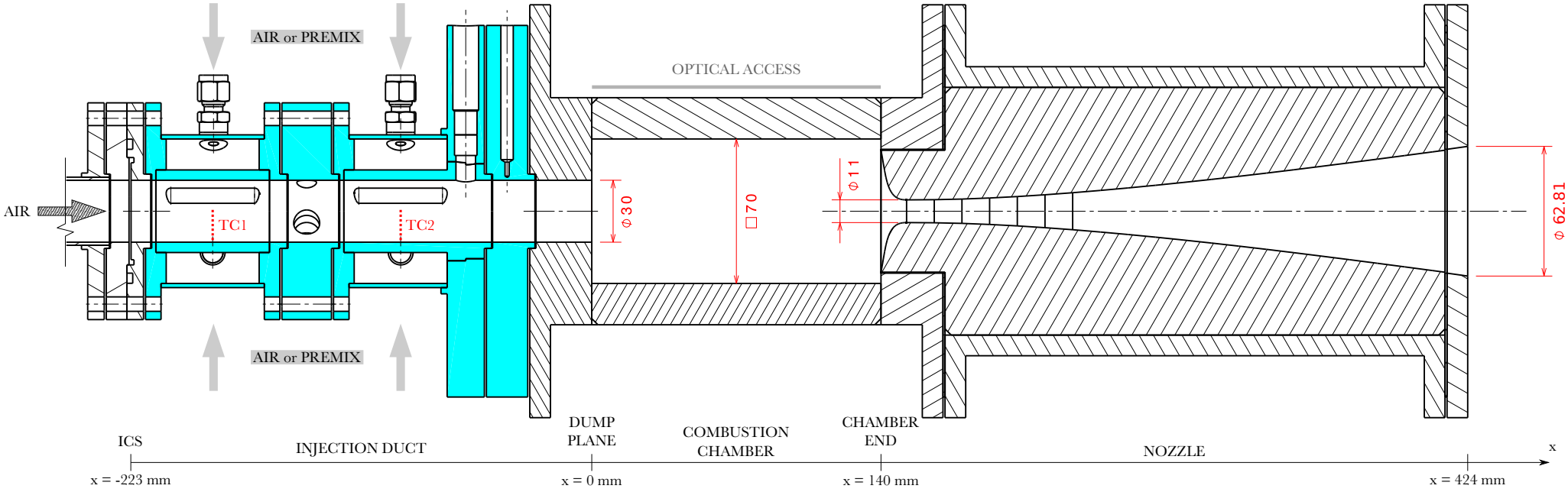

Figure 9.1: Schematic of the CESAM-HP experimental setup.

The ICS is a cavity of controlled length, connected to the domain by a perforated plate. It allows to control the impedance of a given boundary. Its acoustic behavior has been thoroughly studied (Tran *et al.*, 2007): in a similar model combustor the ICS can efficiently damp combustion instabilities (Tran *et al.*, 2009). In this study, the ICS cavity is set to its longest length: this position offers the best damping properties for the low frequency phenomena that are observed here.

The ICS also plays a second role: some of the flow rate is injected through the ICS section because this is necessary to control the acoustic damping performances of the plate (Howe, 1979; Mendez & Eldredge, 2009). This flow rate is not swirled and decreases the overall swirl number of the injection tube. Recent results of Reichel *et al.* (2014) suggest that the swirl number is an important control parameter for swirl-stabilized burners, and that it controls VCF. The flow split between the ICS and the swirled injectors is therefore expected to be a key parameter controlling flashback occurrence.

The ICS flow is pure air in the experiment. However, by the time it reaches the dump plane, it is fully premixed. To simplify the LES to avoid simulating mixing between ICS and main flow, premixed gases are injected everywhere in the **PREMIXED** LESs hereafter.

9.1.1 Experimental investigations

The test bench has been extensively studied for operation ranges at EM2C. Flame stabilization in this system is difficult, and the operation ranges where combustion can be sustained are thin. Because the fuel staging between upstream and downstream injectors can be modulated, a wide variety of operation ranges can be explored. In fully premixed operation, the test bench has proven to be very difficult to operate, as how oscillations of pressure and flame positions were observed. Using fuel staging however, the system became more stable and a map of equivalence ratio ϕ versus total air mass flow rate $\dot{m}_{air}$ could be performed (Fig. 9.2). Two distinct regions appear in the operation range:

- for low air flow rates, the flame is long in the chamber and the range of equivalence ratios which sustain combustion is thin;
- for high air flow rates, namely above $17\,\mathrm{g\,s^{-1}}$ the operation range extends. The flame becomes more compact and resembles more realistic flames encountered in industrial combustion chambers.

A transition zone connects these two regions, where the flame behavior is not well determined.

Because of this general behavior, the operating points for the bench are chosen in the "compact flame" area, *i.e.* for a total air mass flow rate of $18\,\mathrm{g\,s^{-1}}$. Matching conditions were chosen for numerical investigations (Tab. 9.1). One is fully premixed, the second implies fuel staging. The overall equivalence ratio ϕ is 0.9 and 0.85, respectively. In both cases the nozzle is choked, and the total air mass flow rate is $18\,\mathrm{g\,s^{-1}}$.

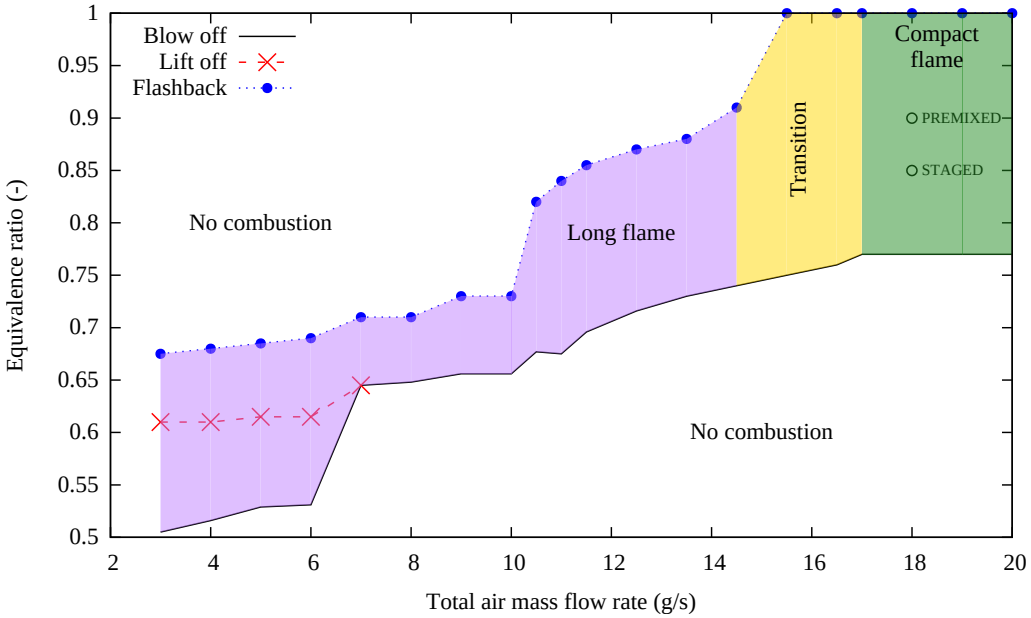

Figure 9.2: Operation map of the CESAM-HP burner versus equivalence ratio ϕ and total air mass flow rate $\dot{m}_{air}$. Map performed under staged conditions. **PREMIXED** and **STAGED** operating points from Tab. 9.1 are positioned for reference. Data provided by EM2C, M. Mazur.

9.2 Numerical setup to simulate CESAM

9.2.1 Boundary conditions

The nozzle walls are treated with slip conditions, for the reasons discussed in the previous section. All other walls are no-slip conditions, *i.e.* impermeable surfaces of null velocity. Inlets and outlets are NSCBC low-reflecting conditions, according to Poinsot *et al.* (1992).

The argument has been made in Chap. 8 that if the flow becomes choked at the outlet, a velocity inlet boundary conditions will not lead to a well-posed problem. Since the nozzle is expected to choke for some regimes, and can be included in the computation domain, the variables imposed at the inlet are chosen to be $(\rho u, \rho v, \rho w, T)$. At the outlet, the pressure is imposed is the Mach number is less than 1. Otherwise, nothing is imposed, as this implies that the nozzle is choked and that all characteristics are leaving the domain.

9.2.2 Numerical domain

The complete test rig shown in Fig. 9.1 cannot be entirely meshed for LES, for two reasons:

1. the sheer volume of the domain would lead to a very high amount of mesh nodes, increasing the cost of simulations dramatically;

	PREMIXED $\phi_{prem} = 0.9$		STAGED $\phi_{stag} = 0.85$	
	$\dot{m}^{air}$	ϕ	$\dot{m}^{air}$	ϕ
Experiment				
ICS	1.0	0.0	1.0	0.0
Injector 1	8.5	0.95	7.0	0.0
Injector 2	8.5	0.95	10.0	1.53
LES				
ICS	1.0	0.9	1.0	0.0
Injector 1	8.5	0.9	7.0	0.0
Injector 2	8.5	0.9	10.0	1.53

Table 9.1: Target operating points for experiments and LES.

2. many different physical phenomena occur throughout the test rig, but we are not interested in all of them here. The most notable example is the very long nozzle, in which the physics can be complex but which is not the main object of this study.

The numerical domain is therefore limited. The elements kept are:

- the ICS;
- the injection duct;
- the combustion chamber;
- a small part of the nozzle, including the convergent and the beginning of the diverging section.

9.2.2.1 OPEN versus CHOKED configurations

This Ph.D. focuses on the effect of the downstream condition on several physical phenomena. Two approaches are used to investigate this effect, namely:

- the **OPEN** (Fig. 9.3a) case, where the domain is cut at the chamber end. A characteristic treatment of the boundary conditions is used to provide either a non-reflecting outlet condition, or a forced one with an upstream acoustic wave. This configuration was not reproduced experimentally, as the only solution to pressurize the domain is to force the flow through the nozzle;
- the **CHOKED** (Fig. 9.3b) case, where the domain includes the nozzle and is cut after the geometric throat in the nozzle. This nozzle termination is expected to generate strong reflections and possible unstable modes. It corresponds to the geometry used experimentally and to the impedance of Fig. 8.12.

Four configurations were retained for numerical simulations (Tab. 9.2), making use of both the **OPEN** and **CHOKED** geometries. Only two of these have experimental equivalents. Experiments are performed only for the pressurized operating points with the nozzle (**CHOKED** setups), and the subsequent acoustic behavior. In the **OPEN** setups, LES allows to control the acoustic behavior of the boundary

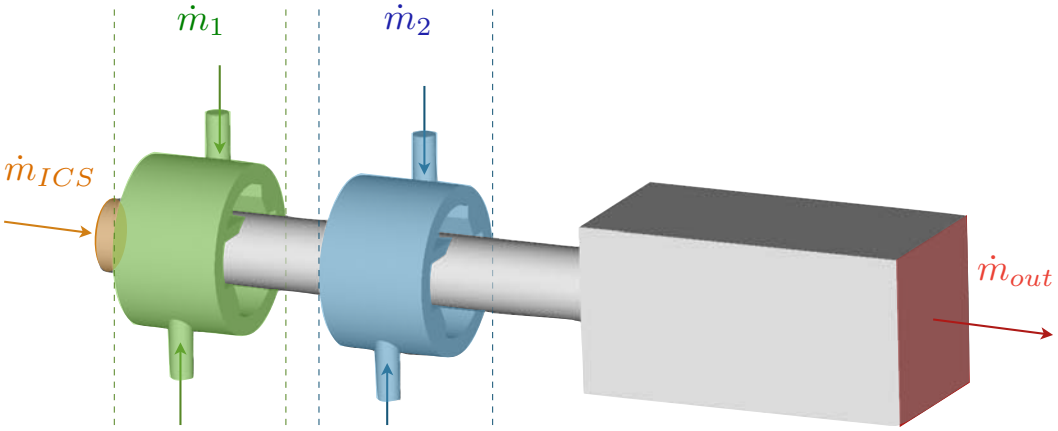

(a) OPEN setup

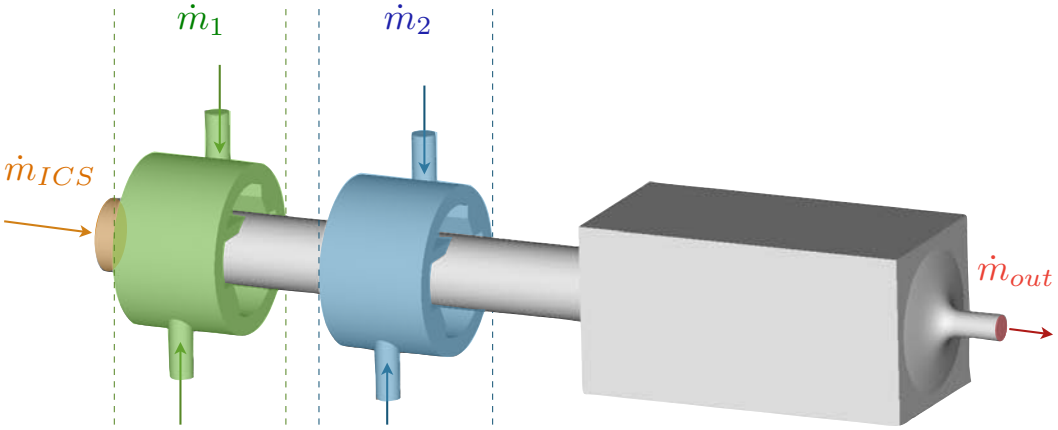

(b) CHOKED setup

Figure 9.3: (a) **OPEN** and (b) **CHOKED** setups used to investigate the effect of outlet nature on flame stabilization and stability in this Ph.D.

conditions, regardless of temperature or pressure issues.

9.2.2.2 Meshes

Because of the multiple investigations and the matching geometry modifications, several meshes have been produced. Their major characteristics are grouped in Tab. 9.3. The coarse grid $\mathbf{MO}_C$ is used with the AVSP code to solve the acoustic eigenmodes of the chamber. A fine grid $\mathbf{MO}_F$ is used for a mesh convergence study. Finally, all other meshes are used for LES investigations. Views of the fluid domains are given in Fig. 9.4. The injection duct and chamber (a) are meshed in **MO** meshes. **MN** meshes attach the nozzle convergent (b) to this domain. Finally, the full domain (c) is meshed in **MNI**.

	OPEN Setup (Fig. 9.3a)		**CHOKED** Setup (Fig. 9.3b)	
Case name	OPEN-NR	OPEN-FO	CHOKED-PM	CHOKED-ST
Domain	OPEN	OPEN	CHOKED	CHOKED
Outlet	**Non-reflecting**	**Acoustic forcing**	Choked nozzle	Choked nozzle
Operating Point	PREMIXED	PREMIXED	**PREMIXED**	**STAGED**
Exp. data	NO	NO	YES	YES

Table 9.2: Numerical setups for the CESAM-HP test bench

Mesh name	Comments	Domain (Fig. 9.4)	Nb points	Nb elements	Δx_{min} (mm)
MO_C	Open end, coarse	a	304 461	1 629 781	1.0
MO	Open end	a	2 259 294	12 632 281	0.5
MN	Nozzle	a+b	2 272 658	12 706 817	0.5
MNI	Nozzle, ICS	c	2 323 792	12 966 101	0.5
MO_F	Open end, fine	a	13 341 183	76 125 123	0.25

Table 9.3: Meshes used and main characteristics

9.2.3 Sub-grid scale model for CESAM-HP

It has been argued in Sec. 7.3.2.2 that the best approach for wall modeling here was a no-slip condition. This implies however the use of a SGS model that degenerates well near the wall. Two options are available in AVBP, namely WALE (Nicoud & Ducros, 1999) and SIGMA (Nicoud *et al.*, 2011). Fig. 9.5 presents the turbulent viscosity in two typical CESAM-HP simulations: one computed with each SGS model. It is clear from these cuts that the WALE model detects rotation in the swirl tube, and SIGMA does not. This indicates that solid body rotation is involved, and that the WALE model adds unnecessary viscosity in the swirl tube. This solid body rotation could be anticipated as the swirl tube is a wide cylinder fed by 2 swirlers and with no obstruction. The SIGMA model is therefore adopted for the simulation of the setup, and is used for all computations.

9.3 Chemical model

The chemical reaction between propane and air at stoichiometric proportions can be simply represented as:

$$C_3H_8 + 5(O_2 + 3.76N_2) \longrightarrow 3CO_2 + 4H_2O + 18.8N_2$$

However, a more detailed look at this combustion reaction shows that it involves a large number of species, and not just the 5 which appear above. Detailed descriptions of such a chemical phenomenon require at least several hundred species and thousands

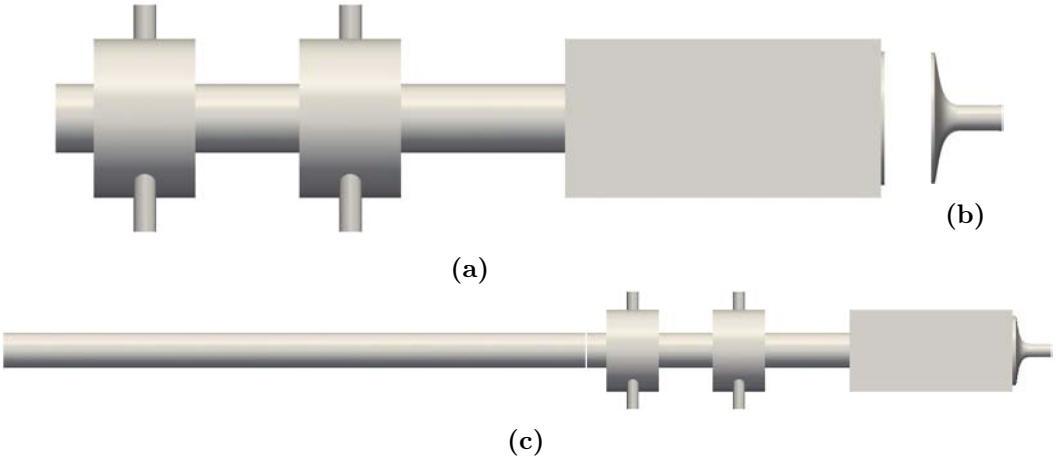

Figure 9.4: Fluid domains. (a) Injection duct and chamber. (b) Nozzle convergent. (c) Complete domain with ICS plenum and convergent outlet.

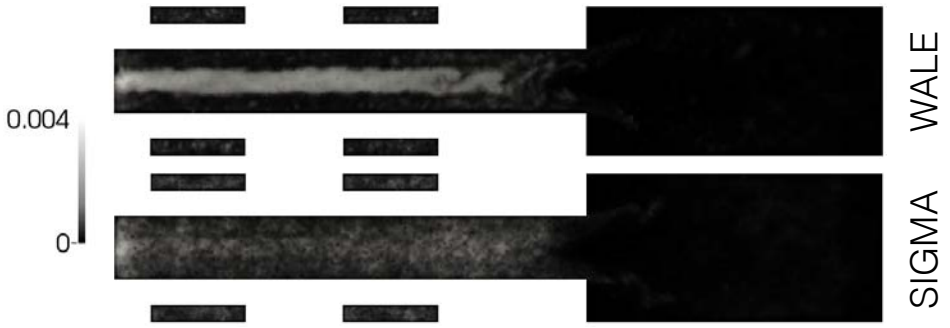

Figure 9.5: Turbulent viscosity (in $\mathrm{kg\,s^{-1}\,m^{-1}}$). Comparison between the WALE (top) and SIGMA (bottom) SGS models.

of reactions. This can be numerically simulated in a perfectly stirred reactor, or in some cases in laminar one-dimensional flames. However, for turbulent LES, the computational and memory cost associated to computing these numerous equilibriums and transporting the chemical species is prohibitive over the large meshes needed. However, the flame properties of interest for LES of a premixed flame are mostly the laminar flame speed s_L and the adiabatic flame temperature T_{adia}. While the combustion reaction can occur in a wide variety of conditions, in the context of this study very few parameters can in fact vary in the fresh gases:

- the fresh gases temperature is fixed at 300 K, and it cannot vary;
- the pressure in the reacting chamber can be subject to some fluctuations, since noise and combustion instabilities are studied. However, detailed mechanisms cover several orders of magnitude of mean pressures. In this study, the pressure is always contained between 2 and 3 bar;
- the system is for premixed and partially premixed operation, but always in lean conditions. The hypothesis that the equivalence ratio $\phi \leq 1$ is therefore made at this point. However, in a turbulent mixing and reacting flow, the control of

the actual equivalence ratio at which the combustion occurs is difficult. The fact that ϕ does in fact stay below 1 will be assessed *a posteriori*, in order to validate this hypothesis.

These restrictions enable considerable simplifications to be made compared to detailed descriptions of the chemical process. Inexpensive single-step schemes can be used to represent with good accuracy s_L and T_{adia} over the range of ϕ encountered in the present conditions. Because none was readily available in the AVBP chemistry database for the combustion of lean propane at the pressures encountered here, a 1-step scheme is derived here for this purpose, called 1S-C3H8-CL.

9.3.1 Reference for the model

Detailed reaction mechanisms are available for propane chemistry (*e.g.* Qin *et al.* (2000)). The CANTERA code of Goodwin (2009) was used to compute adiabatic flame temperature and final composition using an equilibrium computation. A spatially varying one-dimensional laminar free flame was also computed to yield flame speed.

These results were used to optimize a reduced chemistry for propane-air flames near the operating pressure. Several regimes are considered throughout the study: global equivalence ratios ϕ between 0.77 and 0.9 have been used. Moreover, the CESAM-HP setup supports fuel staging, which implies non-premixed combustion and a wide range of ϕ. However, it is designed for lean combustion, hence ϕ is expected to never exceed 1. This hypothesis will be validated *a posteriori* on a non-premixed simulation, as presented in Sec. 9.4 of this chapter. Hence, the simplified chemistry only needs to be validated over a range comprised between lean flammability limits ($\phi \approx 0.5$) and stoichiometry ($\phi = 1$).

Fig. 9.6 shows the result of an equilibrium calculation and the hot gases composition versus ϕ. At least the 10 most abundant species are displayed. It is clear that up to $\phi \approx 0.85$, 4 species are sufficient to capture most of the hot mixture, namely N_2, H_2O, CO_2 and O_2 in order of abundance. Near stoichiometry, O_2 is increasingly consumed by the fuel, and its concentration decreases. Levels of CO cross that of O_2 just before stoichiometry. This is the reason why 2-step schemes generally include CO as an additional specie compared to 1-step schemes. In fact, obtaining good adiabatic temperatures near stoichiometry is a difficult task, as 2 more species (namely OH and H2) are also present in non-negligible quantities. However, in the present case, the burnt gases composition is well reproduced with only 4 species and the fuel up to $\phi \approx 0.9$. For these reasons, a 1-step scheme is chosen to represent this combustion process.

In order to further confirm the model, is was compared to experimental measurements by Metghalchi & Keck (1980). The equivalence ratios investigated in this particular study only ranged from 0.8 to 1.2 in this study, but the CESAM-HP burner is expected to sustain flames at $\phi < 0.8$. Therefore, the results of Metghalchi & Keck (1980) were not chosen for the chemical scheme optimization, but merely to obtain a confirmation. Since no specific measurements were performed at the target

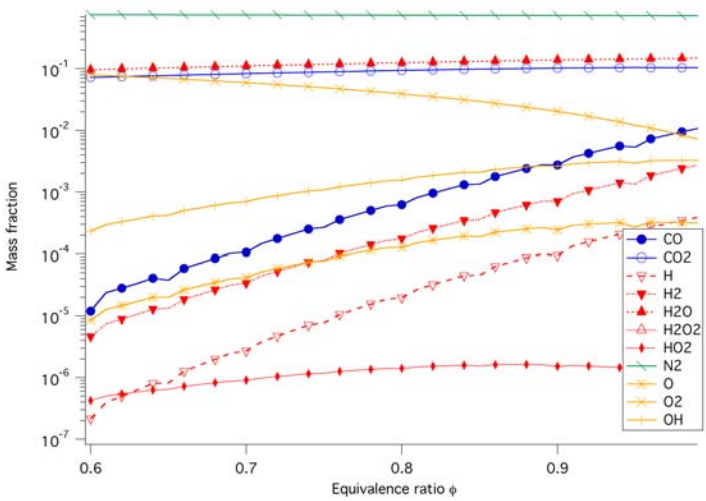

Figure 9.6: Dominant species in burnt gases according to an equilibrium calculation. Detailed chemistry from Qin *et al.* (2000).

pressure of the CESAM-HP setup, namely 2.5 bar, extrapolations of experimental data were used to compute the flame speeds.

9.3.2 Model and results

The choice of a 1-step model, as explained above, leads to excellent final compositions for equivalence ratios up to 0.9. This has a direct impact on the adiabatic flame temperature: Fig. 9.7 displays the adiabatic flame temperature of the detailed chemistry and the 1-step model with 5 total species.

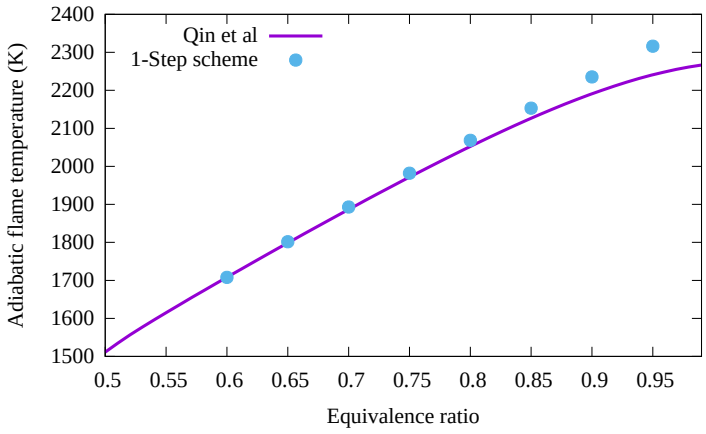

Figure 9.7: Adiabatic flame temperature versus ϕ for the detailed chemistry and the 1-Step model.

The consumption flame speed s_L is also a very important parameter for computation of turbulent combustion, as the flame dynamics will depend directly on it. In

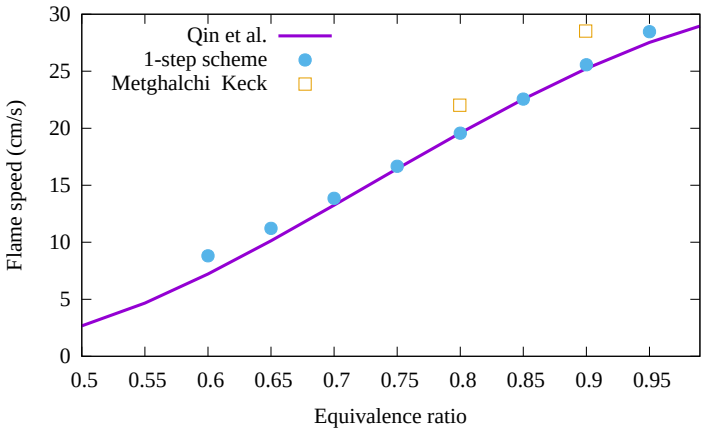

Figure 9.8: Adiabatic flame speed versus ϕ for the detailed chemistry of Qin *et al.* (2000), the 1-step model and the extrapolated values from Metghalchi & Keck (1980)

a 1-step scheme, Poinsot & Veynante (2011) make the hypothesis for lean conditions that the reaction rate $\dot{\omega}_F$ follows an Arrhenius law, and writes:

$$\dot{\omega}_F = BT^{\beta}\rho Y_F e^{-T_a/T} \tag{9.1}$$

where B_1 is called the *preexponential constant*. The authors later show that this implies for the flame consumption speed s_L:

$$s_L \propto \sqrt{|B|T^{\beta}D_{th}} \tag{9.2}$$

This information has been used to tune a 1-step scheme to fit the flame speed simply by modifying B_1. The final equilibrium state is not impacted, as only the thermo-diffusive effects controlling the flame speed are affected. Tab. 9.4 assesses the constants obtained for the single-step scheme, once optimized to best fit the flame speed given by the Qin *et al.* (2000) scheme for $\phi = 0.85$, as this global equivalence ratio has been the most used in the CESAM-HP test bench. $E_a = T_a R$

B_1	E_{ac} (cal/mol)	n_F	n_O	β
1.25×10^{12}	31126	1.097	0.503	0

Table 9.4: Parameters of the single step chemical scheme for propane combustion.

is the activation energy, directly related to the activation temperature. In AVBP, to account for non-unity Lewis number effects the reaction exponents n_F and n_O are also given, and impact the fuel consumption rate $\dot{\omega}_F$ as $\left(\frac{\rho Y_F}{\mathrm{W}_F}\right)^{n_F}$ and $\left(\frac{\rho Y_O}{\mathrm{W}_O}\right)^{n_O}$, respectively (Poinsot & Veynante, 2011).

The resulting flame speeds are displayed in Fig. 9.8. Because of the optimization for $\phi = 0.85$ the agreement between the detailed chemistry of Qin *et al.* (2000) and the 1-step scheme is perfect for this value of equivalence ratio. However, this graph

also shows that the agreement stays very good for values of ϕ in $[0.7, 0.9]$, which is expected to be the bulk of the combustion regimes in this Ph.D. The experimental values do not agree perfectly with the detailed chemistry, but they are however less than 25 % higher, thus confirming the order of magnitude given by the 1-step scheme.

9.4 *A posteriori* validation of the chemical approach

The choice of a single step chemistry has been based on the hypothesis that the combustion process occurred only in lean regimes ($\phi < 1$). Tracking the mixture of fuel and air can be done by introducing the *mixture fraction*, defined assuming unity Lewis numbers as (Poinsot & Veynante (2011)):

$$z = \frac{sY_F - Y_O + Y_O^0}{sY_F^0 + Y_O^0} \qquad \text{where} \quad s = \frac{\nu_O W_O}{\nu_F W_F} \tag{9.3}$$

where Y_F and Y_O are the fuel and oxygen mixture fractions, respectively, and the ^{0} designates the values in the pure streams. ν_F and ν_O are the stoichiometric coefficients. z represents the fuel to oxidizer ratio, with $z = 0$ in pure oxidizer and $z = 1$ in pure fuel. At the stoichiometric mixture, z is noted z_{st}. Burke & Schumann (1928) first represented pure diffusion flame structures in graphs temperature and mass fractions plotted against mixture fraction, known as Burke-Schumann diagrams.

To check the hypothesis on combustion regimes, a scatter plot of temperature versus mixture fraction in the flame is performed on the non-premixed simulation of Chap. 11 (Fig. 9.9) It confirms the preliminary hypothesis that combustion occurs for lean regimes only, since all points are to the left of the dashed line representing the stoichiometric mixture fraction. The width of the mixture fractions occurring in the hot fluid is however large, confirming that this is a stratified combustion regime. The maximum temperatures occurring in the flow are 50 K above the detailed chemistry values, as expected from Fig. 9.7.

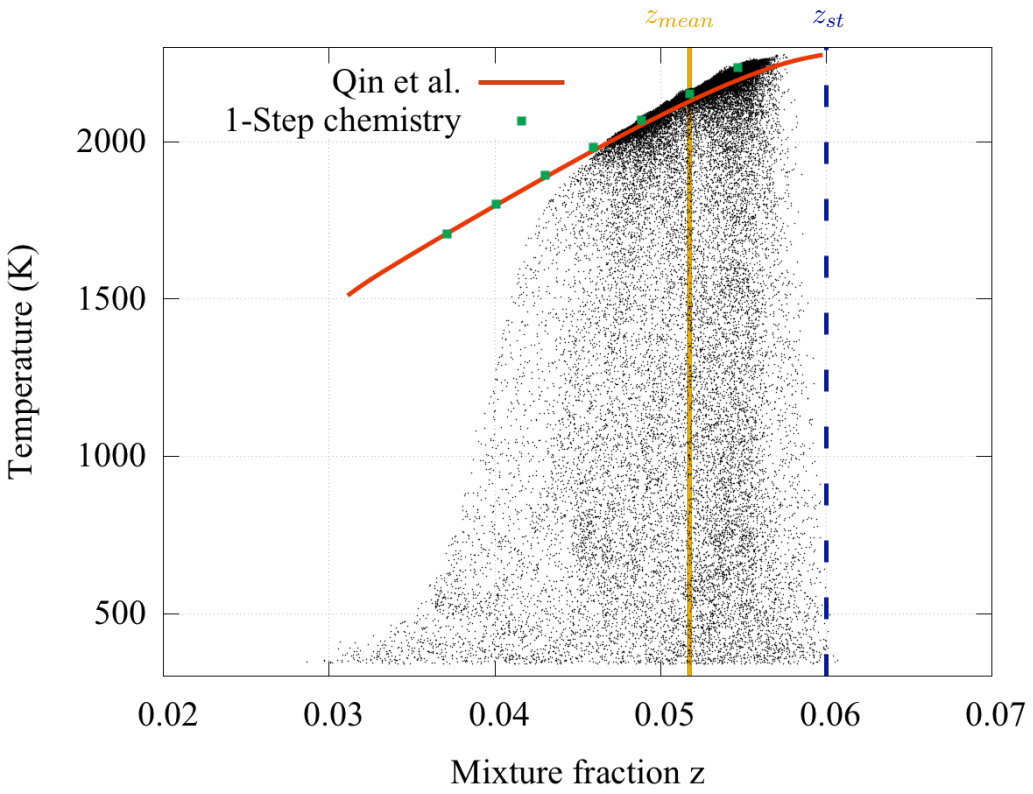

Figure 9.9: Burke-Schumann diagram of temperature versus mixture fraction of random points in the flame zone of the **CHOKED-ST** case. Clipping of cold points has been performed. The full line is the detailed chemistry by Qin *et al.* (2000). Stars are the laminar flame results with the current 1 step chemistry. The vertical solid line is the average value of z, and the vertical dotted line is z_{st}.

Chapter 10

LES of unchoked regimes

*While the experimental operation can be continuous between unchoked and choked regimes, this can have dramatic impact on numerical approaches. A non-choked outlet is a mean for control (via acoustic waves) on the system, and it offers much more flexibility than a choked setup. At the target mass flow rate, the CESAM-HP setup is not choked in cold conditions, hence this case is studied in Sec. 10.2. For reacting conditions, the nozzle is choked. However, it is possible numerically to simply exclude the nozzle from the domain, and replace it by a tunable outlet condition where pressure is imposed (Mesh **MO** of Tab. 9.3). This is done here and results are presented in Sec. 10.3. Finally, the **OPEN** setup offers a unique opportunity to investigate the effect of swirl on flame stablization, and this is done in Sec. 10.3.2.*

10.1 Introduction

Academic test benches often operate at atmospheric pressure for simplicity reasons: the instrumentation of a test rig requires access to the chamber for probing and possible direct optical visualization, which can be problematic for pressurized chambers, as the latter require flow confinement and minimal leakage of the flow. However, the study of combustion noise necessitates a strongly accelerated nozzle flow (see Chap. 5), hence pressurized flow to produce the strong acceleration. As demonstrated in Chap. 4 and 8, a choked nozzle poses a series of numerical difficulties, because it introduces a coupling between mass flow rate, pressure and temperature (Eq. (4.12)).

The study of the unchoked system can however offer valuable information on its dynamics. For low enough combinations of mass flow rate and temperature, the pressure ratio can drop below the critical value necessary to choke the nozzle (Eq. (4.15)). This is the case for the non-reacting CESAM-HP setup, which is therefore naturally unchoked.

Another interesting investigation can be done on the reacting simulation using an artificially unchoked flow: the nozzle is naturally choked for the reacting operating conditions, but the domain can be cut before the nozzle (hence in a low-Mach number area) and pressure imposed at that position. This is done in Sec. 10.3.

10.1.1 Effect of uncertainties on geometry

During the course of the RECORD project, difficulties were encountered in matching the experimental and LES profiles because of uncertainties in the exact swirler geometry: late in the project, an incoherence between the geometries of the test rig and the numerical domain was uncovered. The inner radius of the swirler plenums was incorrect, as shown in Fig. 10.1. Unfortunately, all reacting simulations performed

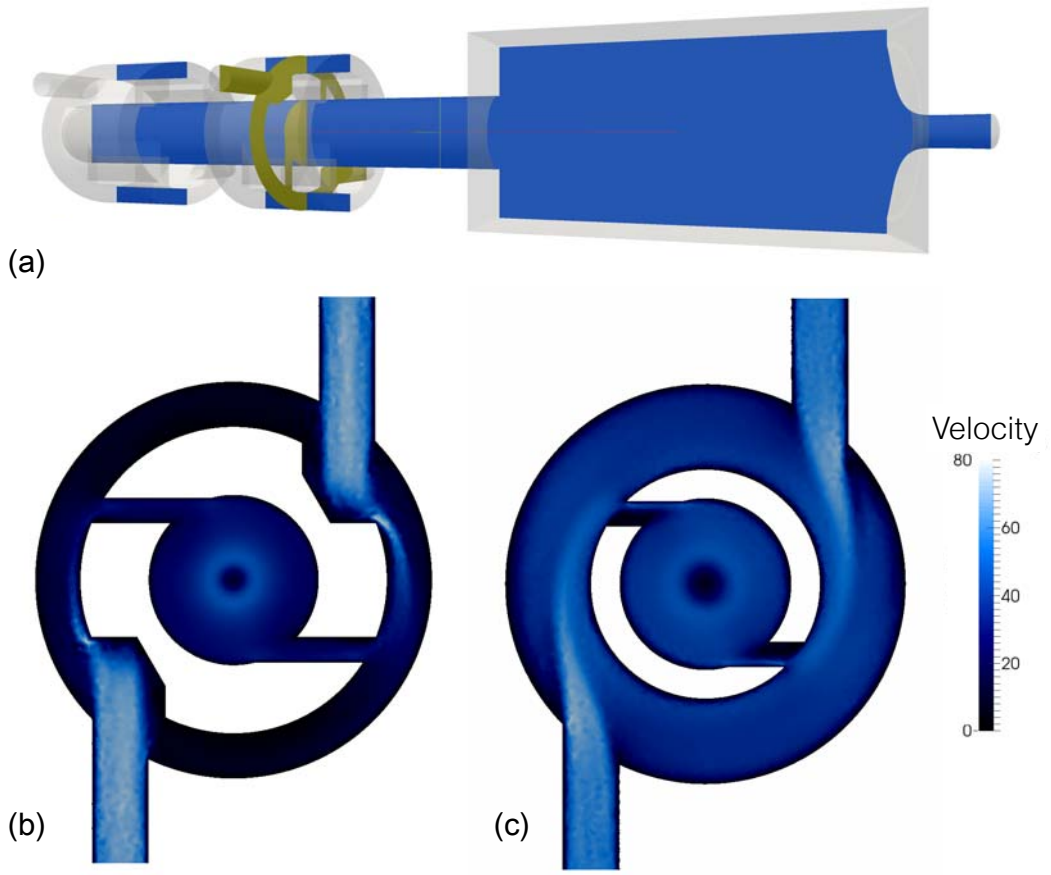

Figure 10.1: Geometry change due to uncovering of an error. (a) Position of the cut in gold. (b) and (c) Initial and corrected geometry in the numerical setup, coloured by velocity magnitude.

on the setup were finished at the time this discrepancy was uncovered, and it was not possible to rerun all of them. However, in order to assess the impact of this modification, new meshes were produced, and cold-flow aerodynamics were once again compared between PIV and LES. This yielded improved agreement, but the trend discrepancies observed with the incorrect geometry were not resolved by the correction. For the sake of coherency with the reacting simulations, the study was continued using the first incorrect geometry. Nevertheless, a comparison of profiles between the incorrect and correct geometry will be performed in Sec. 10.2.

10.2 Non reacting simulations

In order to validate the coherence between the experimental setup and its numerical counterpart, the non-reacting aerodynamics must first be compared. These should yield acceptable agreement before moving on to reacting flow comparisons. The mass flow rate is $18\,\mathrm{g\,s^{-1}}$, equal to the total air mass flow rate in all reacting computations. At 300 K, the nozzle is not choked for this mass flow rate, as the choking mass flow rate in this case is $25.85\,\mathrm{g\,s^{-1}}$.

10.2.1 Operating point

The mass flow rate and flow split of the cold operating point is dictated by the available PIV data. This has been done for the flow parameters given in Tab. 10.1. Temperature of the air at all inlets is 300 K.

	ICS	Upstream injector	Downstream injector
Mass flow rate ($\mathrm{g\,s^{-1}}$)	1	8.5	8.5

Table 10.1: Mass flow rates of air in the non-reacting experiment where PIV data is available.

At the outlet, the only information needed to define the operating point is static pressure. If the domain extended all the way to the atmosphere, a classical value for atmospheric pressure would be used. However, this would necessitate the simulation of the complete nozzle divergent, which is an entire subject of research and is not essential for our core interests here. Instead, the domain with the short nozzle (Mesh **MN** of Tab. 9.3) is used, and an equivalent pressure imposed at the corresponding outlet.

The nozzle divergent of the CESAM-HP bench constitutes a wide expansion, and the area between the inlet and outlet is multiplied by a factor 32. Even though basic nozzle design criteria were followed during its conception, the test bench is not instrumented and no information is available on the flow inside. Without this information, there is no guarantee that the flow behaves isentropically or in a quasi-1D manner. In fact, the problem of correct diffuser design has long been known to cause flow separation (Patterson, 1938). The pressure inside the chamber can therefore not be inferred with a simple quasi-1D theory, as in Chap. 4.

Experimental measurements of pressure reveal that for this operating point the average chamber pressure is 116 923 Pa. Supposing that the flow behaves isentropically and in a quasi-1D manner in the convergent yields, according to the theory of Chap. 4, the equivalent pressure at the outlet. This assumption is safe, because the convergent is very short and flow contraction is less prone to flow separation than the divergent (Patterson, 1938). The resulting pressure for the outlet of the domain (the nozzle throat) is 102 700 Pa. Information regarding the nozzle is grouped in Tab. 10.2.

Chamber static pressure (Pa)	Outlet static pressure (Pa)	Chamber Mach	Throat Mach
116923	102700	0.0078	0.455

Table 10.2: End chamber and nozzle parameters in the non-reacting simulation.

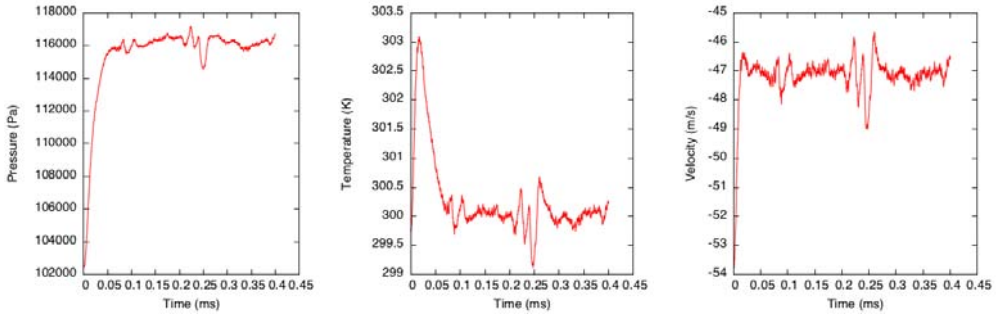

(a) **(b)** **(c)**

Figure 10.2: Evolution of three significant variables at the center of the dump plane: (a) Pressure, (b) Temperature and (c) Velocity. The transient regime up to approximately 5-10 ms gives way to the established regime, used for obtaining mean quantities.

10.2.2 Numerical results

The simulations were run for 400 ms. Fig. 10.2 shows the evolution of pressure, temperature and velocity at a probe located in the center of the dump plane. The transient regime can be seen up to approximately 10 ms. Then, the flow is recorded and averaged over time. The resulting mean and root mean square (or *rms*) values are directly comparable to experimental measurements.

Fig. 10.3 shows a slice of the domain. The flow displays a clear recirculation bubble in the center of the chamber. If this recirculation still exists in the reactive

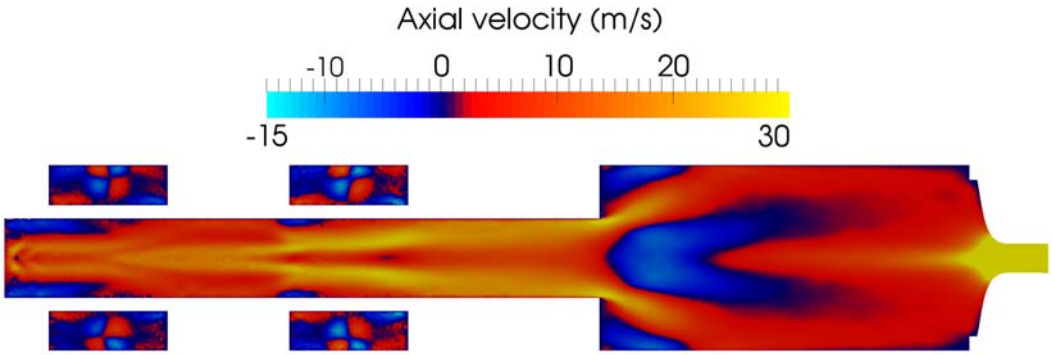

Figure 10.3: Non reacting simulation. Slice of the domain at $z = 0$, coloured by axial velocity.

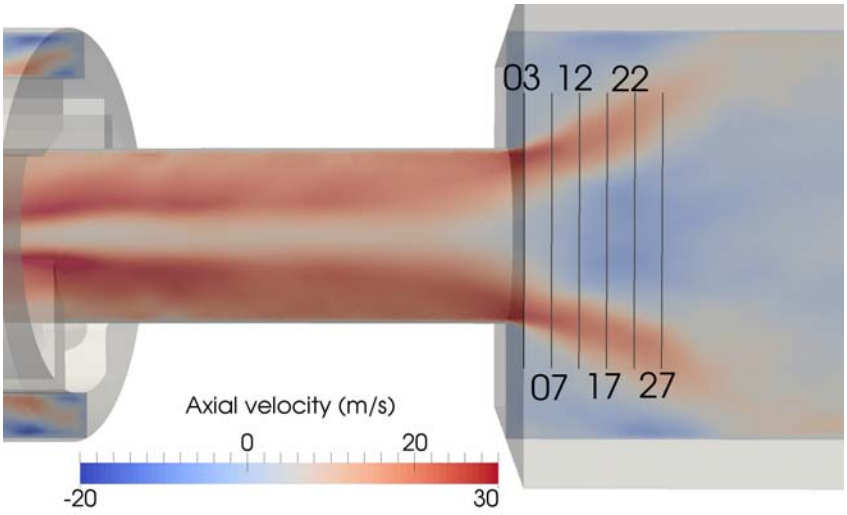

Figure 10.4: Lines used for comparison between experiments and numerics. Numbers near the lines refer to their approximate axial position measured in mm from the dump plane.

case, it will be prone to stabilize the flame aerodynamically, thus relieving the need of a flame holder.

10.2.3 Comparison with experiments

In order to compare experimental and LES mean profiles, 6 lines of measurements are chosen. They correspond to lines of PIV measurements in the experiment. Fig. 10.4 shows these lines in the geometry. The lines are numbered by their approximate axial position from the dump plane in mm. The axial and radial velocity, as well as the axial velocity RMS have been recorded experimentally on the measuring lines. They are compared to the LES results in Fig. 10.5. A reasonable qualitative agreement is found between LES and PIV measurements. However, the following discrepancies can be noted:

- the width of the expansion cone is smaller in the LES than the PIV. Very close to the dump plane this is barely visible, but the difference gradually increases with the axial distance;
- the axial velocity "bump" is qualitatively reproduced in the last LES line, but is generally not in agreement with the PIV;
- unsurprisingly, the insufficient radial expansion is also visible on the radial velocity and the axial velocity RMS values.

Numerous efforts have been conducted to investigate these discrepancies. In the context of the RECORD European project, two other simulations were performed. One, based on the same mesh but with the cell-entered compressible LES code CEDRE from ONERA showed very similar profiles to those of AVBP. The other, conducted on the same geometry but a different and coarser mesh by TU-Darmstadt with the incompressible LES code RR PRECISE, has also lead to underprediction of

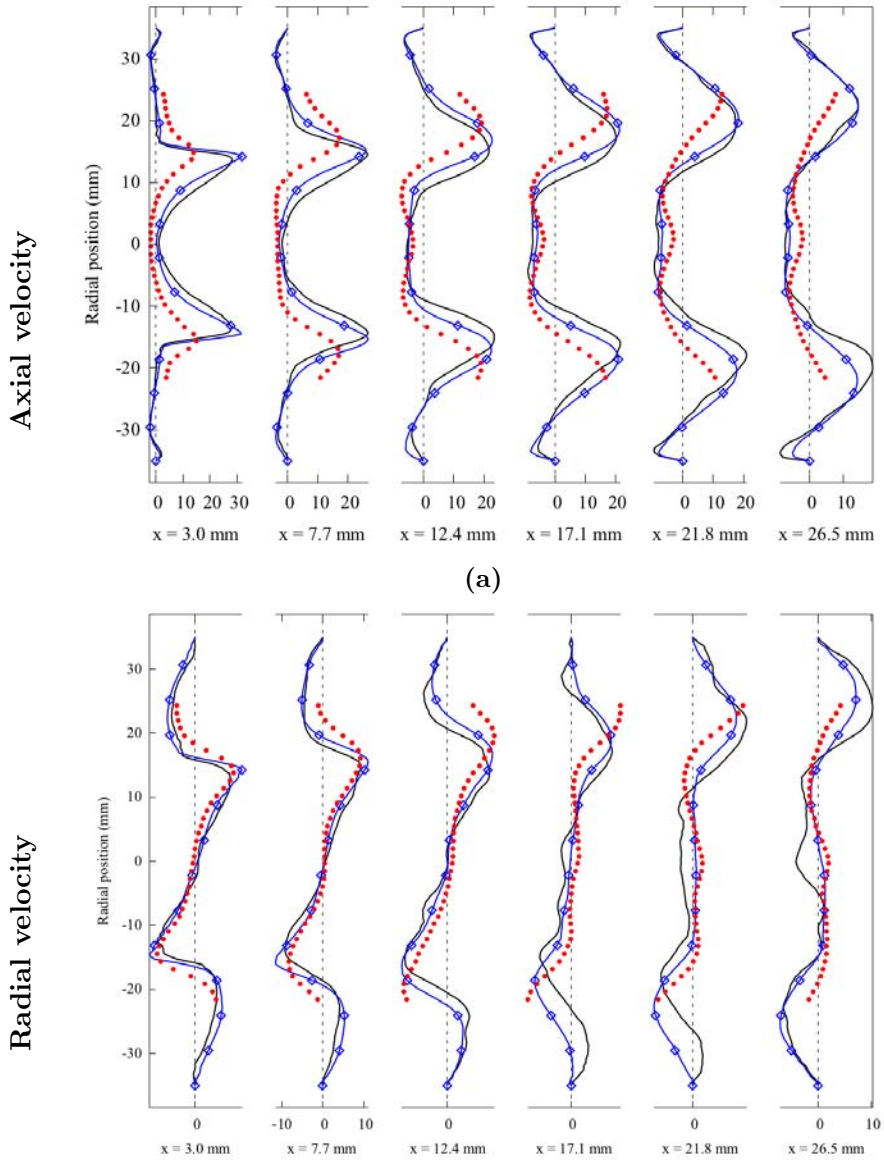

Figure 10.5: Mean velocity profiles (in $\mathrm{m\,s^{-1}}$) along 6 the lines of Fig. 10.4. (a) axial velocity, and (b) radial velocity. Red dots: PIV, blue lines with diamonds: LES with the wrong geometry, Black lines: LES with the correct geometry.

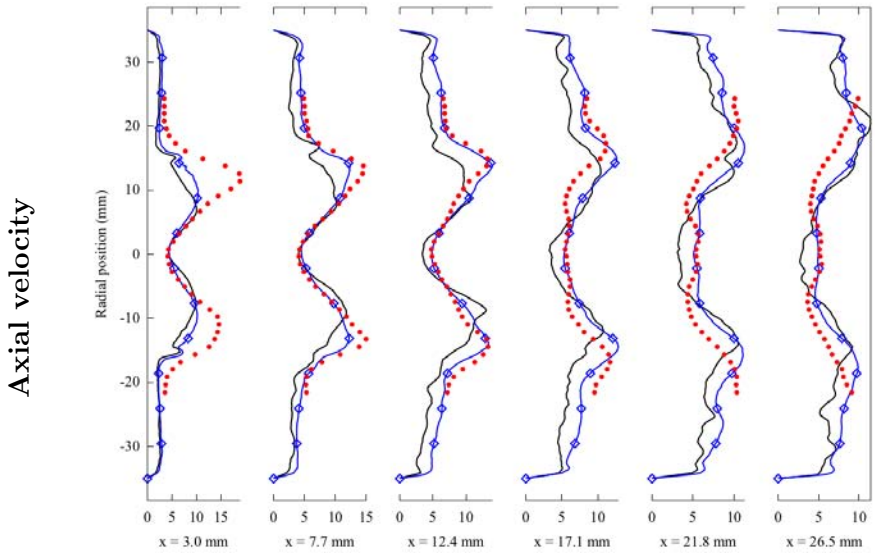

(a)

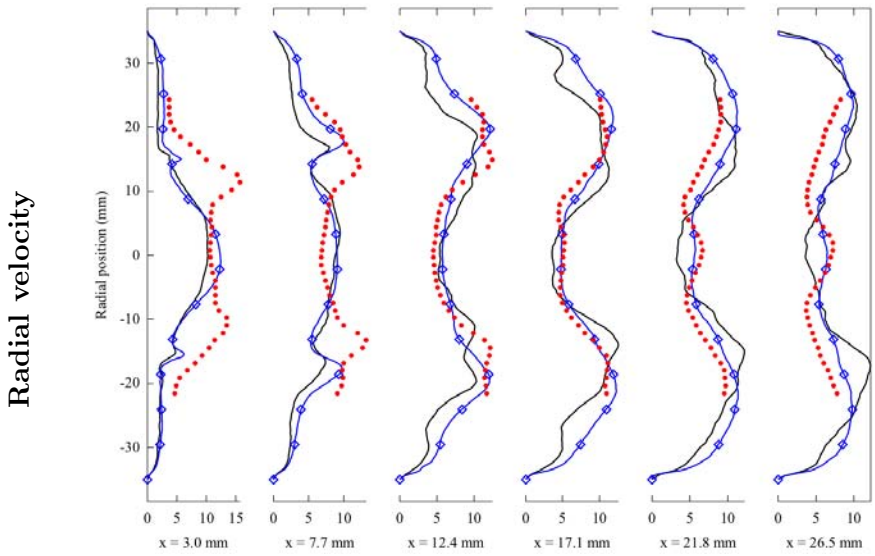

(b)

Figure 10.6: Root mean square velocity profiles (in $\mathrm{m\,s^{-1}}$) along 6 the lines of Fig. 10.4. (a) axial velocity, and (b) radial velocity. Red dots: PIV, blue lines with diamonds: LES with the wrong geometry, Black lines: LES with the correct geometry.

the expansion cone. The experimental operators were confident on the measurement techniques. However, they noted that at the time of these measurements, high-speed PIV was unavailable, and a deeper analysis of the chamber dynamics was not possible. As will be shown in the reacting case, the setup is very sensible to operating conditions, which could explain that a phenomenon has not been captured by the various simulations but occurs in the setup.

10.2.4 Impact of the geometry discrepancy correction

As can be seen from Figs. 10.5 and 10.6, the geometry correction has an impact on the profiles: the old geometry (blue lines with diamonds) and new one (black lines) do not overlap perfectly. However, problems with flow expansion angle and peak levels remain equally strong with both setups. This confirms that the general aerodynamics are only slightly impacted by the geometry change. On the basis of this observation, the reacting simulations are considered representative of the actual setup, even though they were all performed with the wrong inner swirler diameter.

10.3 OPEN reacting simulations

Reacting simulations with open outlet conditions (without nozzle) are lead on the **MO** of Tab. 9.3. This first approach, described in Chap. 9, coupled with the NSCBC methodology, is "soft" in terms of reflections: it enables a thorough control of the acoustic behavior of the system. Reacting LES can be the source of numerous sources of unphysical perturbations. The combustion model and numerical scheme can be noisy. The initialization strategy is rarely physical, and can produce high noise levels. Finally, damping mechanisms present in the real bench are not necessarily modeled in the LES. For all these reasons, the open end simulations offer a solution to study a stable flame by letting all waves leave the domain without reflection.

However, in the real bench, the choked nozzle has an important influence on the chamber pressure. The target pressure chosen in this case is 2.5 bar.

No comparisons can be made with the experiments in the **OPEN** case. The stability of this setup is due to the non-reflecting outlet replacing the normally strongly reflecting nozzle. However, this setup gives important insight on the flame behavior. It can for example lead to linear instability studies of the closed case, as done in the study of thermoacoustic instabilities.

10.3.1 Numerical simulation

The cold air flow of the previous section is now replaced by a mixture of propane and air at 300 K. The chemistry model is activated, and an AVBP "gas out" tool is applied. This procedure consists of replacing a region of the flow with hot burnt gases. Fig. 10.7 shows the initial field used here. The velocity field from cold non-reacting simulations is kept. The pressure is increased to its target value for the reacting case, and the hot gases are then deposited in most of the combustion chamber (see

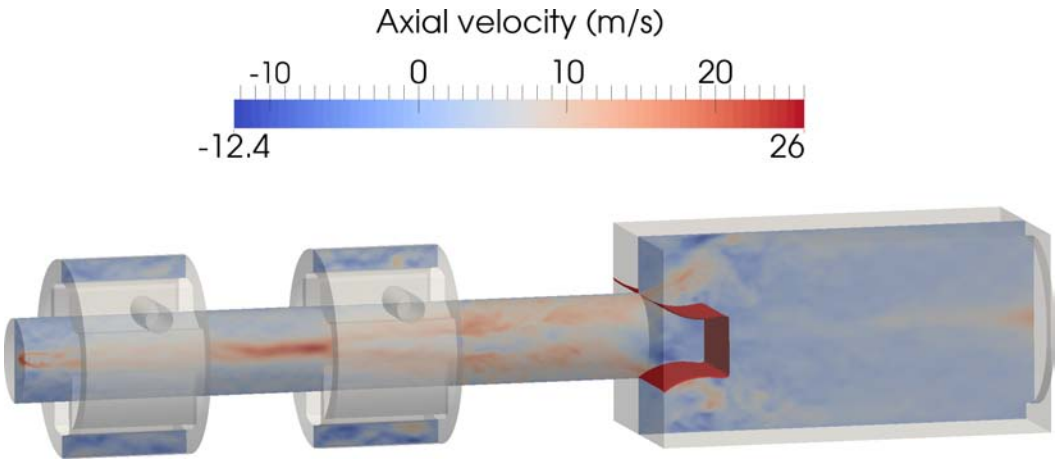

Figure 10.7: Initial field for reacting open simulations. Red surface is 1000 K isoline. Colored plane represents axial velocity.

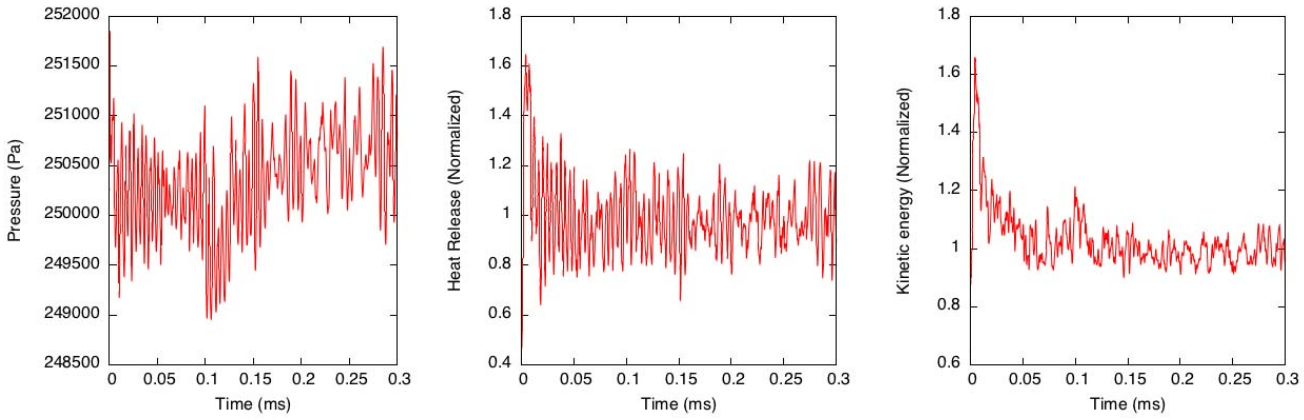

(a) **(b)** **(c)**

Figure 10.8: Transient regime after the flame is ignited. (a) Mean pressure over the domain, (b) Global heat release and (c) Global kinetic energy.

fig. 10.7 for the exact shape: the limits of the burnt gases is shown with the 1000 K isosurface). This leads to the ignition of the cold flow, and the development and stabilization of the flame. Characteristic variables of the domain are averaged and presented in Fig. 10.8. After an initial period of 50 ms, the flame seems to stabilize. The flow is then recorded for the next 250 ms to produce average fields, visible in Fig. 10.9.

Several observations can be made for this case:

1. The flame stabilizes near the dump plane, where it is expected. Indeed, the chamber was conceived with expectations that the flame would stabilize in the chamber inlet plane.

2. The central recirculation zone of the cold case still exists in the reacting case.

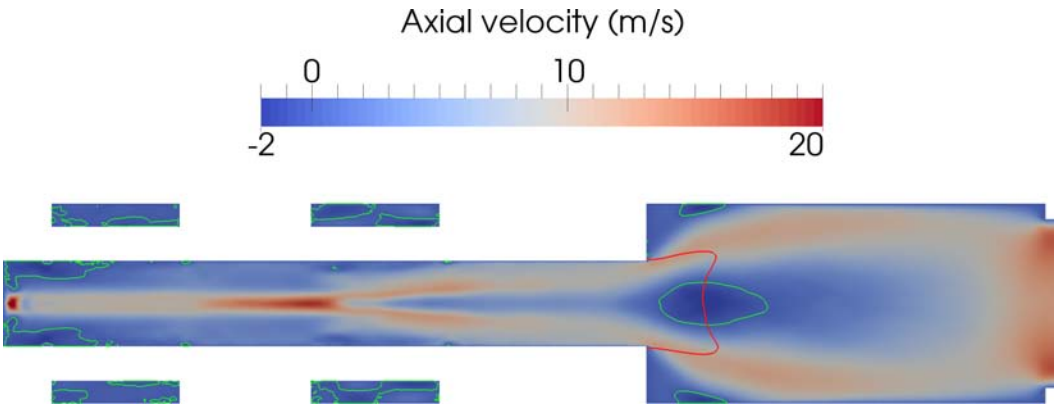

Figure 10.9: Reacting open simulation. Slice of the domain at $z = 0$, coloured by axial velocity. Reacting run without nozzle. Green isoline shows null axial velocity. Red line is 1200 K isoline.

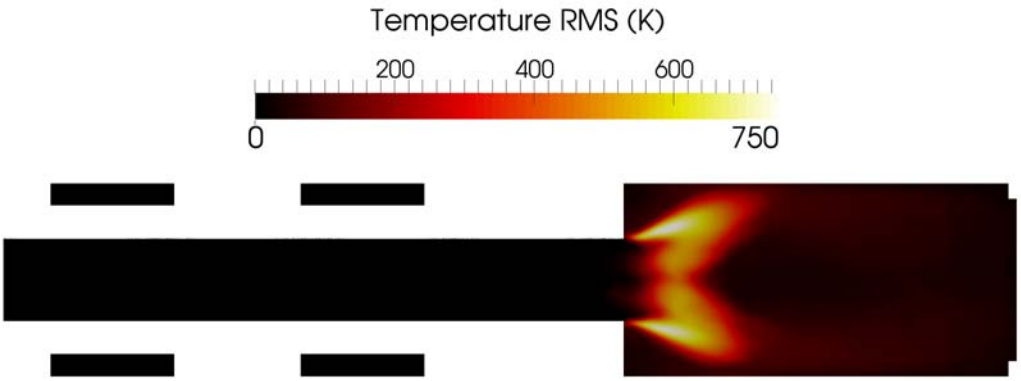

Figure 10.10: Slice of the domain at $z = 0$, coloured by temperature root mean square. Reacting run without nozzle. Red line is 1200 K isoline.

It's position suggests that it helps the flame stabilization by keeping a pocket of hot burnt gases close to the dump plane, thus reigniting the fresh mixture.

3. Oscillations of pressure and heat release (Fig. 10.8) suggest however that this mean position is subject to time fluctuations. The RMS field of temperature (Fig. 10.10) shows that the flame position varies strongly across the length of the simulation even if it always remains in the chamber.

A Fourier analysis of heat release fluctuations reveals that strong perturbations occur in the 200 - 240 Hz range (Fig. 10.11). A probe has been placed on the outlet to record flow characteristics there. A simple acoustic decomposition can be done to yield downstream and upstream travelling waves: Fig. 10.12 shows that strong acoustic perturbations reach the outlet of the domain. The waves entering the domain have much smaller amplitudes, thus demonstrating the efficiency of the non-reflecting outlet condition. This activity does not affect the mean flow very strongly, since the

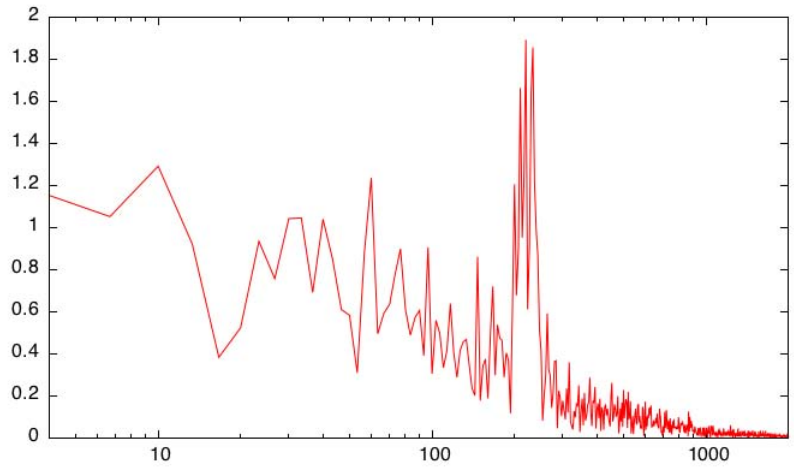

Figure 10.11: Discrete Fourier Transform (arbitrary units) of the heat release signal for the open reacting run. Strong activity is visible in the 200 - 240 Hz range.

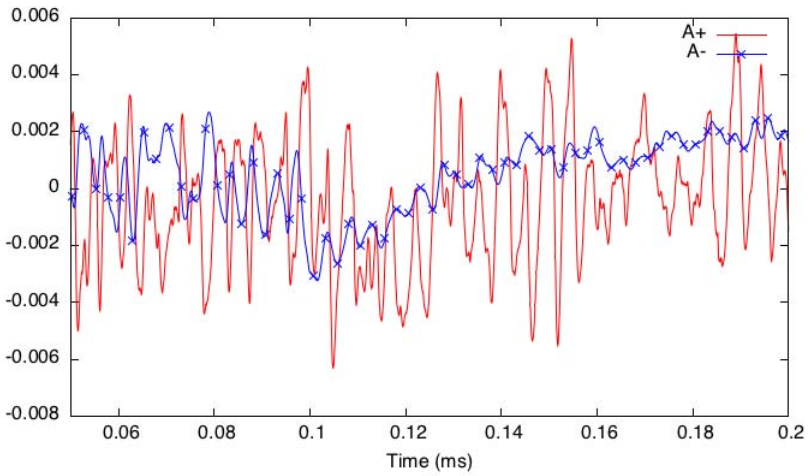

Figure 10.12: Open reacting case: wave decomposition on the center of the outlet patch. A^+ is the downstream travelling wave. A^- is the upstream travelling wave.

acoustic energy exits the domain gradually as it is created, and there is no energy buildup. However, this observation is worrisome for the full simulation with the choked nozzle. If the setup is closed, this energy could be trapped in the chamber and the perturbation intensity could grow to high levels.

10.3.2 Swirl sensitivity study

Chap. 11 will show that the aerodynamic stabilization of this flame with the choked nozzle is difficult. One advantage of the numerical approach is that sensitivity studies can be lead in setups otherwise impossible to produce experimentally. In the following section, the **OPEN** setup (without nozzle) is studied with LES to perform a sensitivity study to the swirl number Sw of the cold flow. To do this, cold non-reacting simulations are used to evaluate the swirl number at the flame, and reacting simulations are then performed to show the flame stabilization position.

10.3.2.1 Swirl definition and measurement

The main parameter controlling the flow swirl is the flow split between ICS ($\dot{m}_{ICS}$) and the two swirled injectors ($\dot{m}_1$, $\dot{m}_2$). The flow through the ICS is not swirled, whereas the flow through the two plenums is strongly swirled. As a result, the staging balance between the ICS and the plenums controls the flow swirl at the dump plane. Swirl is measured in the simulation according to the classical formula:

$$Sw = \frac{\iiint_{(S)} \rho U (rW)\, dS}{R \iiint_{(S)} \rho U^2\, dS} \tag{10.1}$$

where S is a section normal to the flow axis and R is the duct radius. The choice of this section is difficult for complex industrial swirler geometries. Usually the plane is chosen close to the flame, but in a section representative of the swirler size and not of the chamber. The present burner however is fed by a constant section tube with no geometric perturbations in the last 70 mm before the dump plane. Swirl can be computed according to Eq. (10.1) in any section before the burner.

Kitoh (1991) showed experimentally that far from inlet or outlet side effects, swirl in a tube is expected to decay exponentially with the distance from inlet, according to:

$$Sw = Sw^{ref} exp\left\{2a_1 \frac{x - x^{ref}}{d}\right\} \tag{10.2}$$

where Sw^{ref} and x^{ref} are the swirl number and axial position at a given reference point, a_1 is the decay coefficient, a negative value, and d the tube diameter. The same study suggested orders of magnitude of -0.01 for a_1, so that when the swirled flow is maintained for many tube diameters, strong swirl decay is observed. It offers no correlations for Re below 50000. In the present case, $Re = 20000$ and the correlations cannot be directly compared. However, for the values of Sw encountered in this study, these correlations have little dependency on Re, as shown in Tab. 10.3.

	Re	a_1
Kitoh (1991)	50000	-0.014
	100000	-0.013
	150000	-0.013
Present study	20000	-0.03

Table 10.3: Exponential decay correlations by Kitoh (1991) and in the present study

The values of a_1 can therefore be extended to this study as an indication of similar behavior.

Here the swirled flow only spans approximately 2 tube diameters before reaching the dump plane however, hence the decay is expected to be small and approximately linear, and it simplifies to:

$$Sw \approx Sw^{ref}\left(1 + 2a_1\frac{x - x^{ref}}{d}\right) \tag{10.3}$$

Fig. 10.13 shows the swirl number as a function of axial position in the current setup, for ICS00 in non-reacting conditions. Three different sections can be identified

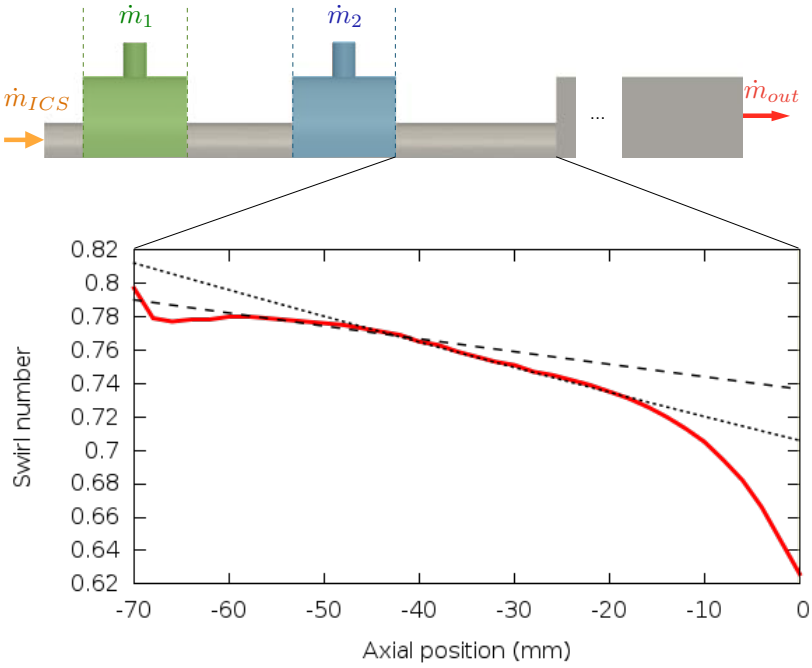

Figure 10.13: Spatial decay of swirl in the second part of the injection duct. Solid line : time-averaged swirl number along the injection tube taken from LES. Dump plane is at $x = 0$. Dashed line: Kitoh (1991) correlation with $a_1 = -0.015$. Dotted line: $a_1 = -0.03$

between the last injector and the dump plane:

$-70\,\text{mm}-45\,\text{mm}$: the flow swirl is not yet established after the second swirl plenum:

−45 mm−15 mm: the swirl is established, and decreases approximately linearly with axial position, as expected from previous studies Kitoh (1991);

−15 mm0 mm: the effect of the vortex breakdown in the chamber changes the value of swirl.

In the linear decrease section, the fit with the results of Kitoh implies a value of a_1 that is doubled. However, the swirl generation method used by Kitoh differs from the double swirler system presented here. Therefore, obtaining the exact same correlations is not expected. The similarities are nevertheless sufficient to conclude that the swirled flow reaches a well described state of decay before it enters the chamber.

As a result, the swirl that would be achieved at the dump plane if no vortex breakdown occurred in the chamber is higher than the one measured directly at that position. The swirl measured 10 mm before the dump plane is a good measure of this theoretical value. For this reason, the reference position for all swirl estimations hereafter is $x = -10$ mm.

10.3.2.2 Effect of swirl on flame stabilization

For **OPEN-NR** swirl sensitivity investigations, the following swirl-control strategy is used: the total mass flow rate is kept constant while the value of mass flow rate through the ICS is varied between 0 and 20% of the total mass flow rate. Each case is numbered as ICSXX where XX is the percentage of mass flow rate through the ICS. The two experimental configurations have a 5.6% ICS mass flow rate.

A preliminary study has been conducted with extreme values for the ICS mass flow rate, namely ICS00 and ICS20. It exhibits two different stabilization positions for the flame:

- ICS20 is the case with lowest swirl number. It exhibits a typical 'M' shaped flame fully stabilized inside the combustion chamber. The swirl number measured in this case is 0.62.
- ICS00 shows a different behavior. Independently of the initialization procedure, the flame eventually propagates upstream all the way to the ICS. It then stabilizes in this position, referred to hereafter as the 'flashback' position. The swirl number measured in this case is 0.71.

The previous analysis confirms, as expected, that swirl controls the flame stabilization. A study of flame stability versus swirl number has been conducted. The flow is ignited in the **OPEN** configuration for several ICS mass flow rates. Run times of 100 ms are used to show whether the flame stabilizes in the chamber or in the swirl tube. Results are summarized in Tab. (10.4). The critical swirl number leading to flashback is of the order of 0.7. 5% mass flow rate through the ICS is not enough to prevent flashback in the reacting **OPEN-NR** setup. 10% is sufficient. This conclusion cannot however be directly transposed to the **CHOKED** system. To do so, it must be shown that the flame stabilization point is robust to the various perturbations that it will undergo in the complete system and especially to thermoacoustics.

Case name	ICS00	ICS05	ICS10	ICS20
$\dot{m}_{ICS}/\dot{m}_{total}$	0	0.05	0.1	0.2
Swirl number	0.71	0.70	0.64	0.62
Flashback ?	Yes	Yes	No	No

Table 10.4: Flame stabilizing position for each configuration

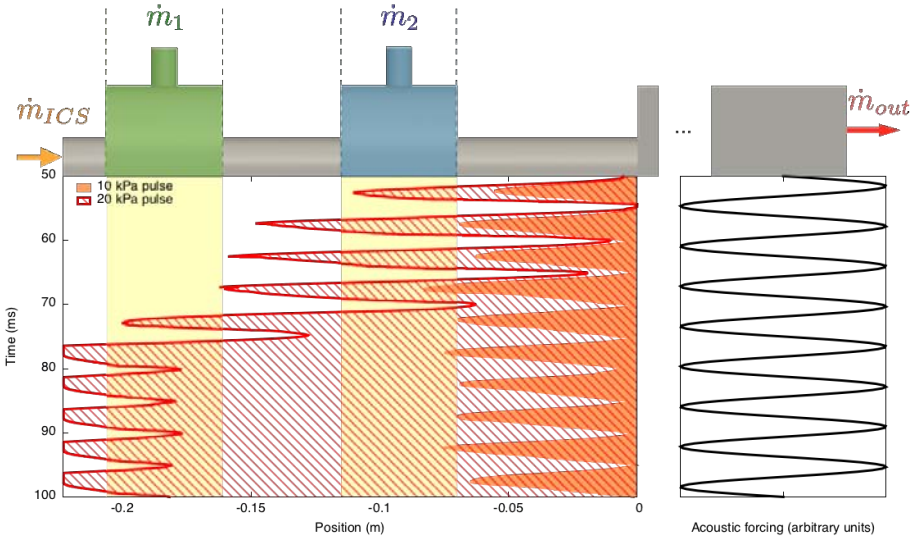

Figure 10.14: Flame tip position versus time for two acoustic forcing strengths.

10.3.3 Forced outlet numerical investigation

The following section discusses the effect of acoustic forcing on flame stabilization. As mentioned above, no experimental data is available for these cases, and their purpose is only to assess the flame response to independent parameters. In order to evaluate the robustness of the flame stabilization, the **OPEN** setup in the ICS10 case (10% of the flow is fed through the ICS) is perturbed at the exit plane with a harmonic acoustic perturbation (`OUTLET_RELAX_P_PULSE` in AVBP). This wave then travels upstream, changes the local velocity and triggers a change in the flame position.

Starting from the naturally robust ICS10 case, two excitation strengths are imposed: 10 kPa and 20 kPa. The frequency is fixed (200 Hz) and it matches approximately the first acoustic mode of the **CHOKED** configuration. Results for each strength are shown in Fig. 10.14.

The 10 kPa case shows that a strong acoustic wave is able to affect the flame, but unable to force a complete flashback : the flame tip enters the swirl tube in phase when the velocity perturbation resulting from the acoustic wave is negative and carries the flame upstream. However, it exits the tube when the acoustic velocity changes sign, and its upstream position (from the dump plane) never exceeds approximately 7 cm in the tube. A different behavior is observed for the 20 kPa forcing. The flame

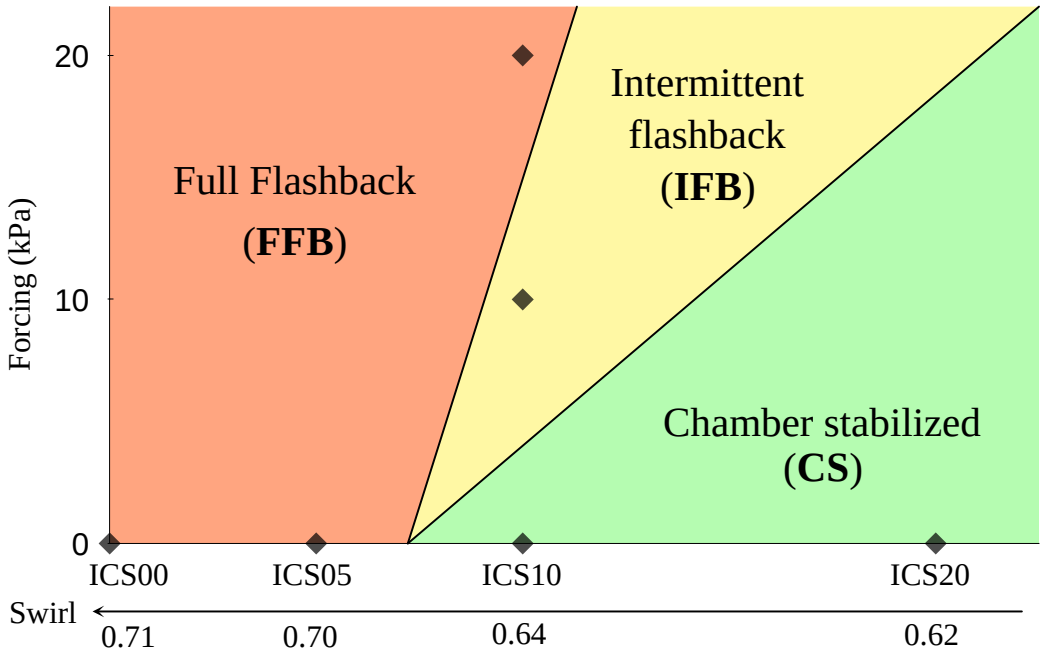

Figure 10.15: Schematic stability map of the **OPEN** setup versus swirl number Sw and forcing amplitude (in kPa). Symbols: actual LESs performed.

tip in this case progressively recedes in the swirl tube, until it reaches the ICS and stabilizes there, leading to a permanent flashback. This combination of vortex core propagation and acoustic perturbation is called acoustically induced vortex core flashback (AI-VCF) in the rest of this paper.

10.4 Conclusion

OPEN-NR LES (cases where the outlet nozzle is removed and replaced by a plane here pressure is controlled) have shown the link between swirl and flashback occurrence, and **OPEN-FO** LES (similar to **OPEN-NR** but forced at the outlet) investigated the robustness of a chamber stabilized flame. Results are summarized in Fig. 10.15. Several conclusions arise from this numerical investigation:

- as expected, swirl is an important control parameter for flame flashback. Higher swirl values lead to flashback-prone configurations. Underneath a critical swirl value (0.7 here), no flashback is observed for an unforced flame in CESAM-HP.
- a flame with sufficiently low swirl will exhibit intermittent VCF (Vortex Core Flashback) when submitted to pressure oscillations, as could be expected because of the flow reversal induced by the acoustic velocity perturbations;
- sufficiently high acoustic forcing triggers a permanent change in flame stabilization and full flashback.

Chapter 11

Choked flow study

*Choked outlets are commonly used in combustion chambers of real gas turbines. In the CESAM-HP case, the chamber pressure is high enough for the nozzle to be choked at all reacting operating points. This chapter presents the results of the LES of the **CHOKED** setup, where the compressible nozzle is included in the computational domain. In Sec. 11.1, practical details about the two chosen operating points and the initialization strategy are given. Sec. 11.2 then proceeds to describe the first, fully premixed LES of the **CHOKED** setup, where a flashback is induced by thermoacoustics. Sec. 11.3 describes the second operating point, in which fuel staging is applied, leading to a stable, dump-stabilized flame. In Sec. 11.4, acoustic tools from Chap. 7 are applied to the CESAM-HP configuration in an attempt to shed light on the flame stability problems observed in the LES.*

11.1 Compressible LES strategy

The complete CESAM-HP setup can only be correctly represented numerically if the outlet acoustic behavior is accurate. In this case, a choked nozzle ends the domain, and no NSCBC-type boundary condition can reproduce its acoustic reflection coefficient. Since AVBP is a compressible code, it can compute unsteady high-speed flows, which can therefore be included in the computational domain and yield the exact acoustic behavior. Meshes including the nozzle will therefore be used in this study, *i.e.* **MN** and **MNI** (Tab. 9.3). In fact, only the converging section and a small length of the diverging section are included in the LES, as once the sonic line is included in the numerical domain, the acoustic behavior upstream is completely determined by the flow upstream of the choked zone. AVBP's capacity to compute the flow through this nozzle, as well as tools to monitor these simulations have been demonstrated in Chap. 8.

11.1.1 Operating points

The test bench is fed with cool pressurized air at 300 K and 2.5 bar. As described in Tab. 9.1, two points were retained for this study following the experimental results.

- a **PREMIXED** point were a fuel-air mixture with $\phi = 0.9$ is sent through both upstream and downstream injectors;

- a **STAGED** point were a rich mixture containing all the fuel was injected through the downstream stage, and only air was sent through the upstream one. The overall equivalence ratio was $\phi = 0.85$.

11.1.2 Initialization strategy

The flow in the CESAM-HP setup is very different in the cold and hot reacting configurations. The average chamber pressure increases when the flow is ignited and the nozzle chokes. Experimentally, operating points are achieved by igniting the flow at a low mass flow rate, then gradually increasing the inlet mass flow rates according to optimized "paths". The complete process lasts several minutes. Numerically, this realistic ignition and pressure rise sequence is unachievable because of the very long physical times involved. For this reason, using the cold field as initial condition for the reacting case is an expensive path, and another solution was used here.

Indeed, an initial solution for the reacting pressurized field is readily available at this stage: the OPEN reacting simulation is stabilized at the correct pressure, because it is directly imposed at the outlet. However, the OPEN domain does not overlap the CHOKED domain, since it does not include the nozzle. Fig. 10.12 shows that the acoustic amplitudes at the end of the OPEN chamber are of the order of 0.5 % maximum. The objective of an initialisation strategy should therefore be not to exceed a 1 % pressure jump between the OPEN simulation and the matching nozzle, otherwise a strong acoustic wave would be present in the initial field and disturb the simulation. Initializing the nozzle is not a straightforward task however: since it operates under choked conditions, it behaves according to Eq. (4.12). Its geometry is fixed, hence the Mach number distribution too. Since the pressure is fixed by the chamber simulation, the only variables of adjustment are the mass flow rate and the temperature. NSCBC conditions can be adjusted to many sets of variables, and a condition available in AVBP called `INLET_RELAX_P_T_Y` enables to give target values of pressure, temperature and gas mixture, as the name suggests. The mass flow rate through the nozzle is therefore not exactly right compared to the chamber simulation, but this does not produce any violent sound wave that might perturb the system.

Bearing these arguments in mind, an initialization strategy is derived for the setup, in which a solution for the nozzle that is exactly compatible with the OPEN solution is created and used in conjunction with this OPEN solution. Fig. 11.1 describes the entire strategy which can be summarized as follows:

1. an instantaneous snapshot of the OPEN reacting simulation is identified;
2. a small domain including the nozzle and starting one half chamber height from it is fed with these conditions;
3. once the nozzle simulation is converged, it is merged with the instantaneous OPEN simulation.

A view of the NOZZLE domain and a slice of temperature is shown in Fig. 11.2 to illustrate this initial simulation.

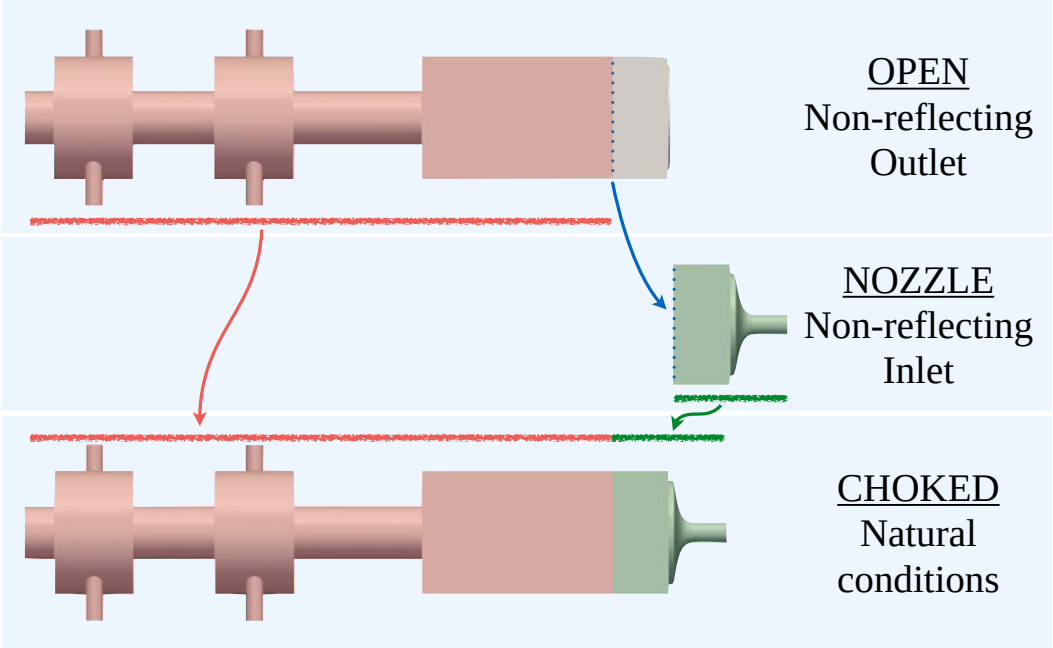

Figure 11.1: Initialization strategy for the CHOKED setup. An instantaneous solution for the OPEN setup is identified. A small domain including the nozzle and the end of the combustion chamber is created, and it is fed by the exact values of the OPEN snapshot. Once converged, both solutions are merged to generate the final CHOKED initial solution.

11.2 CHOKED-PR: Auto-excited AI-VCF in the fully premixed case

Tab. 9.2 has shown the different geometries used in this Ph.D. It is reminded here for simplicity of reading. The flame sensibility to flashback when acoustic oscillations are imposed has been exposed using the **OPEN-FO** test cases in Chap. 10. The **CHOKED-PR** is therefore used now to observe the flame stabilization behavior in the complete natural setup. A 90 ms LES run of the **CHOKED-PR** test case

	OPEN Setup (Fig. 9.3a)		**CHOKED** Setup (Fig. 9.3b)	
Case name	OPEN-NR	OPEN-FO	CHOKED-PM	CHOKED-ST
Domain	OPEN	OPEN	CHOKED	CHOKED
Outlet	**Non-reflecting**	**Acoustic forcing**	Choked nozzle	Choked nozzle
Operating Point	PREMIXED	PREMIXED	**PREMIXED**	**STAGED**
Exp. data	NO	NO	YES	YES

Table 11.1: Numerical setups for the CESAM-HP test bench

with ICS10 flow split has been conducted. In order to observe the flame stabilization behavior during this run, the most upstream flame position on the x axis is tracked

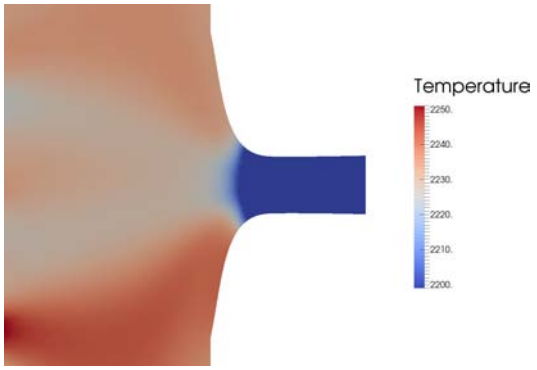

Figure 11.2: Cut colored by temperature of the nozzle domain.

(Fig. 11.3). When this value crosses the dump plane, it means the flame is no longer completely stabilized in the chamber and flashback is occurring. Once the setup has been initialized, the computation can be run. The initial state is reasonably silent and the flame is stabilized. However, the initialization methodology cannot be perfectly silent, as the resulting solution does not respect the Navier-Stokes equations. The initial pressure wave must be monitored to separate it from any intrinsic pressure waves resulting from the flame and the chamber modes. Fig. 11.4 shows the evolution of mean pressure chamber versus time. Three distinct regimes appear in the 90 ms following the run start:

0-13 ms: pressure activity increases rapidly in the chamber;

13-60 ms: the pressure fluctuations have a constant amplitude. Mean pressure drifts slightly;

60-90 ms: the pressure oscillations completely disappear, and are replaced by a strong pressure peak.

The initial pressure perturbation is clearly much smaller than during the regime achieved in phase **2**. The pressure perturbation induced by the initial solution could be triggering the behavior observed in the next hundred ms. But since no quieter methodology has been proposed, the initial phases and triggering cannot be studied. Efforts will therefore concentrate on describing phases **2** and **3**.

Initial growth The solution of the **OPEN-NR** case is used to initialize a flame without thermoacoustic activity. During the first 5 ms, the pressure oscillations are very weak, and the flame is stabilized in the chamber (Fig. 11.5). Pressure oscillations grow slowly at a frequency of 188 Hz.

Thermoacoustic instability After 5 ms, pressure oscillations increase, and the flame movements amplify (Fig. 11.6). After 40 ms, the flame undergoes high amplitude variations in position and surface (Fig. 11.5). This self-excited mode oscillates at 188 Hz, as determined using the autocorrelation of pressure fluctuations at a reference point in the swirl tube. This behavior is sustained until approximately 55 ms (10 cycles), and because the flame recedes far into the swirl tube but complete

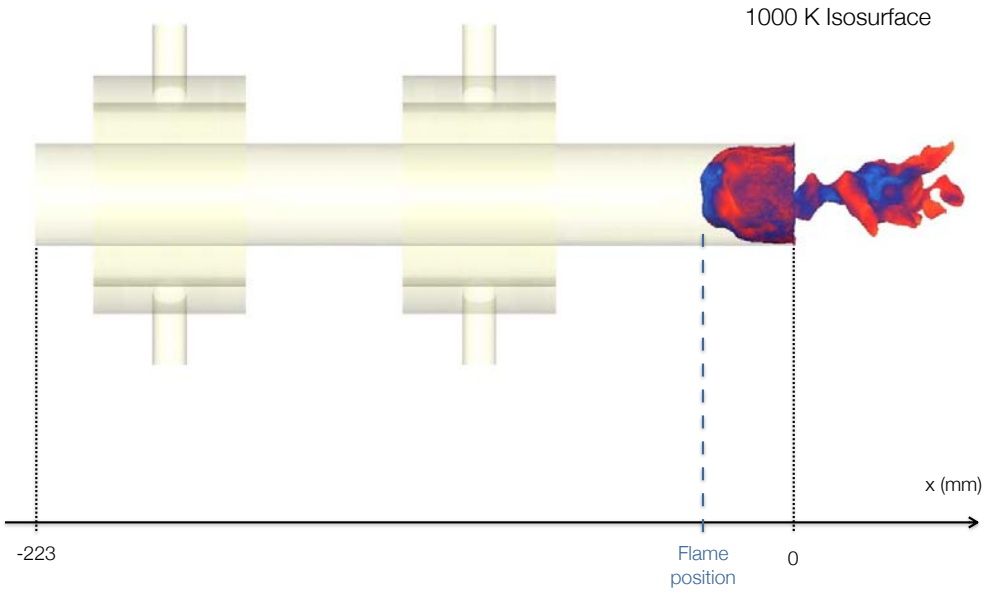

Figure 11.3: The most upstream flame position on the x axis is tracked during the computation.

flashback is not triggered, it is called intermittent flashback (IFB) in this paper.

This regime is difficult to study with the Helmholtz solver, as it only exists in this transient state. A passive flame approach can be conducted on the mean sound-speed field. A more precise active flame analysis is difficult to enact because the definition of the reference point for the $n-\tau$ model is prevented by the intermittent flashback. For an acoustic analysis under reacting conditions, the stabilized **CHOKED-ST** LES (where fuel is staged) is more adequate, and is therefore performed in Sec. 11.4. This acoustic analysis shows good agreement with the LES acoustic activity, confirming that during this phase the flame is essentially driven by the first longitudinal mode.

Flashback When pressure oscillations reach a critical level ($t = 60\,\text{ms}$ in Fig. 11.6), the flame enters the swirl tube but does not exit it anymore. It then recedes gradually towards the ICS in 15 ms. Fig. 11.5 displays two views of the flame during the flashback phase. The flame tip velocity during this phase is $13\,\text{m}\,\text{s}^{-1}$ on average. This result agrees with VCF theories of Ishizuka (2002) discussed in Chap. 6: flame propagation along a vortex axis is a peculiar phenomenon in which the flame velocity is much higher than a simple laminar or even turbulent flame speed.

Fig. 11.6 confirms the link between flame recession in the swirl tube and acoustic activity: flashback is triggered at instant **H** when pressure perturbations reach approximately 15 kPa, confirming the critical level of sustained pressure oscillations necessary to trigger flashback computed in Sec. 10.3.3 by acoustic forcing.

This LES suggests that the flame cannot remain in the chamber for this regime and this is also what experiments showed at EM2C: it is impossible to maintain

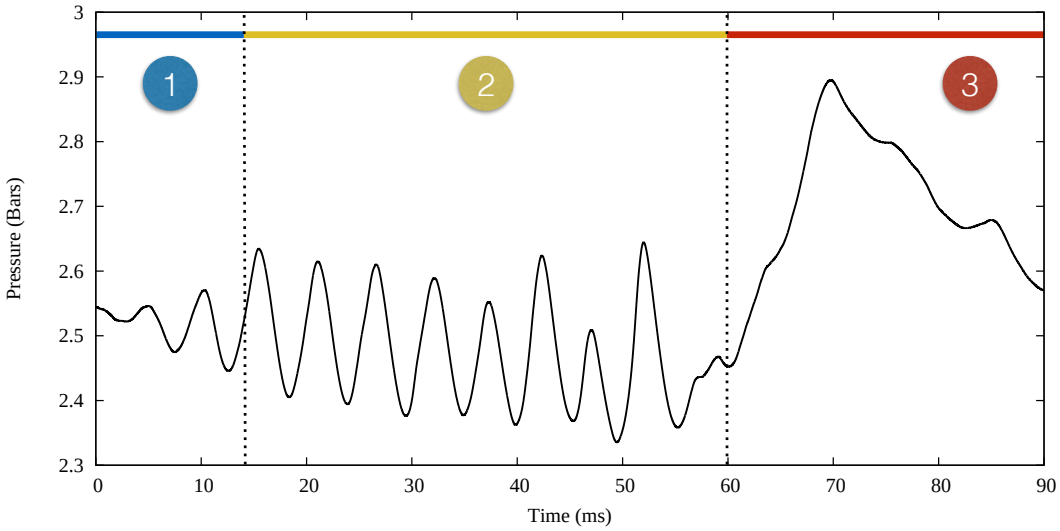

Figure 11.4: Mean pressure in the domain versus time for the CHOKED case initialized using the strategy described in Fig. 11.1.

a stable flame in the chamber for these operating conditions. Flashback occurs very rapidly and the experiment must be stopped to avoid damaging the injection tube. Note that LES were performed before the experiment and that this blind test confirmed the capacity of LES to predict flashback before experimental tests were conducted.

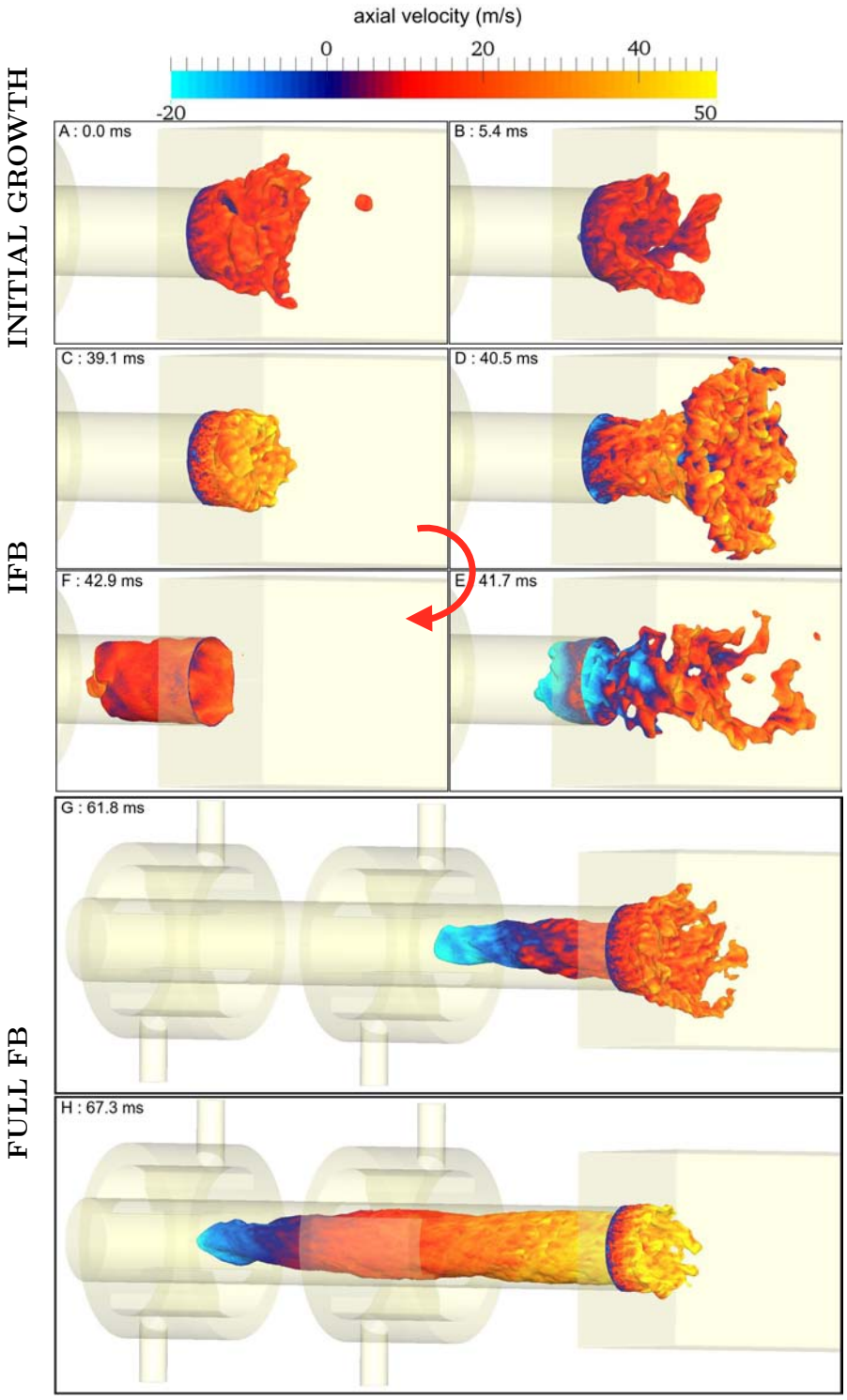

Figure 11.5: 1000 K isosurface colored by axial velocity, during the initial growth (top), intermittent flashback (center) and full flashback (bottom) phases.

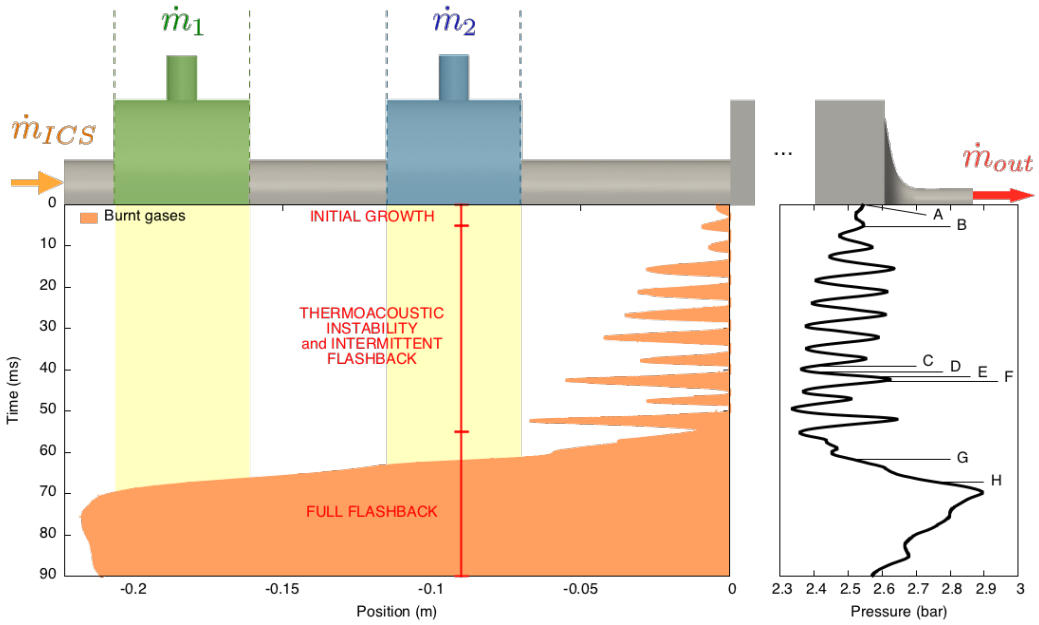

Figure 11.6: Flame position versus time for ICS10 **CHOKED-PR** configuration. Mean chamber pressure is displayed on right side. Snapshot positions of Fig. 11.5 are shown.

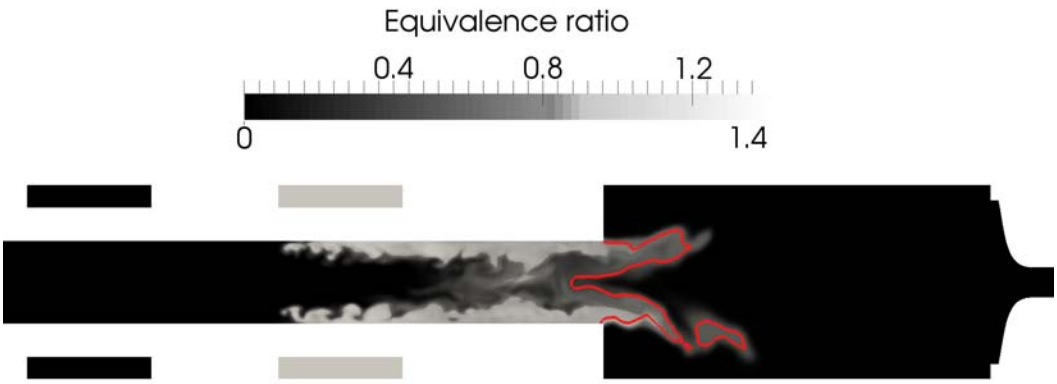

Figure 11.7: Equivalence ratio ϕ near the dump plane in the **CHOKED-ST** setup, on an instantaneous field. Solid red line is a temperature isocontour at 1000 K.

11.3 CHOKED-ST: Control of AI-VCF using fuel staging

The two injector stages of the test bench offer the possibility to stage both air and fuel mass flow rates. The previous analysis has shown that flashback occurs when the flame can propagate along the vortex axis. This observation was the reason why the staged case (**CHOKED-ST**) was tested both experimentally and numerically. For this case, fuel is entirely injected through the downstream injector (Tab. 9.1). The objective is to create a lean vortex core where flashback is inhibited. Fig. 11.7 provides a map of equivalence ratio ϕ in the **CHOKED-ST** case. If the instability arises, the flame will be pushed into the swirl tube but flashback should not be triggered because this region is lean. A 50 ms LES simulation of this setup was performed. Fig. 11.8 shows the flame position and the domain mean pressure versus time. The following observations can be made:

- acoustic activity is still present at a frequency of 209 Hz, similar to the LES of *CHOKED-PR*. However, amplitudes are smaller than in the **CHOKED-PR** case. The instability does not grow with time anymore;
- IFB still takes place in the swirl tube in phase with pressure oscillations. However, the flame tip never intrudes by more than 1.5 cm in the swirl tube. No flashback occurs over the course of the simulation. A typical view of the flame is given in Fig. 11.9.

The flame oscillates with amplitudes of approximately one half injection duct diameter and at a well-defined frequency. Phase averaging is performed: Figs. 11.10 and 11.11 shows the temperature and pressure in the domain for 4 different phases of the 209 Hz instability.

The pressure fields (Fig. 11.11) shows clearly that the acoustic activity in the chamber is constant in space, confirming the "bulk" behavior of the mode there. The temperature fields (Fig. 11.10) delimit the amplitude of flame movement, showing that indeed the flame does not recede inside the injection tube more than one tube

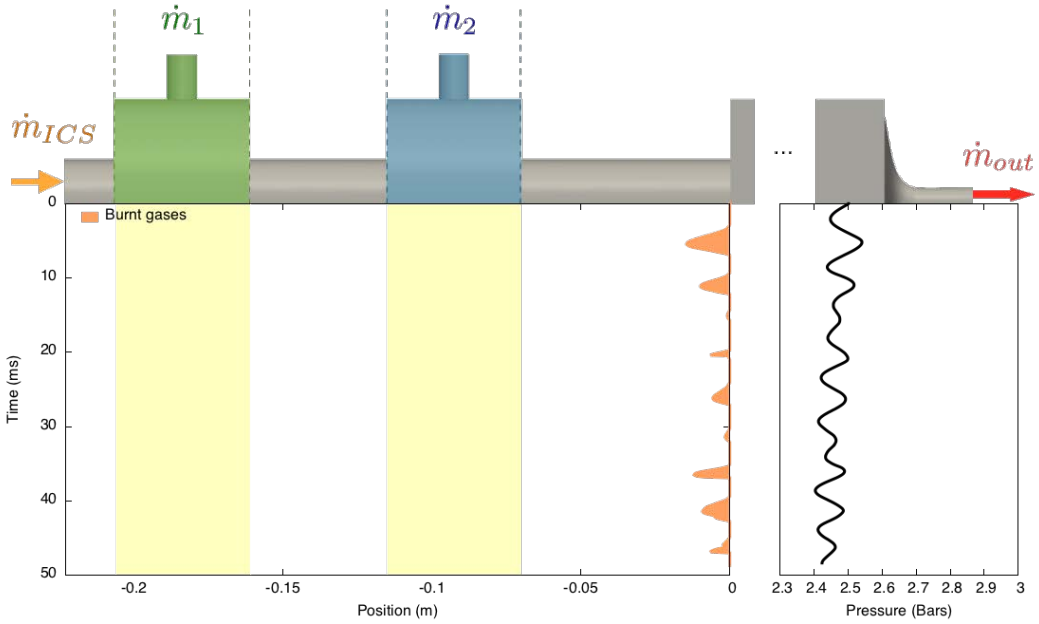

Figure 11.8: Flame position and chamber pressure for the **CHOKED-ST** test case. 50 ms LES run.

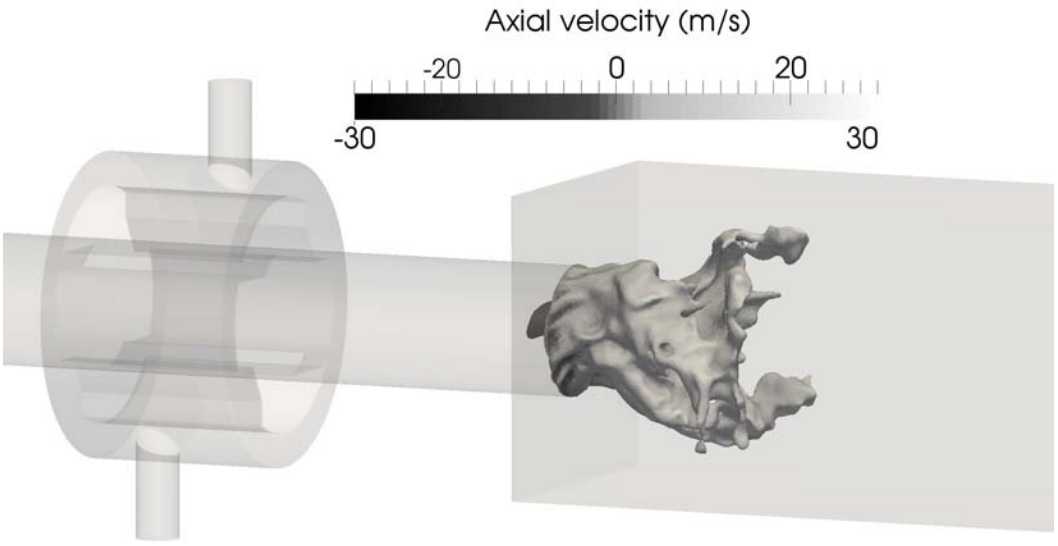

Figure 11.9: Typical view of the flame in the LES during the **CHOKED-ST** run.

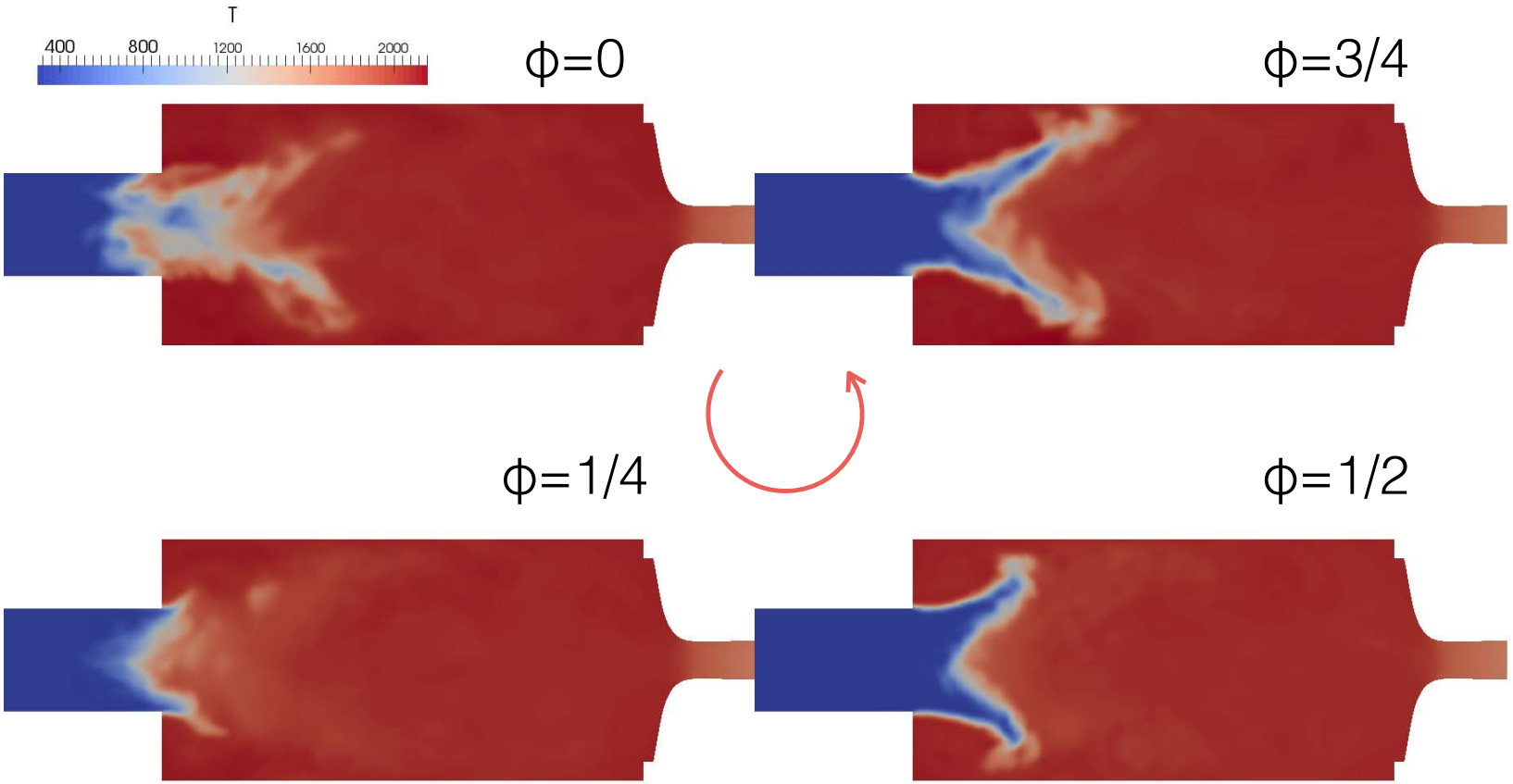

Figure 11.10: Phase averaged temperature of the **CHOKED-ST** LES at 4 phases: 0, 1/4, 1/2 and 3/4 of the period matching the 209 Hz instability.

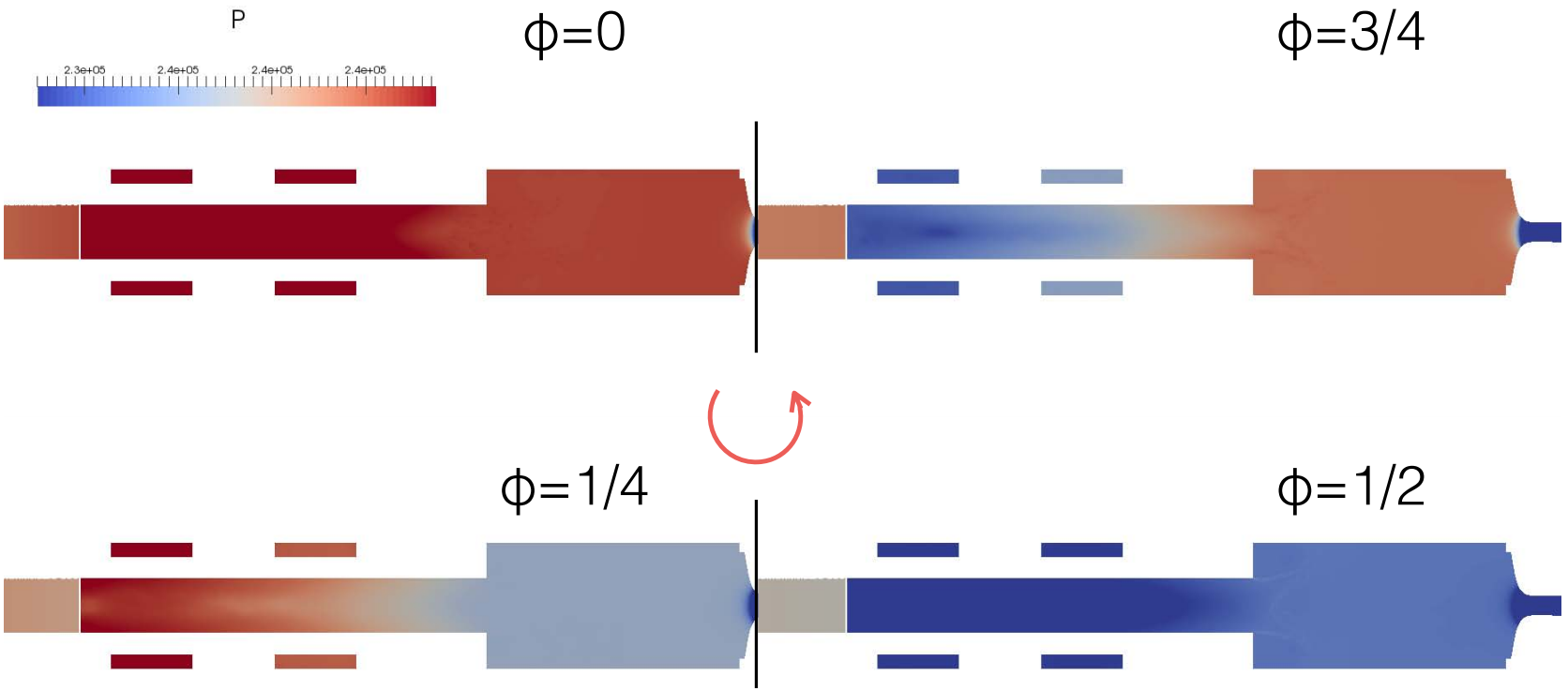

Figure 11.11: Phase averaged pressure of the **CHOKED-ST** LES at 4 phases: 0, 1/4, 1/2 and 3/4 of the period matching the 209 Hz instability.

diameter.

11.4 Thermoacoustic Analysis

The CHOKED setup exhibits strong pressure oscillations (Fig. 11.4), as the full closed chamber constitutes an efficient resonator, with specific intrinsic frequencies. If the excitation frequency is close enough to one of the resonant frequencies of the chamber, then growth and damping rate of the concerned mode compete. If growth rate exceeds damping rate, the mode is amplified, and after a small number of cycles the oscillation amplitude can become very high.

The premixed cases (CHOKED-PR) do not lead to a steady-state regime, but instead flashback is triggered after a period of instability growth (Sec. 11.2). An autocorrelation of the signal of mean pressure in the combustion chamber during the instability growth yields an estimation of its frequency at 194 Hz, but the non-permanent nature of these runs makes the study of its acoustic behavior very difficult. The staged case however (CHOKED-ST) exhibits steady-state oscillations, and the same frequency measurement strategy yields 211 Hz, close to the value of the premixed case. For these reasons, the staged case is chosen for thermoacoustic analysis. Here we will use the Helmholtz tools presented in Chap. 7 to see if the mode which develops in the LES is indeed a thermoacoustic one.

11.4.1 Passive flame

The AVSP Helmholtz solver described in Sec. 7.4 can provide the frequencies and shapes of the cavity's modes. The CESAM-HP setup has been therefore computed using the coarse mesh $\mathbf{MO}_C$ with the AVSP acoustic solver. The sound speed distribution is taken from an average solution of the reacting open setup, accounting for a so-called "passive flame" approach. Since the Helmholtz analysis is linear, it makes sense to choose the OPEN setup —which is "artificially stable" because of non-reflecting boundary conditions —to determine the growth and damping rates. The sound speed is shown in Fig. 11.12 The boundary conditions for this problem

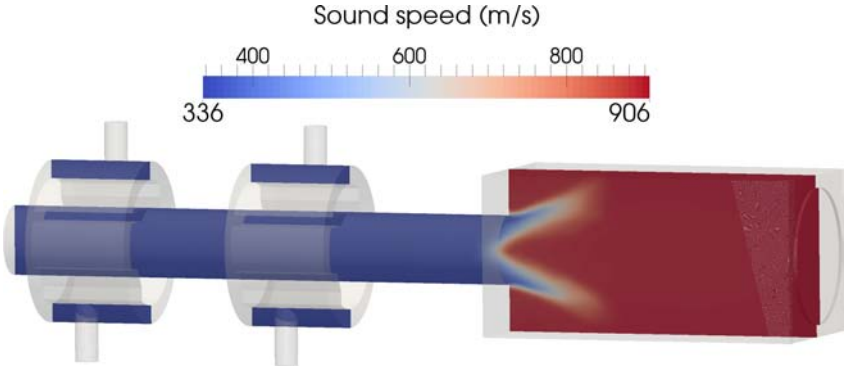

Figure 11.12: Distribution of the sound speed used for the AVSP computation.

are all set to null velocity fluctuation. For walls, this is a good approximation of the physical behavior. For inlets, mass flow rate is generally well imposed, hence this approximation is reasonable. The outlet condition is the choked nozzle. Its actual impedance can be approximated as a null velocity ($u' = 0$), or using the improved Magnus method of Duran & Moreau (2013), as described in Sec. 8.3. Both methods are used to assess the influence of correct outlet modeling on the eigenfrequencies found. The ICS must also be modeled, and since it is a slightly porous plate it is taken as a solid wall with ($u' = 0$) in a first approach. However, realistic multiperforated conditions based on the model of Howe (2010) are available in AVSP thanks to the work of Gullaud *et al.* (2009), and are also used to assess the influence of this condition on the modes found. The summary of these approaches for the first 4 modes obtained by AVSP are given in Tab. 11.2. As shown in Sec. 8.3.3,

$u' = 0$ outlet		Magnus outlet		Magnus outlet + MLPF ICS	
Real	Imag	Real	Imag	Real	Imag
279	0	279	-1.74	303	-1.88
581	0	581	-0.15	595	-1.56
1219	0	1219	-3.39	1260	-1.98
1491	0	1491	-0.15	1398	-1.25

Table 11.2: First 4 frequencies found by the AVSP solver. "Magnus outlet" refers to simulations where the complex reflection coefficient R of the nozzle was computed using the Magnus expansion method of Duran & Moreau (2013). "MLPF ICS": simulations with multiperforated ICS treated with the acoustic model of Howe (2010).

the nozzle reflection coefficient is close to 1, the behavior of an ideal fully reflecting wall. The difference between the $u' = 0$ and the Magnus outlet cases is therefore expected to be very small, and this is confirmed by AVSP (Tab. 11.2). The ICS however has been shown in the past to have a strong effect on acoustic fluctuations in this range of frequencies (Tran *et al.*, 2009), and in this case it introduces shifts of the frequencies of the order of 5 %. In all cases, the first mode appears around 280-300 Hz. This is far from the 211 Hz observed in the self-excited oscillations of the CHOKED-ST setup. In order to confirm that the mode is in fact the same in both LES and acoustic calculation, the mode shape can be compared. This is done in Fig. 11.13 where RMS values of the LES are compared to the respective mode amplitudes given by the acoustic solver. The values are non-dimensionalized by their respective maximum values, in order to be comparable. The axial velocity fluctuations are very similar between the LES and the acoustic mode. Agreement is not as good for pressure fluctuations, where the global mode shape is the same but there are significant quantitative differences in amplitude ratio, noticeably in the chamber. Since the coefficient for non-dimensionalization is arbitrary, the modes could be made to agree quantitatively in the combustion chamber, at the expense of the injection duct. This failure to capture the pressure jump through the flame

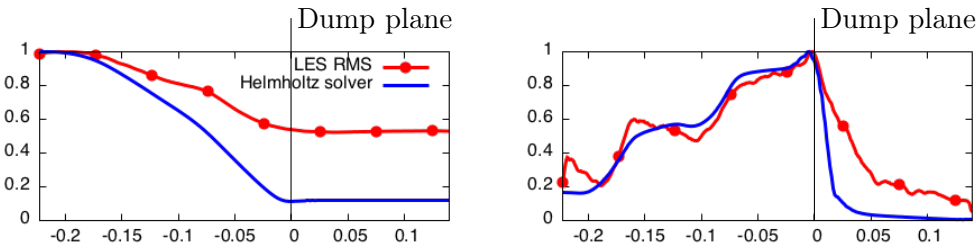

(a) Pressure fluctuation **(b)** Axial velocity fluctuation

Figure 11.13: Comparison along the setup centerline between the RMS activity in the **CHOKED-ST** LES (red line with dots) and the acoustic mode found with the Helmholtz solver (blue solid line).

is a classical issue with Helmholtz solvers, but otherwise the reasonable agreement suggests that the correct mode has been identified by the Helmholtz solver.

The imaginary part of the eigenmodes is also an interesting parameter. It relates directly to mode damping, and the lower the value the more the mode would be damped. In this approach, acoustic sources are of course not included, hence the small damping values induced by the nozzle and the ICS may not be sufficient to damp strong noise production in the system. Many other phenomena can lead to acoustic damping, and typical values measured for complete chamber damping are of the order of 30 to 50 Hz, *e.g.* as measured by Silva *et al.* (2013) in a very similar configuration as CESAM-HP (namely the CESAM setup). This result suggests that both the choked nozzle outlet and the ICS do not produce efficient damping on the first modes of the system, and that this configuration must rely on other mechanisms to dissipate acoustic energy.

11.4.2 Active flame

In order to better represent the chamber acoustic modes, the flame dynamics are taken into account using to an "active flame" approach based on the $n-\tau$ model of Crocco (1951) as described in Chap. 3. In order to evaluate the values of N_3 (the dimensional value, with a dimension of $\mathrm{J\,m^{-1}}$) and τ, LES of the **CHOKED** setup are post-processed. The heat release fluctuations over the entire domain are correlated to the velocity fluctuations at a point of coordinates $(-30\,\mathrm{mm}, 0, 0)$. This point is chosen as close as possible to the flame, but in order for the flame to never reach it during the measuring phase of the computation. This choice has been shown to be very important for the reliability of the estimation of the parameter τ (Truffin *et al.*, 2003).

The resulting values of N_3 and τ for the auto-excited mode of the **CHOKED** case are presented in Tab. 11.3. The AVSP solver can perform active flame computations (Martin *et al.*, 2006), hence the first mode of Tab. 11.2 can be computed again but this time including the active flame effect. The resulting mode is also described in Tab. 11.3. In order to better understand the effect of the active flame and because Helmholtz computations are inexpensive, several other values of n and τ are used to

Setup	N_3	τ	Real	Imag
CHOKED-PR	$1835\,\mathrm{J\,m^{-1}}$	2.35 ms	255.64 Hz	−32.19 Hz
CHOKED-ST	$900\,\mathrm{J\,m^{-1}}$	1.8 ms	285.45 Hz	−4.16 Hz

Table 11.3: Active flame Helmholtz simulation parameters and resulting mode decomposed as real and imaginary part.

compute the first eigenmode of the setup:

1. the value of τ is varied between 0 and 3 ms with the value of N measured in the LES, to see the effect of delay on the mode frequency and stability;
2. the same values of τ are tested for a value of N of only one tenth of the LES value.

The mode frequencies (real parts) and growth rates (imaginary parts) are presented in the complex plane in Fig. 11.14. Only the real part of the **CHOKED-ST** LES

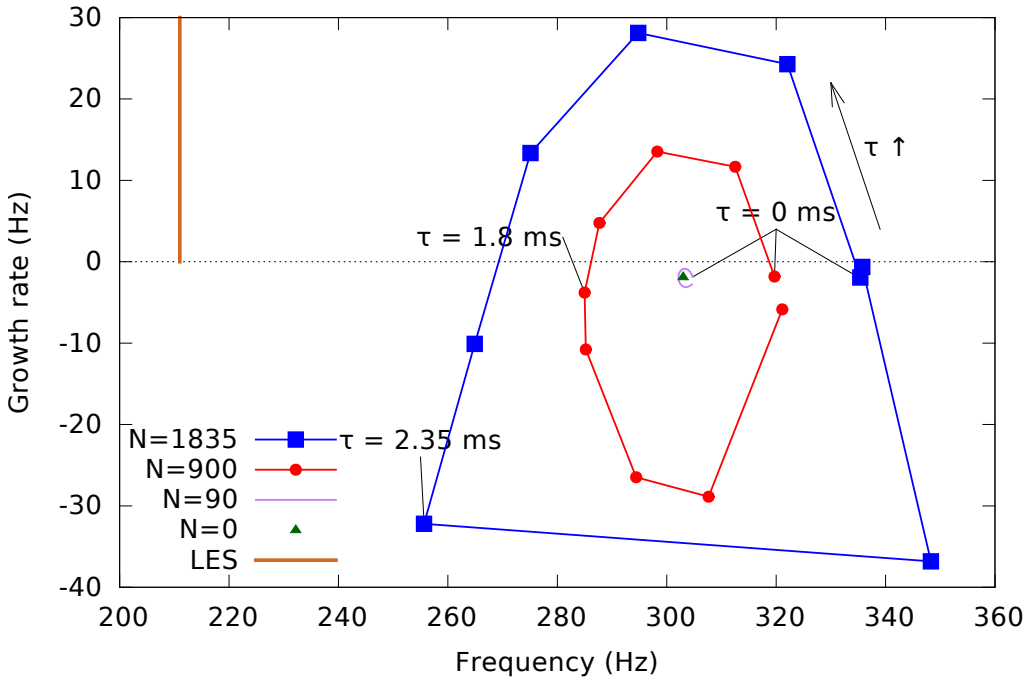

Figure 11.14: Map in the complex plane of the first eigenmode found with AVSP for several values of τ and values of N of 900 (the LES value, blue squares) and 90 (red circles).

value has been identified, namely 211 Hz. The growth rate is expected to be positive since the mode is amplified, but its value is difficult to estimate in the LES because the transient regime is very short.

This figure shows that none of the frequencies found with the acoustic solver give satisfactory results for the LES value. While it is clear that for the approximate value of τ measured in the LES, the frequencies tend to shift down towards the LES

value, a systematic overestimation of at least 35 % is observed in all computations.

11.4.3 On the role of convective phenomena

The smallest frequency of pure acoustic modes is limited by the size of the domain and the speed of sound: the lowest frequency can be roughly estimated using the time needed for an acoustic wave to do one round-trip between the two furthest points in the domain (see Chap. 4). When the LES or experimental measurements show repeated activity at a frequency lower than the first acoustic eigenmode, an explanation can be that part of this loop is due to a convective phenomenon where information travels at a velocity much smaller than the sound speed. One candidate is entropy, which has been shown to produce acoustics when reaching the nozzle in Chap. 5). Such a hybrid acoustic-entropic mode has recently been described in a real aircraft engine burner (Motheau *et al.*, 2013). The basic mechanism for this convective/acoustic loop is compared to the classical acoustic/acoustic loop in Fig. 11.15.

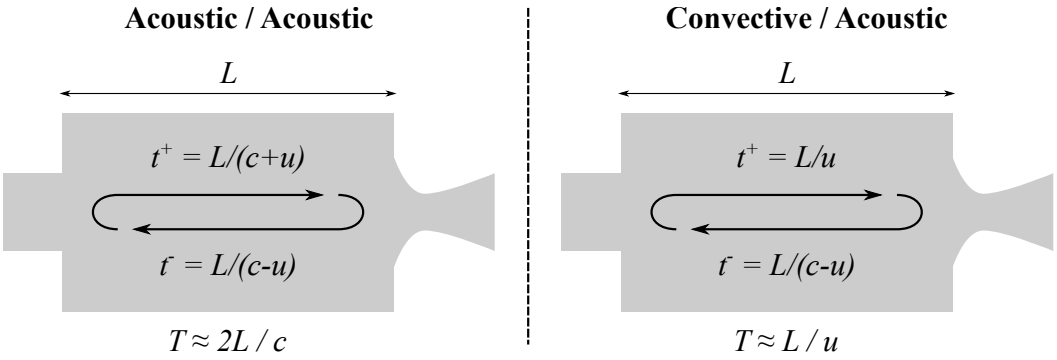

Figure 11.15: Simplified representation of an acoustic/acoustic loop (left), associated with a round-trip time of $T \approx {}^{2L}/_{c}$, and a convective/acoustic loop (right), where $T \approx {}^{L}/_{u}$. Note that these values arise from a low Mach number approximation, *i.e.* $u \ll c$.

This phenomenon could explain the frequency overestimations observed in Fig. 11.14. In order to validate this hypothesis and see whether convection plays a strong role, one solution is to change the mean velocity of the flow in the chamber: according to Fig. 11.15, for a low Mach number in the chamber the round-trip period is governed mostly by the convective velocity. It was decided to double the mass flow rate through the chamber, and observe the impact on the instability frequency. Tab. 11.4 shows the resulting frequency of the natural instability for the general mass flow rate target of this Ph.D ($18\,\mathrm{g\,s^{-1}}$) and for a doubled mass flow rate of $36\,\mathrm{g\,s^{-1}}$. This result suggests that no convective phenomenon can explain part of the instability cycle that is observed in the CESAM-HP setup.

Mass flow rate	Frequency
$18\,\mathrm{g\,s^{-1}}$	211 Hz
$36\,\mathrm{g\,s^{-1}}$	214 Hz

Table 11.4: Effect of mass flow rate doubling on acoustic frequency, assessed with 2 LES simulations of the **CHOKED-ST** case at varying mass flow rate.

11.5 Conclusions

A new mechanism for flashback in swirled burners has been described, called acoustically induced vortex core flashback (AI-VCF). In the swirled burner developed here, AI-VCF causes the flame to flashback systematically when the outlet is choked because strong thermoacoustic instabilities are excited. AI-VCF is due to the combination of strong swirl levels and acoustic waves. It is non linear and a threshold of typically 15 kPa was obtained by forcing LES acoustically. LES is shown to predict correctly the experimental observations of flashback. Flashback-prone and flashback-robust configurations can be obtained by changing fuel staging and LES recovers experimental results too, predicting which configuration will be AI-VCF resistant. Helmholtz simulations however fail to capture with precision the frequency of the mode which grows in the LES before full flashback occurs. Tests at different flow rates show that no convective mechanism can explain this discrepancy. It is likely that more precise impedances should be used to explain these results.

Conclusion and Perspectives

In this Ph.D, the issue of turbulent premixed combustors ended by choked nozzles has been investigated, both from an analytical and a numerical perspective. This study is a buildup on the investigations previously lead on the CESAM test rig at EM2C, both experimentally (Lamraoui, 2011) and numerically (Silva, 2010), and these studies yielded accurate descriptions of the behavior of this swirled flame under atmospheric conditions. Following these encouraging results, a pressurized version of the CESAM burner, named CESAM-HP was developed in the context of the DISCERN ANR project in 2011. The present Ph.D aimed at performing the numerical description and investigations of this new setup. The pressurized version was meant to achieve several goals:

1. provide a short compact flame, close to those found in real high-pressure gas turbines;
2. introduce a choked nozzle in the setup, necessary to achieve the target pressure and also a better representation of industrial combustion chamber outlets than an open atmosphere;
3. study combustion noise production and characteristics in this realistic configuration, where indirect noise was expected to be strong because of the flow acceleration through the nozzle.

These objectives stretch further than the scope of combustion noise studies: future efforts to describe real gas turbines need to continue to expand the range of physical phenomenon included, and as shown in this Ph.D the downstream conditions can have important effects on the chamber dynamics.

Analytical developments

Bringing together the issue of swirled combustion with a choked flow outlet raises a series of questions on several distinct subjects. Turbulent premixed combustion must be described, which is done here with LES. The specific study of acoustics however can be performed in a simpler framework, based on wave equations alone, and a Helmholtz solver has been used for this purpose.

The initial aim of the setup was in part to study combustion noise, and to determine the importance of indirect combustion noise compared to direct noise in the presence of a real flame and a choked nozzle. Consequently, in Chap. 5, theories concerning the indirect to direct noise ratio were presented. The classic toy model of Leyko (2010) was revisited and a new toy model was proposed to describe the effect of the flame in this regard. This new model accounts for flame response to upstream waves and shows that the ratio of indirect to direct noise depends not only on upstream and downstream Mach numbers, but also on the level of mixedness.

Replacing the atmospheric outlet (imposing roughly constant pressure) of the CESAM rig by a choked nozzle in CESAM-HP (imposing roughly constant velocity)

has also had a strong effect on the chamber dynamics. After describing the basic mechanisms of thermo-acoustic instabilities, Chap. 4 tackled the question of the effect of this outlet condition change on the system's global stability.

Finally, the issue of flame stabilization in swirled combustors was investigated. Previous work on flame propagation along a vortex axis (Ishizuka, 2002) was reminded, and the numerical code was validated on a simple toy model to show that the major flame propagation effects in this case are not due to thermo-diffusive effects, but are instead controlled mainly by inertial effect. This test in a closed configuration confirmed the observations of Domingo & Vervisch (2007) in an open free-vortex setup.

Large Eddy Simulation of the CESAM-HP combustor

With these analytical descriptions and trends in mind, the CESAM-HP setup was simulated with the AVBP code. Compressible LES has the capacity to describe with great precision both the chemical process in the turbulent flame, and the compressible supersonic flow through the nozzle. This is an excellent asset to investigate the behavior of the setup in parallel with the experimental measurements. While the objective was to study combustion noise, results rapidly showed that combustion instabilities and even stabilization issues and flashback had to be considered. To isolate the effects of combustion instabilities and combustion noise, the strategy chosen in this Ph.D was to run 2 types of simulations: some terminated with a pressure outlet in the chamber (called **OPEN** setups), and some including the choked nozzle in the domain, and letting the natural impedance of the nozzle control the domain outlet (called **CHOKED**). The **OPEN** simulations (Chap. 10) enable to artificially decouple the flame from the nozzle and control combustion instabilities, which is not possible in the experiment. Flame characteristics such as stabilization robustness were investigated using these setups. In the next chapter (Chap. 11), the complete setup known as **CHOKED** was computed using the LES, showing that self-excited combustion instabilities occurred. The fully premixed simulations also showed that this instability reached high enough levels to trigger intermittent, and finally full flashback of the setup. This work was lead in close collaboration with experimental observations by the EM2C team on the test rig, and lead to a submission in Combust. Flame, currently under review (Lapeyre *et al.*, 2015).

Perspectives

This work has shown that several challenges arise from the joint study of a turbulent flame and a choked nozzle. This issue concerns many modern combustors, from gas turbines to aircraft engines. In order to pursue the increase in knowledge and understanding of such systems, future simulations will need to include the combustion chamber in its environment, including the upstream and downstream component effects. Currently, the CESAM-HP setup is still under investigation in the framework

of the RECORD European project, with the objective of evaluating combustion noise properties of the setup. The geometry has been altered to get rid of thermo-acoustic and flame stabilization issues, and the knowledge gained on this flame-nozzle setup is expected to enable noise studies and possibly yield a better understanding of the relationship between direct and indirect noise production. More generally, combustion noise and combustion instabilities appear as topics which should not be dissociated and must be studied together.

Appendix A

NSCBC Inlet acoustic impedance

Selle *et al.* (2004*b*) derived the impedance of a charateristic relaxed outlet condition. A direct analogy is possible for an inlet boundary condition with target velocity. For such a non-reflecting inlet, the following waves are outgoing and as such imposed by the domain : (L_1, L_2, L_3, L_4). The only ingoing wave that must be given to the code is L_5. A non reflecting conditions implies $L_5 = 0$. However, in order to ensure that the inlet velocity does not deviate from it's target u^t, L_5 is imposed as a relaxed spring towards the target. Namely:

$$L_5 = 2K(u - u^t) \tag{A.1}$$

Let now an L_1 wave travel from the domain towards the inlet boundary, in the form :

$$L_1 = 2P_0 i\omega e^{i\omega t} \tag{A.2}$$

According to the LODI relations, these two waves are related by :

$$\begin{aligned} \frac{\partial u}{\partial t} + \frac{2}{\rho c}\left(L_5 - L_1\right) &= 0 \\ \frac{\partial u}{\partial t} + \frac{K}{2}\left(u - u^t\right) - \frac{P_0}{\rho c} i\omega e^{-i\omega t} &= 0 \end{aligned} \tag{A.3}$$

the solution to which, including transient regime, is of the form :

$$u(t) = u^t + A_0 e^{\frac{K}{2}t} + \frac{P_0 i\omega}{\rho c\left(\frac{K}{2} - i\omega\right)} e^{-\omega t} \tag{A.4}$$

Once the initial transient regime is over, the reflection coefficient of the boundary is therefore simply :

$$R = \frac{L_5}{L_1} = \frac{1}{1 - i\frac{2\omega}{K}} \tag{A.5}$$

Appendix B

LODI for spherically symmetric flows

B.1 The LODI formalism

Numerical computations of acoustic waves require smart acoustic treatment of boundary conditions in order to have minimal reflections and let the waves propagate outwards through the boundary silently. The now famous "LODI" (Locally One Dimensional Inviscid) formalism, introduced by Poinsot & Lele Poinsot & Lele (1992), enables a wave decomposition at the boundary that is very natural for pure acoustic waves. Therefore, a plane wave impacting on a correctly treated plane boundary condition exits the domain with negligible reflections.

Starting from the set of Euler equations for a gas composed of a single specie, in conservative form :

$$\begin{aligned}
\frac{\partial \rho}{\partial t} + \frac{\partial}{\partial x}(\rho u) + \frac{\partial}{\partial y}(\rho v) + \frac{\partial}{\partial z}(\rho w) &= 0 \\
\frac{\partial \rho u}{\partial t} + \frac{\partial}{\partial x}(\rho uu + p) + \frac{\partial \rho uv}{\partial y} + \frac{\partial \rho uw}{\partial z} &= 0 \\
\frac{\partial \rho u}{\partial t} + \frac{\partial \rho uv}{\partial x} + \frac{\partial}{\partial y}(\rho vv + p) + \frac{\partial \rho vw}{\partial z} &= 0 \\
\frac{\partial \rho u}{\partial t} + \frac{\partial \rho uw}{\partial x} + \frac{\partial \rho wv}{\partial y} + \frac{\partial}{\partial z}(\rho ww + p) &= 0 \\
\frac{\partial \rho E}{\partial t} + \frac{\partial \rho Hu}{\partial x} + \frac{\partial \rho Hv}{\partial y} + \frac{\partial \rho Vw}{\partial z} &= 0
\end{aligned}$$

which can be seen as :

$$\frac{\partial \boldsymbol{U}}{\partial t} + \frac{\partial \boldsymbol{F}_U}{\partial x} + \frac{\partial \boldsymbol{G}_U}{\partial y} + \frac{\partial \boldsymbol{H}_U}{\partial z} = 0 \tag{B.1}$$

where :

$$\begin{aligned}
\boldsymbol{U} &= (\rho u, \rho v, \rho w, \rho E, \rho) \\
\boldsymbol{F}_U &= (\rho uu + p, \rho uv, \rho uw, \rho Hu, \rho u) \\
\boldsymbol{G}_U &= (\rho uu, \rho uv + p, \rho uw, \rho Hu, \rho u) \\
\boldsymbol{H}_U &= (\rho uu, \rho uv, \rho uw + p, \rho Hu, \rho u)
\end{aligned}$$

Therefore, by using the 3 Jacobian matrices :

$$A_U = \frac{\partial \boldsymbol{F}_U}{\partial \boldsymbol{U}} \qquad B_U = \frac{\partial \boldsymbol{G}_U}{\partial \boldsymbol{U}} \qquad C_U = \frac{\partial \boldsymbol{H}_U}{\partial \boldsymbol{U}}$$

Eq. B.1 can be rewritten as :

$$\frac{\partial \boldsymbol{U}}{\partial t} + A_U \frac{\partial \boldsymbol{U}}{\partial x} + B_U \frac{\partial \boldsymbol{U}}{\partial y} + C_U \frac{\partial \boldsymbol{U}}{\partial z} = 0 \tag{B.2}$$

Consider a plane boundary at $x =$ constant. Let the various perturbations coming from the computational domain and impacting this boundary be mostly normal to it, *i.e.* $\frac{\partial \boldsymbol{U}}{\partial y}, \frac{\partial \boldsymbol{U}}{\partial z} \ll \frac{\partial \boldsymbol{U}}{\partial x}$. this assumption is often met in real-wrold simulations, where inlet and outlet boundary conditions are "far" from the perturbed part of the flow. Then Eq. B.2 reduces to :

$$\frac{\partial \boldsymbol{U}}{\partial t} + A_U \frac{\partial \boldsymbol{U}}{\partial x} \approx 0 \tag{B.3}$$

The key concept behind the LODI approach is to notice that Eq. B.3 is an advection equation for the conservative variables. To express this more clearly, the matrix A_U is diagonalized. This operation yields two new matrices L_U and D (where D is diagonal) according to :

$$D = L_U A_U L_U^{-1}$$

Eq. B.3 becomes :

$$\frac{\partial \boldsymbol{W}}{\partial t} + D \frac{\partial \boldsymbol{W}}{\partial x} \approx 0$$

where $\partial \boldsymbol{W}$ is defined as :

$$\partial \boldsymbol{W} = L_U \partial \boldsymbol{U}$$

This yields 5 advection equations on the components of $\boldsymbol{W}$, where the convection speed of each quantity is the matching diagonal coefficient of D. Therefore, from the boundary's point of view, all flow perturbations can be seen as 5 "waves" traveling at various convection speeds. In primitive variables, some algebra yields the expressions of these waves and the matching convection speeds :

$$\begin{aligned}
\partial W^1 &= \partial u + \frac{\partial p}{\rho c}\lambda^1 && = u + c \\
\partial W^2 &= -\partial u + \frac{\partial p}{\rho c}\lambda^2 && = u - c \\
\partial W^3 &= \partial v \lambda^3 && = u \\
\partial W^4 &= \partial w \lambda^4 && = u \\
\partial W^3 &= -\frac{\partial p}{c^2} + \partial \rho \lambda^5 && = u
\end{aligned}$$

B.2 A non-reflecting boundary with the LODI formailsm

For the present case, an acoustically non-reflecting boundary condition is needed. Therefore, at the outlet, the "waves" described in the previous paragraph can be

analyzed. Waves ∂W^1 and ∂W^3 through ∂W^5 are convected from the domain to the outside, through the boundary. Their values therefore simply result from the flow field in the domain, and nothing is needed from the boundary condition to impose them.

However, ∂W^2 is convected at $\lambda^2 = u - c < 0$ since the flow is subsonic. Therefore, this wave is convected from outside the domain to the inside. Of course, it can not be computed using any flow field, since there is no such information outside the domain. This wave must therefore be user-defined for the computation. This is precisely what is needed for the present computation: since the boundary is expected to be non-reflecting, the incoming wave should be zero. Therefore, the most simple way to impose the condition here is simply :

$$\partial W^2 = 0$$

B.3 LODI applied to a spherical problem

The previous approach is sturdy and has been successfully used in many computations since the original paper by Poinsot *et al.* (1992). However, the present problem is not plane, it has a spherical symmetry. Eq. 5.9b shows that the pressure wave is expected to depend spatially only on the radius r. In first approach, since the computational domain is spherical, it could seem that the flow will be "locally one dimensional" in the sense that all flow properties are constant along the boundary condition.

As seen in the details of the LODI approach, all transverse terms in the *cartesian* sense are considered negligible. However, the present problem is spherically symmetric, which is different from saying that all transverse terms in the cartesian sense are negligible. The classical spherical definitions for referencing a given point P are given in Fig. B.1. Subscripts will be used to designate vectors and matrices expressed in the three coordinate systems : c, n and s will designate the cartesian, local cartesian (normal / transverse) and spherical coordinate systems, respectively.

The composition of rotation matrices, for any vector $\boldsymbol{A}$, leads to :

$$\begin{pmatrix} A_x \\ A_y \\ A_z \end{pmatrix}_c = \begin{pmatrix} sin(\theta)cos(\phi) & cos(\theta)cos(\phi) & -sin(\phi) \\ sin(\theta)sin(\phi) & cos(\theta)sin(\phi) & cos(\phi) \\ cos(\theta) & -sin(\theta) & 0 \end{pmatrix} \begin{pmatrix} A_r \\ A_\theta \\ A_\phi \end{pmatrix}_s \tag{B.4}$$

and

$$\begin{pmatrix} A_r \\ A_\theta \\ A_\phi \end{pmatrix}_s = \begin{pmatrix} sin(\theta)cos(\phi) & sin(\theta)sin(\phi) & cos(\theta) \\ cos(\theta)cos(\phi) & cos(\theta)sin(\phi) & -sin(\theta) \\ -sin(\phi) & cos(\phi) & 0 \end{pmatrix} \begin{pmatrix} A_x \\ A_y \\ A_z \end{pmatrix}_c \tag{B.5}$$

These matrices will be further noted $M_{s,c}(\theta, \phi)$ (spherical to cartesian) and $M_{c,s}(\theta, \phi)$ (cartesian to spherical), respectively.

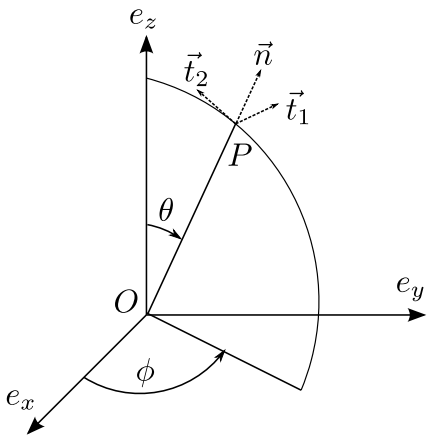

Figure B.1: Scheme of the point considered for the present reasoning

Consider a specific point P on the boundary, referenced by it's spherical coordinates : (R, θ_0, ϕ_0). In order to perform the characteristic wave decomposition at this point, a "local" cartesian coordinate system must be used. This system, composed of $(\vec{n}, \vec{t_1}, \vec{t_2})$, is locally confounded with the spherical system $(\vec{e_r}, \vec{t_\theta}, \vec{t_\phi})$. However, the local cartesian system does not rotate when considering a different point of space. In other words, it is linked to the definition of P in the sense that :

$$\begin{pmatrix} \vec{n} & \vec{t_1} & \vec{t_2} \end{pmatrix}_c = M_{c,s}(\theta_0, \phi_0) \cdot \begin{pmatrix} \vec{n} & \vec{t_1} & \vec{t_2} \end{pmatrix}_n \tag{B.6}$$

where of course :

$$\begin{pmatrix} \vec{n} & \vec{t_1} & \vec{t_2} \end{pmatrix}_n = \begin{pmatrix} 1 & 0 & 0 \\ 0 & 1 & 0 \\ 0 & 0 & 1 \end{pmatrix}_n$$

In order to demonstrate that in this configuration, the transverse terms in the LODI sense are not zero, let us calculate the gradient of $\boldsymbol{u}$ at P. This is done more easily in spherical coordinates. The solution field expression given in Eq. 5.9b is brought to a more simple form :

$$p'(r,t) = \frac{A}{r}\, e^{i\omega\left(t - \frac{r}{c_0}\right)}$$

The conservation of momentum in general coordinates writes :

$$\frac{\partial \rho \boldsymbol{u}}{\partial t} + \boldsymbol{u} \cdot \nabla(\rho \boldsymbol{u}) = -\nabla p \tag{B.7}$$

The classical linearization introduced in Chap. 3 for small amplitudes is:

$$\begin{aligned} \boldsymbol{u} &= \bar{\boldsymbol{u}} + \boldsymbol{u'} \\ \rho &= \bar{\rho} + \rho' \\ p &= \bar{p} + p' \end{aligned}$$

and in the present case, $\bar{\boldsymbol{u}} = 0$. Eq. B.7 becomes :

$$\frac{\partial(\bar{\rho}+\rho')\boldsymbol{u'}}{\partial t} + \boldsymbol{u'}\cdot\nabla((\bar{\rho}+\rho')\boldsymbol{u'}) = -\nabla\bar{p} - \nabla p'$$

Of course, $\nabla\bar{p} = 0$, and by eliminating second order quantities, this reduces to :

$$\bar{\rho}\frac{\partial \boldsymbol{u'}}{\partial t} = -\nabla p'$$

To lighten notations, since ρ' does not appear anymore, $\bar{\rho}$ will be noted simply ρ hereafter. By supposing that $\boldsymbol{u}$ is also harmonic, since p is :

$$i\omega\rho\boldsymbol{u'} = -\nabla p'$$

In vector form, this writes :

$$i\omega\rho\begin{pmatrix} u_r \\ u_\theta \\ u_\phi \end{pmatrix}_s = \begin{pmatrix} (\frac{1}{r}+\frac{i\omega}{c})p \\ 0 \\ 0 \end{pmatrix}_s$$

hence $u_\theta = u_\phi = 0$, as can be expected form the spherical symmetry of the problem. The final form for $\boldsymbol{u}$ is :

$$\boldsymbol{u} = \begin{pmatrix} -\frac{A}{r}(\frac{1}{i\omega\rho r}+\frac{1}{\rho c})e^{i\omega\left(t-\frac{r}{c_0}\right)} \\ 0 \\ 0 \end{pmatrix}_s \tag{B.8}$$

The tensor defined by the gradient of the velocity vector in spherical coordinates is :

$$\nabla_s\boldsymbol{u} = \begin{pmatrix} \frac{\partial u_r}{\partial r} & \frac{1}{r}\frac{\partial u_r}{\partial\theta} & \frac{1}{rsin(\theta)}\frac{\partial u_r}{\partial\phi} \\ \frac{\partial u_\theta}{\partial r} & \frac{1}{r}\frac{\partial u_\theta}{\partial\theta} & \frac{1}{rsin(\theta)}\frac{\partial u_\theta}{\partial\phi} \\ \frac{\partial u_\phi}{\partial r} & \frac{1}{r}\frac{\partial u_\phi}{\partial\theta} & \frac{1}{rsin(\theta)}\frac{\partial u_\phi}{\partial\phi} \end{pmatrix}_s$$

Where the s subscript denotes the spherical coordinates gradient. Hence when applied to Eq. B.8 :

$$\nabla_s\boldsymbol{u} = \begin{pmatrix} -\frac{A}{r}\left(-\frac{2}{\rho cr}+i\left(-\frac{\omega}{\rho c^2}+\frac{2}{\rho\omega r^2}\right)\right)e^{i\omega\left(t-\frac{r}{c_0}\right)} & 0 & 0 \\ 0 & 0 & 0 \\ 0 & 0 & 0 \end{pmatrix}_s$$

and only $(\nabla_s\boldsymbol{u})_{rr} \neq 0$.

In order to estimate the error made by the LODI approximation, this result must be expressed in the cartesian coordinates. The matrix $M_{c,s}(\theta,\phi)$ defined in Eq. B.4

yields :

$$\begin{aligned}\nabla_c \boldsymbol{u} &= M_{s,c}(\theta,\phi)\cdot(\nabla_s \boldsymbol{u}) \\ &= \begin{pmatrix} sin(\theta)cos(\phi)(\nabla_s \boldsymbol{u})_{rr} & 0 & 0 \\ sin(\theta)sin(\phi)(\nabla_s \boldsymbol{u})_{rr} & 0 & 0 \\ 0 & 0 & 0 \end{pmatrix}_c\end{aligned}$$

However, as shown in Eq. B.6, the LODI decomposition is done in the local cartesian coordinates, hence the righteous comparison can be done using :

$$\begin{aligned}\nabla_n \boldsymbol{u} &= M_{c,s}(\theta_0,\phi_0)\cdot M_{s,c}(\theta,\phi)\cdot(\nabla_s \boldsymbol{u}) \\ &= \begin{pmatrix} sin(\theta_0)sin(\theta)cos(\phi-\phi_0)(\nabla_s \boldsymbol{u})_{rr} & 0 & 0 \\ cos(\theta_0)sin(\theta)cos(\phi-\phi_0)(\nabla_s \boldsymbol{u})_{rr} & 0 & 0 \\ sin(\theta)sin(\phi-\phi_0)(\nabla_s \boldsymbol{u})_{rr} & 0 & 0 \end{pmatrix}_n\end{aligned}$$

The value of this gradient at the point P and expressed in the local cartesian coordinates is therefore :

$$(\nabla_n \boldsymbol{u})\cdot\begin{pmatrix} R \\ \theta_0 \\ \phi_0 \end{pmatrix}_n = \begin{pmatrix} R\ sin^2(\theta_0)(\nabla_s \boldsymbol{u})_{rr}(R) \\ R\ cos(\theta_0)sin(\theta_0)(\nabla_s \boldsymbol{u})_{rr}(R) \\ 0 \end{pmatrix}_n$$

B.4 A spherically symmetric problem is not LODI

The important conclusion of this paragraph is that the term "Locally One Dimensional" must be correctly understood. Since "transverse" terms imply gradients of the various flow variables near every boundary point, only flows with one dimensional intrinsic structure can be treated by this simple approach.

Bibliography

ACARE 2002 Strategic Research Agenda. *Tech. Rep.* October. Advisory Council for Aeronautical Research in Europe. (Cited on page 3.)

Aguilar, M. 2013 Method and thermal reactor for single-valve propulsion with multiple injections and combustions per rotation cycle. (Cited on page 1.)

Asato, K., Wada, H., Hiruma, T. & Takeuchi, Y. 1997 Characteristics of flame propagation in a vortex core: validity of a model for flame propagation. *Combust. Flame* **110** (4), 418–428. (Cited on page 105.)

Ashurst, W. T. 1996 Flame propagation along a vortex: the baroclinic push. *Combust. Sci. Tech.* **112** (1), 175–185. (Cited on pages 102 and 106.)

Bailly, C., Bogey, C. & Candel, S. 2010 Modelling of sound generation by turbulent reacting flows. *International Journal of Aeroacoustics* **9** (4), 461–490. (Cited on pages 71, 72, 77 and 79.)

Bailly, C., Bogey, C. & Gloerfelt, X. 2005 Some useful hybrid approaches for predicting aerodynamic noise. *Comptes Rendus Mécanique* **333** (9), 666–675. (Cited on page 4.)

Bake, F., Kings, N., Fischer, A. & I., R. 2008 Experimental investigation of the entropy noise mechanism in aero-engines. *International Journal of Aeroacoustics* **8** (1-2), 125–142. (Cited on page 42.)

Bake, F., Richter, C., Muhlbauer, B., Kings, N., I.Rohle, F.Thiele & B.Noll 2009 The entropy wave generator (ewg): a reference case on entropy noise. *J. Sound Vib.* pp. 574–598. (Cited on page 81.)

Bauerheim, M., Nicoud, F. & Poinsot, T. 2014 Theoretical analysis of the mass balance equation through a flame at zero and non-zero mach numbers. *Combust. Flame* . (Cited on page 92.)

Bauerheim, M., Parmentier, J., Salas, P., Nicoud, F. & Poinsot, T. 2013 An analytical model for azimuthal thermoacoustic modes in an annular chamber fed by an annular plenum. *Combust. Flame* (0), –. (Cited on page 36.)

Bodony, D. J. & Lele, S. K. 2008 On the current status of jet noise predictions using large-eddy simulation. *AIAA Journal* **46**, 364–380. (Cited on page 83.)

Boussinesq, J. 1877 Théorie de l'écoulement tourbillant. *Mém. Présentés par Divers Savants. Acad. Sci. Inst. Fr.* **23**, 46–50. (Cited on page 126.)

Bragg, S. 1963 Combustion noise. *J. Inst. of Fuel* **36**, 12–16. (Cited on page 74.)

Bragg, S. L. 1962 *Rocket engines*. Newnes. (Cited on page 74.)

Burke, S. P. & Schumann, T. E. W. 1928 Diffusion flames. *Industrial and Engineering Chemistry* **20** (10), 998–1005. (Cited on page 168.)

Cabrit, O. 2009 *Modelisation des flux parietaux sur les tuyeres des moteurs a propergol solide*. PhD Thesis, INPT. (Cited on pages 114 and 133.)

Candel, S. 1972 Acoustic transmission and reflection by a shear discontinuity separating hot and cold regions. *J. Sound Vib.* **24**, 87–91. (Cited on page 80.)

Candel, S. 1995 *Mécanique des Fluides*. Dunod, Paris. (Cited on pages 44, 50 and 138.)

Charlette, F., Veynante, D. & Meneveau, C. 2002 A power-law wrinkling model for LES of premixed turbulent combustion: Part I - non-dynamic formulation and initial tests. *Combust. Flame* **131**, 159–180. (Cited on page 104.)

Chen, L. S., Bomberg, S. & Polifke, W. 2014 On the jump conditions for flow perturbations across a moving heat source. In *Interational Congress on Sound and Vibration*. (Cited on page 92.)

Chiu, H. . H. & Summerfield, M. 1974 Theory of combustion noise. *Acta Astronautica* **1**, 967–984. (Cited on page 75.)

Chomiak, J. 1977 Dissipation fluctuations and the structure and propagation of turbulent flames in premixed gases at high reynolds numbers. In *Proc. Combust. Inst.*, , vol. 16, pp. 1665–1673. Elsevier. (Cited on pages 102 and 105.)

Clanet, C. & Searby, G. 1975 Basic principles of aerodynamic noise generation. *Prog. Aerospace Sci.* **16** (1), 31–96. (Cited on page 70.)

Clanet, C. & Searby, G. 1996 On the "tulip flame" phenomenon. *Combust. Flame* **105** (1), 225–238. (Cited on page 108.)

Clavin, P. & Siggia, E. D. 1991 Turbulent premixed flames and sound generation. *Combust. Sci. Tech.* **78**, 147–155. (Cited on page 75.)

Cocks, P., Sankaran, V. & Soteriou, M. 2013 Is les of reacting flows predictive? part 1: Impact of numerics. In *51st AIAA Aerospace Sciences Meeting including the New Horizons Forum and Aerospace Exposition*. (Cited on page 39.)

Crighton, D. G., Dowling, A. P., Williams, J. E. F., Heckl, M. & Leppington, F. 1992 *Modern methods in analytical acoustics*. Springer Verlag, New-York. (Cited on pages 70, 72 and 79.)

Crocco, L. 1951 Aspects of combustion instability in liquid propellant rocket motors. Part I. *J. American Rocket Society* **21**, 163–178. (Cited on pages 35, 52, 57, 58, 61 and 201.)

Crocco, L. 1952 Aspects of combustion instability in liquid propellant rocket motors. part II. *J. American Rocket Society* **22**, 7–16. (Cited on page 61.)

Crocco, L. 1969 Research on combustion instability in liquid propellant rockets. In *12th Symp. (Int.) on Combustion*, pp. 85–99. The Combustion Institute, Pittsburgh. (Cited on page 90.)

Culick, F. E. C. & Kuentzmann, P. 2006 *Unsteady Motions in Combustion Chambers for Propulsion Systems*. NATO Research and Technology Organization. (Cited on pages 42, 52 and 58.)

Cumpsty, N. & Marble, F. 1977*a* Core noise from gas turbine exhausts. *J. Sound Vib.* **54** (2), 297–309. (Cited on pages 82, 83 and 135.)

Cumpsty, N. A. & Marble, F. E. 1977*b* The interaction of entropy fluctuations with turbine blade rows; a mechanism of turbojet engine noise. *Proc. R. Soc. Lond. A* **357**, 323–344. (Cited on pages 82 and 83.)

Curle, N. 1955 The influence of solid boundaries upon aerodynamic sound. *Proc. R. Soc. Lond.* **Series A**. (Cited on page 71.)

Daneshyar, H. & Hill, P. 1987 The structure of small-scale turbulence and its effect on combustion in spark ignition engines. *Prog. Energy Comb. Sci.* **13** (1), 47–73. (Cited on page 105.)

De Laval, G. 1894 de laval steam turbine. US Patent 522,066. (Cited on page 44.)

De Oliviera, A. 2015 Unsteady simulations with a high-order CFD code. *Tech. Rep.* WN_CFD_15_6. CERFACS. (Cited on page 128.)

DeHoff, R. 2006 *Thermodynamics in materials science*. CRC Press. (Cited on pages 13 and 19.)

Doak, P. E. 1973 Fundamentals of aerodynamic sound theory and flow duct acoustics. *J. Sound Vib.* **28**, 527–561. (Cited on page 71.)

Domingo, P. & Vervisch, L. 2007 Dns of partially premixed flame propagating in a turbulent rotating flow. *Proc. Combust. Inst.* **31** (1), 1657–1664. (Cited on pages 107 and 206.)

Domingo, P., Vervisch, L. & Veynante, D. 2007 Large-eddy simulation of a lifted methane jet flame in a vitiated coflow. *Combust. Flame* **152**, 415–432. (Cited on page 114.)

Dowling, A. P. 1995 The calculation of thermoacoustic oscillations. *J. Sound Vib.* **180** (4), 557–581. (Cited on page 92.)

Ducros, F., Comte, P. & Lesieur, M. 1996 Large-eddy simulation of transition to turbulence in a boundary layer developing spatially over a flat plate. *J. Fluid Mech.* **326**, 1–36. (Cited on page 130.)

Duran, I. 2013 *Prediction of combustion noise in modern aero engines combining large eddy simulations and analytical methods.*. PhD Thesis, INPT. (Cited on page 152.)

Duran, I., Leyko, M., Moreau, S., Nicoud, F. & Poinsot, T. 2013*a* Computing combustion noise by combining Large Eddy Simulations with analytical models for the propagation of waves through turbine blades. *Comptes Rendus de l'Académie des Sciences - Mécanique* **341** (1-2), 131–140. (Cited on page 83.)

Duran, I., Leyko, M., Moreau, S., Nicoud, F. & Poinsot, T. 2013*b* Computing combustion noise by combining large eddy simulations with analytical models for the propagation of waves through turbine blades. *Comptes Rendus Mécanique* **341** (1), 131–140. (Cited on page 135.)

Duran, I. & Moreau, S. 2011 Analytical and numerical study of the entropy wave generator experiment on indirect combustion noise. In *17th AIAA/CEAS Aeroacoustics Conference - AIAA-2011-2829*. Portland, Oregon. (Cited on page 151.)

Duran, I. & Moreau, S. 2013 Solution of the quasi-one-dimensional linearized euler equations using flow invariants and the magnus expansion. *J. Fluid Mech.* **723**, 190–231. (Cited on pages 42, 52, 82, 135, 151 and 200.)

Eichler, C. & Sattelmayer, T. 2011 Experiments on flame flashback in a quasi-2d turbulent wall boundary layer for premixed methane-hydrogen-air mixtures. *J. Eng. Gas Turb. and Power* **133** (1), 011503. (Cited on page 102.)

Fabre, B., Gilbert, J., Hirschberg, A. & Pelorson, X. 2012 Aeroacoustics of musical instruments. *Ann. Rev. Fluid Mech* **44**, 1–25. (Cited on page 73.)

Fritz, J., Kröner, M. & Sattelmayer, T. 2004 Flashback in a swirl burner with cylindrical premixing zone. *J. Eng. Gas Turb. and Power* **126** (2), 276–283. (Cited on page 101.)

Germano, M., Piomelli, U., Moin, P. & Cabot, W. 1991 A dynamic subgrid-scale eddy viscosity model. *Phys. Fluids* **3** (7), 1760–1765. (Cited on page 130.)

Goh, C. S. & Morgans, A. S. 2011 The effect of entropy wave dissipation and dispersion on thermoacoustic instability in a model combustor. In *17th AIAA/CEAS Aeroacoustics Conference - AIAA-2011-2914*. Portland. (Cited on page 80.)

Goldstein, M. E. 1976 *Aeroacoustics*. McGraw-Hill, New York. (Cited on page 70.)

Goodwin, D. G. 2009 Cantera code site. (Cited on page 165.)

Goy, C. J., James, S. R. & Rea, S. 2005 *Monitoring combustion instabilities: E. ON UK's experience*, , vol. 210. AIAA. (Cited on page 35.)

Granet, V., Vermorel, O., Leonard, T., Gicquel, L., & Poinsot, T. 2010 Comparison of nonreflecting outlet boundary conditions for compressible solvers on unstructured grids. *AIAA Journal* **48** (10), 2348–2364. (Cited on pages 30 and 129.)

Grönstedt, T., Irannezhad, M., Lei, X., Thulin, O. & Lundbladh, A. 2014 First and second law analysis of future aircraft engines. *J. Eng. Gas Turb. and Power* **136** (3), 031202. (Cited on page 1.)

Gruber, A., Chen, J., Valiev, D. & Law, C. 2012 Direct numerical simulation of premixed flame boundary layer flashback in turbulent channel flow. *J. Fluid Mech.* **709**, 516–542. (Cited on pages 102 and 107.)

Gu, K., Chen, J. & Kharitonov, V. L. 2003 *Stability of time delay systems*. Springer. (Cited on page 63.)

Gullaud, E., Mendez, S., Sensiau, C., Nicoud, F. & Poinsot, T. 2009 Effect of multiperforated plates on the acoustic modes in combustors. *C. R. Acad. Sci.Mécanique* **337** (6-7), 406–414. (Cited on page 200.)

Gad-el Hak, M. 1995 Questions in fluid mechanics. *Journal of Fluids Engineering* **117**, 3–5. (Cited on page 22.)

Han, J., Dutta, S. & Ekkad, S. 2000 *Gas Turbine Heat Transfer and Cooling Technology*. Taylor & Francis, New York, NY, USA. (Cited on page 42.)

Hasegawa, T., Michikami, S., Nomura, T., Gotoh, D. & Sato, T. 2002 Flame development along a straight vortex. *Combust. Flame* **129** (3), 294–304. (Cited on pages 108, 116 and 117.)

Hasegawa, T., Nishikado, K. & Chomiak, J. 1995 Flame propagation along a fine vortex tube. *Combust. Sci. Tech.* **108** (1-3), 67–80. (Cited on page 104.)

Hasegawa, T., Nishikado, K. & Chomiak, J. 1996 Effect of density ratio on flame propagation along a vortex tube . *Proc. Combust. Inst.* **26** (1), 291–297. (Cited on page 116.)

Hasegawa, T., Nishiki, S. & Michikami, S. 2000 Mechanism of flame propagation along a vortex tube. (Cited on page 107.)

Hassan, H. 1974 Scaling of combustion generated noise. *J. Fluid Mech.* **49**, 445–453. (Cited on page 75.)

Hendricks, E. S. 2011 Development of an open rotor cycle model in npss using a multi-design point approach. In *ASME 2011 Turbo Expo: Turbine Technical Conference and Exposition*, pp. 441–450. American Society of Mechanical Engineers. (Cited on page 1.)

Hirschfelder, J. O., Curtiss, F. & Bird, R. B. 1964 *Molecular theory of gases and liquids*. John Wiley & Sons. (Cited on page 23.)

Howe, M. S. 1975 The generation of sound by aerodynamic sources in an homogeneous steady flow. *J. Fluid Mech.* **67** (3), 597–610. (Cited on page 71.)

Howe, M. S. 1979 On the theory of unsteady high reynolds number flow through a circular aperture. *Proc. R. Soc. Lond. A, Mathematical and Physical Sciences* **366** (1725), 205–223. (Cited on page 159.)

Howe, M. S. 2010 Indirect combustion noise. *J. Fluid Mech.* **659**, 267–288. (Cited on pages 81 and 200.)

Huang, Y. & Yang, V. 2009 Dynamics and stability of lean-premixed swirl-stabilized combustion. *Prog. Energy Comb. Sci.* **35** (4), 293–364. (Cited on page 2.)

Huber, J. & Illa, S. 2007 Jet noise assessment and sensitivity at aircraft level. *AIAA Paper* **3728**. (Cited on pages 3 and 4.)

Huet, M. & Giauque, A. 2013 A nonlinear model for indirect combustion noise through a compact nozzle. *J. Fluid Mech.* **733**, 268–301. (Cited on pages 52, 80 and 82.)

Hurle, I. R., Price, R. B., Sugden, T. M. & Thomas, A. 1968 Sound emission from open turbulent premixed flames. *Proc. R. Soc. Lond. A* **303** (409). (Cited on page 75.)

ICAO 2007 Outlook for Air Transport to the Year 2025. *Tech. Rep.* September. International Civil Aviation Organization. (Cited on page 3.)

Ihme, M., Bodony, D. & Pitsch, H. 2005 Towards the prediction of combustion-generated noise in non-premixed turbulent flames using large-eddy simulation. *CTR Annual Research Briefs* pp. 311–323. (Cited on page 77.)

Ihme, M., Pitsch, H. & Bodony, H. 2009 Radiation of noise in turbulent flames. *Proc. Combust. Inst.* **32**, 1545–1554. (Cited on page 77.)

Ishizuka, S. 1990 On the flame propagation in a rotating flow field. *Combust. Flame* **82** (2), 176–190. (Cited on page 108.)

Ishizuka, S. 2002 Flame propagation along a vortex axis. *Prog. Energy Comb. Sci.* **28** (6), 477–542. (Cited on pages 107, 191 and 206.)

Ishizuka, S. & Hirano, T. 1993 Behavior of propagating flame in a rotating flow-field. *Prog. in Astronautics and Aeronautics* **151**, 284–284. (Cited on page 108.)

Ishizuka, S. & Hirano, T. 1994 Aerodynamic structure of the propagating flame in a rotating combustible mixture. *Nensho-no-Kagakuto-Gijutu* **2**, 15–26. (Cited on page 105.)

Ishizuka, S., Murakami, T., Hamasaki, T., Koumura, K. & Hasegawa, R. 1998 Flame speeds in combustible vortex rings. *Combust. Flame* **113** (4), 542–553. (Cited on pages 106, 107 and 108.)

Jarosinski, J., Lee, J. & Knystautas, R. 1988 Interaction of a vortex ring and a laminar flame. In *22nd Symp. (Int.) on Combustion*, pp. 505–514. The Combustion Institute, Pittsburgh. (Cited on page 104.)

Jiménez, C., Haghiri, A., Brear, M., Talei, M. & Hawkes, E. 2014 Sound generation by premixed flame annihilation with full and simple chemistry. *Proc. Combust. Inst.* . (Cited on page 77.)

Jones, W. P. & Launder, B. E. 1972 The prediction of laminarization with a 2-equation model of turbulence. *Int. J. Heat and Mass Transfer* **15**, 301. (Cited on page 126.)

Kadowaki, S. & Hasegawa, T. 2005 Numerical simulation of dynamics of premixed flames: flame instability and vortex–flame interaction. *Prog. Energy Comb. Sci.* **31** (3), 193–241. (Cited on pages 104 and 107.)

Karagozian, A. R. & Marble, F. E. 1986 Study of a diffusion flame in a stretched vortex. *Combust. Sci. Tech.* **46**, 65–84. (Cited on page 104.)

Keller, J. O., Vaneveld, L., Korschelt, D., Hubbard, G. L., Ghoniem, A. F., Daily, J. W. & Oppenheim, A. K. 1982 Mechanism of instabilities in turbulent combustion leading to flashback. *AIAA Journal* **20** (2), 254–262. (Cited on page 102.)

Kiesewetter, F., Hirsch, C., Fritz, J., Kroner, M. & Sattelmayer, T. 2003 Two-dimensional flashback simulation in strongly swirling flows. In *ASME Turbo Expo 2003, collocated with the 2003 International Joint Power Generation Conference*, pp. 293–300. American Society of Mechanical Engineers. (Cited on page 103.)

Kiesewetter, F., Konle, M. & Sattelmayer, T. 2007 Analysis of combustion induced vortex breakdown driven flame flashback in a premix burner with cylindrical mixing zone. *J. Eng. Gas Turb. and Power* **129** (4), 929–936. (Cited on page 103.)

Kim, J., Moin, P. & Moser, R. 1987 Turbulence statistics in fully developed channel flow at low Reynolds number. *J. Fluid Mech.* **177**, 133–166. (Cited on page 132.)

Kitoh, O. 1991 Experimental study of turbulent swirling flow in a straight pipe. *J. Fluid Mech.* **225**, 445–479. (Cited on pages 182, 183 and 184.)

Klein, S. A. & Kok, J. B. W. 1999 Sound Generation by Turbulent Non-premixed Flames. *Combust. Sci. Tech.* **149**, 267–295. (Cited on page 75.)

Knipschild, P. 1977 VIII. Medical effects of aircraft noise: review and literature. *International archives of occupational and environmental health* **40** (3), 201–4. (Cited on page 2.)

Kolmogorov, A. 1942 Equations of motion of an incompressible turbulent fluid. *Izv Akad Nauk SSSR Ser Phys* **6**, 56–58. (Cited on page 126.)

Kolmogorov, A. N. 1941 The local structure of turbulence in incompressible viscous fluid for very large reynolds numbers. *C. R. Acad. Sci., USSR* **30**, 301. (Cited on page 124.)

Kröner, M., Fritz, J. & Sattelmayer, T. 2002 Flashback limits for combustion induced vortex breakdown in a swirl burner. *J. Eng. Gas Turb. and Power* **125** (3), 693–700. (Cited on page 103.)

Lamraoui, A. 2011 *Acoustique et dynamique de flamme dans un foyer turbulent prémélangé swirlé : application à l'étude du bruit de combustion dans les chambres de turbines à gaz*. PhD Thesis, École Centrale Paris. (Cited on pages 157 and 205.)

Lapeyre, C., Mazur, M., Scouflaire, P., Richecoeur, F., Ducruix, S. & Poinsot, T. 2015 Acoustically induced vortex core flashback in a staged swirl-stabilized combustor. *Under consideration for publication in Combust. Flame* . (Cited on page 206.)

Lewis, B. & von Elbe, G. 1943 Stability and structure of burner flames. *J. Chem. Phys.* **11** (2), 75–97. (Cited on page 102.)

Leyko, M. 2010 *Mise en oeuvre et analyse de calculs aéroacoustiques de type SGE pour la prévision du bruit de chambres de combustion aéronautiques*. Phd thesis, INP Toulouse. (Cited on pages 12, 69, 86, 87, 89, 90, 91, 92, 93, 94, 95, 96, 97, 98, 99 and 205.)

Leyko, M., Duran, I., Moreau, S., Nicoud, F. & Poinsot, T. 2013 Simulation and modelling of the waves transmission and generation in a stator blade row in a combustion-noise framework. *JSV* **submitted**. (Cited on page 83.)

Leyko, M., Moreau, S., Nicoud, F. & Poinsot, T. 2010 Waves transmission and generation in turbine stages in a combustion-noise framework. In *16th AIAA/CEAS AeroAcoustics Conference*. (Cited on page 83.)

Leyko, M., Nicoud, F., Moreau, S. & Poinsot, T. 2008 Numerical and analytical investigation of the indirect noise in a nozzle. In *Proc. of the Summer Program*, pp. 343–354. Center for Turbulence Research, NASA AMES, Stanford University, USA. (Cited on page 81.)

Leyko, M., Nicoud, F. & Poinsot, T. 2009 Comparison of direct and indirect combustion noise mechanisms in a model combustor. *AIAA Journal* **47** (11), 2709–2716. (Cited on pages 82, 88 and 99.)

Lieuwen, T. & Yang, V. 2005 *Combustion Instabilities in Gas Turbine Engines. Operational Experience, Fundamental Mechanisms and Modeling*. Prog. in Astronautics and AeronauticsAIAA Vol 210. (Cited on page 2.)

Lieuwen, T. & Zinn, B. T. 1998 The role of equivalence ratio oscillations in driving combustion instabilities in low nox gas turbines. *Proc. Combust. Inst.* **27**, 1809–1816. (Cited on page 36.)

Lighthill, M. J. 1951 On sound generated aerodynamically. *Proc. R. Soc. Lond.* . (Cited on page 71.)

Lighthill, M. J. 1952 On sound generated aerodynamically. i. general theory. *Proc. R. Soc. Lond. A, Mathematical and Physical Sciences* **211** (1107), 564–587. (Cited on pages 25 and 72.)

Lilley, G. M. 1974 On the noise from jets. Agard cp-131. (Cited on page 71.)

Liu, J. T. C. 1977 Aerodynamic sound in a relaxing medium. *J. Fluid Mech.* **83** (04), 775. (Cited on page 75.)

Liu, Y., Dowling, A. P., Swaminathan, N. & Dunstan, T. D. 2012 Spatial correlation of heat release rate and sound emission from turbulent premixed flames. *Combust. Flame* **159** (7), 2430–2440. (Cited on page 77.)

Liu, Y., Dowling, A. P., Swaminathan, N., Morvant, R., Macquisten, M. A. & Caracciolo, L. F. 2014 Prediction of combustion noise for an aeroengine combustor. *J. Prop. Power* **30** (1), 114–122. (Cited on page 4.)

Lodato, G., Domingo, P. & L., V. 2008 Three-dimensional boundary condtions for direct and large-eddy simulation of compressible viscous flow. *J. Comput. Phys.* **227** (10), 5105–5143. (Cited on page 30.)

Lovachev, L. 1976 On flame propagation in vortices. *Combust. Flame* **27**, 125–127. (Cited on pages 102 and 105.)

Marble, F. E. & Candel, S. 1974 Acoustic attenuation by vaporization of liquid droplets. application to noise reduction in fans and ducts. In *7th Fluid and Plasma Dynamics Conference* (ed. A. p. 74-526). Palo Alto. (Cited on page 75.)

Marble, F. E. & Candel, S. 1977*a* Acoustic disturbances from gas nonuniformities convected through a nozzle. *J. Sound Vib.* **55**, 225–243. (Cited on pages 20, 42, 81, 88, 150 and 151.)

Marble, F. E. & Candel, S. 1977*b* Acoustic disturbances from gas nonuniformities convected through a nozzle. *J. Sound Vib.* **55**, 225–243. (Cited on pages 70, 80, 135 and 150.)

Martin, C., Benoit, L., Sommerer, Y., Nicoud, F. & Poinsot, T. 2006 LES and acoustic analysis of combustion instability in a staged turbulent swirled combustor. *AIAA Journal* **44** (4), 741–750. (Cited on page 201.)

McCormack, P., Scheller, K., Mueller, G. & Tisher, R. 1972 Flame propagation in a vortex core. *Combust. Flame* **19** (2), 297–303. (Cited on pages 105 and 108.)

Mendez, S. & Eldredge, J. 2009 Acoustic modeling of perforated plates with bias flow for large-eddy simulations. *J. Comput. Phys.* **228** (13), 4757–4772. (Cited on page 159.)

Meneveau, C. & Poinsot, T. 1991 Stretching and quenching of flamelets in premixed turbulent combustion. *Combust. Flame* **86**, 311–332. (Cited on page 104.)

Métais, O. & Lesieur, M. 1992 Spectral large-eddy simulation of isotropic and stably stratified turbulence. *J. Fluid Mech.* **239**, 157–194. (Cited on page 130.)

Metghalchi, M. & Keck, J. C. 1980 Laminar burning velocity of propane-air mixtures at high temperature and pressure. *Combust. Flame* **38**, 143–154. (Cited on pages 165 and 167.)

Moase, W., Brear, M. & Manzie, C. 2007 The forced response of choked nozzles and supersonic diffusers. *Journal of Fluid Mechanics* **585**, 281–304. (Cited on pages 80 and 151.)

Morfey, C. L. 1973 Amplification of aerodynamic noise by convected flow inhomogeneities. *J. Sound Vib.* **31**, 391–397. (Cited on pages 21 and 31.)

Morrell, S., Taylor, R. & Lyle, D. 1997 A review of health effects of aircraft noise. *Australian and New Zealand journal of public health* **21** (2), 221–36. (Cited on page 3.)

Motheau, E., Méry, Y., Nicoud, F. & Poinsot, T. 2013 Analysis and modeling of entropy modes in a realistic aeronautical gas turbine. *J. Eng. Gas Turb. and Power* **135** (9), 092602. (Cited on page 203.)

Muthukrishnan, M., Strahle, W. & Neale, D. 1978 Separation of hydrodynamic, entropy, and combustion noise in a gas turbine combustor. *AIAA Journal* **16** (4), 320–327. (Cited on page 81.)

Nicoud, F., Baya Toda, H., Cabrit, O., Bose, S. & Lee, J. 2011 Using singular values to build a subgrid-scale model for large eddy simulations. *Phys. Fluids* **23** (8), 085106. (Cited on pages 130 and 163.)

Nicoud, F., Benoit, L., Sensiau, C. & Poinsot, T. 2007 Acoustic modes in combustors with complex impedances and multidimensional active flames. *AIAA Journal* **45**, 426–441. (Cited on page 134.)

Nicoud, F. & Ducros, F. 1999 Subgrid-scale stress modelling based on the square of the velocity gradient. *Flow, Turb. and Combustion* **62** (3), 183–200. (Cited on pages 130 and 163.)

Patterson, G. 1938 Modern diffuser design: The efficient transformation of kinetic energy to pressure. *Aircraft Engineering and Aerospace Technology* **10** (9), 267–273. (Cited on page 173.)

Peters, N. 2001 *Turbulent combustion*. Cambridge University Press. (Cited on page 104.)

Phillips, O. M. 1960 On the generation of sound by supersonic turbulent shear layers. *J. Fluid Mech.* **9**, 1–28. (Cited on pages 71 and 75.)

Pitsch, H. 2006 Large eddy simulation of turbulent combustion. *Ann. Rev. Fluid Mech* **38**, 453–482. (Cited on page 104.)

Poinsot, T., Echekki, T. & Mungal, M. G. 1992 A study of the laminar flame tip and implications for premixed turbulent combustion. *Combust. Sci. Tech.* **81** (1-3), 45–73. (Cited on pages 41, 129, 160 and 213.)

Poinsot, T. & Lele, S. 1992 Boundary conditions for direct simulations of compressible viscous flows. *J. Comput. Phys.* **101** (1), 104–129. (Cited on pages 30 and 211.)

Poinsot, T. & Veynante, D. 2011 *Theoretical and Numerical Combustion*. Third Edition (www.cerfacs.fr/elearning). (Cited on pages 36, 52, 56, 61, 93, 98, 104, 105, 118, 127, 138, 167 and 168.)

Poinsot, T., Veynante, D. & Candel, S. 1991 Quenching processes and premixed turbulent combustion diagrams. *J. Fluid Mech.* **228**, 561–605. (Cited on page 104.)

Pope, S. B. 2000 *Turbulent flows*. Cambridge University Press. (Cited on pages 124, 126, 131, 132 and 133.)

Powell, A. 1964 Theory of vortex sound. *J. Acous. Soc. Am.* **36** (1), 177–195. (Cited on page 71.)

Putnam, A. A. & Faulkner, L. 1983 An overview of combustion noise. *J. Energy* **7** (6), 458–469. (Cited on page 74.)

Qin, Z., Lissianski, V. V., Yang, H., Gardiner, W. C., Davis, S. G. & Wang, H. 2000 Combustion chemistry of propane: a case study of detailed reaction mechanism optimization. *Proc. Combust. Inst.* **28** (2), 1663–1669. (Cited on pages 165, 166, 167 and 169.)

Reichel, T. G., Terhaar, S. & Paschereit, O. 2014 Increasing flashback resistance in lean premixed swirl-stabilized hydrogen combustion by axial air injection. In *Proceeding of ASME Turbo Expo 2014: Turbine Technical Conference and Exposition*, , vol. 4B. American Society of Mechanical Engineers. (Cited on page 159.)

Richardson, L. F. 1922 *Weather Prediction by Numerical Process*, cambridge edn. Cambridge University Press. (Cited on page 124.)

Rienstra, S. W. & Hirschberg, A. 2003 *An introduction to acoustics*. Eindhoven University of Technology. (Cited on pages 27, 31, 52, 79 and 95.)

Roberts, W. L. & Driscoll, J. F. 1991 A laminar vortex interacting with a premixed flame: measured formation of pockets of reactants. *Combust. Flame* **87**, 245–256. (Cited on page 104.)

Saad, M. A. 1985 Compressible fluid flow. *Englewood Cliffs, NJ, Prentice-Hall, Inc., 1985. 570 p.* **1**. (Cited on page 44.)

Sakai, Y. & Ishizuka, S. 1996 The phenomena of flame propagation in a rotating tube. In *Proc. Combust. Inst.*, , vol. 26, pp. 847–853. Elsevier. (Cited on pages 106 and 108.)

Sattelmayer, T. 2003 Influence of the combustor aerodynamics on combustion instabilities from equivalence ratio fluctuations. *J. Eng. Gas Turb. and Power* **125**, 11–19. (Cited on page 82.)

Sattelmayer, T., Mayer, C. & Sangl, J. 2014 Interaction of flame flashback mechanisms in premixed hydrogen-air swirl flames. In *Proceeding of ASME Turbo Expo 2014: Turbine Technical Conference and Exposition*, , vol. 4A. American Society of Mechanical Engineers. (Cited on page 157.)

Scalo, C., Lele, S. K. & Hesselink, L. 2015 Linear and nonlinear modelling of a theoretical travelling-wave thermoacoustic heat engine. *J. Fluid Mech.* **766**, 368–404. (Cited on page 2.)

Schlüter, J., Apte, S., Kalitzin, G., van der Weide, E., Alonso, J. J. & Pitsch, H. 2005 Large-scale integrated LES-RANS simulations of a gas turbine engine. In *Annual Research Briefs*, pp. 111–120. Center for Turbulence Research, NASA Ames/Stanford Univ. (Cited on page 39.)

Schuller, T., Durox, D. & Candel, S. 2002 Dynamics of and noise radiated by a perturbed impinging premixed jet flame. *Combust. Flame* **128**, 88–110. (Cited on page 75.)

Selle, L., Lartigue, G., Poinsot, T., Koch, R., Schildmacher, K.-U., Krebs, W., Prade, B., Kaufmann, P. & Veynante, D. 2004*a* Compressible large-eddy simulation of turbulent combustion in complex geometry on unstructured meshes. *Combust. Flame* **137** (4), 489–505. (Cited on pages 41 and 43.)

Selle, L., Nicoud, F. & Poinsot, T. 2004*b* The actual impedance of non-reflecting boundary conditions: implications for the computation of resonators. *AIAA Journal* **42** (5), 958–964. (Cited on pages 43 and 209.)

Silva, C. 2010 *Numerical study of combustion noise in gas turbines*. PhD Thesis. (Cited on page 205.)

Silva, C. F., Nicoud, F., Schuller, T., Durox, D. & Candel, S. 2013 Combining a Helmholtz solver with the flame describing function to assess combustion instability in a premixed swirled combustor. *Combust. Flame* **160** (9), 1743 – 1754. (Cited on page 201.)

Sinai, Y. 1980 The generation of combustion noise by chemical inhomogeneities in steady, low-Mach-number duct flows. *Journal of Fluid Mechanics* **99**. (Cited on page 75.)

Smagorinsky, J. 1963 General circulation experiments with the primitive equations: 1. the basic experiment. *Mon. Weather Rev.* **91**, 99–164. (Cited on pages 126 and 130.)

Smith, T. J. B. & Kilham, J. K. 1963 Noise generation by open turbulent flames. *J. Acous. Soc. Am.* **35** (5), 715–724. (Cited on page 74.)

Sommerer, Y., Galley, D., Poinsot, T., Ducruix, S., Lacas, F. & Veynante, D. 2004 Large eddy simulation and experimental study of flashback and blow-off in a lean partially premixed swirled burner. *J. Turb.* **5**. (Cited on pages 101 and 102.)

Spalart, P. R. & Watmuff, H. 1993 Experimental and numerical study of a turbulent boundary layer with pressure gradients. *J. Fluid Mech.* **249**, 337–371. (Cited on page 126.)

Stodola, A. 1905 *Steam Turbines*. Ripol Classic Publishing House. (Cited on page 44.)

Stokes, G. G. 1845 printed in 1847. *On the theories of the internal friction of fluids in motion and of the equilibrium and motion of elastic solids.'Transactions of the Cambridge Philosophical Society* **8**, 287–319. (Cited on page 23.)

Stow, S., Dowling, A. & Hynes, T. 2002 Reflection of circumferential modes in a choked nozzle. *Journal of Fluid Mechanics* **467**, 215–239. (Cited on pages 80 and 151.)

Strahle, W. 1978 Combustion noise. *Prog. Energy Comb. Sci.* **4**, 157–176. (Cited on page 75.)

Strahle, W. C. 1971 On combustion generated noise. *J. Fluid Mech.* **49**, 399–414. (Cited on pages 70 and 75.)

Strahle, W. C. 1972 Some results in combustion generated noise. *J. Sound Vib.* **23** (1), 113–125. (Cited on pages 70 and 75.)

Suder, K. L. 2012 Overview of the nasa environmentally responsible aviation project's propulsion technology portfolio. *AIAA Paper* **4038**, 2012. (Cited on page 2.)

Summerfield, M. 1951 A theory of unstable combustion in liquid propellant rocket systems. *Journal of the American Rocket Society* **21** (5), 108–114. (Cited on page 57.)

Sutherland, W. 1893 The viscosity of gases and molecular force. *Philosophical Magazine* **5** (36), 507–531. (Cited on page 23.)

Syred, N. & Beer, J. 1974 Combustion in swirling flows: a review. *Combust. Flame* **23** (2), 143–201. (Cited on pages 40, 101, 102 and 103.)

Talei, M., Brear, M. J. & Hawkes, E. R. 2010 Lewis number and curvature effects on sound generation by premixed flame annihilation. *Annual Research Briefs* . (Cited on page 77.)

Talei, M., Brear, M. J. & Hawkes, E. R. 2011 Sound generation by laminar premixed flame annihilation. *Journal of Fluid Mechanics* **679**, 194–218. (Cited on page 77.)

Talei, M., Brear, M. J., Hawkes, E. R., Nicoud, F. & Cuenot, B. 2009 A Numerical Study of Sound Generation by Premixed Flames. *Proceedings of the Australian Combustion Symposium* pp. 1–4. (Cited on page 77.)

Tam, C. K., Pastouchenko, N. N., Mendoza, J. & Brown, D. 2005 Combustion noise of auxiliary power units. *AIAA Paper* **2829** (11). (Cited on page 81.)

Thibaut, D. & Candel, S. 1998 Numerical study of unsteady turbulent premixed combustion: Application to flashback simulation. *Combust. Flame* **113** (1), 53–65. (Cited on page 102.)

Thomas, A. & Williams, G. T. 1966 Flame noise: sound emmission from spark-ignited bubbles of combustible gas. *Proc. R. Soc. Lond. A* **294**, 449–466. (Cited on pages 74 and 76.)

Thompson, K. W. 1987 Time dependent boundary conditions for hyperbolic systems. *J. Comput. Phys.* **68**, 1–24. (Cited on pages 28, 29 and 129.)

Tran, N., Ducruix, S. & Schuller, T. 2007 Analysis and control of combustion instabilities by adaptive reflection coefficients. In *13th AIAA/CEAS Aeroacoustics Conference, Paper No. AIAA-2007-3716*. (Cited on page 159.)

Tran, N., Ducruix, S. & Schuller, T. 2009 Damping combustion instabilities with perforates at the premixer inlet of a swirled burner. *Proc. Combust. Inst.* **32** (2), 2917–2924. (Cited on pages 159 and 200.)

Trouvé, A. & Poinsot, T. 1994 The evolution equation for the flame surface density. *J. Fluid Mech.* **278**, 1–31. (Cited on page 104.)

Truffaut, J.-M. 1998 *Etude expérimentale de l'origine du bruit émis par les flammes de chalumeaux*. PhD Thesis, Aix-Marseille I. (Cited on page 69.)

Truffin, K., Varoquié, B. & Poinsot, T. 2003 Measurements of transfer functions in reacting flows using large eddy simulations. In *10th International Congress on Sound and Vibration*, pp. 785–793. Stockholm, Sweden. (Cited on pages 35 and 201.)

Tsien, H. S. 1952 The transfer functions of rocket nozzles. *J. American Rocket Society* **22** (3), 139–143. (Cited on page 80.)

Umemura, A. & Tomita, K. 2001 Rapid flame propagation in a vortex tube in perspective of vortex breakdown phenomena. *Combust. Flame* **125** (1), 820–838. (Cited on pages 102 and 107.)

Van Driest, E. R. 1956 On turbulent flow near a wall. *J. Aeronaut. Sci.* **23** (11). (Cited on page 130.)

White, F. 1986 *Fluid mechanics*. International Edition, McGraw-Hill. (Cited on pages 44 and 49.)

Wilcox, D. C. *et al.* 1998 *Turbulence modeling for CFD*, , vol. 2. DCW industries La Canada, CA. (Cited on page 126.)

Williams, F. A. 1985 *Combustion Theory*. Benjamin Cummings, Menlo Park, CA. (Cited on page 104.)

Williams, J. E. F. & Hawkings, D. L. 1969 Sound generated by turbulence and surfaces in arbitrary motion. *Philosophical Transactions of the Royal Society of London* **A264**, 321–342. (Cited on page 71.)

Wintenberger, E. 2004 *Application of steady and unsteady detonation waves to propulsion*. PhD Thesis, California Institute of Technology. (Cited on page 1.)

Wray, A. A. & Hunt, J. C. R. 1989 Algorithms for classifiaction of turbulent structures. In *Proceedings of IUTAM Symposium Topological Fluid Mechanics*, pp. 95–104. (Cited on page 130.)

Xu, L. & Grönstedt, T. 2010 Design and analysis of an intercooled turbofan engine. *J. Eng. Gas Turb. and Power* **132** (11), 114503. (Cited on page 1.)

Yoo, C. & Im, H. 2007 Characteristic boundary conditions for simulations of compressible reacting flows with multi-dimensional, viscous, and reaction effects. *Combust. Theory and Modelling* **11**, 259–286. (Cited on page 129.)

Yoo, C., Wang, Y., Trouvé, A. & Im, H. 2005 Characteristic boundary conditions for direct simulations of turbulent counterflow flames. *Combust. Theory and Modelling* **9**, 617–646. (Cited on page 129.)

Zeldovich, Y. B. 1946 The oxidation of nitrogen in combustion and explosions. *Acta Physicochim. URSS* **21** (4), 577–628. (Cited on page 2.)

Zinn, B. 1972 Longitudinal mode acoustic losses in short nozzles. *J. Sound Vib.* **22** (1), 93 – 105. (Cited on pages 42, 52, 60, 80 and 150.)

Numerical study of thermoacoustic instabilities and flashback in a swirled combustor under choked conditions

Abstract: Civil air traffic increase requires to decrease future aircraft emissions. Aeronautic engine combustor technology has evolved towards Lean Prevaporized Premixed combustion to increase efficiency and reduce noxious emissions. Unfortunately, this technology tends to reduce engine robustness, with a decrease in flame stability and stabilization margins, and an increase in combustion noise. Compressible Large Eddy Simulation (LES), a promising numerical approach to describe full combustors, is used in this Ph.D on an academic test rig of a typical modern combustor flame in confined conditions. This investigation gives insight on the effects of full system dynamics on combustion instabilities, flame flashback and combustion noise. Is shows how these tools can yield understanding of the phenomena controlling flame stability and stabilization, which is essential in order to operate future engines safely.

Keywords: Combustion Noise, Thermoacoustic Instabilties, Flame Flashback, Large Eddy Simulation